PROBABILISTIC MODEL CONSTRAINTS FOR FULL-WAVEFORM INVERSION

by

Odette C. A. de Aragao

© **Copyright by Odette C. A. de Aragao, 2021**

All Rights Reserved

A thesis submitted to the Faculty and the Board of Trustees of the Colorado School of Mines in partial fulfillment of the requirements for the degree of PhD (Geophysics).

Golden, Colorado

Date _____

Signed: _____
Odette C. A. de Aragao

Signed: _____
Dr. Paul Sava
Thesis Advisor

Golden, Colorado

Date _____

Signed: _____
Dr. Paul Sava
Professor and Head
Department of Geophysics

ABSTRACT

A reliable understanding of the Earth's subsurface is one of the main goals of Geophysics. In seismic exploration, for example, an accurate subsurface image is needed for characterization of hydrocarbon reservoirs. Seismic images could be constructed using elastic or anelastic models using techniques like full-waveform inversion (FWI) that represents the state-of-the-art in subsurface model building. FWI operates by minimizing the difference between observed seismic data and data simulated using models subjected to a wave equation. When the FWI objective function is purely based on this data misfit, the inversion could become highly non-linear and ill-posed, which may prevent convergence towards the true subsurface model. For multiparameter FWI, such as elastic or viscoelastic, artifacts due to the interparameter crosstalk and unphysical models that do not represent feasible geological units could arise rendering FWI useless.

In this thesis, I propose to include in the FWI objective function a petrophysical penalty term formulated in a probabilistic framework to constrain elastic and viscoelastic subsurface models. I use petrophysical information, such as that provided by well logs, to build probability density functions (PDFs), representing the model parameter space, and formulate the penalty function such that the update models have to be consistent with this petrophysical distribution. I show that this probabilistic penalty term can be used in different FWI configurations: isotropic or anisotropic models, elastic or anelastic properties, single or multiple distributions representing different lithological units or spatial trends of petrophysical parameters. I validate the proposed method with complex and realistic numerical examples that show that the petrophysical penalty term reduces the ill-posedness and non-linearity nature of FWI, while mitigating the interparameter crosstalk artifacts and ensuring that the inverted models represent feasible geological units. The ability to directly use observed petrophysical information without assuming potentially inaccurate relationships among the

inverted parameters paves the way to define a high-standard for recovering reliable high-resolution subsurface models that simultaneously honor both seismic and petrophysical data. This technique avoids unfeasible model updates in areas where seismic data do not constrain sufficiently the subsurface properties. A similar formulation prevents the inversion from producing models that violate conditions that cause numerical dispersion and instability in wavefield modeling.

The techniques I propose in this thesis have a general character and could be used for a variety of inversion problems supported by multiple geophysical measurements. It can thus inspire new geophysical application that aim to characterize multiple subsurface parameters, while exploiting prior petrophysical information in a consistent and easy to implement numerical optimization framework.

TABLE OF CONTENTS

ABSTRACT iii

LIST OF FIGURES viii

LIST OF ABBREVIATIONS xvi

ACKNOWLEDGMENTS xvii

DEDICATION xix

CHAPTER 1 INTRODUCTION 1

CHAPTER 2 ELASTIC FULL WAVEFORM INVERSION WITH PROBABILISTIC PETROPHYSICAL MODEL CONSTRAINTS 9

2.1 Introduction 10

2.2 Elastic Wavefield Tomography 13

2.3 Examples 20

2.3.1 Gaussian anomalies model 20

2.3.2 Marmousi 2 model 24

2.4 Discussion 38

2.5 Conclusions 39

2.6 Acknowledgments 39

CHAPTER 3 ELASTIC FULL WAVEFIELD INVERSION WITH PROBABILISTIC PETROPHYSICAL CLUSTERING 41

3.1 Introduction 42

3.2 Elastic Wavefield Tomography 46

3.3 Examples 50

3.3.1 Clustered Marmousi 2 model 53

3.3.2 Marmousi 2 model with clustering 70

3.4 Conclusions 75

3.5 Acknowledgments 78

CHAPTER 4 ELASTIC ANISOTROPIC FULL WAVEFORM INVERSION USING PROBABILISTIC PETROPHYSICAL CONSTRAINTS 79

4.1 Introduction 80

4.2 Method 82

4.3 Examples 85

4.4 Conclusions 92

4.5 Acknowledgements 92

CHAPTER 5 VISCOELASTIC FULL-WAVEFORM INVERSION WITH SPATIAL PROBABILISTIC PETROPHYSICAL CONSTRAINTS 95

5.1 Introduction 96

5.2 Theory 100

5.3 Examples 105

5.3.1 Model 1: Rectangular low-velocity anomalies 105

5.3.2 Model 2: BP 2004 Benchmark 112

5.4 Conclusions 120

5.5 Acknowledgements 121

CHAPTER 6 EXPLICIT CONTROL OF NUMERICAL DISPERSION AND INSTABILITY IN WAVEFIELD MODELING AND INVERSION . . 128

6.1 Introduction 128

6.2 Method 130

6.3 Examples 133
6.3.1 Gaussian Anomalies 133
6.3.2 Marmousi model 135
6.4 Conclusions 137
6.5 Acknowledgments 138
CHAPTER 7 CONCLUSION 141
REFERENCES CITED 143
APPENDIX PERMISSIONS FOR CHAPTERS 153

LIST OF FIGURES

Figure 2.1 (a) Example of a λ and μ crossplot. (b) Model PDF associated to the crossplot in panel (a), characterizing the dependence of λ and μ. (c) Distribution of the distance $D(\mathbf{m})$ and its gradient for the distribution shown in (b). Note that high probability models are associated with small values of $D(\mathbf{m})$ and with zero gradients. 17

Figure 2.2 Sketch indicating how each point in the updated model space (red dot) communicates with all cells of the model PDF. Each cell of the model PDF contributes proportionally with its probability value and inverse proportionally to the distance to the analyzed model. 19

Figure 2.3 True λ and μ models and their crossplot in the $\lambda - \mu$ space. The top panels show the sources (dots) located at $x = 0.1\,\text{km}$ and the vertical line corresponds to receivers at $x = 2.4\,\text{km}$. The negative and positive Gaussian anomalies for the λ and μ models are centered at $(1.25, 0.75)\,\text{km}$ and $(1.25, 1.75)\,\text{km}$, respectively. The crossplot shows two linear relationships between λ and μ: corresponding to each of the Gaussian anomalies. 21

Figure 2.4 Updated λ and μ models using the objective function $\mathcal{J}_D$. The Gaussian anomalies are not recovered well and the inverted models present artifacts from inter-parameter crosstalk. The crossplot shows that the parameters do not follow the same trend of the true models (Figure 2.3). . 23

Figure 2.5 Crossplot in the $\lambda - \mu$ space of the true models superimposed by the upper and lower boundaries used in the logarithmic penalty function $\mathcal{J}_L$. The linear barriers ensure that the inversion recovers models confined to this feasible region. 24

Figure 2.6 Updated λ and μ models using the objective function $\mathcal{J}_D + \mathcal{J}_L$. The lines define the upper and lower boundaries used in the logarithmic penalty function $\mathcal{J}_L$. The Gaussian anomalies are not recovered well and the backgrounds are modified during the inversion. 25

Figure 2.7 Updated λ and μ models using the objective function $\mathcal{J}_D + \mathcal{J}_P$. The contours in the crossplot represent the PDF used to define the petrophysical constraint $\mathcal{J}_P$. Both Gaussian anomalies are better recovered for the λ and μ models. 26

Figure 2.8 Comparison between true and recovered models in a vertical profile at $x = 1.0$ km. In the top row, black lines are the true λ model and colored lines are the updated models using the objective function (a) $\mathcal{J}_D$ (red line), (b) $\mathcal{J}_D + \mathcal{J}_{C_L}$ (green line) and (c) $\mathcal{J}_D + \mathcal{J}_{C_P}$ (blue line). In the bottom row, black lines are the true μ model and colored lines are the updated models using the objective function as (d) $\mathcal{J}_D$ (red line), (e) $\mathcal{J}_D + \mathcal{J}_{C_L}$ (green line) and (f) $\mathcal{J}_D + \mathcal{J}_{C_P}$ (blue line). 27

Figure 2.9 Marmousi 2 model: True λ and μ models and their crossplot. The vertical lines correspond to the location of the wells, providing information for the petrophysical constraint. 29

Figure 2.10 Crossplot of λ and μ provided by the well logs indicated in Figure 2.9. The relationship between the model parameters is not linear and does not follow a simple trend. 30

Figure 2.11 Marmousi 2 model: Initial λ and μ models and their crossplot in the $\lambda - \mu$ space. 31

Figure 2.12 Marmousi 2 model: Recovered λ and μ models using objective function $\mathcal{J}_D$. The inverted μ model has more structural details than the λ model. . 32

Figure 2.13 Crossplot of the λ and μ parameters extracted at the well location, superimposed by the upper and lower boundaries used in the logarithmic penalty function $\mathcal{J}_L$. As in the Gaussian example (Figure 2.5), the linear barriers ensure that the inversion recovers models confined to this feasible region. 33

Figure 2.14 Marmousi 2 model: Recovered λ and μ models using objective function $\mathcal{J}_D + \mathcal{J}_L$. The lines in the crossplot define the upper and lower boundaries used in the logarithmic penalty function $\mathcal{J}_L$. The inverted model is forced to be in the middle area of the feasible region, which does not reflect correctly the trend shown in Figure 2.9 for the true model. 34

Figure 2.15 Marmousi 2 model: Recovered λ and μ models using objective function $\mathcal{J}_D + \mathcal{J}_P$ with $a = 5 \times 10^{-8}$. The contours in the crossplot represent the feasible area for the probabilistic constraint $\mathcal{J}_P$. The probabilistic petrophysical constraint leads to better recovered models than the unconstrained inversion (Figure 2.12) or the inversion with approximate analytic constraints (Figure 2.14). 35

Figure 2.16 Marmousi 2 model: Recovered λ and μ models using objective function $\mathcal{J}_D + \mathcal{J}_P$ with $a = 3 \times 10^{-8}$. These recovered model are very similar to the ones shown in Figure 2.15, where $a = 5 \times 10^{-8}$. 36

Figure 2.17 Marmousi 2 model: Recovered λ and μ models using objective function $\mathcal{J}_D + \mathcal{J}_P$ with $a = \times 10^{-9}$. As we use a smaller a than in the previous examples, the impact of the petrophysical penalty term in the object function is greatly reduced, which leads to poor recovered models compared to the ones shown in Figures 2.15 and 2.16 where a is equal to, respectively, 5×10^{-8} and 3×10^{-8}. 37

Figure 3.1 Examples of PDFs consisting of (a) two Gaussian functions and (b) two boxcar functions of different sizes and magnitudes. 51

Figure 3.2 Distribution of the distance $D(\mathbf{m})$ and its gradient for the distributions shown in (a) Figure 3.1a and (b) Figure 3.1b. Note that high probability models are associated with small values of $D(\mathbf{m})$ and with zero gradients. 52

Figure 3.3 Clustered Marmousi 2 model: true λ and μ models and their crossplot for experiments A and B. The vertical lines correspond to well locations that provide information for the petrophysical penalty term. 54

Figure 3.4 Crossplot of λ and μ provided by the well logs indicated in Figure 3.3. Note that different lithologies are well defined and isolated in the petrophysical space. 55

Figure 3.5 Experiment A: Initial λ and μ models and their crossplot in the $\lambda - \mu$ space. We obtain these initial models by smoothing the true model, which helps the inversion to converge to a global minimum. 56

Figure 3.6 Experiment A: (a) vertical and (b) horizontal components of the data residual. The predicted data are computed using the initial models shown in Figure 3.5. 57

Figure 3.7 Experiment A: Recovered λ and μ models obtained using the objective function $\mathcal{J}_D$. Note that the μ model has more structural details than the λ model 58

Figure 3.8 Experiment A: (a) vertical and (b) horizontal components of the data residual for the unconstrained inversion. The predicted data are computed using the recovered models shown in Figure 3.7. 59

Figure 3.9 (a) PDF associated with the term $\mathcal{J}_{P1}$ and (b) PDF associated with the term $\mathcal{J}_{P2}$. We estimate the PDFs in (a) and (b) from the well logs shown in Figure 3.4. 59

Figure 3.10 Experiment A: Recovered λ and μ models using the objective function $\mathcal{J}_D + \mathcal{J}_{P1}$. The green contours overlain on the crossplot illustrate the probabilistic penalty term based on a single PDF $\mathcal{J}_{P1}$. 60

Figure 3.11 Experiment A: (a) vertical and (b) horizontal components of the data residual for the inversion using the objective function $\mathcal{J}_D + \mathcal{J}_{P1}$. The predicted data are computed using the recovered models shown in Figure 3.10. 61

Figure 3.12 Experiment A: Recovered λ and μ models using the objective function $\mathcal{J}_D + \mathcal{J}_{P2}$. The contours with different colors overlain on the crossplot illustrate multiple PDFs used in the probabilistic penalty $\mathcal{J}_{P2}$. Note that three separate PDFs are used to constrain the model, although we display them together for simplicity. 62

Figure 3.13 Experiment A: (a) vertical and (b) horizontal components of the data residual for the inversion using the objective function $\mathcal{J}_D + \mathcal{J}_{P2}$. The predicted data are computed using the recovered models shown in Figure 3.12. 63

Figure 3.14 Experiment B: Initial λ and μ models and their crossplot in the $\lambda - \mu$ space. As these models are far from the true models (Figure 3.3), the inversion does not converge to a global minimum. 65

Figure 3.15 Experiment B: illustration of cycle skipping with the 1D starting model. The variable density plot in the background represents the vertical component of the simulated data computed using the initial 1D model (Figure 3.14) and the overlaying black and white wiggles are the vertical component of observed data. 66

Figure 3.16 Experiment B: Recovered λ and μ models using the objective function $\mathcal{J}_D$. The inaccuracy of the initial models (Figure 3.14) leads FWI a local minimum. 67

Figure 3.17 Experiment B: Recovered λ and μ models using the objective function $\mathcal{J}_D + \mathcal{J}_{P1}$. The green contours overlain on the crossplot illustrate the probabilistic penalty term based on a single PDF. 68

Figure 3.18 Experiment B: Recovered λ and μ models using the objective function $\mathcal{J}_D + \mathcal{J}_{P2}$. The contours with different colors overlain on the crossplot illustrate the multiple PDFs used in the probabilistic penalty. 69

Figure 3.19 True λ and μ models and their crossplot for the inversion with clustering. The vertical lines correspond to well locations that provide information for the petrophysical penalty term. 71

Figure 3.20 Initial λ and μ models and their crossplot in the $\lambda - \mu$ space for the inversion with clustering. 72

Figure 3.21 Recovered λ and μ models obtained using the objective function $\mathcal{J}_D$ for the inversion with clustering. 73

Figure 3.22 Crossplot of λ and μ provided by the well logs indicated in Figure 3.19. Note that different lithologies are not distinct in the petrophysical space. . 74

Figure 3.23 (a) PDF associated with the term $\mathcal{J}_{P1}$ and (b) PDF associated with the term $\mathcal{J}_{P2}$ for the inversion with clustering. We estimate the PDFs in (a) and (b) from the well logs shown in Figure 3.22. 74

Figure 3.24 Recovered λ and μ models using the objective function $\mathcal{J}_D + \mathcal{J}_{P1}$ for the inversion with clustering. The green contours overlain on the crossplot illustrate the probabilistic penalty term based on a single PDF $\mathcal{J}_{P1}$. . . . 76

Figure 3.25 Experiment A: Recovered λ and μ models using the objective function $\mathcal{J}_D + \mathcal{J}_{P2}$ for the inversion with clustering. The contours with different colors overlain on the crossplot illustrate the multiple PDFs used in the probabilistic penalty $\mathcal{J}_{P2}$. 77

Figure 4.1 True (a) V_{P0}, (b) V_{S0}, (c) $V_{P,hor}$ and (d) $V_{P,nmo}$ models. The vertical lines correspond to well locations that provide information for the petrophysical penalty term. 86

Figure 4.2 Initial (a) V_{P0}, (b) V_{S0}, (c) $V_{P,hor}$ and (d) $V_{P,nmo}$ models, which we obtain by smoothing the true models. 87

Figure 4.3 Contours representing 2D projections of the 4D PDF associated with the term $\mathcal{J}_{P1}$ for the parameters (a) V_{P0} and V_{S0}, (b) V_{P0} and $V_{P,nmo}$, (c) V_{P0} and $V_{P,hor}$, (d) V_{S0} and $V_{P,nmo}$, (e) V_{S0} and $V_{P,hor}$, and (f) $V_{P,hor}$ and $V_{P,nmo}$. In each plot, the contour lines surround locations of peak, such that the probability values increase from the edge to the center. We estimate these PDFs from the well logs shown in Figure 4.1. 88

Figure 4.4 Recovered (a) V_{P0}, (b) V_{S0}, (c) $V_{P,hor}$ and (d) $V_{P,nmo}$ models using the objective function $\mathcal{J}_D$. 89

Figure 4.5 Recovered (a) V_{P0}, (b) V_{S0}, (c) $V_{P,hor}$ and (d) $V_{P,nmo}$ models using the objective function $\mathcal{J}_D + \mathcal{J}_{P1}$. 90

Figure 4.6 Recovered (a) V_{P0}, (b) V_{S0}, (c) $V_{P,hor}$ and (d) $V_{P,nmo}$ models using the objective function $\mathcal{J}_D + \mathcal{J}_{P2}$. 91

Figure 4.7 Vertical component of the data residuals using (a) the initial models (Figure 4.2), (b) the models recovered using the objective function $\mathcal{J}_D$ (Figure 4.4), (c) or $\mathcal{J}_D + \mathcal{J}_{P1}$ (Figure 4.5) (d) or $\mathcal{J}_D + \mathcal{J}_{P2}$ (Figure 4.6). . . 93

Figure 4.8 Horizontal component of the data residuals using (a) the initial models (Figure 4.2), (b) the models recovered using the objective function $\mathcal{J}_D$ (Figure 4.4), (c) or $\mathcal{J}_D + \mathcal{J}_{P1}$ (Figure 4.5) (d) or $\mathcal{J}_D + \mathcal{J}_{P2}$ (Figure 4.6). . 94

Figure 5.1 Synthetic models for (a)v_{P0} and (b)Q_{P0}. 107

Figure 5.2 Hypothetical (a) v_P and (b) Q_{P0} logs at $x = 1.0\,\text{km}$ in the model depicted in Figure 5.1. We add random noise to the models to calculate v_P and assume that Q_{P0} is determined using an empirical relationship between seismic attenuation and petrophysical properties. 108

Figure 5.3 The distributions (a) f_1, (b) f_2, (c) f_3, and (d) f_4 using the spatial trends in petrophysical information from the well log in Figure 5.2. . . . 109

Figure 5.4 Mask operators used to constrain PDFs at corresponding spatial locations. Panels (a)-(d) correspond to K_1-K_4. Black regions correspond to 1, and white to 0. 110

Figure 5.5 The distance $D_i(\mathbf{m})$ and its gradient for the distributions (a) f_1, (b) f_2, (c) f_3, and (d) f_4 (Figure 5.3). Note that high probability models are associated with small values of $D_i(\mathbf{m})$ and with zero petrophysical gradients.. 111

Figure 5.6 Recovered (a) v_{P0} and (b) Q_{P0} models obtained using the objective function $\mathcal{J}_D$. The inversion is not able to recover the low velocity anomalies and the deep reflector present in the true models (Figure 5.1). 113

Figure 5.7 Recovered (a) v_{P0} and (b) Q_{P0} models obtained using the objective function $\mathcal{J}_D + \mathcal{J}_P$, where $\mathcal{J}_P$ is based on multiple PDFs, determined considering spatial trends in the available petrophysical data (Figure 5.2). The inverted models are closer to the true models (Figure 5.1) compared to the cases when we use only the data misfit (Figure 5.6). 114

Figure 5.8 BP 2004 Benchmark model: Synthetic models for (a) v_{P0} and (b) Q_{P0}. . 116

Figure 5.9 BP 2004 Benchmark model: Synthetic models for (a) v_{S0} and (b) Q_{S0}. . 117

Figure 5.10 BP 2004 Benchmark model: Initial models, (a) v_{P0} and (b) Q_{P0} used for the viscoelastic waveform inversion. 118

Figure 5.11 BP 2004 Benchmark model: Mask operators (a) K_1 and (b) K_2 used to constrain petrophysical PDFs at corresponding spatial locations. Black regions correspond to 1, and white to 0. 121

Figure 5.12 BP 2004 Benchmark model: The distributions (a) f_1 and (b) f_2 using the spatial trends in petrophysical information from the well logs at $x = 2.1\,\text{km}$ and $x = 3.9\,\text{km}$. 122

Figure 5.13 BP 2004 Benchmark model: The distances (a) $D_1(\mathbf{m})$ and (b) $D_2(\mathbf{m})$, and their gradients. The high probability models are associated with small values of $D_i(\mathbf{m})$ and with zero gradients. 122

Figure 5.14 BP 2004 Benchmark model: Recovered (a) v_{P0} and (b) Q_{P0} models obtained using the objective function $\mathcal{J}_D$. The inversion is not able to recover the low velocity anomalies and the models are contaminated with artifacts due to the interparameter cross-talk between velocity and attenuation parameters. 123

Figure 5.15 BP 2004 Benchmark model: Recovered (a) v_{P0} and (b) Q_{P0} models obtained using the objective function $\mathcal{J}_D + \mathcal{J}_P$, where $\mathcal{J}_P$ is based on multiple PDFs, which are determined considering spatial trends in the available petrophysical data. With petrophysical penalties, the inversion is able to recover the low velocity anomalies in both models. . 124

Figure 5.16 BP 2004 Benchmark model: (a) vertical and (b) horizontal components of the data residual using the initial models (Figure 5.10) for the central shot; (c) vertical and (d) horizontal components of the data residual, where the predicted data is simulated using the models recovered with unconstrained inversion (Figure 5.14) for the central shot; (e) vertical and (f) horizontal components of the data residual, where the predicted data is simulated using the models recovered with constrained inversion (Figure 5.15) for the central shot. 125

Figure 5.17 BP 2004 Benchmark model: normalized objective functions for unconstrained (solid line) and constrained (dashed line) QEFWI. Note how constrained inversion performs better than the unconstrained in terms of both convergence speed and misfit reduction. 126

Figure 5.18 BP 2004 Benchmark model: Comparison between Q_{P0} models: true (black line), initial (pink), and updated models using for the unconstrained (green) and constrained (red) inversion for a vertical profile at $x = 3.75$ km. 127

Figure 6.1 Synthetic models with two positive Gaussian anomalies for the (a) V_P and (b) V_S models centered at $(1.2, 0.75)\,\text{km}$ and $(1.2, 1.75)\,\text{km}$. 134

Figure 6.2 (a) Example of a PDF consisting of boxcar function representing the range of velocities in which the forward simulations remain stable. (b) The distance $D(\mathbf{m})$ and its gradient. Models inside the boxcar function are subjected to zero gradients from the stability constraint, and thus inversion in this region is driven solely by the data misfit. 134

Figure 6.3 Inversion updates for the (a) V_P and (b) V_S models using the objective function $\mathcal{J}_D$ after 5 iterations. The V_S updates below $-20\,\mathrm{m/s}$ cause inversion instabilities. 136

Figure 6.4 Recovered (a) V_P and (b) V_S models using the objective function $\mathcal{J}_D + \mathcal{J}_S$ after 50 iterations. 136

Figure 6.5 Inversion updates for the (a) V_P and (b) V_S models using the objective function $\mathcal{J}_D + \mathcal{J}_S$ after 50 iterations. Note that the inversion does not produce any updates below $-20\,\mathrm{m/s}$ for the V_S model, thus avoiding modeling instability. 137

Figure 6.6 Marmousi 2 model: true V_P and V_S models. 138

Figure 6.7 Marmousi 2 model: initial V_P and V_S models, obtained by smoothing the true models (Figure 6.6). 139

Figure 6.8 Marmousi 2 model: recovered V_P and V_S models using objective function $\mathcal{J}_D$. The inverted V_S model has negative values, which cause wavefield simulation instability. 139

Figure 6.9 Marmousi 2 model: recovered V_P and V_S models using the objective function $\mathcal{J}_D + \mathcal{J}_S$. The stability penalty prevents negative V_S velocities, thus guaranteeing modeling stability. 140

Figure A.1 Permission from *Geophysics* hightlighted in yellow. 153

Figure A.2 Permission from John Wiley and Sons, publisher for *Geophysical Prospecting*. 154

LIST OF ABBREVIATIONS

Center for Wave Phenomena . . . . . CWP

Central-Frequency Shift . . . . . CFS

European Association of Geoscientists & Engineers . . . . . EAGE

Elastic Full-Waveform Inversion . . . . . EFWI

Finite Difference Method . . . . . FDM

Full-Waveform Inversion . . . . . FWI

Ocean Bottom Survey . . . . . OBS

Probability Density Function . . . . . PDF

Projection Onto Convex Sets . . . . . POCS

Viscoelastic Full-Waveform Inversion . . . . . QEFWI

Society of Exploration Geophysicist . . . . . SEG

Society for Industrial and Applied Mathematics . . . . . SIAM

Spectral-Ratio . . . . . SR

Total Variation . . . . . TV

Vertical Transverse Isotropy . . . . . VTI

ACKNOWLEDGMENTS

Throughout the four years of my PhD, I have received a great deal of support and assistance from many people. I would like to start thanking Dr. Paul Sava. Paul cares about students, he listens to them and he always tries to help even when he is very busy (i.e., always). So I consider myself very lucky and proud to have him as my advisor. He accepted me as his student, gave me support in my research with his knowledge and great insights, and he always believed in my potential, even during times that I doubt myself. Paul also helped me to improve my writing and presentation skills, and he is responsible for me not being able to appreciate any passive voice in scientific papers. I will definitely miss our meetings and the moments we had great laughs and honest conversations (I will even miss the "so what?" in my manuscripts). Thank you, Paul!

I would like to thank Jeffrey Shragge, Mahadevan Ganesh, Michael Wakin and Yaoguo Li, who accepted to be my graduate committee members and contributed to my research with insightful comments. Also, I can not measure the support I got from the faculty, staff and students from the Geophysics department, especially from the Center for Wave Phenomena (CWP). I really appreciate all the administrative support from Dawn Umpleby, Gina Schwieger, Emilia Clayton and Noelle Vance. Michelle Szobody, the department would not function without you, thank you. I also want to show my gratitude to Debra Marrufo, who always took good care of me and treated me like her daughter. I really appreciate all the help and support Diane Witters offered me since my first week at Mines.

During my PhD, I have been through good times and tough times, but I was, and am, fortunate to have made awesome friends who were with me for laughs and tears. Daniel Rocha, thank you for being my friend and helping me whenever necessary since 2010. Ivan Lim, my Asian twin brother, I know with my eyes closed that I can count on you anytime. My dear friend Tuğrul Konuk, we have been through a lot together and I am glad to have

shared these past four years with you. I am also honored to have great memories with Azar Hasanov, Can Oren, Jihyun Yang, Jim Simmons, Mandy Schindler, Oscar Jarillo, Thomas Rapstine and Ufuk Durmuş. I enjoyed my time spent with Andrea Damasceno, Iga Pawelec, Khalid Almuteri, Max Velasques, Paul El Khoury, Qifan Liu and Youfang Liu. A special thanks for my Denver and Houston friends, for all the quality time we have spent together. I also cannot forget to thank my friends in Brazil who were always supporting me and cheering for my achievements despite of the physical distance.

From the bottom of my heart, I want to thank my family. My mom, Francisca Costa, is the reason for everything that I am and everything that I do. Her pure love, care and support give me the strength to be strong and overcome the challenges I face in this life. This thesis is for you, mom. To my "cousin-sisters", Sheila Cristina and Sonia Mara, thank you for always being there for me, since I was born. To my godson, Zaion Aquino, whose smile bring light into my life. To all my relatives, thank for your constant love and support.

For my mom, source of unconditional love

CHAPTER 1

INTRODUCTION

Seismic tomography represents the state-of-the-art technique used to estimate physical properties of the subsurface from seismic recorded data (Biondi, 2006; Djebbi and Alkhalifah, 2018; Mora, 1989; Pratt, 1999; Schuster and Quintus-Bosz, 1993; Taillandier et al., 2009; Tarantola, 1984, 1986; Woodward, 1992). Full-waveform inversion (FWI) is the most promising technique among all wavefield tomography methods as it aims to provide a high resolution quantitative description of the subsurface properties by using entire seismic waveforms recorded at the surface or in a borehole (Pratt, 1999; Sirgue and Pratt, 2004; Tarantola, 1984; Virieux and Operto, 2009). FWI is formulated as an inverse problem constrained by a wave equation and conventionally it works by iteratively minimizing an objective function that evaluates the misfit between observed and predicted data. However the objective function based purely on the data misfit is multimodal and thus FWI is a non-linear problem with a non-unique solution.

Multiparameter full-waveform inversion, as elastic full-waveform inversion (EFWI) or anelastic full-waveform inversion (QEFWI) take into account elastic or anelastic phenomena, respectively, and thus adequately describes significant wave propagation mechanisms, such as mode conversions and the amplitude behavior of seismic waves (Plessix, 2006; Pratt, 1990; Tarantola, 1988). However, both EFWI and QEFWI are hampered by significant problems (Operto et al., 2013). Implementations using an elastic or anelastic wave equation, jointly estimate several models of subsurface physical properties, increasing the number of model combinations that can equally well explain the data, thus leading to large ambiguity. Moreover, the different recovered models may have different spatial resolutions, due to the varying wavefield wavelengths of the wave modes most responsible for their behavior. Additionally, different subsurface properties may be coupled by similar radiation patterns

and updates of one parameter could be mapped into the estimation of another, an effect known as interparameter crosstalk, which produces unwanted artifacts that may result in biased and unreliable models. This problem is more severe in QEFWI applications (Kamei and Pratt, 2013; Keating and Innanen, 2019a,b; Malinowski et al., 2011a; Metivier et al., 2015; Operto et al., 2013; Ouellet et al., 2017; Yang et al., 2018). Furthermore, some components of the recovered model parameters can be lithologically implausible or even impossible (e.g., negative Poisson ratio), and not represent feasible lithological units. This effect is due to the fact that model parameters are updated simultaneously, but independently during multiparameter FWI.

A well-known approach to counter the deficiencies related to local minima is to include model regularization in the inversion, which mitigates the ill-posedness and non-uniqueness of the inverse problem (Tarantola, 2005; Tikhonov and Arsenin, 1977). To deal with these challenging situations, one can rely on Tikhonov regularization, which corresponds to adding differentiable quadratic penalties into the objective function. Alternatively, nonquadratic L_1-norm-based regularization, such as total variation, smooths the model by enhancing the sparsity of the spatial gradient of the velocity, thereby preserving the edges. Guitton (2012) uses blocky regularization in order to enforce blockiness in the recovered model thus preserving strong velocity contrasts that better represent layer-based models, for example. Peters and Herrmann (2017) compare the effectiveness of including into the FWI objective function total variation norm constraints in contrast with the total-variation regularization used by Guitton (2012). Additionally, one can include prior information on the unknown model, such as from well logs or geological information, which also regularizes the inverse problem (Asnaashari et al., 2013; Peters et al., 2019; Zhang and Alkhalifah, 2019; Zhang et al., 2018).

Although regularization methods have resulted in enormous progress in ill-posed geophysical inverse problems, challenges remain when the prior information is derived from sources that characterize the model only at few specific locations. As they operate in the spatial domain, the efficiency of regularization methods strongly depends on feasible subsurface

geological information related to the entire studied region. In addition, model regularization techniques do not solve the problem where, because the model parameters are updated simultaneously but independently, different model components can be physically contradictory, creating combinations of model parameters that are lithologically implausible or even impossible. Baumstein (2013) and Peters et al. (2015) use, respectively, projection onto convex sets (POCS), or projection onto intersections of convex sets to constrain acoustic FWI, by imposing velocity bounds (box constraints) and specify a minimum smoothness for the model parameters. The updated models must be at the intersection of all convex sets, leading to stable simulations and geologically feasible recovered models. Manukyan et al. (2018) apply similarity constraints to EFWI to mitigate parameter trade-off artifacts and reconcile the different spatial resolutions of elastic parameters. They show that structurally constrained FWI can deliver higher-quality models when compared to conventional FWI. However, the assumption of structural similarity between different elastic parameters can potentially compromise the final outcome. Peters et al. (2019) use multiple convex and nonconvex constraints sets, using sparse prior information and improve the accuracy of the recovered models while preventing the inversion from converging towards local minima.

As an alternative, one can apply petrophysical constraints in the model parameter space, in order to constrain the relationship between the model parameters during the inversion. Petrophysical data, such as that derived from well logs, can be used to assemble these constraints. Geological constraints represent realistic lithological units by forcing the inverted models to be consistent with known physical relationships. Duan and Sava (2016) and Rocha and Sava (2018) use a logarithmic penalty function to constrain, respectively, elastic wavefield tomography and elastic reflection waveform inversion, assuming a general linear relationship between the model parameters. However, complex models may have a more complex, non-linear relationship between the elastic parameters. Moreover, the logarithmic penalty requires user-defined parameters, and their selection may be arduous, especially when different geological formations are present in the same area. Thus, it is necessary to

define more general and automated petrophysical constraints that provide flexibility and exploit known information available from external sources, e.g. well logs.

In light of the all aforementioned limitations of multiparameter FWI, in this thesis, I develop and apply ways to explicitly incorporate petrophysical information into the objective function of elastic and anelastic FWI through a penalty term that uses probability density functions (PDFs) in the model parameter space. In contrast to previous work, the methodology I propose does not require user-defined parameters or rely on defined analytic relationships between different subsurface parameters, and prevents incorrect model updates in regions where seismic data are inefficient and do not constrain sufficiently the subsurface properties. This novel, general, flexible and automated technique reduces the non-linearity and ill-posed nature of FWI, while avoiding geologically implausible subsurface models of physical parameters and mitigating the artifacts created by interparameter crosstalk, as it links the subsurface parameters during inversion. In addition, the probabilistic petrophysical penalty term weakens the potentially harmful effects of the source radiation pattern, and of limited acquisition aperture. The formulation of the penalty term enable us to also apply it as a stability constraint to ensure that wavefield modeling and inversion is free of numerical dispersion and instability when using the finite-difference method (FDM). My developments establish a high standard and robust foundation for multiparameter inversion by explicitly guiding inversion towards feasible subsurface models in the characteristic geological context of the geophysical inverse problem.

This thesis is structured into chapters that are based on expanded abstracts presented at International conferences and articles that were published or submitted to peer-reviewed journals. Each chapter contains relevant literature review, theory, and numerical examples. Different physics of wave propagation (elastic or anelastic), assumptions about the medium (isotropic or anisotropic), number of PDFs (single or multiple PDFs that are defined using clustering or spatial trends) and types of the constraint (petrophysical or stability) are grouped into the specific chapters:

In chapter 2, titled "Elastic full-waveform inversion with probabilistic petrophysical model constraints", I develop the concept and theory for the petrophysical penalty term based on a single PDF, which is automated calculated without assumptions or analytic bounds. In support of the theoretical development, I perform numerical simulations using isotropic elastic synthetic models of arbitrary complexity and demonstrate that imposing the probabilistic petrophysical penalty term leads to reliable models, while reducing the non-linearity and ill-posed nature of FWI. It also avoids geologically implausible models by mitigating artifacts produced by interparameter crosstalk and maintaining robust and realistic petrophysical relationships between the model parameters. This chapter was presented at a Society of Exploration Geophysicist (SEG) Annual Meeting and ranked in the Top 25 papers, and it was also published in **Geophysics**:

- Aragao, O., Sava, P.C., 2019, Elastic full waveform inversion with probabilistic petrophysical model constraints. Proceedings of the 89th Annual International Meeting, Society of Exploration Geophysicists.

- Aragao, O., Sava, P.C., 2020, Elastic full-waveform inversion with probabilistic petrophysical model constraints, **Geophysics**, 85, no 2, R101-R111.

In chapter 3, titled "Elastic full-waveform inversion with probabilistic petrophysical clustering", I propose to use a petrophysical penalty term based on multiple PDFs, each representing a different lithological unit. In order to do so, I categorize each given model to a specific class using K-means clustering. In support of this work, I perform numerical simulations using isotropic elastic synthetic models, which show the critical effect of the probabilistic penalty term based on multiple PDFs compared to the cases of unconstrained FWI or of a single PDF used to describe the entire model. This chapter was presented at a Society of Exploration Geophysicist (SEG) Annual Meeting, and was also published in **Geophysical Prospecting**:

- Aragao, O., Sava, P.C., 2019, Elastic wavefield tomography with probabilistic petrophysical clustering. Proceedings of the 89th Annual International Meeting, Society of Exploration Geophysicists.

- Aragao, O., Sava, P.C., 2020, Elastic full waveform inversion with probabilistic petrophysical clustering, **Geophysical Prospecting**, 68, no 4, R1341-R1355.

In addition, this chapter was also presented in several workshops:

- Aragao, O., Sava, P.C., 2020, Incorporating probabilistic petrophysical information into elastic full waveform inversion. Workshop Acoustic and Elastic Wave Equation Imaging and Velocity Model Building presented at the 82th EAGE Conference & Exhibition, European Association of Geoscientists & Engineers.

- Aragao, O., Sava, P.C., 2020, A probabilistic approach to incorporate petrophysical information into elastic FWI. Workshop Value in Elastic Imaging and Elastic Full-waveform Inversion presented at the 90th Annual International Meeting, Society of Exploration Geophysicists.

- Aragao, O., Sava, P.C., 2020, Elastic Full-Waveform Inversion With Petrophysical Information In A Probabilistic Approach. Workshop Elastic Imaging and Full waveform inversion for hydrocarbon exploration and production presented at the 3rd Annual Meeting, SIAM Texas-Louisiana Section.

In chapter 4, titled "Elastic anisotropic full-waveform inversion using probabilistic petrophysical constraints", I propose the use of petrophysical penalty term based on multiple PDFs defined for anisotropic media, when the number of model parameters is larger than for isotropic media, thus increasing the intrinsic FWI non-linearity, ill-posedness, and inter-parameter trade-off. I demonstrate that the resolution and accuracy of anisotropic models are enhanced when using the penalty term based on multiple PDFs. This chapter was presented at an European Association of Geoscientists and Engineers (EAGE) Annual Meeting:

- Aragao, O., Sava, P.C., 2021, Elastic anisotropic full waveform inversion using probabilistic petrophysical constraints. Proceedings of the 83th EAGE Conference Exhibition, European Association of Geoscientists & Engineers.

In chapter 5, titled "Viscoelastic full-waveform inversion with spatial probabilistic petrophysical constraints", I introduce a new formulation for the penalty term based on multiple PDFs in order to simultaneously recover viscoelastic models of velocity and attenuation parameters. These new formulation takes into account spatial distributions patterns of the subsurface and is robust to uncertainty of the petrophysical information. As I show with numerical examples, this technique guides the inversion to accurate geological models with reduced interparameter crosstalk artifacts. This chapter was presented at two Society of Exploration Geophysicist (SEG) Annual Meeting, and it has been submitted for publication to **Geophysical Prospecting**:

- Aragao, O., Sava, P.C., 2020, Elastic full-waveform inversion with spatial probabilistic petrophysical constraints. Proceedings of the 90th Annual International Meeting, Society of Exploration Geophysicists.

- Aragao, O., Sava, P.C., 2021, Viscoelastic full-waveform inversion with spatial probabilistic petrophysical constraints. Proceedings of the 91th Annual International Meeting, Society of Exploration Geophysicists.

- Aragao, O., Sava, P.C., 2021, Viscoelastic full-waveform inversion with spatial probabilistic petrophysical constraints, **Geophysical Prospecting** (submitted).

In addition, this chapter was also presented at a technical workshop:

- Aragao, O., Sava, P.C., 2021, Incorporating probabilistic petrophysical information into viscoelastic full waveform inversion. Workshop Acoustic and Elastic Wave Equation Imaging and Velocity Model Building presented at the 83th EAGE Conference Exhibition, European Association of Geoscientists & Engineers.

In chapter 6, titled "Explicit control of numerical dispersion and instability in wavefield modeling and inversion", I propose to use the penalty term as a stability constraint in order to prevent numerical dispersion and instabilities in wavefield modeling and inversion using the finite-difference method (FDM). I present examples that prove that the method ensures the stability of the FDM engine, while increasing the quality of the recovered models. I intend to publish this chapter as an article in a peer-reviewed journal. This chapter was presented at an European Association of Geoscientists and Engineers (EAGE) Annual Meeting:

- Aragao, O., Sava, P.C., 2021, Explicit control of numerical dispersion and instability in elastic wavefield modeling and inversion. Proceedings of the 83th EAGE Conference Exhibition, European Association of Geoscientists & Engineers.

The thesis concludes with a common discussion of insight accumulated in each chapter and with speculation on future research directions in petrophysical and stability probabilistic penalty terms for multiparameter geophysical inversion.

CHAPTER 2

ELASTIC FULL WAVEFORM INVERSION WITH PROBABILISTIC PETROPHYSICAL MODEL CONSTRAINTS

A paper published in *Geophysics*

Odette Aragao[1,2], Paul Sava[2]

Full waveform inversion (FWI) based on the minimization of data residuals may not enhance our understanding of the subsurface and can at times lead to misleading subsurface models. Additionally, unconstrained multiparameter FWI may also lead to models that do not represent realistic lithology for independently derived parameters. We develop a method for elastic FWI that explicitly imposes petrophysical restrictions in order to guide models toward realistic and feasible lithology, i.e., to subsurface models consistent with the seismic data and with the underlying petrophysics. We exploit petrophysical information, such as that provided by well logs, to constrain the inversion and to avoid implausible models. We achieve this goal by confining the inverted models to a feasible region defined by a model probability density function instead of imposing lithological facies as a function of position. Inside this feasible petrophysical regime, the inverted models do not need to obey a specific trend, i.e., we do not link the parameters with explicit and potentially inaccurate petrophysical relations. Instead, we define a petrophysical basin of attraction that confines models to a feasible region validated by regional lithological and petrophysical information. We demonstrate through elastic models that incorporating probabilistic petrophysical constraints into the inversion objective function leads to models that are superior to models obtained either without constraints or with approximate analytic constraints. In addition, we show that these constraints can help in mitigating common issues affecting elastic FWI, such as the artifacts produced by interparameter crosstalk and limited acquisition coverage.

[1]Primary researcher and author.
[2]Department of Geophysics, Colorado School of Mines, Golden, Colorado, United States of America.

2.1 Introduction

One of the greatest challenges in seismic exploration consists of estimating accurate subsurface elastic models. Seismic tomography is becoming a standard technique for subsurface imaging at various scales, and aims to build high-resolution models of the physical parameters underlying the wave propagation. The main approaches to seismic tomography use either traveltimes (Djebbi and Alkhalifah, 2018; Schuster and Quintus-Bosz, 1993; Taillandier et al., 2009; Woodward, 1992) or wavefields (Biondi, 2006; Diaz and Sava, 2017; Duan and Sava, 2016; Mora, 1989; Tarantola, 1984). Wavefield tomography has advantages over traveltime tomography because it recovers parameters with higher resolution (Alkhalifah and Choi, 2014; Operto et al., 2013; Pratt, 1999; Tarantola, 1986) by exploiting both the kinematics and dynamics of the observed waveforms.

Full waveform inversion (FWI) is among the most promising techniques in the wavefield tomography category as it delivers highly accurate subsurface models from seismic data (Pratt, 1999; Sirgue and Pratt, 2004; Tarantola, 1984; Virieux and Operto, 2009). FWI operates by iteratively updating model parameters based on the mismatch between observed and simulated data. This optimization exploits seismic wavefield modeling (the forward problem) and solves the associated inverse problem by minimizing an objective function. The gradient of the objective function estimates model perturbations that progressively decrease the data residual. Conventional FWI implementations use the adjoint state method (Plessix, 2006) to compute the objective function gradient, since this method is among the most efficient and requires the least amount of storage.

Early implementations of FWI used the acoustic wave equation (Pratt, 1990; Pratt et al., 1996; Tarantola, 1984). However, acoustic FWI does not take into account elastic effects and the presence of S waves in the data. Several parameters are necessary for describing elastic models (e.g., density ρ and Lamé parameters λ and μ, or density and P- and S-wave velocities). Therefore, elastic FWI (EFWI) better describes the subsurface properties (Oh et al., 2018; Plessix, 2006; Pratt, 1990; Tarantola, 1988; Zhang et al., 2019a).

Despite its popularity, FWI is hampered by several challenges undermining its practical application. FWI is a highly non-linear and ill-posed problem, so its convergence is subjected to falling into local minima (Symes, 2008; Virieux and Operto, 2009). Therefore, one needs to include prior information into inversion to find a plausible solution (Tarantola, 2005; Tikhonov and Arsenin, 1977). Also, the wave extrapolator can become unstable when model updates fluctuate, thus impending further updates.

Elastic FWI suffers from a number of additional practical difficulties. First, using multiple parameters increases the degrees of freedom in the model space, thereby increasing the non-linearity of the inversion (Operto et al., 2013). In addition, as model parameters are updated simultaneously but independently, different model components can be physically contradictory to one-another, creating combinations that are lithologically implausible or impossible. This situation may create inaccurate and unstable forward solutions and lead to poor convergence (Baumstein, 2013). Moreover, similar radiation patterns among various elastic parameters create crosstalk, i.e. different models are viewed similarly in data (Kamath and Tsvankin, 2016; Operto et al., 2013) resulting in ambiguous model inversion. Radiation pattern analysis can partially correct for crosstalk, but is largely ineffective in poorly illuminated areas.

In order to recover models that are self-consistent and properly characterize the subsurface, we need to explicitly impose model constraints during the inversion (Baumstein, 2013; Duan and Sava, 2016; Manukyan et al., 2018; Peters et al., 2015; Rocha and Sava, 2018; Zhang et al., 2018). These constraints can use petrophysical information, such as that contained in well logs or from other sources, as core or basin analysis. Incorporating constraints into the objective function defines model space bounds, forcing the inverted models to be consistent with known petrophysical relationships and thus represent realistic lithological units.

Baumstein (2013) and Peters et al. (2015) use, respectively, projection onto convex sets (POCS), or projection onto intersections of convex sets to incorporate constraints into acous-

tic FWI. Both constraints impose velocity bounds (box constraints) and specify a minimum smoothness for the model parameters. The updated models must be at the intersection of all convex sets, which leads to more stable simulations and a geologically plausible structure. Manukyan et al. (2018) constrain the inversion by assuming that the elastic parameters have structural similarity and thus mitigate parameter trade-off problems and the different spatial resolution of elastic parameters. They show that structurally constrained FWI can deliver higher-quality models when compared to conventional FWI. However, the assumption of structural similarity between different elastic parameters can potentially compromise the final outcome. Zhang et al. (2018) and Zhang and Alkhalifah (2019) use seismic facies to build a model regularization term for the EFWI in order to deliver more reliable models. Zhang et al. (2018) updates the distribution of the facies at each iteration using a Bayesian approach, while Zhang and Alkhalifah (2019) estimate the facies distribution by training deep neural networks.

Duan and Sava (2016) use a logarithmic penalty function to constrain the elastic wavefield tomography assuming a general linear relationship between the model parameters. Rocha and Sava (2018) also use this type of constraint, but in the context of elastic reflection waveform inversion. Both examples demonstrate that an explicit petrophysical constraint can yield consistent and plausible models even if conventional spatial regularization is not explicitly applied during the inversion. However, complex models do have non-linear petrophysical relationships between the elastic parameters. Moreover, the analytic logarithmic barrier constraint works with user-defined parameters, and their selection may be challenging, especially when different lithofacies are present in the same area. Thus, it is necessary to define more general and automated petrophysical constraints that provide flexibility and adapt to the specific geologic situation in the imaged area.

We propose elastic wavefield tomography with an objective function that constrains the relationship between the elastic parameters using model probability density functions (PDFs) (Aragao and Sava, 2019). In the following sections, we first discuss general aspects of elastic

FWI, emphasizing the mechanisms used to incorporate constraints into the inversion. We demonstrate that PDFs can be used in EFWI without knowing or defining an analytic relationship among the different elastic parameters. Finally we illustrate the features and performance of the proposed method with two synthetic examples.

2.2 Elastic Wavefield Tomography

In this section, we discuss the basis of elastic full waveform inversion and introduce the framework for probabilistic petrophysical model constraints.

We consider the isotropic elastic wave equation

$$\rho\ddot{\mathbf{u}} - \lambda[\nabla(\nabla\cdot\mathbf{u})] - \mu\left[\nabla\cdot\left(\nabla\mathbf{u}+\nabla\mathbf{u}^T\right)\right] = \mathbf{f}, \tag{2.1}$$

where $\mathbf{u}(e,\mathbf{x},t)$ is the elastic wavefield, $\mathbf{f}(e,\mathbf{x},t)$ is the source function, $\lambda(\mathbf{x})$ and $\mu(\mathbf{x})$ are the Lamé parameters, $\rho(\mathbf{x})$ is the density and e, $\mathbf{x}$ and t are, respectively, the experiment index, space coordinates and time. Equation 2.1 assumes that Lamé parameters vary slowly, such that their spatial gradient can be neglected.

Considering $\mathbf{u}_s$ as the source wavefield, the waveform inversion problem is solved by minimizing an objective function $\mathcal{J}(\mathbf{u}_s,\lambda,\mu)$ consisting of three parts: a term that evaluates the misfit between the simulated and observed data $\mathcal{J}_D(\mathbf{u}_s,\lambda,\mu)$; a model regularization term $\mathcal{J}_M(\lambda,\mu)$; that enforces spatial correlation of the model parameters, and a term that enforces petrophysical model constraints, $\mathcal{J}_C(\lambda,\mu)$:

$$\mathcal{J}(\mathbf{u}_s,\lambda,\mu) = \mathcal{J}_D(\mathbf{u}_s,\lambda,\mu) + \mathcal{J}_M(\lambda,\mu) + \mathcal{J}_C(\lambda,\mu). \tag{2.2}$$

We can define the data residual

$$\mathbf{r}_D(e,\mathbf{x},t) = \mathbf{W}_u(e,\mathbf{x},t)\mathbf{u}_s(e,\mathbf{x},t) - \mathbf{d}_{obs}(e,\mathbf{x},t), \tag{2.3}$$

and then the data misfit term

$$\mathcal{J}_D(\mathbf{u}_s,\lambda,\mu) = \sum_e \frac{1}{2}\left\|\mathbf{r}_D(e,\mathbf{x},t)\right\|^2, \tag{2.4}$$

where $\mathbf{W}_u(e,\mathbf{x},t)$ are weights that restrict the source wavefield $\mathbf{u}_s(e,\mathbf{x},t)$ to the known receiver locations, and $\mathbf{d}_{obs}(e,\mathbf{x},t)$ are the observed data.

To update the model iteratively using a gradient-based method (Tarantola, 1988), one can compute the gradient of $\mathcal{J}_D$ with respect to the model parameters λ and μ using the adjoint-state method (Plessix, 2006). This method consists of four steps:

1. Compute the seismic wavefield $\mathbf{u}_s(e,\mathbf{x},t)$ from a source function $\mathbf{f}_s$, such that $\mathbf{L}\mathbf{u}_s - \mathbf{f}_s = \mathbf{0}$, where $\mathbf{L}$ is the linear elastic wave operator derived from equation 2.1,

2. Compute the adjoint source $\mathbf{g}_s = \partial\mathcal{J}/\partial\mathbf{u}_s$, which exploits the difference between the observed and simulated data (equation 2.3),

3. Compute the adjoint wavefield $\mathbf{a}_s(e,\mathbf{x},t) = \mathbf{L}^T\mathbf{g}_s$, which uses the adjoint elastic wave operator $\mathbf{L}^T$,

4. Compute the gradient of $\mathcal{J}_D$ with respect to the parameters λ and μ using

$$\begin{bmatrix} \dfrac{\partial\mathcal{J}_D}{\partial\lambda} \\ \dfrac{\partial\mathcal{J}_D}{\partial\mu} \end{bmatrix} = \sum_e \begin{bmatrix} -\nabla(\nabla\cdot\mathbf{u}) \star \mathbf{a}_s \\ -\nabla\left(\nabla\mathbf{u} + \nabla\mathbf{u}^T\right) \star \mathbf{a}_s \end{bmatrix}, \tag{2.5}$$

where the symbol $\star$ represents zero-lag time crosscorrelation.

Incorporating a model regularization term into the objective function may reduce the inversion ill-posedness, and accelerates convergence towards the global minimum (Asnaashari et al., 2013; Jun et al., 2017; Masmoudi and Alkhalifah, 2018; Zhang et al., 2018). Prior information can be estimated from non-seismic data, e.g. well logs, or by incorporating knowledge about the model geometry, e.g., smoothness or consistency with a migrated image. Considering the model residuals:

$$\mathbf{r}_\lambda(\mathbf{x}) = \mathbf{W}_\lambda(\mathbf{x})(\lambda(\mathbf{x}) - \bar{\lambda}(\mathbf{x})), \tag{2.6}$$

$$\mathbf{r}_\mu(\mathbf{x}) = \mathbf{W}_\mu(\mathbf{x})(\mu(\mathbf{x}) - \bar{\mu}(\mathbf{x})), \tag{2.7}$$

the term $\mathcal{J}_M(\lambda, \mu)$ is

$$\mathcal{J}_M(\lambda, \mu) = \frac{1}{2} \left\| \mathbf{r}_\lambda(\mathbf{x}) \right\|^2 + \frac{1}{2} \left\| \mathbf{r}_\mu(\mathbf{x}) \right\|^2, \tag{2.8}$$

where $\bar{\lambda}(\mathbf{x})$ and $\bar{\mu}(\mathbf{x})$ are prior (reference) models. The weighting operators $\mathbf{W}_\lambda(\mathbf{x})$ and $\mathbf{W}_\mu(\mathbf{x})$ are related to the model covariance matrices such that $\mathbf{W}_\lambda = \mathbf{C}_\lambda^{-\frac{1}{2}}$ and $\mathbf{W}_\mu = \mathbf{C}_\mu^{-\frac{1}{2}}$.

The gradient of $\mathcal{J}_M(\lambda, \mu)$ with respect to the model parameters λ and μ is

$$\begin{bmatrix} \dfrac{\partial \mathcal{J}_M}{\partial \lambda} \\ \dfrac{\partial \mathcal{J}_M}{\partial \mu} \end{bmatrix} = \begin{bmatrix} \mathbf{W}_\lambda^T \mathbf{W}_\lambda (\lambda - \bar{\lambda}) \\ \mathbf{W}_\mu^T \mathbf{W}_\mu (\mu - \bar{\mu}) \end{bmatrix} \tag{2.9}$$

It is apparent from equations 2.5 and 2.9 that the model components λ and μ for multiparameter inversion are updated independently, and thus, can become physically inconsistent with each other, producing inaccurate models, images, and inaccurate geologic interpretation. Explicitly incorporating petrophysical constraints improves the quality of the inversion by restricting the updated models to a feasible region, resulting in more accurate subsurface characterization.

Duan and Sava (2016) propose a logarithmic penalty function $\mathcal{J}_L$ to constrain the inversion to a feasible region by enforcing physical relationships between the updated model parameters:

$$\mathcal{J}_L(\lambda, \mu) = -a \sum_{\mathbf{x}} \left[\log\left(h_u\right) + \log\left(h_l\right) \right]. \tag{2.10}$$

The scalar parameter a determines the strength of the constraint term in the objective function, and h_u and h_l are linear functions such that

$$h_u = -\lambda + c_u \mu + b_u, \tag{2.11}$$

$$h_l = \lambda - c_l \mu - b_l. \tag{2.12}$$

The coefficients c_u and c_l are the slopes of the boundary lines, and b_u and b_l are their intercepts. At the two linear boundaries of the feasible region

$$h_u = 0, \tag{2.13}$$

$$h_l = 0. \tag{2.14}$$

The $\mathcal{J}_L$ term forces the recovered models to the interior of a feasible region, i.e., between the upper and lower boundaries, where h_u and h_l are positive. Outside this feasible region, h_u and h_l are negative, and thus the constraint term given by equation 2.10 prevents undesirable model updates. The distance of a given model parameter in the parameter space $\{\lambda, \mu\}$ to the boundary lines h_u and h_l determines the value of $\mathcal{J}_L$, such that this term dominates the objective function when models are close to either one of the barriers. This constraint forces the inverted models to move away from those boundaries, which acts like a barrier that favors model parameters in a given feasible region.

The gradients of $\mathcal{J}_L$ with respect to the model parameters λ and μ are

$$\begin{bmatrix} \dfrac{\partial \mathcal{J}_L}{\partial \lambda} \\ \dfrac{\partial \mathcal{J}_L}{\partial \mu} \end{bmatrix} = a \begin{bmatrix} \dfrac{-1}{\lambda - c_u\mu - b_u} - \dfrac{1}{\lambda - c_l\mu - b_l} \\ \dfrac{c_u}{\lambda - c_u\mu - b_u} + \dfrac{c_l}{\lambda - c_l\mu - b_l} \end{bmatrix}. \tag{2.15}$$

The term $\mathcal{J}_L$ assumes that the relationship between the model parameters λ and μ is linear. Therefore, the inversion may not be able to recover complex, nonlinear true physical relationships between the model parameters. Alternatively, if we have access to petrophysical information obtained, for example, from well logs, we can impose a more general kind of petrophysical constraint. In this situation, we can construct a model probability density function (PDF) of the reference well log parameters to characterize the interdependence between the elastic model parameters.

Consider, for example, the crossplot in Figure 2.1a illustrating a possible petrophysical relationship between the Lamé parameters, λ and μ. The linear barrier constraint $\mathcal{J}_L$ would not be appropriate for this example, as λ and μ do not share a linear relationship. Instead, we can create a model PDF Figure 2.1b based on the available values of λ and μ.

Considering the vector $\mathbf{m} = [\lambda \ \ \mu]$ as the elastic model components of a given position $\mathbf{x}$, we evaluate distances to all points of the PDF, represented by coordinates $\mathbf{p} = [\lambda_p \ \ \mu_p]$. For any given model represented by $\mathbf{m} = [\lambda \ \ \mu]$, we would like to evaluate a model space

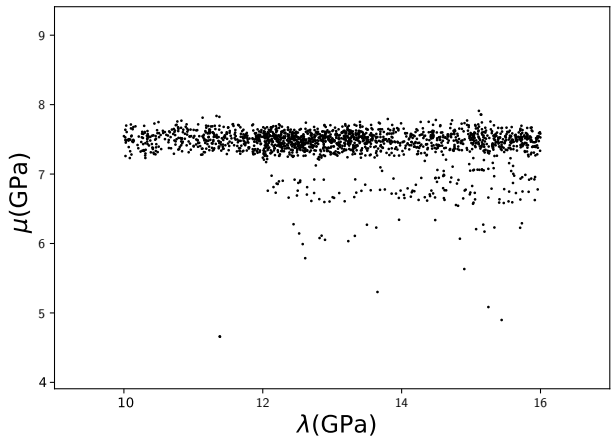

(a)

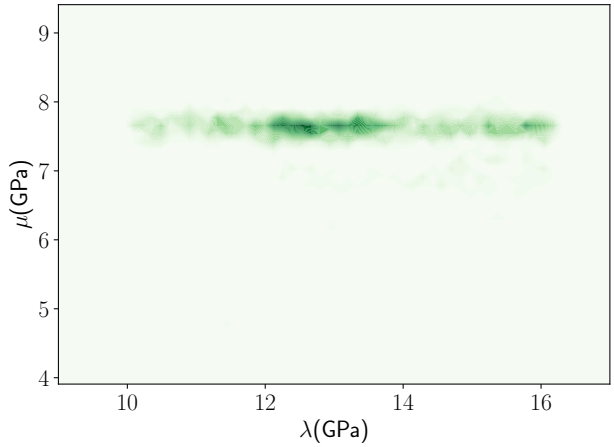

(b)

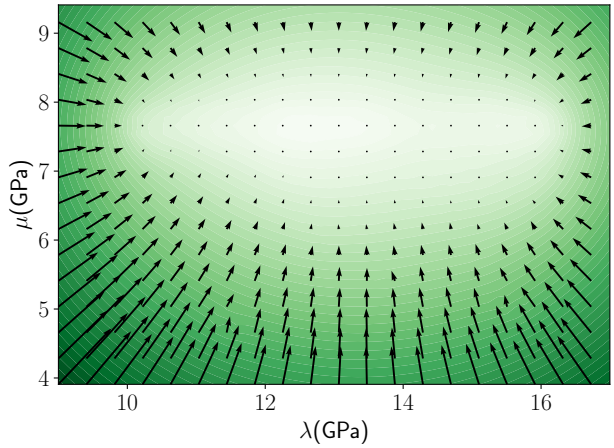

(c)

Figure 2.1: (a) Example of a λ and μ crossplot. (b) Model PDF associated to the crossplot in panel (a), characterizing the dependence of λ and μ. (c) Distribution of the distance $D(\mathbf{m})$ and its gradient for the distribution shown in (b). Note that high probability models are associated with small values of $D(\mathbf{m})$ and with zero gradients.

distance to the entire distribution (Figure 2.2). The distance between a given $\mathbf{m}$ to a point of coordinates $\mathbf{p}$ is

$$d(\mathbf{m}, \mathbf{p}) = \|\mathbf{m} - \mathbf{p}\|_2. \tag{2.16}$$

Then, considering the probability density of each cell of the PDF as $f(\mathbf{p})$, we determine the distance $D(\mathbf{m})$ from $\mathbf{m}$ to the distribution as

$$\frac{1}{D(\mathbf{m})} = \sum_{\mathbf{p}} \frac{f(\mathbf{p})}{d(\mathbf{m}, \mathbf{p})}. \tag{2.17}$$

Therefore, each point in the updated model space represented by $\mathbf{m}$ is connected to all cells of the PDF, i.e., we have constructed the distance from this model to the distribution. Since the quantity $1/D(\mathbf{m})$ is small for points that are far from regions of high probability, we can define the petrophysical constraint $\mathcal{J}_P$ as

$$\mathcal{J}_P = a \sum_{\mathbf{m}} D(\mathbf{m}). \tag{2.18}$$

This definition imposes the condition that all points representing inverted models are as close as possible to the original petrophysical distribution without being drawn especially to any value of the model, but rather close in a statistical sense to the entire distribution. For stability, we explicitly exclude situations where the model space distance from $\mathbf{m}$ to a given $\mathbf{p}$ is equal to zero.

The gradient of $\mathcal{J}_P$ with respect to the model parameters λ and μ is

$$\frac{\partial \mathcal{J}_P}{\partial \lambda} = a\, D^2(\mathbf{m}) \sum_{\mathbf{p}} \frac{f(\mathbf{p})(\lambda - \lambda_p)}{d^3(\mathbf{m}, \mathbf{p})}, \tag{2.19}$$

and

$$\frac{\partial \mathcal{J}_P}{\partial \mu} = a\, D^2(\mathbf{m}) \sum_{\mathbf{p}} \frac{f(\mathbf{p})(\mu - \mu_p)}{d^3(\mathbf{m}, \mathbf{p})}. \tag{2.20}$$

Figure 2.1c display the distribution of the gradient of $D(\mathbf{m})$, which is close to zero in the region where the PDF is high. The distance to high probabilities in the model parameter space defines the value of $\mathcal{J}_P$, such that the gradient of this term dominates in the total gradient of the objective function $\mathcal{J}$ if the updated models are far from high probability.

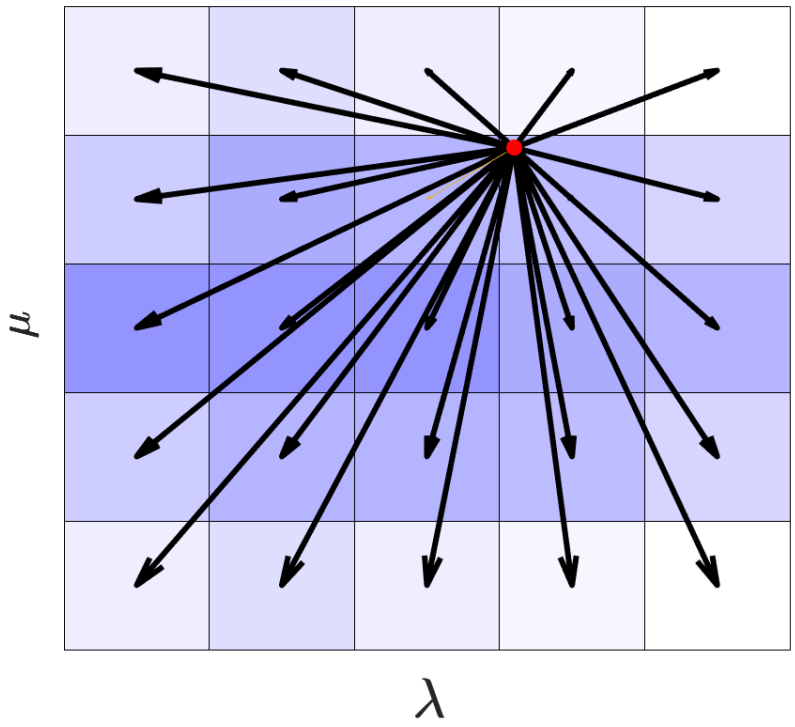

Figure 2.2: Sketch indicating how each point in the updated model space (red dot) communicates with all cells of the model PDF. Each cell of the model PDF contributes proportionally with its probability value and inverse proportionally to the distance to the analyzed model.

Otherwise, once a point $\mathbf{m}$ in the updated model is consistent with the distribution given by the PDF, the data misfit $\mathcal{J}_D$ fully controls the gradient as the gradients of $\mathcal{J}_P$ are zero.

The probabilistic petrophysical model constraint $\mathcal{J}_P$ addresses many issues related to elastic FWI. First, it can reduce the non-linearity and the ill-posed nature of FWI as it incorporates prior information into the inversion, which reduces the number of model solutions and improves the inversion convergence to realistic and feasible inverted models, preventing instabilities in wavefield extrapolation. In addition, it avoids geologically implausible earth models and reduces the artifacts created by the interparameter crosstalk, as it links the elastic parameters during the inversion and restricts them to a feasible region.

2.3 Examples

We illustrate our EFWI method with two synthetic examples and compare inversions using only the data misfit term $\mathcal{J}_D$, the data misfit with the logarithmic penalty function $\mathcal{J}_D + \mathcal{J}_L$, and the data misfit with the probabilistic petrophysical constraints $\mathcal{J}_D + \mathcal{J}_P$. In the second example, we also repeat the inversion with the objection function $\mathcal{J}_D + \mathcal{J}_P$ for different choices of the trade-off parameter a which determines the of $\mathcal{J}_P$ in the objective function.

2.3.1 Gaussian anomalies model

The first synthetic example uses a model with negative and positive Gaussian anomalies centered at $(1.25, 0.75)$ and $(1.25, 1.75)$ km, respectively (Figure 2.3). We simulate 20 vertical displacement sources in a well at $x = 0.1$ km and a line of geophones at $x = 2.4$ km. (Figure 2.3) shows the true λ and μ models along with a crossplot of the models. We choose this simple example to show how the inversion using data misfit with the logarithmic penalty function fails when the model is characterized by two clusters, which represent lithology with different linear relationships between parameters λ and μ. We initiate the inversion with constant backgrounds.

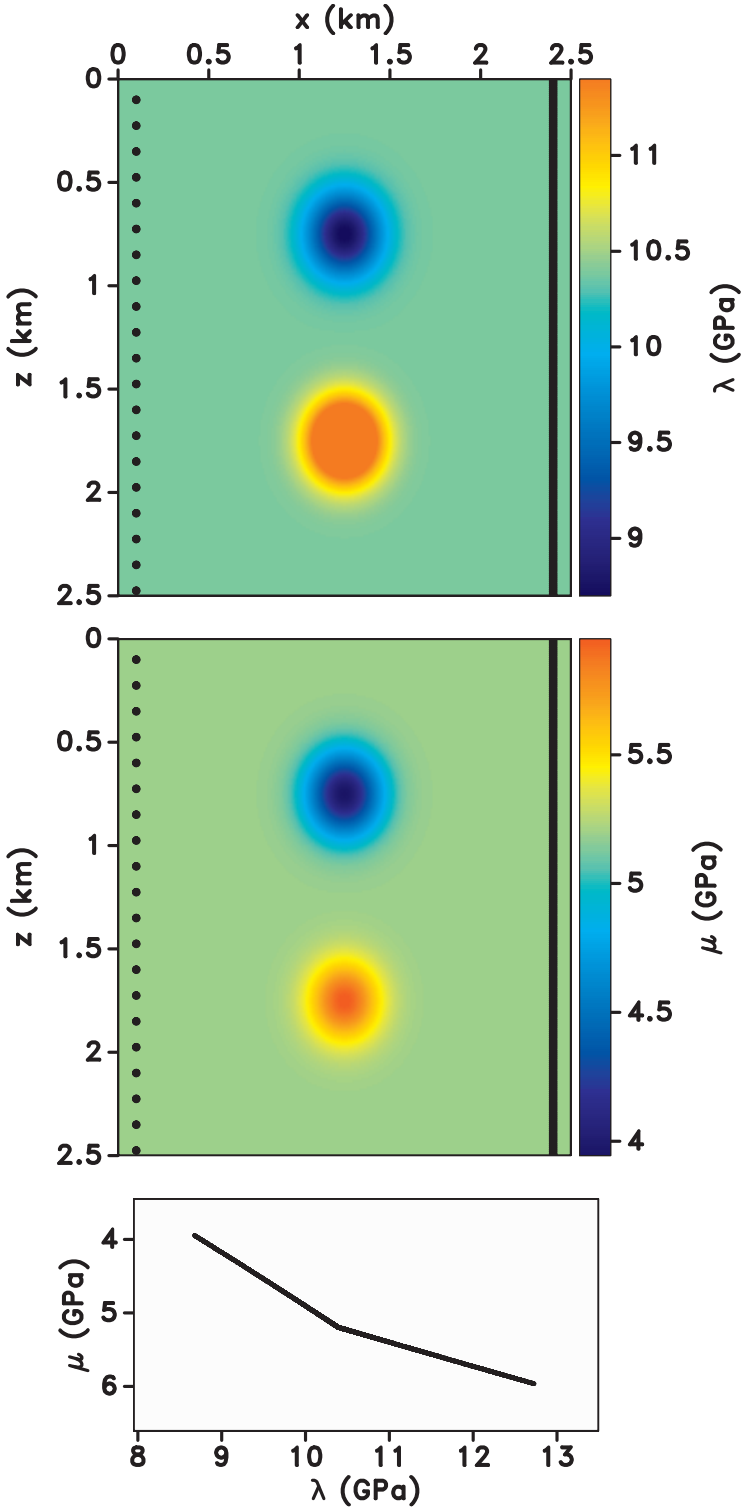

Figure 2.3: True λ and μ models and their crossplot in the $\lambda - \mu$ space. The top panels show the sources (dots) located at $x = 0.1\,\text{km}$ and the vertical line corresponds to receivers at $x = 2.4\,\text{km}$. The negative and positive Gaussian anomalies for the λ and μ models are centered at $(1.25, 0.75)\,\text{km}$ and $(1.25, 1.75)\,\text{km}$, respectively. The crossplot shows two linear relationships between λ and μ: corresponding to each of the Gaussian anomalies.

Figure 2.4 shows the recovered λ and μ models using the objective function $\mathcal{J}_D$ along with a crossplot in the $\lambda-\mu$ space. Without imposing petrophysical constraints, the λ and μ values deviate from the true model as the similar radiation patterns of different model parameter perturbations result in crosstalk among physical properties. This problem is enlarged due to the limited acquisition coverage and varying illumination. The inversion does not recover the correct magnitude or size of the λ model. Additionally, the μ model has a lot of artifacts due to the crosstalk between the elastic parameters. Although a linear relationship between the parameters characterizes the true model (Figure 2.3), the crossplot shown in Figure 2.4 indicates that the parameters λ and μ are uncorrelated, which agrees with the fact the data misfit objective function updates them independently, thus leading to unphysical models.

Based on the crossplot of true λ and μ parameters (Figure 2.3), we choose the linear boundaries shown in Figure 2.5 to define the logarithmic penalty function. Adding the logarithmic penalty function $\mathcal{J}_L$ to $\mathcal{J}_D$ in the objective function, we obtain the λ and μ models shown in Figure 2.6. $\mathcal{J}_L$ is not flat in the interval between the upper and lower boundaries and forces the recovered models towards a central region, as seen in Figure 2.6. The point $(10.4, 5.2)$ GPa, which represents the background models, is not mid-way between the two boundaries and, consequently, inversion using $\mathcal{J}_L$ changes the background parameters (Figure 2.6).

Figure 2.7 shows the recovered λ and μ models using the objective function $\mathcal{J}_D + \mathcal{J}_P$. For simplicity, we define in this example the PDF as a Gaussian distribution covering the true model. This is not necessary for more complex examples, where the relationship between the parameters is non-linear and derived from actual well logs. The lines in the crossplot correspond to the feasible region used to define the probabilistic constraint $\mathcal{J}_P$. Notice that when we include the probabilistic constraint term both anomalies have amplitude and shape closer to the true λ and μ models (Figure 2.3). Imposing the probabilistic constraint confines the model to the feasible region defined by the PDF, but within this area the models do not follow any predefined trend, which does not happen when we use the logarithmic boundaries.

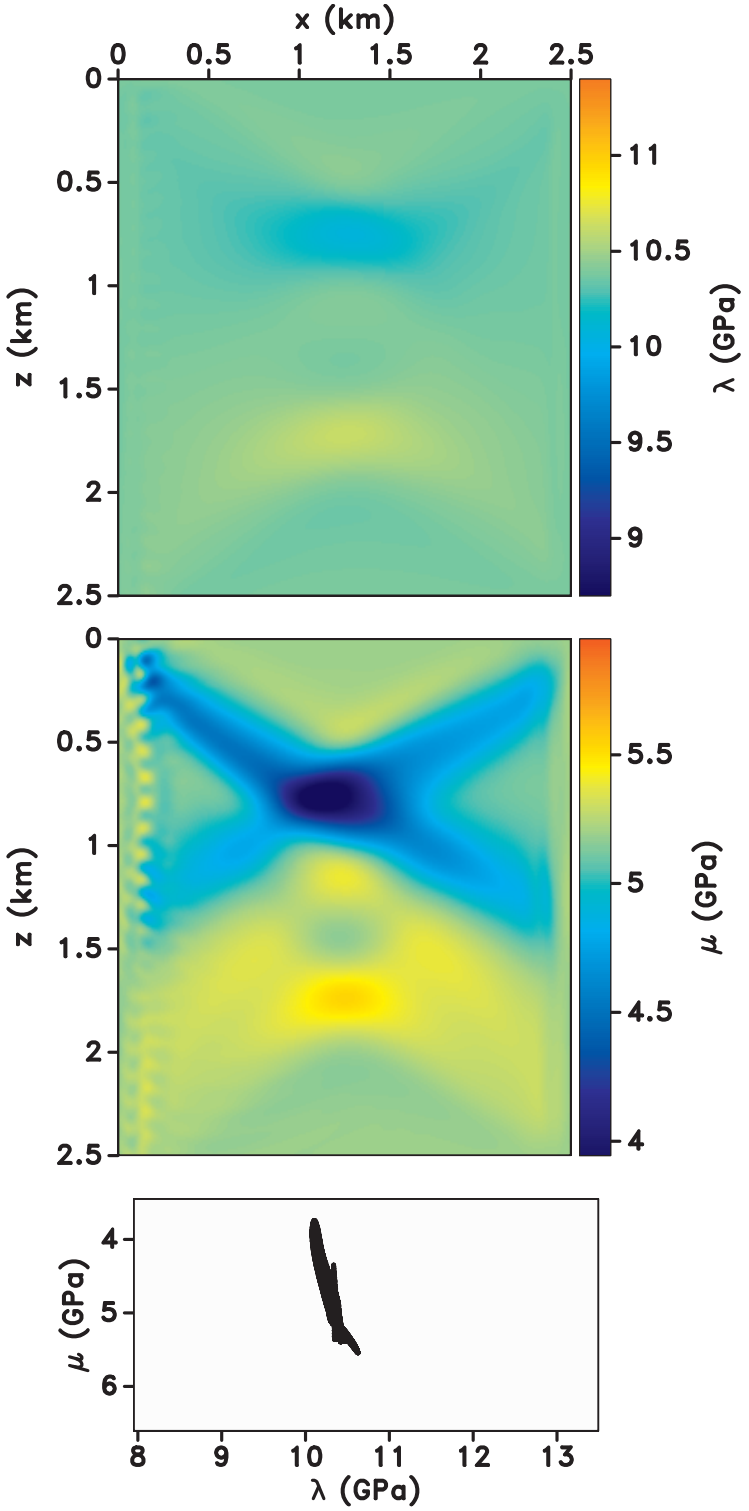

Figure 2.4: Updated λ and μ models using the objective function $\mathcal{J}_D$. The Gaussian anomalies are not recovered well and the inverted models present artifacts from inter-parameter crosstalk. The crossplot shows that the parameters do not follow the same trend of the true models (Figure 2.3).

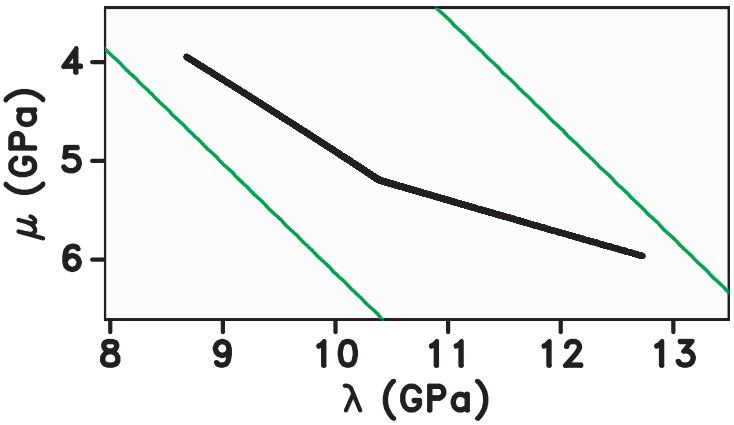

Figure 2.5: Crossplot in the $\lambda - \mu$ space of the true models superimposed by the upper and lower boundaries used in the logarithmic penalty function $\mathcal{J}_L$. The linear barriers ensure that the inversion recovers models confined to this feasible region.

Also, the crossplot shown in Figure 2.7 has two main linear relationships between the inverted models, what conforms to the true models.

Vertical profiles from the inverted λ and μ models at $x = 1.0$ km are shown in Figure 2.8, where the black lines indicate the true models and the colored lines are recovered models. Using the objective function $\mathcal{J}_D$, we obtain a reliable model update for λ (Figure 2.8a), but an incorrect model update for μ (Figure 2.8d). Using the objective function $\mathcal{J}_D + \mathcal{J}_{C_L}$, we distort the background values and do not recover the anomalies (Figures 2.8b and 2.8e). Using the objective function $\mathcal{J}_D + \mathcal{J}_{C_P}$, we obtain models that better represent the true ones (Figures 2.8c and 2.8f), without negatively affecting the background model.

2.3.2 Marmousi 2 model

The second synthetic example uses a portion of the Marmousi 2 model (Martin et al., 2002). For this example, we consider that prior petrophysical data from three well logs are available and we use this information to build the petrophysical model constraints. Figure 2.9 shows the correct λ and μ models, the well locations for our experiment and the crossplot of the model parameters. We simulate a multicomponent ocean bottom seismic survey (OBS) with a line of receiver at the water bottom ($z = 0.17$ km) and 20 evenly spaced pressure

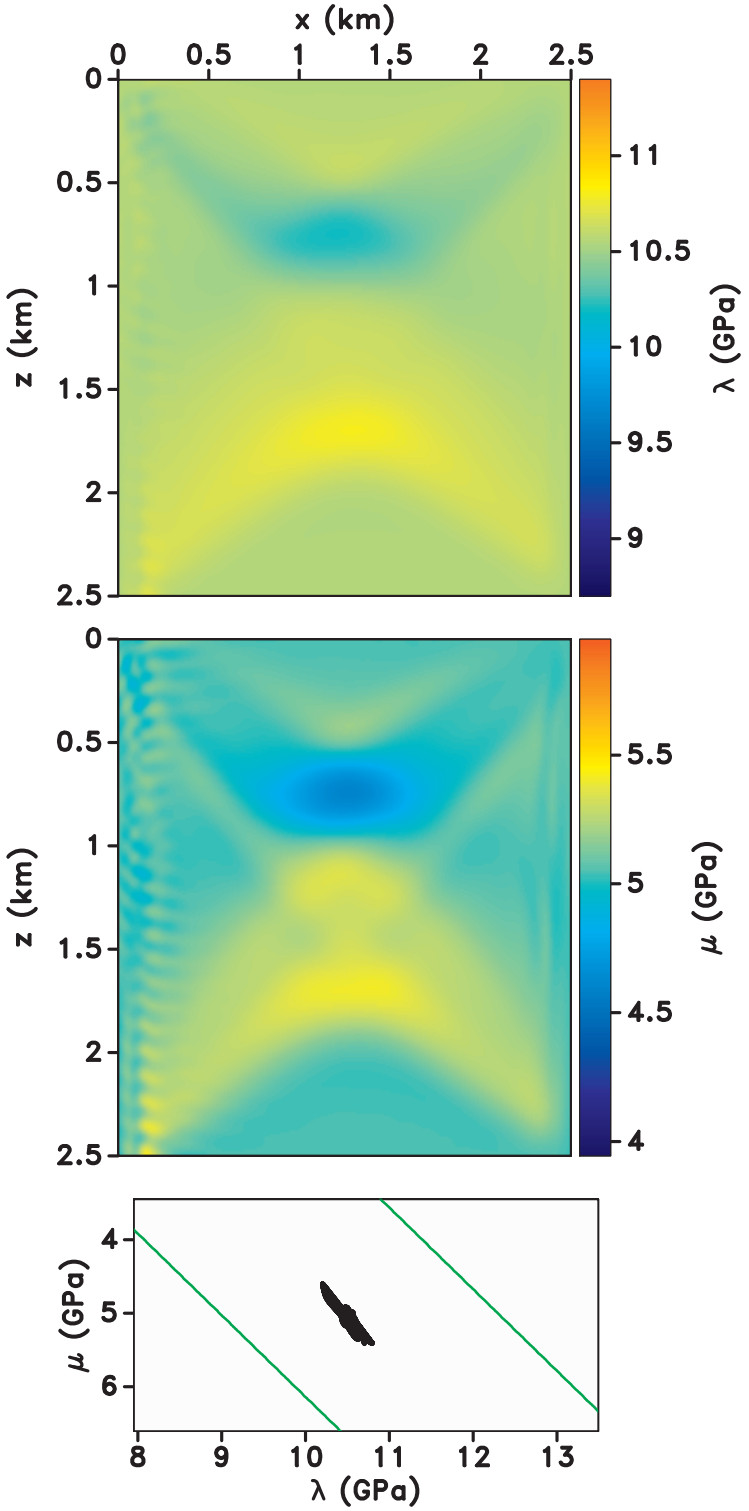

Figure 2.6: Updated λ and μ models using the objective function $\mathcal{J}_D + \mathcal{J}_L$. The lines define the upper and lower boundaries used in the logarithmic penalty function $\mathcal{J}_L$. The Gaussian anomalies are not recovered well and the backgrounds are modified during the inversion.

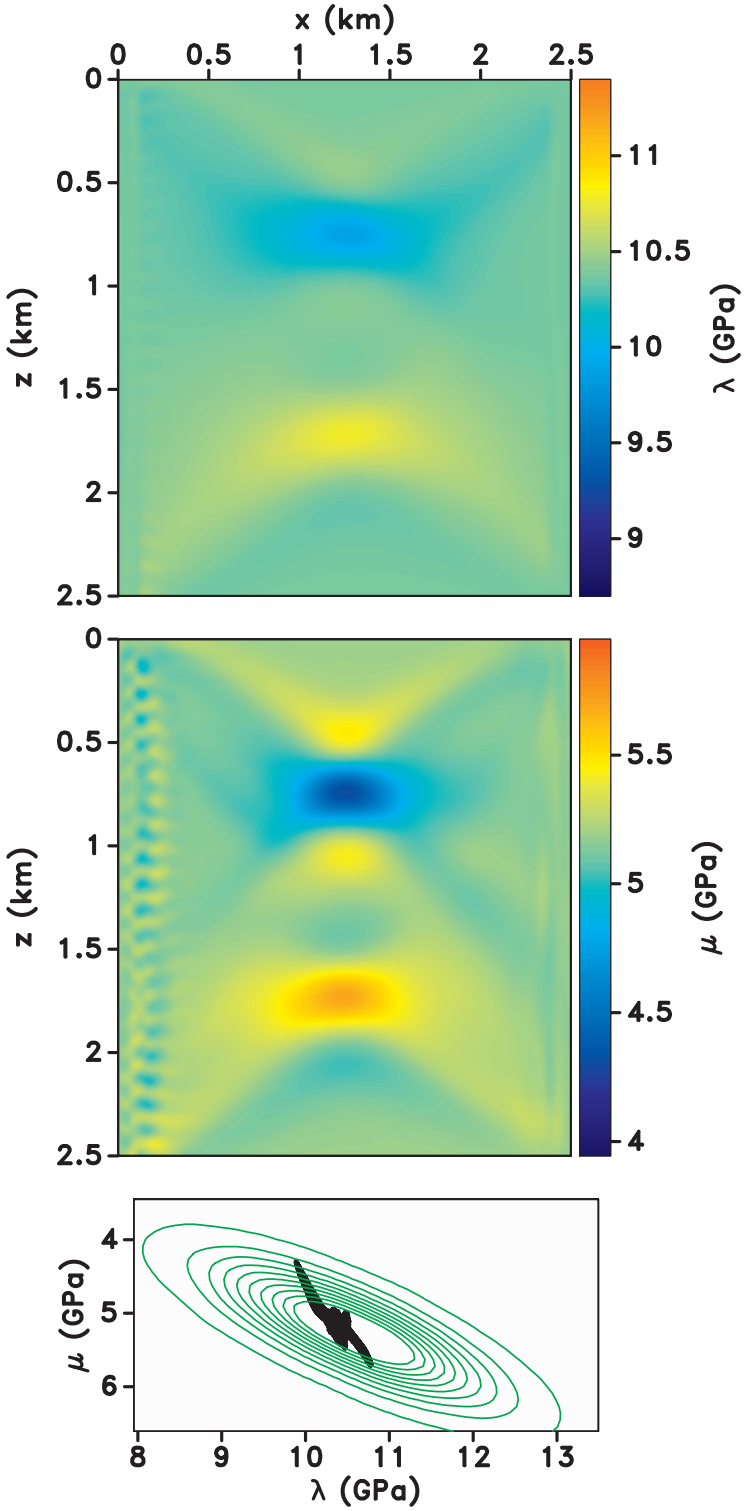

Figure 2.7: Updated λ and μ models using the objective function $\mathcal{J}_D + \mathcal{J}_P$. The contours in the crossplot represent the PDF used to define the petrophysical constraint $\mathcal{J}_P$. Both Gaussian anomalies are better recovered for the λ and μ models.

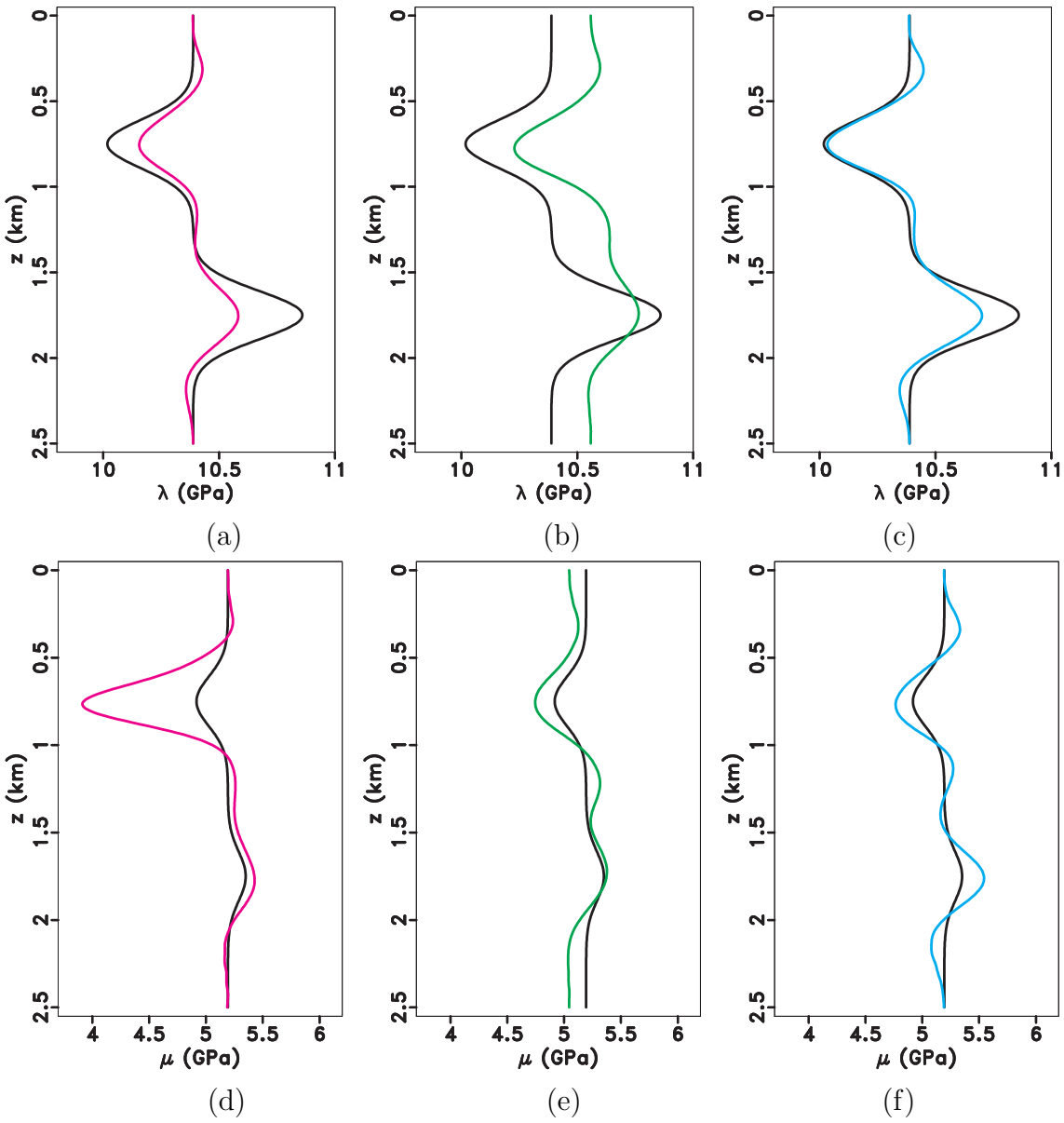

Figure 2.8: Comparison between true and recovered models in a vertical profile at $x = 1.0$ km. In the top row, black lines are the true λ model and colored lines are the updated models using the objective function (a) $\mathcal{J}_D$ (red line), (b) $\mathcal{J}_D + \mathcal{J}_{C_L}$ (green line) and (c) $\mathcal{J}_D + \mathcal{J}_{C_P}$ (blue line). In the bottom row, black lines are the true μ model and colored lines are the updated models using the objective function as (d) $\mathcal{J}_D$ (red line), (e) $\mathcal{J}_D + \mathcal{J}_{C_L}$ (green line) and (f) $\mathcal{J}_D + \mathcal{J}_{C_P}$ (blue line).

sources located at $z = 0.05\,\text{km}$. Figure 2.10 shows the crossplot of λ and μ models extracted at the wells located at $x = 1.1$, 2.0 and 3.0 km (Figure 2.9). We use a 7.5 Hz peak Ricker source wavelet. Figure 2.11 shows the initial λ and μ models and the corresponding crossplot in the model parameter space.

Figure 2.12 shows the recovered λ and μ models using the objective function $\mathcal{J}_D$. As expected, the inverted μ model has more structural detail than the λ model, as it only depends on density and S-velocities, while λ depends on density as well as the P- and S-velocities. The wavelength of the S waves is shorter than that of the P waves, and therefore the inverted μ model has higher spatial resolution. However, as in this example we do not impose petrophysical constraints, the μ model has spurious artifacts due to parameter crosstalk. Note that the values of the main structure presented in the initial λ model (Figure 2.11) that conforms to the true λ model (Figure 2.9) are not preserved during the unconstrained inversion (Figure 2.12). Additionally, the crossplot shown in Figure 2.12 does not resemble the true model (Figure 2.9) because the updates are not restricted to a feasible petrophysical region.

From the crossplot of the λ and μ models extracted at the wells (Figure 2.10), we choose the linear boundaries shown in Figure 2.13 to estimate the logarithmic penalty function as $h_l = \lambda - 1.3\mu - 0.2$ and $h_u = -\lambda + 1.3\mu + 3.15$. Figure 2.14 shows the recovered λ and μ models using the objective function $\mathcal{J}_D + \mathcal{J}_L$. We also ensure that initial models for the inversion (Figure 2.11) are within the feasible region. As for the case of inversion using the objective function $\mathcal{J}_D$ (Figure 2.12), the inverted μ model has spurious artifacts. The main structure presented in the initial λ model (Figure 2.11) is not preserved during this kind of constrained inversion (Figure 2.14). As expected, the crossplot shown in Figure 2.14 indicates that the model samples follow the linear trend imposed by the barriers. However this trend does not correspond to the true models (Figure 2.9).

Figures 2.15, 2.16 and 2.17 show the recovered λ and μ models using the objective function $\mathcal{J}_D + \mathcal{J}_P$ with a equal to, respectively, 5×10^{-8}, 3×10^{-8} and 10^{-9}. We estimate

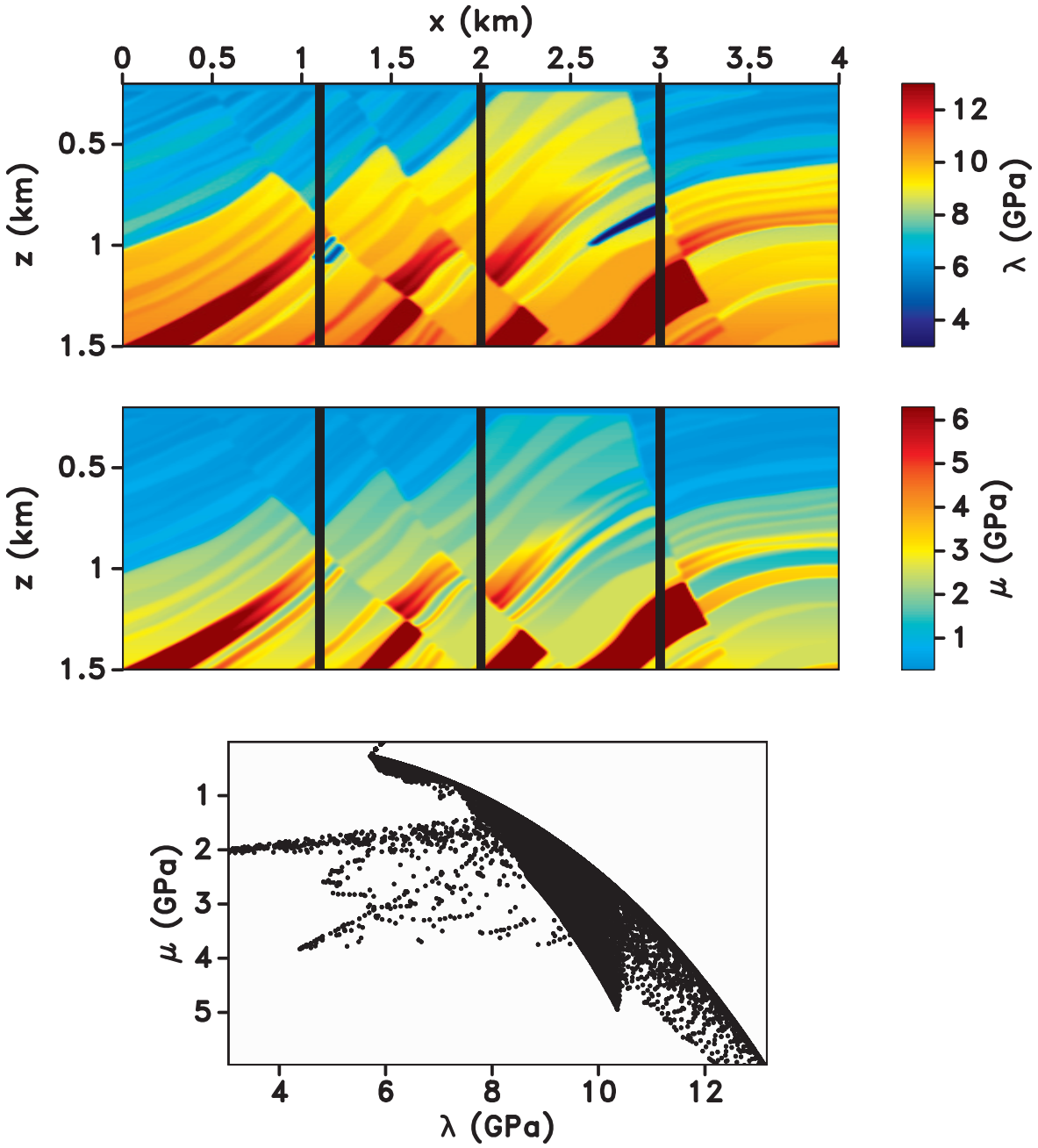

Figure 2.9: Marmousi 2 model: True λ and μ models and their crossplot. The vertical lines correspond to the location of the wells, providing information for the petrophysical constraint.

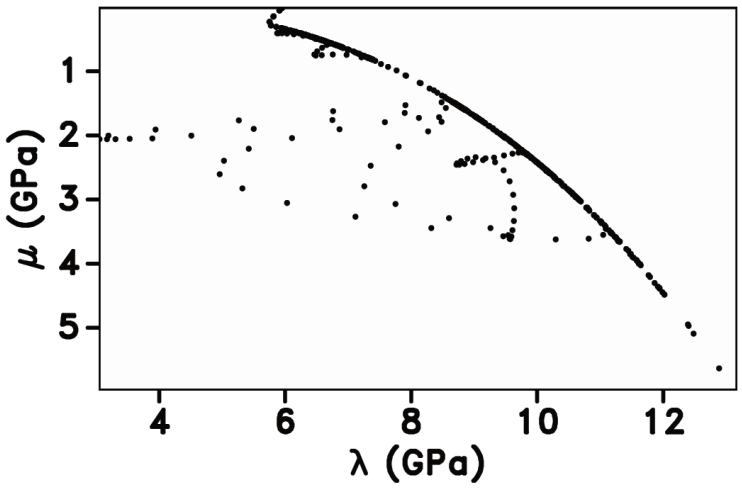

Figure 2.10: Crossplot of λ and μ provided by the well logs indicated in Figure 2.9. The relationship between the model parameters is not linear and does not follow a simple trend.

the PDF presented in the crossplots as the contour lines from the well log data, but without user-defined parameters. Both λ and μ models in Figures 2.15, 2.16 and 2.17 present similar resolution and are better recovered compared with the cases when we use the objective functions $\mathcal{J}_D$ (Figure 2.12) or $\mathcal{J}_D + \mathcal{J}_L$ (Figure 2.14). Additionally, the μ model artifacts are attenuated when we incorporate the probabilistic petrophysical constraints in the inversion. Also, the crossplot built with the inverted models (Figures 2.15, 2.16 and 2.17) is closer to the similar crossplot built with the correct model parameters relative to the crossplots obtained for the less robust objective functions $\mathcal{J}_D$ (Figure 2.12) or $\mathcal{J}_D + \mathcal{J}_L$ (Figure 2.14). When comparing the recovered models shown in Figures 2.15, 2.16 and 2.17, one can see that when $a = 10^{-9}$ (Figure 2.17) the inversion does not recover such accurate and feasible models as when $a = 5 \times 10^{-8}$ (Figure 2.15) or $a = 3 \times 10^{-8}$ (Figure 2.16). Therefore, when we reduce the strength of the $\mathcal{J}_P$ term the quality of the recovered models is compromised as the artifacts in the μ model located in the shallow depths, for example, are better attenuated when $a = 5 \times 10^{-8}$ (Figure 2.15) or $a = 3 \times 10^{-8}$ (Figure 2.16) than when $a = 10^{-9}$ (Figure 2.17).

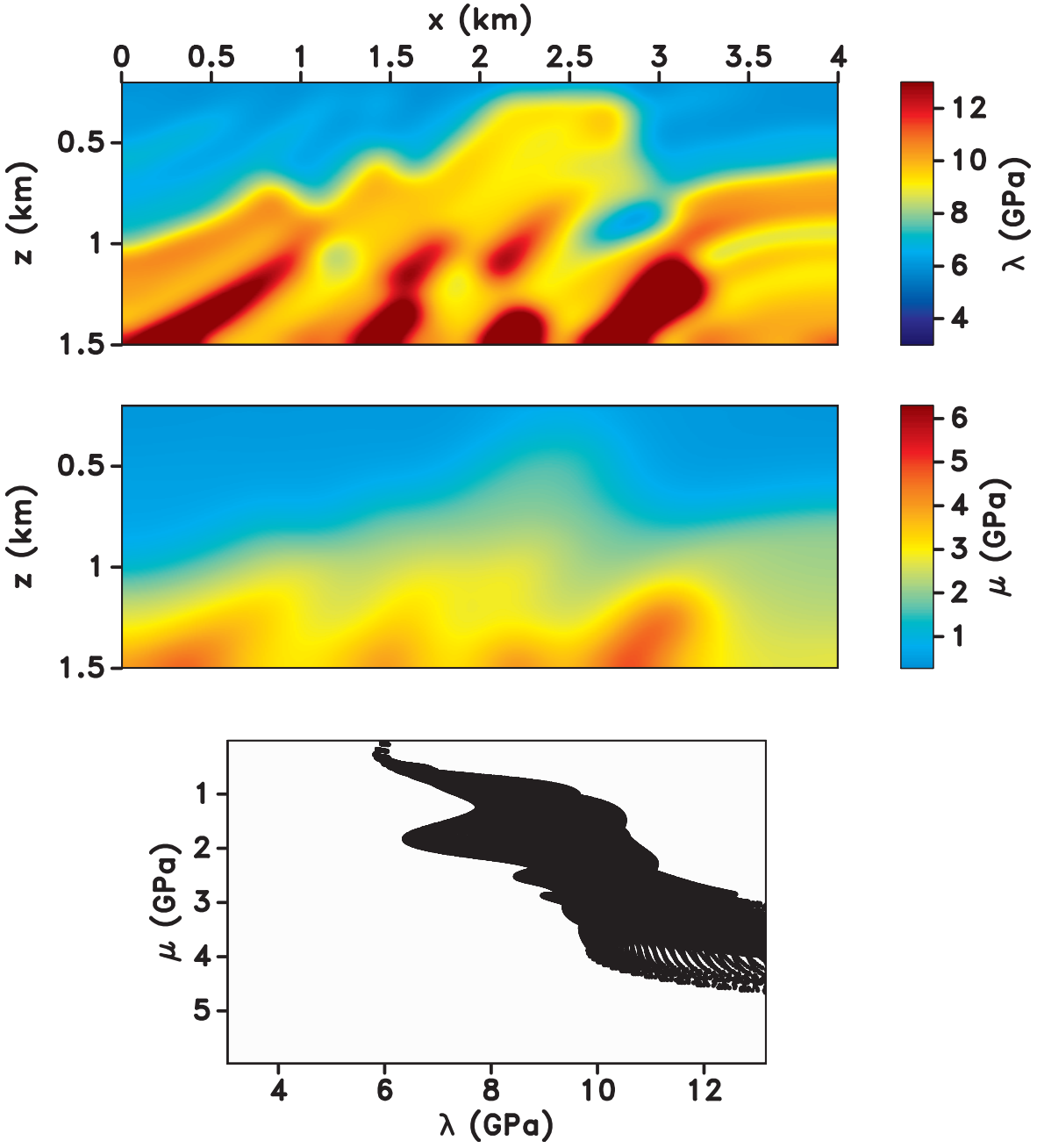

Figure 2.11: Marmousi 2 model: Initial λ and μ models and their crossplot in the $\lambda - \mu$ space.

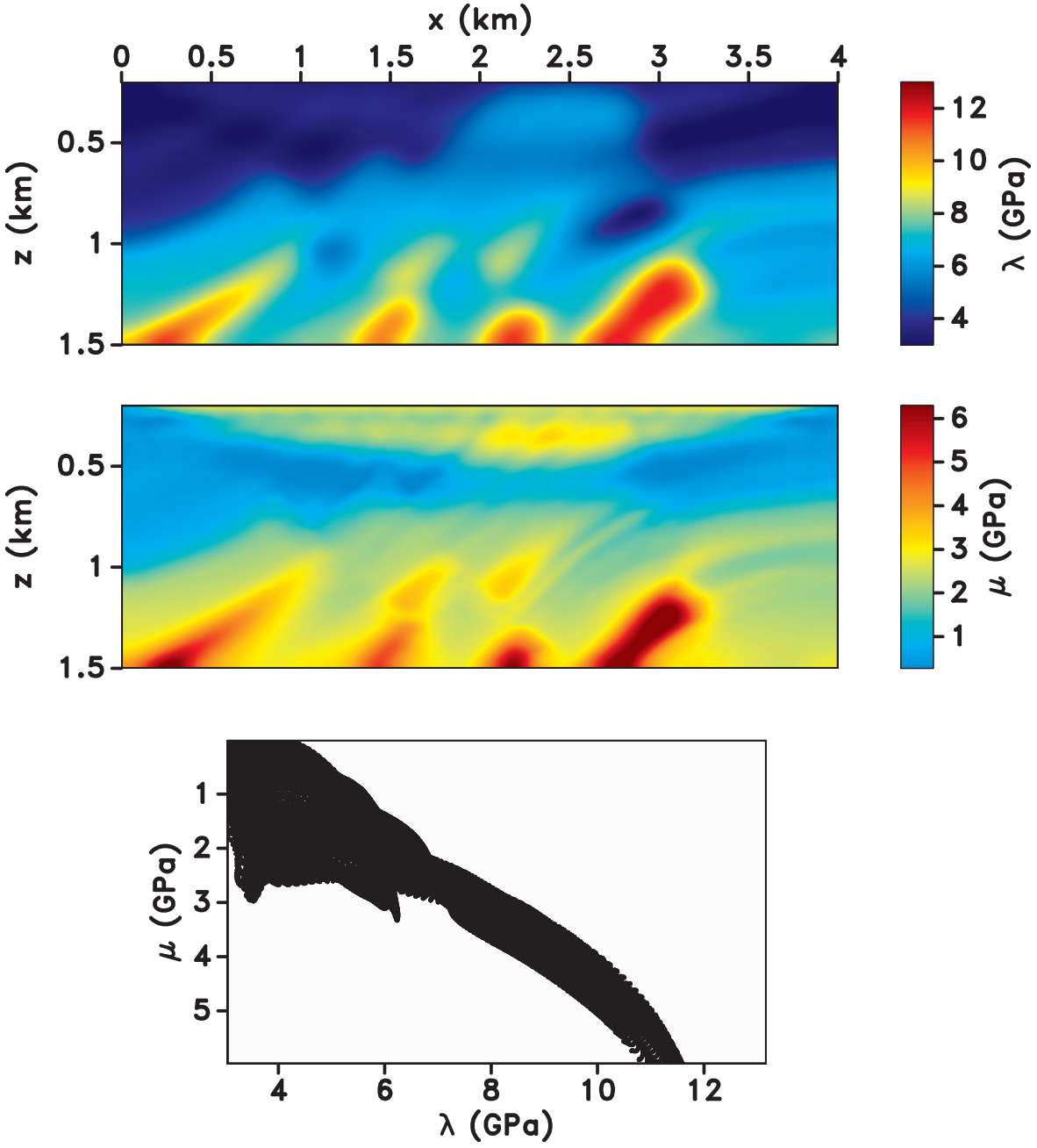

Figure 2.12: Marmousi 2 model: Recovered λ and μ models using objective function $\mathcal{J}_D$. The inverted μ model has more structural details than the λ model.

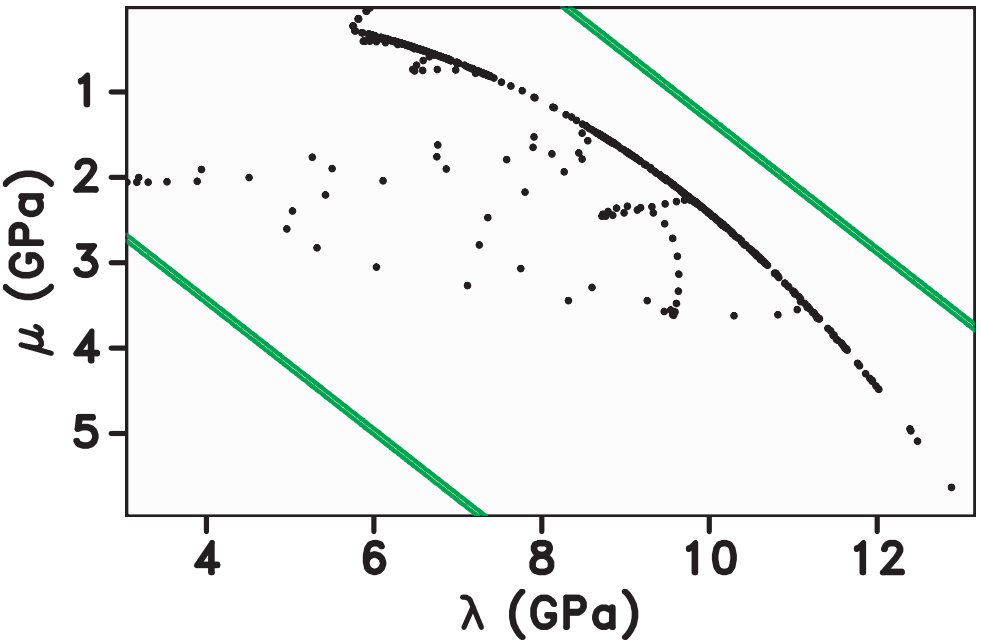

Figure 2.13: Crossplot of the λ and μ parameters extracted at the well location, superimposed by the upper and lower boundaries used in the logarithmic penalty function $\mathcal{J}_L$. As in the Gaussian example (Figure 2.5), the linear barriers ensure that the inversion recovers models confined to this feasible region.

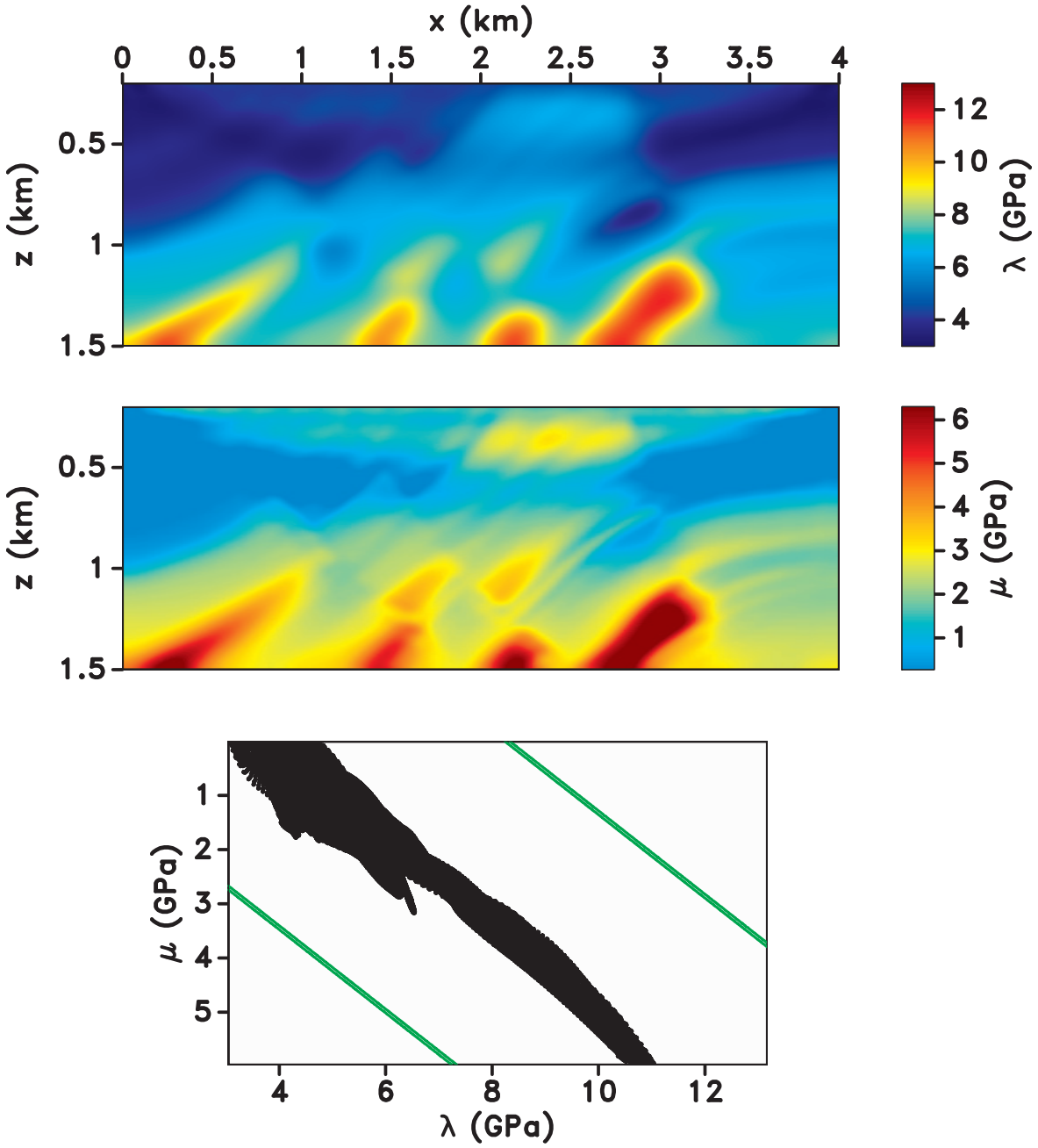

Figure 2.14: Marmousi 2 model: Recovered λ and μ models using objective function $\mathcal{J}_D + \mathcal{J}_L$. The lines in the crossplot define the upper and lower boundaries used in the logarithmic penalty function $\mathcal{J}_L$. The inverted model is forced to be in the middle area of the feasible region, which does not reflect correctly the trend shown in Figure 2.9 for the true model.

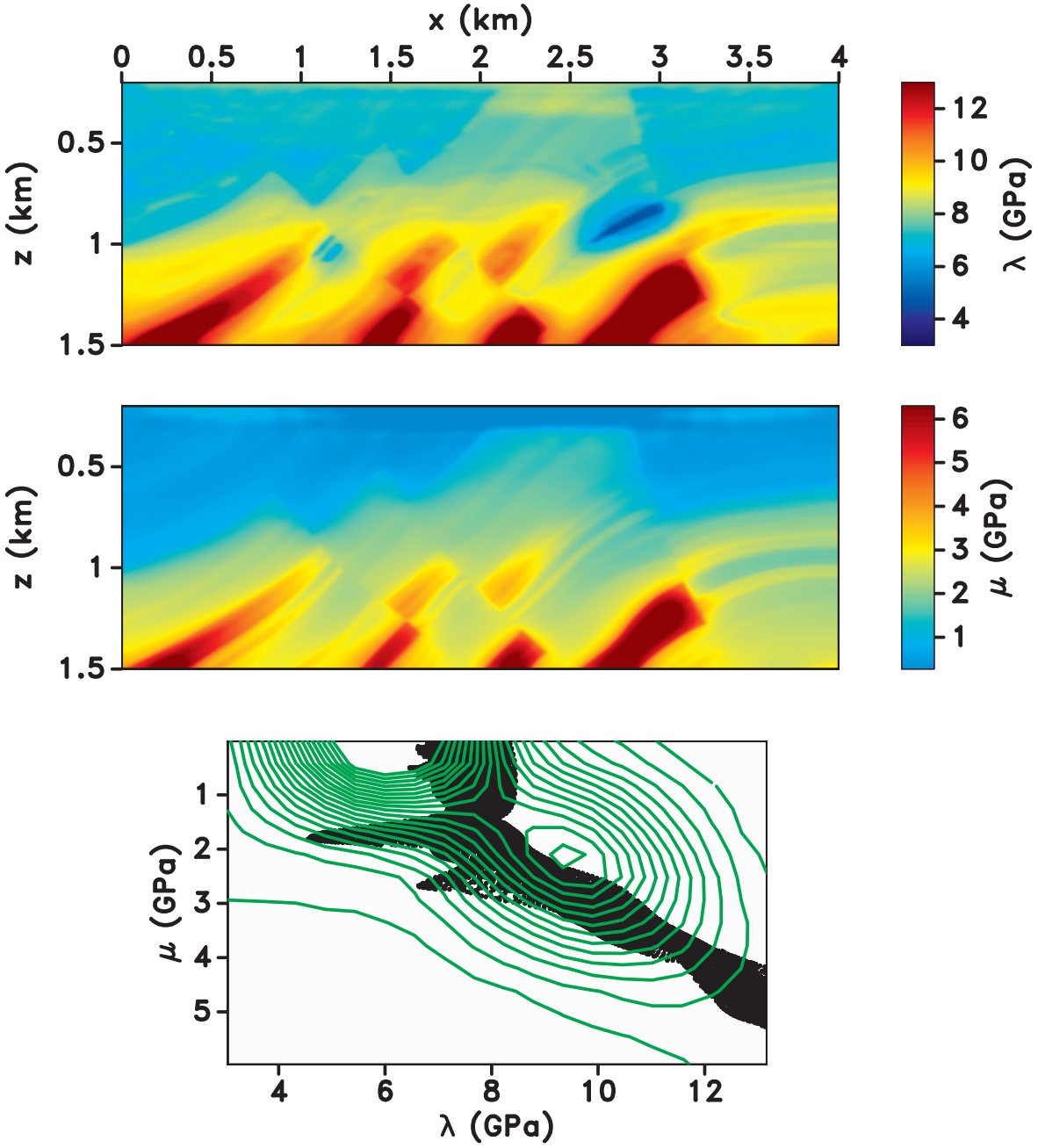

Figure 2.15: Marmousi 2 model: Recovered λ and μ models using objective function $\mathcal{J}_D + \mathcal{J}_P$ with $a = 5 \times 10^{-8}$. The contours in the crossplot represent the feasible area for the probabilistic constraint $\mathcal{J}_P$. The probabilistic petrophysical constraint leads to better recovered models than the unconstrained inversion (Figure 2.12) or the inversion with approximate analytic constraints (Figure 2.14).

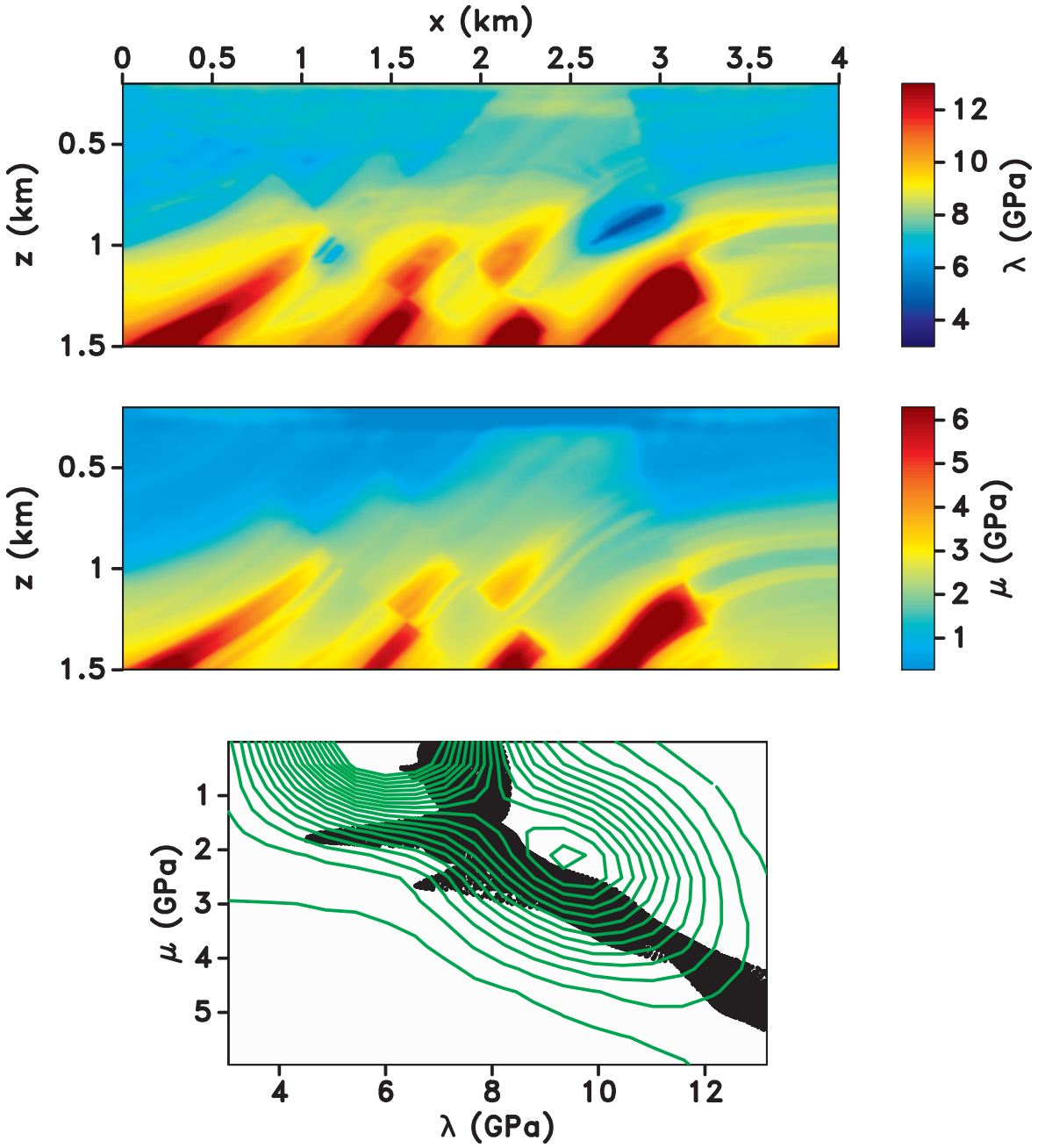

Figure 2.16: Marmousi 2 model: Recovered λ and μ models using objective function $\mathcal{J}_D + \mathcal{J}_P$ with $a = 3 \times 10^{-8}$. These recovered model are very similar to the ones shown in Figure 2.15, where $a = 5 \times 10^{-8}$.

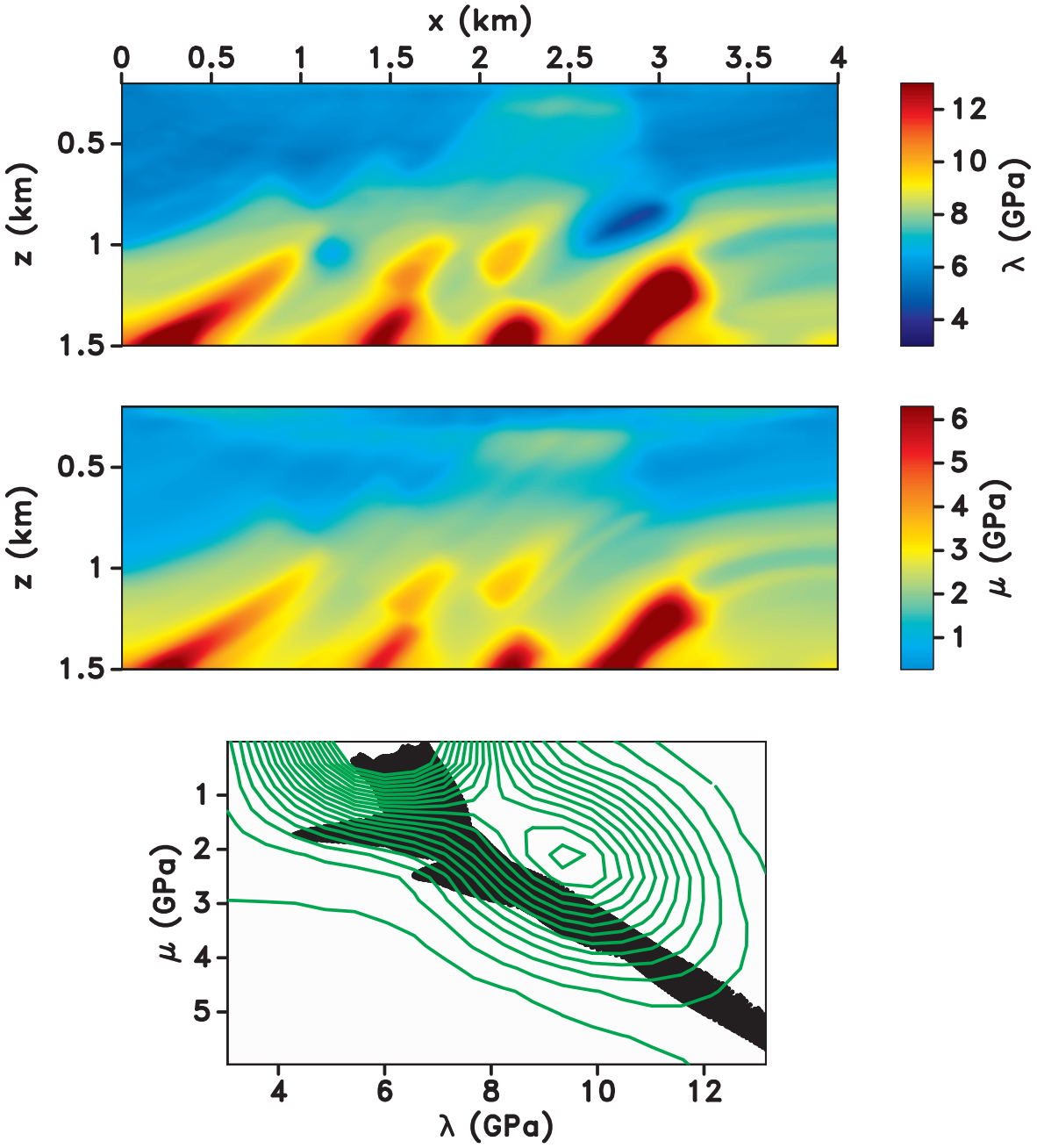

Figure 2.17: Marmousi 2 model: Recovered λ and μ models using objective function $\mathcal{J}_D + \mathcal{J}_P$ with $a = \times 10^{-9}$. As we use a smaller a than in the previous examples, the impact of the petrophysical penalty term in the object function is greatly reduced, which leads to poor recovered models compared to the ones shown in Figures 2.15 and 2.16 where a is equal to, respectively, 5×10^{-8} and 3×10^{-8}.

2.4 Discussion

The quality of elastic models derived from seismic wavefield tomography is often poor because the inversion is non-linear and ill-posed, and the objective function is non-convex. Thus, the inversion may converge to a local minimum due to the lack of access to good starting models, data noise and modeling errors, the absence of low frequencies in the data, incomplete acquisition coverage and the dimensionality of the model space. Additionally, simultaneous determination of multiple physical parameters using FWI suffers from interparameter trade-offs and model updates provided by this methodology may not represent real lithologies in unconstrained multiparameter inversion. A well-known approach to counter these deficiencies is to include model regularization in the inversion, which mitigates the ill-posedness and non-uniqueness of the inverse problem. Although regularization methods have enabled enormous progress in ill-posed geophysical inverse problems, they can guide inversion towards models that do not truly represent the subsurface, when accurate geological information about the entire studied region is not available. Petrophysical information provided by well logs or other sources describes the model only at sparse locations and therefore well log information cannot easily form the basis of model regularization in the space domain.

The technique we present in this study does not rely on accurate prior information about the whole investigated area. Instead, it uses petrophysical information in the model parameter domain without assuming any specific analytic relationship among the different elastic parameters. Such technique prevents incorrect model updates in regions where seismic data are inefficient and do not constrain sufficiently the subsurface properties. This technique addresses many relevant problems of elastic FWI. By incorporating prior information into the inversion, we reduce the number of possible model solutions and improve the inversion convergence towards the global minimum. Additionally, by linking the elastic parameters during the inversion, we can avoid geologically implausible earth models, and mitigate the artifacts created by interparameter crosstalk. From the synthetic examples we present in this

study, one can see that the use of the probabilistic petrophysical penalty term also mitigates the potentially deleterious effects of the source radiation pattern, and of limited acquisition aperture. Thus, the methodology outlined here would establish a more robust foundation for full-waveform inversion by explicitly guiding models toward plausible solutions in the specific geological context of the exploration problem. Full-waveform inversion augmented with petrophysical information would define a higher standard for estimating high-resolution, accurate and lithologically feasible subsurface models in land and marine environments.

An alternative to further enhance the geologic model realism is given by imposing a model regularization term in addition to petrophysical model constraints. Petrophysical constraints are complementary to spatial regularization and confine model updates to realistic combinations that represent the known geologic context in the investigated area.

2.5 Conclusions

We incorporate petrophysical information into the elastic full-waveform inversion, using model probability density functions derived from information provided by well logs or from other forms of rock physics analysis. We demonstrate that imposing petrophysical constraints in elastic wavefield tomography improves the quality of the recovered models, by restricting them to a feasible region, and therefore guiding the inversion towards geologically plausible solutions. Two synthetic examples show that the models recovered with the proposed method are closer to the true models, while maintaining robust and realistic petrophysical relationships between the model parameters. This constraint term also helps mitigate the interparameter crosstalk created by similar radiation patterns among the elastic parameters.

2.6 Acknowledgments

We acknowledge CAPES (Brazilian Federal Agency for Support and Evaluation of Graduate Education) for financial support. We thank the sponsors of the Center for Wave Phenomena (CWP) for additional support of this research. The synthetic examples in this paper

uses the Madagascar open-source software package (Fomel et al., 2013) freely available from http://www.ahay.org.

CHAPTER 3

ELASTIC FULL WAVEFIELD INVERSION WITH PROBABILISTIC PETROPHYSICAL CLUSTERING

A paper published in *Geophysical Prospecting*

Odette Aragao[1,2], Paul Sava[2]

Full waveform inversion (FWI) aims to use all information provided by seismic data to deliver high resolution models of subsurface parameters. However, multiparameter FWI suffers from an inherent trade-off between parameters and from ill-posedness due to the highly nonlinear nature of FWI. Also, the models recovered using elastic FWI are subject to local minima if the initial models are far from the optimal solution. In addition, an objective function purely based on the misfit between recorded and modeled data may honor the seismic data, but disregard the geological context. Hence, the inverted models may be geologically inconsistent, and not represent feasible lithological units. We propose that all the aforementioned difficulties can be alleviated by explicitly incorporating petrophysical information into the inversion through a penalty function based on multiple probability density functions (PDFs), where each PDF represents a different lithology with distinct properties. We treat lithological units as clusters and use unsupervised K-means clustering to separate the petrophysical information into different units of distinct lithologies are not easily distinguishable. Through several synthetic examples, we demonstrate that the proposed framework leads FWI to elastic models that are superior to models obtained either without incorporating petrophysical information, or with a probabilistic penalty function based on a single PDF.

[1]Primary researcher and author.
[2]Department of Geophysics, Colorado School of Mines, Golden, Colorado, United States of America.

3.1 Introduction

The capability to deliver high resolution subsurface models has made full waveform inversion (FWI) a powerful process for building models of seismic properties underlying wave propagation (Pratt, 1999; Sirgue and Pratt, 2004; Tarantola, 1984; Virieux and Operto, 2009). Conventionally, FWI functions as a data-fitting iterative procedure, i.e., the minimization of an objective function based on the misfit between recorded and simulated data, where the latter is modeled using a two-way wave equation in order to consider all wave propagation mechanisms. At each iteration, the considered wave equation employs the current subsurface model, which is updated by perturbations derived from the gradient of an objective function, usually computed using the adjoint state method (Plessix, 2006).

However, the inverse problem constrained by wave-equation presents many difficulties. First, the inverse problem is ill-posed and highly non-linear in relation to the model parameters, essentially because seismic waves are oscillatory in nature (Symes, 2008). Second, if the initial subsurface models are not kinematically accurate enough to predict data with an error lower than half of the wavelength, the data residual suffers from cycle skipping and the inversion leads to models corresponding to local minima.

Compared to implementations using the isotropic acoustic wave equation (Pratt, 1990; Pratt et al., 1996; Tarantola, 1984), elastic FWI is more accurate in describing the physics of wave propagation in the earth (Pratt, 1990; Tarantola, 1988). An isotropic elastic wave equation can be written in terms of P- and S-wave velocities or Lamé parameters, λ and μ. However, the inverse problem is more ill-posed when estimating multiple parameters, as we introduce more degrees of freedom in the model space (Operto et al., 2013). Moreover, different elastic properties may be coupled and updates of one parameter leak into others, an effect known as crosstalk. In addition, the combinations of different components in the recovered model parameters can be lithologically implausible or impossible as model parameters are updated simultaneously, but independently.

One can reduce the number of possible solutions for the ill-posed FWI problem by adding a model regularization term to the objective function (Tarantola, 2005; Tikhonov and Arsenin, 1977). First- and second-order Tikhonov regularization can be used to generate smooth updates of the parameters, while total variation (TV) regularization preserves sharp features in the models (Guitton, 2012). Additionally, one can also include a prior model term if additional information (well logs or geological information, for example) is available prior to the inversion. Asnaashari et al. (2013) exploit first-order Tikhonov regularization and a prior model norm term in the FWI objective function in order to increase the image reliability and to reduce the inversion sensitivity to inaccurate initial models. Zhang et al. (2018), Singh et al. (2018) and Zhang and Alkhalifah (2019) use seismic facies as *a priori* information to regularize elastic FWI and derive higher-resolution isotropic and anisotropic models. They achieve this goal by defining a model regularization related to the facies. As the spatial distribution of the facies is generally unknown, Zhang et al. (2018) and Singh et al. (2018) propose to update the facies at each iteration using a Bayesian inversion workflow, while Zhang and Alkhalifah (2019) build the distribution of facies in the subsurface by training deep neural networks.

However, these regularization techniques do not solve the problem of model updates that represent implausible lithologies. Inverted models may satisfy the regularization terms, while not actually describing realistic lithologies. Additionally, although regularization methods have advanced ill-posed geophysical inverse problems, challenges remain when the prior information consists of sparse data. Moreover, as the model regularization terms operate in the spatial domain, they can guide inversion towards models that do not truly represent the subsurface, when accurate geological information about the entire studied region is not taken into account.

Petrophysical information provided by well logs describes the model only at sparse locations and therefore well log information cannot easily form the basis of model regularization in the space domain. As an alternative, one can apply petrophysical constraints in the model

parameter space, in order to constrain the relationship between the model parameters during the inversion. This is the approach we take in this paper. Baumstein (2013) and Peters et al. (2015) use, respectively, the projection onto convex sets (POCS method) and projection onto intersections of convex sets to incorporate constraints into acoustic FWI, which lead to more stable simulations and geologically plausible structures. Manukyan et al. (2018) constrain the inversion by assuming that the elastic parameters have structural similarity and thus mitigate parameter trade-off problems and the different spatial resolution of elastic parameters. Peters et al. (2019) build a framework that favors sparse prior information using multiple convex and nonconvex constraints, in order to improve the accuracy of the recovered models and mitigate the effects of local minima. Duan and Sava (2016) and Rocha and Sava (2018) use a logarithmic penalty function to constrain, respectively, elastic wavefield tomography and elastic reflection waveform inversion, assuming a general linear relationship between the model parameters.

Aragao and Sava (2019) apply probabilistic model constraints, by explicitly using petrophysical information during the inversion in order to recover models that honor both geophysical and petrophysical data. They achieve this goal by incorporating a penalty function, based on probability density functions (PDFs), into the FWI objective function. They demonstrate through elastic models that incorporating a probabilistic petrophysical penalty into the inversion objective function leads to reliable models that are superior to models obtained either without constraints or with approximate analytic constraints. The petrophysical data are analyzed in the model parameter space represented by the probability density functions (PDFs) formed in $\lambda - \mu$ coordinates, while the geophysical data are treated in the physical space defined in space coordinates. The updates at different locations are driven by the data misfit term, but the petrophysical penalty prevents incorrect model updates in regions where data are inefficient and do not constrain sufficiently the subsurface properties.

However, Aragao and Sava (2019) use a single PDF to constrain the entire subsurface model, whereas the available petrophysical information may indicate the occurrence of many

lithological units. On the one hand, this indication can be evident, such that different lithologies are well defined and isolated in the petrophysical space. In this case, the PDF represents a multimodal distribution. On the other hand, when building the petrophysical PDF from well log data, one may not be able to differentiate distinct lithological units because the range of elastic parameters for these lithologies overlap. Still, one can use classification methods, such as K-means clustering (MacQueen, 1967), to categorize the petrophysical information into different units. We refer to a lithological unit as a *cluster*, representing a group of objects that have similar or correlated properties (Hartigan, 1975) and to the techniques that perform the classification task as *clustering*.

In order to recover subsurface models that represent different lithologies with distinct properties through constrained FWI, we propose to apply modified petrophysical constraints that use different PDFs for each lithological unit consistent with the available petrophysical information. Before this probabilistic penalty term can be applied, we categorize each point of the updated model to the most representative cluster. For this purpose, we determine the distance from each point in the model to the center of the considered clusters, and then we use the closest cluster to build the petrophysical penalty.

We illustrate the performance of the proposed framework with three synthetic examples. We show the critical effect of the probabilistic penalty term when we use multiple PDFs compared to the cases of unconstrained FWI or of a single PDF used to describe the entire model. We also show that, even when we can not differentiate classes of distinct lithologies in crossplots of model parameters, we can group the petrophysical data into different clusters, representing specific lithological units. We also highlight how cycle skipping may be mitigated when we explicitly incorporate petrophysical constraints into the inversion.

3.2 Elastic Wavefield Tomography

We use the isotropic elastic wave equation that assumes slowly varying Lamé parameters, such that their spatial gradients can be neglected,

$$\rho\ddot{\mathbf{u}} - \lambda[\nabla(\nabla \cdot \mathbf{u})] - \mu\left[\nabla \cdot \left(\nabla\mathbf{u} + \nabla\mathbf{u}^T\right)\right] = \mathbf{f}, \tag{3.1}$$

where $\mathbf{u}(e, \mathbf{x}, t)$ is the elastic wavefield, $\mathbf{f}(e, \mathbf{x}, t)$ is the source function, $\lambda(\mathbf{x})$ and $\mu(\mathbf{x})$ are the Lamé parameters, $\rho(\mathbf{x})$ is the density and e, $\mathbf{x}$ and t are, respectively, the experiment index, space coordinates and time.

The full waveform inverse problem is solved by minimizing an objective function $\mathcal{J}(\mathbf{u}_s, \lambda, \mu)$ consisting of three parts:

- a term that estimates the misfit between the predicted and observed data $\mathcal{J}_D(\mathbf{u}_s, \lambda, \mu)$,
- a model regularization term $\mathcal{J}_M(\lambda, \mu)$ that operates in the spatial domain and emphasize spatial correlation among the model parameters,
- a term that applies probabilistic model constraints using a petrophysical penalty term, $\mathcal{J}_P(\lambda, \mu)$.

Then,

$$\mathcal{J}(\mathbf{u}_s, \lambda, \mu) = \mathcal{J}_D(\mathbf{u}_s, \lambda, \mu) + \mathcal{J}_M(\lambda, \mu) + \mathcal{J}_P(\lambda, \mu). \tag{3.2}$$

We can define the misfit term $\mathcal{J}_D(\mathbf{u}_s, \lambda, \mu)$ as

$$\mathcal{J}_D(\mathbf{u}_s, \lambda, \mu) = \sum_e \frac{1}{2} \left\|\mathbf{W}_u(e, \mathbf{x}, t)\mathbf{u}_s(e, \mathbf{x}, t) - \mathbf{d}_{obs}(e, \mathbf{x}, t)\right\|^2, \tag{3.3}$$

where $\mathbf{d}_{obs}(e, \mathbf{x}, t)$ are the observed data and $\mathbf{W}_u(e, \mathbf{x}, t)$ are weights that restrict the source wavefield $\mathbf{u}_s(e, \mathbf{x}, t)$ to the known receiver locations.

We use a gradient-based method (Tarantola, 1988) to update the model, and we compute the gradient of $\mathcal{J}_D$ with respect to λ and μ using the adjoint-state method (Plessix, 2006), which consists of four steps:

1. Calculate the seismic wavefield $\mathbf{u}_s(e, \mathbf{x}, t)$, such that $\mathbf{L}\mathbf{u}_s - \mathbf{f}_s = \mathbf{0}$, where $\mathbf{f}_s$ and $\mathbf{L}$ represent, respectively, the source function and the linear elastic wave operator computed from equation 3.1.

2. Calculate the adjoint source $\mathbf{g}_s = \partial \mathcal{J}_D / \partial \mathbf{u}_s$, which uses the misfit between the observed and simulated data, according to equation 3.3.

3. Calculate the adjoint wavefield $\mathbf{a}_s(e, \mathbf{x}, t) = \mathbf{L}^T \mathbf{g}_s$, where $\mathbf{L}^T$ is the adjoint elastic wave operator.

4. Calculate the gradient of $\mathcal{J}_D$ with respect to the parameters λ and μ by

$$\begin{bmatrix} \dfrac{\partial \mathcal{J}_D}{\partial \lambda} \\ \dfrac{\partial \mathcal{J}_D}{\partial \mu} \end{bmatrix} = \sum_e \begin{bmatrix} -\nabla(\nabla \cdot \mathbf{u}) \star \mathbf{a}_s \\ -\nabla\left(\nabla \mathbf{u} + \nabla \mathbf{u}^T\right) \star \mathbf{a}_s \end{bmatrix}, \tag{3.4}$$

where the symbol $\star$ represents zero-lag time crosscorrelation.

Incorporating a model regularization term into the objective function reduces the number of possible solutions for the ill-posed FWI problem (Asnaashari et al., 2013; Jun et al., 2017; Tarantola, 2005; Tikhonov and Arsenin, 1977; Zhang et al., 2018). One can perform regularization by adding the first-order Tikhonov regularization term $\mathcal{J}_M^{Tik}(\lambda, \mu)$ into the objective function in order to provide smoothness to the estimated models, such that

$$\mathcal{J}_M^{Tik}(\lambda, \mu) = \frac{1}{2}\|\nabla \lambda(\mathbf{x})\|^2 + \frac{1}{2}\|\nabla \mu(\mathbf{x})\|^2, \tag{3.5}$$

where ∇ represents the first-order spatial derivative operator. For a second-order Tikhonov regularization, one can replace ∇ by the second-order Laplacian operator. An alternative regularization approach uses total variation (TV) by adding another term $\mathcal{J}_M^{TV}(\lambda, \mu)$ to the objective function in order to preserve sharp interfaces in the recovered models (Guitton, 2012; Zhang et al., 2019b),

$$\mathcal{J}_M^{TV}(\lambda, \mu) = \int_\Omega \sqrt{\|\nabla \lambda(\mathbf{x})\|^2}\, d\mathbf{x} + \int_\Omega \sqrt{\|\nabla \mu(\mathbf{x})\|^2}\, d\mathbf{x}, \tag{3.6}$$

where Ω represents the subsurface spatial domain.

One can also include a prior model regularization term $\mathcal{J}_M^{prior}(\lambda, \mu)$ into the objective function (Asnaashari et al., 2013; Tarantola, 2005; Zhang et al., 2018), such that

$$\mathcal{J}_M^{prior}(\lambda, \mu) = \frac{1}{2} \left\| \mathbf{W}_\lambda(\mathbf{x})(\lambda(\mathbf{x}) - \bar{\lambda}(\mathbf{x})) \right\|^2 + \frac{1}{2} \left\| \mathbf{W}_\mu(\mathbf{x})(\mu(\mathbf{x}) - \bar{\mu}(\mathbf{x})) \right\|^2, \tag{3.7}$$

where $\bar{\lambda}(\mathbf{x})$ and $\bar{\mu}(\mathbf{x})$ are prior models. $\mathbf{W}_\lambda(\mathbf{x})$ and $\mathbf{W}_\mu(\mathbf{x})$ are weighting operators in the model space, and represent the inverse square-root of the model covariance matrices. Prior information can be based on knowledge about the model geometry, e.g., smoothness or prior geological information.

When one considers the objective function for the elastic FWI problem as $\mathcal{J}_D + \mathcal{J}_M$, the components of the model parameters λ and μ are updated independently. Therefore, they can become physically inconsistent with each other, leading to an infeasible geologic representation of the subsurface. Additionally, the terms in equations 3.5, 3.6 and 3.7 operate in the spatial domain, therefore, they can cause the elastic inversion to deliver unphysical and artifact-contaminated models.

Alternatively, if we have access to petrophysical information obtained, for example, from well logs, we can impose a penalty term that operate in the model parameter space. Aragao and Sava (2019) include a petrophysical penalty term $\mathcal{J}_P(\lambda, \mu)$, built using a probabilistic approach, into the objective function.

From available well log data, they create a probability density function (PDF) using a normalized multidimensional histogram. Considering the vector $\mathbf{m} = [\lambda \ \ \mu]$ as the elastic model components of a given position $\mathbf{x}$, they evaluate distances to all points of the PDF, represented as $\mathbf{p} = [\lambda_p \ \ \mu_p]$. The distance between a given $\mathbf{m}$ to a point of coordinates $\mathbf{p}$ is

$$d(\mathbf{m}, \mathbf{p}) = \|\mathbf{m} - \mathbf{p}\|_2. \tag{3.8}$$

By defining the probability density of each cell of the PDF as $f(\mathbf{p})$, they determine the distance $D(\mathbf{m})$ from $\mathbf{m}$ to the distribution as

$$\frac{1}{D(\mathbf{m})} = \sum_{\mathbf{p}} \frac{f(\mathbf{p})}{d(\mathbf{m}, \mathbf{p})}, \tag{3.9}$$

and then define the petrophysical penalty term $\mathcal{J}_P$ as

$$\mathcal{J}_P = \eta \sum_{\mathbf{m}} D(\mathbf{m}). \tag{3.10}$$

where η is a scalar parameter that determines the strength of the term $\mathcal{J}_P(\lambda, \mu)$ in the overall objective function. The gradient of $\mathcal{J}_P$ with respect to the model parameters λ and μ is

$$\frac{\partial \mathcal{J}_P}{\partial \lambda} = \eta\, D^2(\mathbf{m}) \sum_{\mathbf{p}} \frac{f(\mathbf{p})(\lambda - \lambda_p)}{d^3(\mathbf{m}, \mathbf{p})}, \tag{3.11}$$

and

$$\frac{\partial \mathcal{J}_P}{\partial \mu} = \eta\, D^2(\mathbf{m}) \sum_{\mathbf{p}} \frac{f(\mathbf{p})(\mu - \mu_p)}{d^3(\mathbf{m}, \mathbf{p})}. \tag{3.12}$$

For illustration, let's consider the PDFs illustrated in Figures 3.1a and 3.1b describing petrophysical information for different scenarios. Figures 3.2a and 3.2b show the distribution of $D(\mathbf{m})$, which is small in the proximity of the given PDFs and increases away from the distribution. Additionally, Figures 3.2a and 3.2b display the distribution of the gradient of $D(\mathbf{m})$, which is close to zero in the region where the PDF is high. Thus, once a point $\mathbf{m}$ in the updated model is consistent with the distribution given by the PDF, the data misfit $\mathcal{J}_D$ fully controls the gradient and the action of the petrophysical penalty term ceases.

By incorporating $\mathcal{J}_P(\lambda, \mu)$ into the FWI object function, the elastic parameters are linked during the inversion. Aragao and Sava (2019) also show that, by using the term $\mathcal{J}_P$, one can:

- reduce the non-linearity and ill-posed nature of FWI,
- avoid geologically implausible earth models,
- mitigate artifacts produced by interparameter crosstalk,
- maintain robust and realistic petrophysical relationships between the model parameters.

However, the method proposed by Aragao and Sava (2019) uses a petrophysical penalty term based on a single PDF to represent the entire model, i.e., a single PDF to describe

many lithologies. However, the occurrence of many lithological units may be indicated by the available petrophysical information, with different lithologies well defined and isolated in the petrophysical space. In this case, we propose to use a petrophysical penalty term based on multiple PDFs, each representing a different lithological unit. In order to do so, we categorize each given model with components $(\lambda_{\mathbf{x}}, \mu_{\mathbf{x}})$ to a specific cluster, by calculating the distance between $(\lambda_{\mathbf{x}}, \mu_{\mathbf{x}})$ and the center of each PDF. Then, we use the closest PDF to build the petrophysical penalty related to $(\lambda_{\mathbf{x}}, \mu_{\mathbf{x}})$.

Nevertheless, the occurrence of different lithologies may not be evident in the available petrophysical data. In this case, one may not be able to differentiate distinct lithological units in the PDF. One solution is to apply K-means clustering to separate the petrophysical information into different PDFs, where each PDF represents a lithological unit. K-means clustering consists of five steps (Hartigan, 1975; MacQueen, 1967):

1. define the number of clusters k,
2. initiate the algorithm with randomly selected center for each cluster,
3. assign each point of the available petrophysical data to the closest center,
4. update the center of each cluster as the mean of the points that were assigned to that cluster,
5. repeat steps 3 and 4 until no points are re-assigned, i.e., there is no change in center values.

After defining the clusters, we build a different PDF for each cluster and then follow the same approach as discussed above.

3.3 Examples

We illustrate our EFWI method with three examples. For all examples, we compare inversions using only the data misfit term $\mathcal{J}_D$, the data misfit with the petrophysical penalty

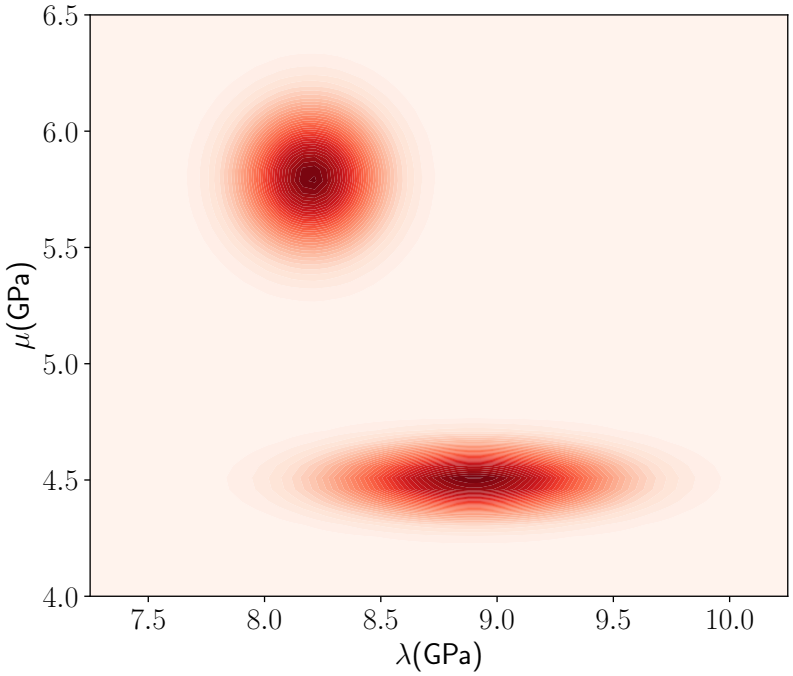

(a)

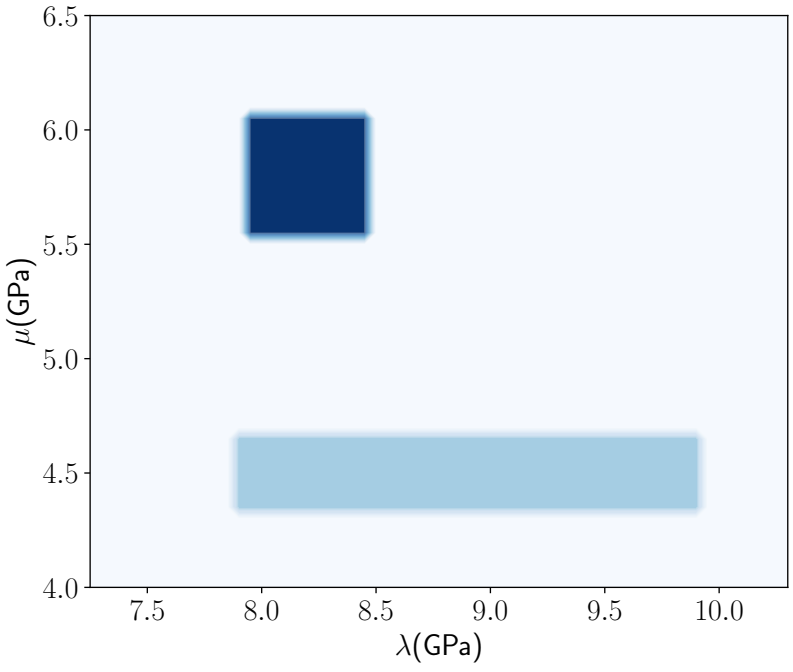

(b)

Figure 3.1: Examples of PDFs consisting of (a) two Gaussian functions and (b) two boxcar functions of different sizes and magnitudes.

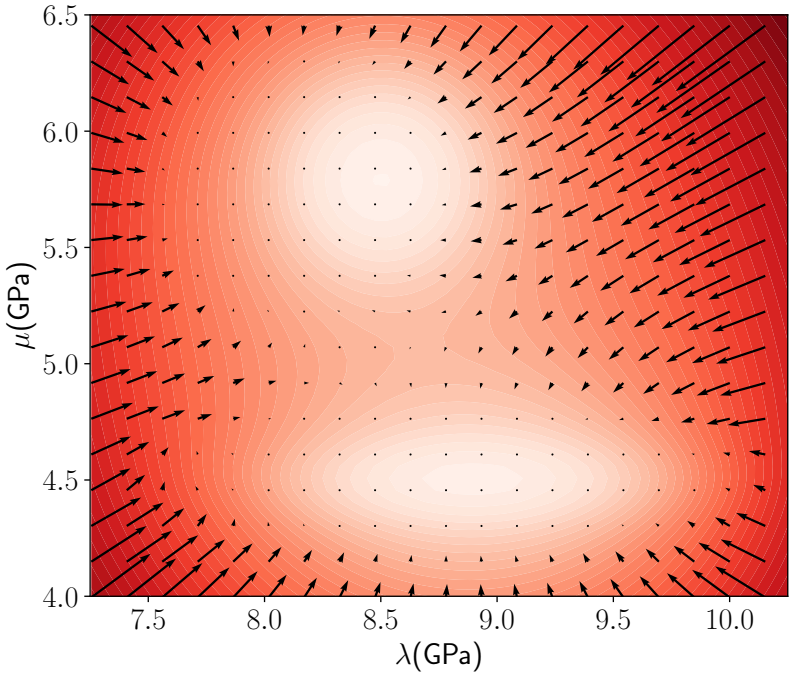

(a)

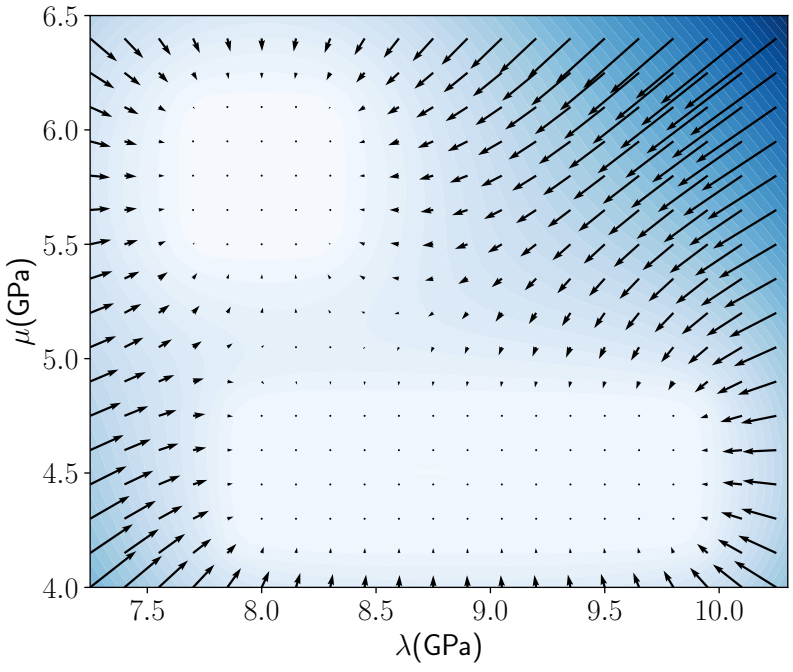

(b)

Figure 3.2: Distribution of the distance $D(\mathbf{m})$ and its gradient for the distributions shown in (a) Figure 3.1a and (b) Figure 3.1b. Note that high probability models are associated with small values of $D(\mathbf{m})$ and with zero gradients.

term based on a single PDF $\mathcal{J}_D + \mathcal{J}_{P1}$, and the data misfit with the petrophysical penalty term based on multiple PDFs $\mathcal{J}_D + \mathcal{J}_{P2}$.

For the first example, different lithologies are well defined and isolated in the petrophysical space. We aim to show how the probabilistic penalty term based on multiple PDFs guides the inversion toward more accurate models compared to the cases of unconstrained FWI or FWI using a probabilistic penalty term based on a single PDF.

The second example uses the same setup as for the first example, but a different initial model. In particular, we show how the petrophysical penalty based on multiple PDFs alleviates the lack of low wavenumbers in the initial model and, as a consequence, helps mitigating cycle skipping.

In the third example, we use a different correct model, where the available petrophysical information do not indicate the occurrence of separate lithological units. We use the K-means clustering technique to categorize the petrophysical information into clusters and to create different PDFs for the petrophysical penalty term. We demonstrate that K-means clustering is an effective classification method to separate the petrophysical data into several lithological units.

3.3.1 Clustered Marmousi 2 model

The first and second synthetic examples use a portion of the Marmousi 2 model (Martin et al., 2002). We modify the model to represent well-defined and distinct lithologies. We consider that prior petrophysical data from three well logs are available and we use this information to build the petrophysical model penalty. Figure 3.3 shows the correct λ and μ models, the well locations and the model parameters crossplot. We simulate a multicomponent seismic survey with a line of receivers and 20 evenly spaced sources located at the surface ($z = 0\,\text{km}$). Figure 3.4 shows the crossplot of λ and μ models extracted at the wells located at $x = 1.1$, 2.0 and 3.0 km (Figure 3.3), which indicates the presence of three separate lithological units (Figure 3.4). We use a 7.5 Hz peak Ricker source wavelet and perform two different experiments using the same correct λ and μ models (Figure 3.3) and the same

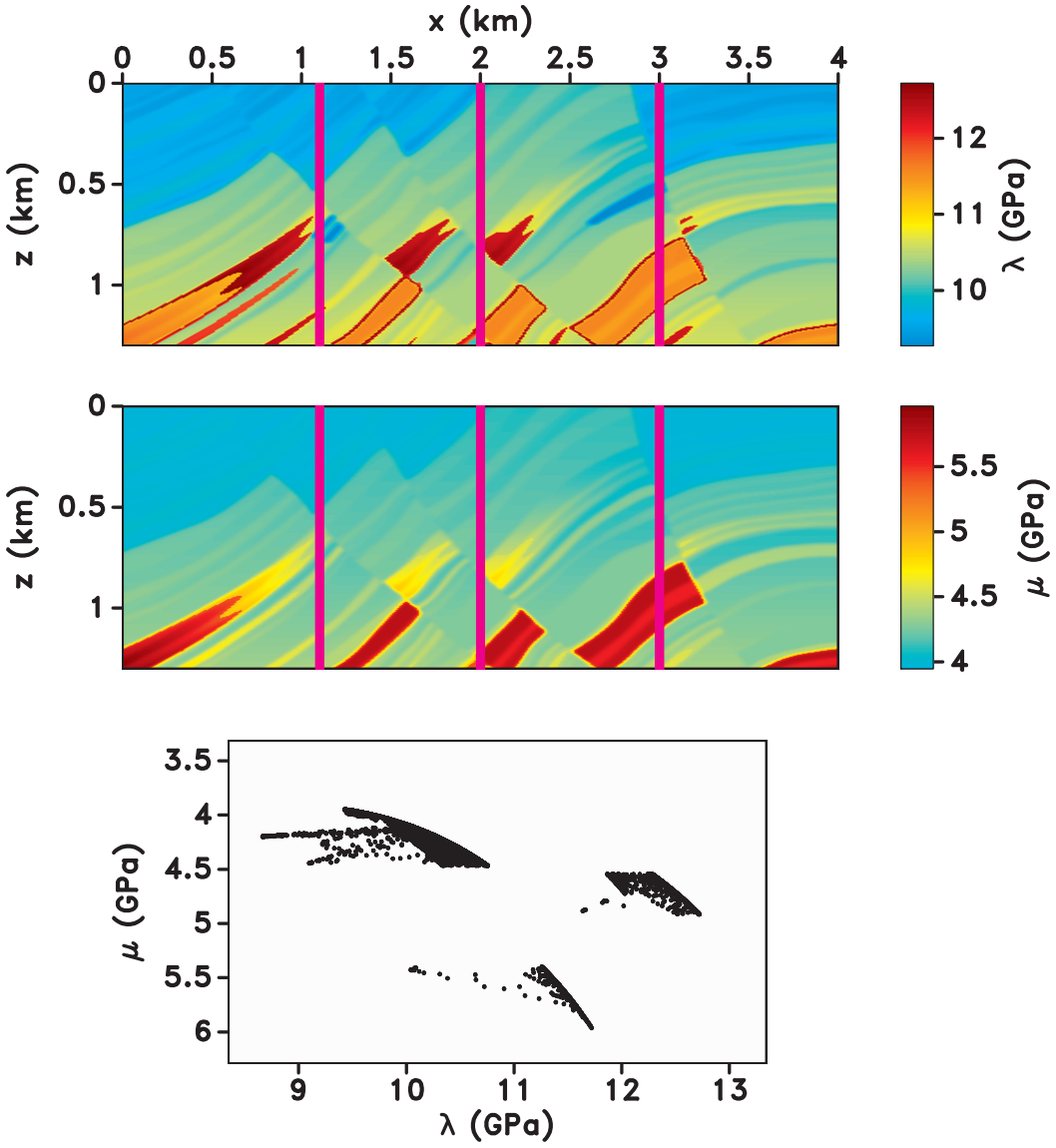

Figure 3.3: Clustered Marmousi 2 model: true λ and μ models and their crossplot for experiments A and B. The vertical lines correspond to well locations that provide information for the petrophysical penalty term.

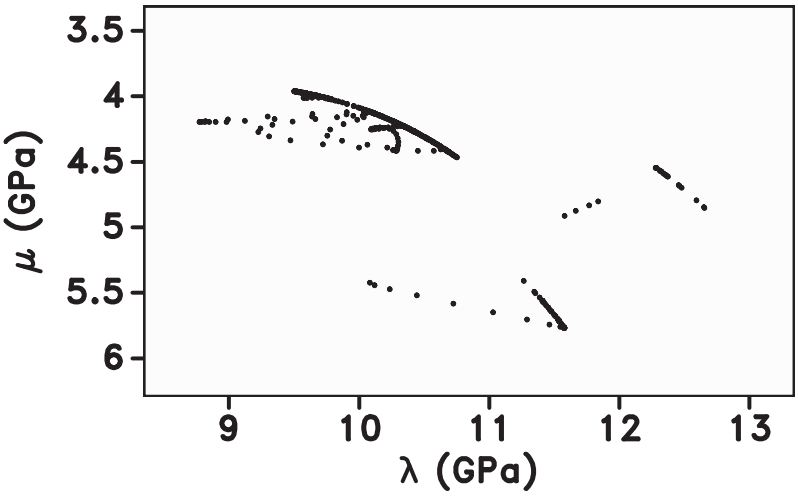

Figure 3.4: Crossplot of λ and μ provided by the well logs indicated in Figure 3.3. Note that different lithologies are well defined and isolated in the petrophysical space.

petrophysical information (Figure 3.4), but with different starting models.

Experiment A: clustered Marmousi 2 model with a 2D smooth initial model

For the first experiment, we use the initial λ and μ models shown in Figure 3.5. Figures 3.6a and 3.6b show, respectively, the vertical and horizontal components of the data residual before inversion. Notice that the data residual computed using the initial model (Figure 3.5) shows reflections, diving and head waves, thus highlighting the kinematic inaccuracy of the initial λ and μ models.

Figure 3.7 shows the recovered λ and μ models using the objective function $\mathcal{J}_D$. As we do not include petrophysical information during inversion, the μ model shows spurious artifacts due to the trade-off between the elastic parameters λ and μ. The recovered μ model also has more structural detail than the recovered λ model, as the S-wave wavelength is shorter than that of P waves. Therefore, the different models recovered from unconstrained inversion have distinct spatial resolution. Additionally, the amplitude of the low velocity anomaly presented in the true λ model (Figure 3.3) at $x = 3\,\text{km}$ and $z = 0.5\,\text{km}$ is not well recovered during the inversion. Moreover, the crossplot shown in Figure 3.7 does not resemble that of the true model (Figure 3.3). Figures 3.8a and 3.8b show, respectively, the vertical and horizontal

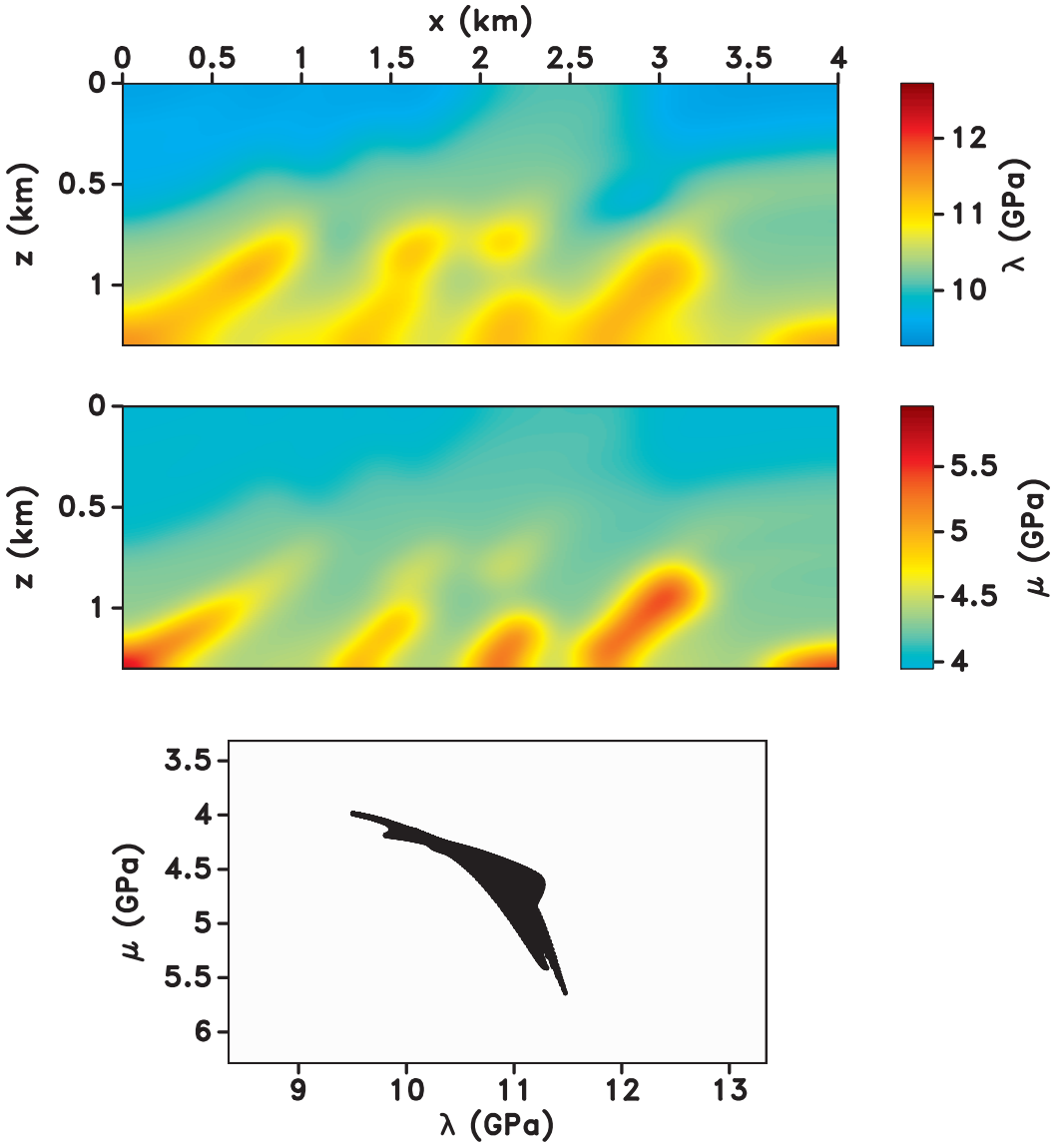

Figure 3.5: Experiment A: Initial λ and μ models and their crossplot in the $\lambda - \mu$ space. We obtain these initial models by smoothing the true model, which helps the inversion to converge to a global minimum.

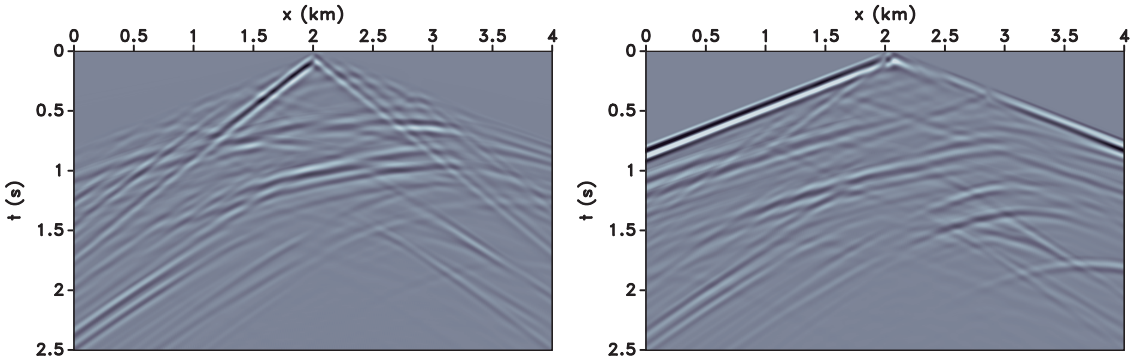

(a) (b)

Figure 3.6: Experiment A: (a) vertical and (b) horizontal components of the data residual. The predicted data are computed using the initial models shown in Figure 3.5.

components of the residual constructed using the recorded and the predicted data computed using the recovered models shown in Figure 3.7. The data residuals contain almost as many reflections, diving and head waves as in the case when we predict the data using the initial model (Figures 3.6a and 3.6b). Therefore, the recovered λ and μ models using the objective function $\mathcal{J}_D$ are kinematically inaccurate.

In order to perform the inversion using the petrophysical penalty term, we carry out two tests. For the first test, we use a single PDF to constrain the entire model, even though the crossplot of λ and μ provided by the well logs (Figure 3.4) indicates well defined separate lithologies. Therefore, the first test uses the objective function $\mathcal{J}_D + \mathcal{J}_{P1}$. Figure 3.9a shows the single PDF used in $\mathcal{J}_{P1}$, which corresponds to three clusters. For the second test, we use different PDFs to constrain the model, and the objective function uses $\mathcal{J}_D$ and $\mathcal{J}_{P2}$. Figure 3.9b shows the different PDFs used in $\mathcal{J}_{P2}$. The black dot inside each PDF in Figure 3.9b represents the center of the PDF and we use these points to decide which PDF is used to constrain each point in the model, i.e., decide to which cluster each point of the updated model is more likely to represent.

Figure 3.10 shows the recovered λ and μ models using the objective function $\mathcal{J}_D + \mathcal{J}_{P1}$. Different from the unconstrained inversion (Figure 3.7), the recovered λ and μ models have similar spatial resolution. Additionally, the inversion is able to recover the amplitude of the

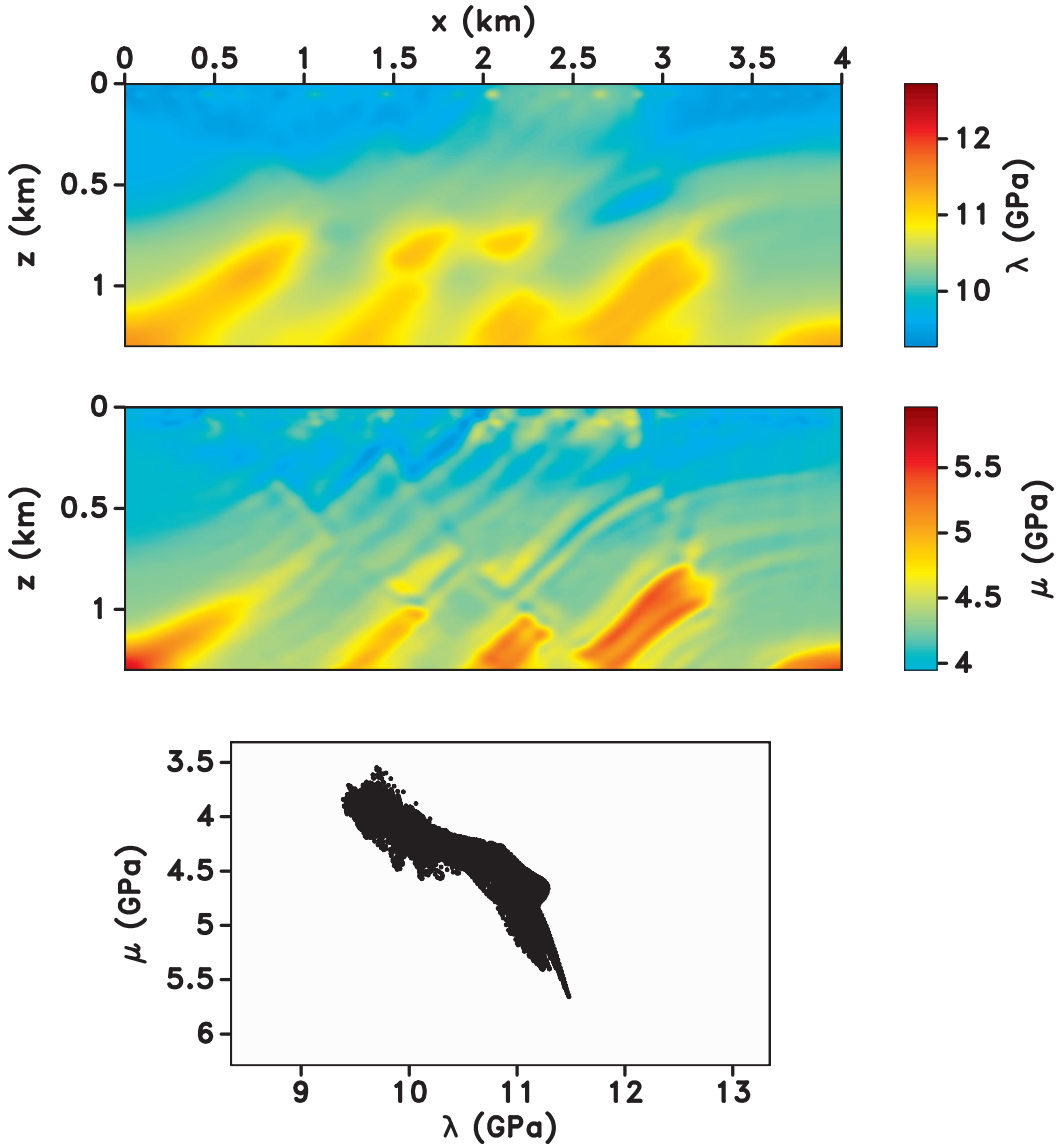

Figure 3.7: Experiment A: Recovered λ and μ models obtained using the objective function $\mathcal{J}_D$. Note that the μ model has more structural details than the λ model

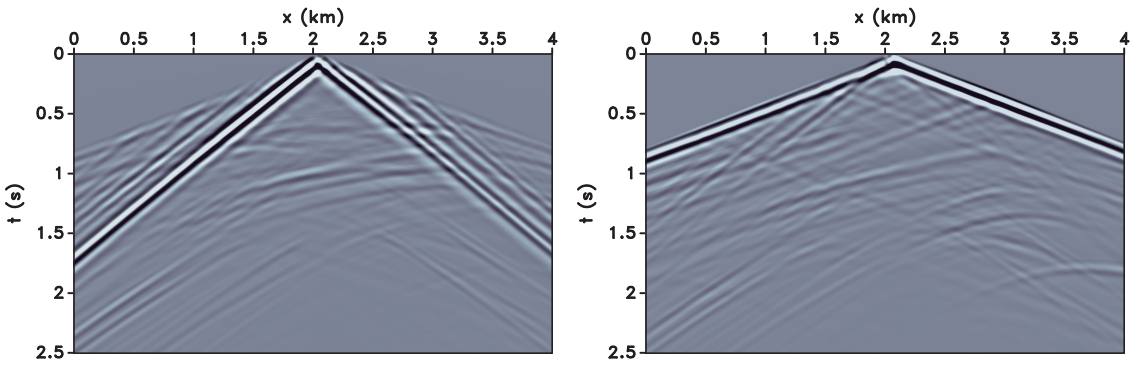

(a) (b)

Figure 3.8: Experiment A: (a) vertical and (b) horizontal components of the data residual for the unconstrained inversion. The predicted data are computed using the recovered models shown in Figure 3.7.

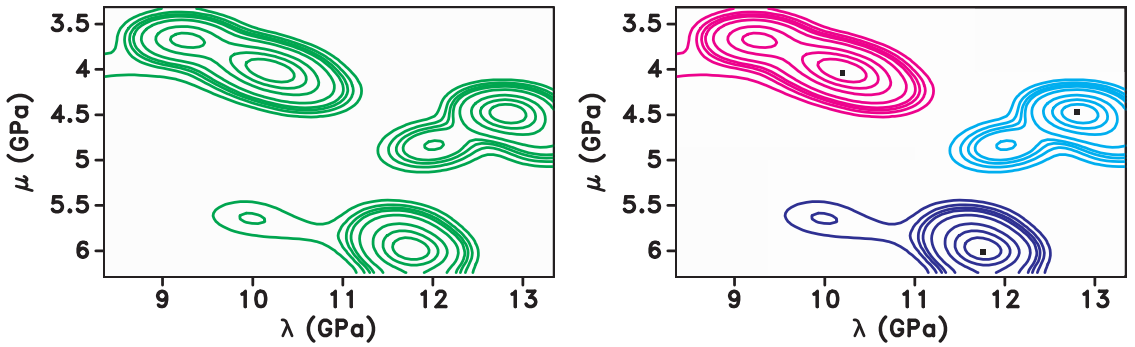

(a) (b)

Figure 3.9: (a) PDF associated with the term $\mathcal{J}_{P1}$ and (b) PDF associated with the term $\mathcal{J}_{P2}$. We estimate the PDFs in (a) and (b) from the well logs shown in Figure 3.4.

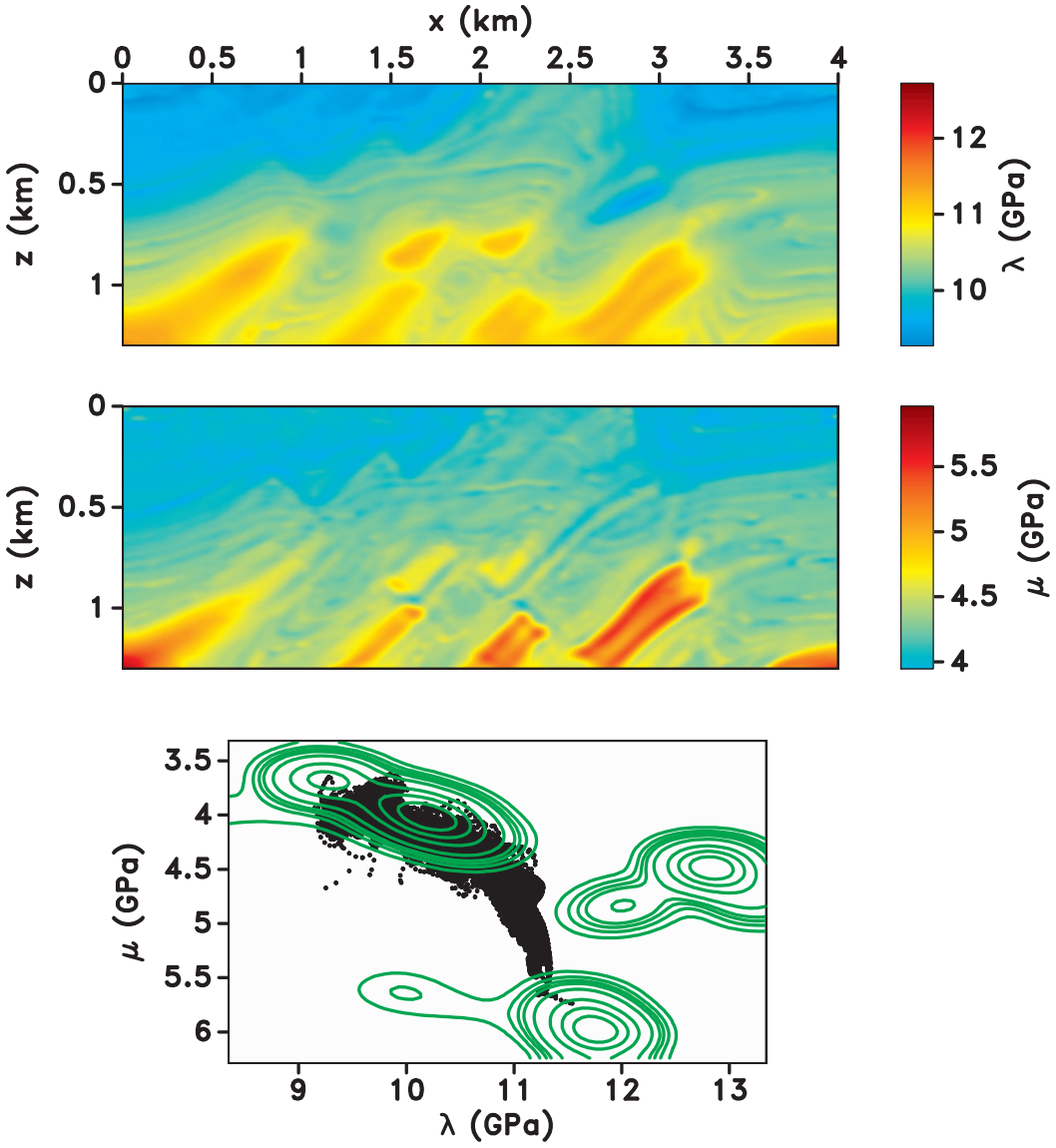

Figure 3.10: Experiment A: Recovered λ and μ models using the objective function $\mathcal{J}_D + \mathcal{J}_{P1}$. The green contours overlain on the crossplot illustrate the probabilistic penalty term based on a single PDF $\mathcal{J}_{P1}$.

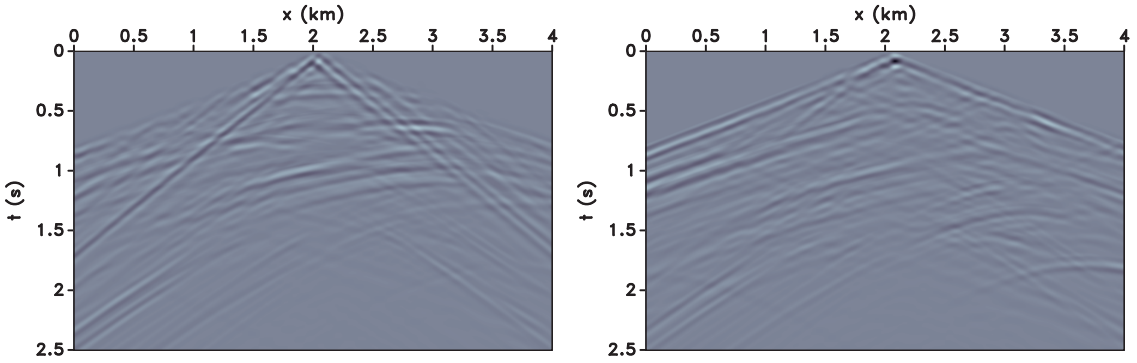

(a) (b)

Figure 3.11: Experiment A: (a) vertical and (b) horizontal components of the data residual for the inversion using the objective function $\mathcal{J}_D + \mathcal{J}_{P1}$. The predicted data are computed using the recovered models shown in Figure 3.10.

low velocity anomaly present in the true λ model (Figure 3.3) at $x = 3\,\text{km}$ and $z = 0.5\,\text{km}$ better than the inversion using the objective function $\mathcal{J}_D$ (Figure 3.7). However, the inverted models depicted in Figure 3.10 are noisy and do not show blocky structures as in the true models (Figure 3.3). In addition, the crossplot shown in Figure 3.10 shows that the inversion could not recover model with $\lambda > 11.5\,\text{GPa}$ and $4.0 < \mu < 5.0\,\text{GPa}$. Also, the majority of the points in the crossplot of Figure 3.10 are inside the distribution with $\lambda < 11.0\,\text{GPa}$ and $\mu < 4.5\,\text{GPa}$. Therefore, when petrophysical information indicates the presence of distinct lithologies, but we choose to use a penalty term based on a single PDF for the entire model, the cluster with larger probability attracts most model points during the inversion. Figures 3.11a and 3.11b show, respectively, the vertical and horizontal components of the data residual computed using the recorded and the predicted data computed using the recovered models shown in Figure 3.10. Notice that the amplitudes of the data residuals are smaller compared to the case where the data are predicted using the models recovered with the unconstrained inversion (Figures 3.8a and 3.8b), which indicates that the recovered λ and μ models using the objective function $\mathcal{J}_D + \mathcal{J}_{P1}$ are more accurate kinematically compared to the models recovered using the objective function $\mathcal{J}_D$.

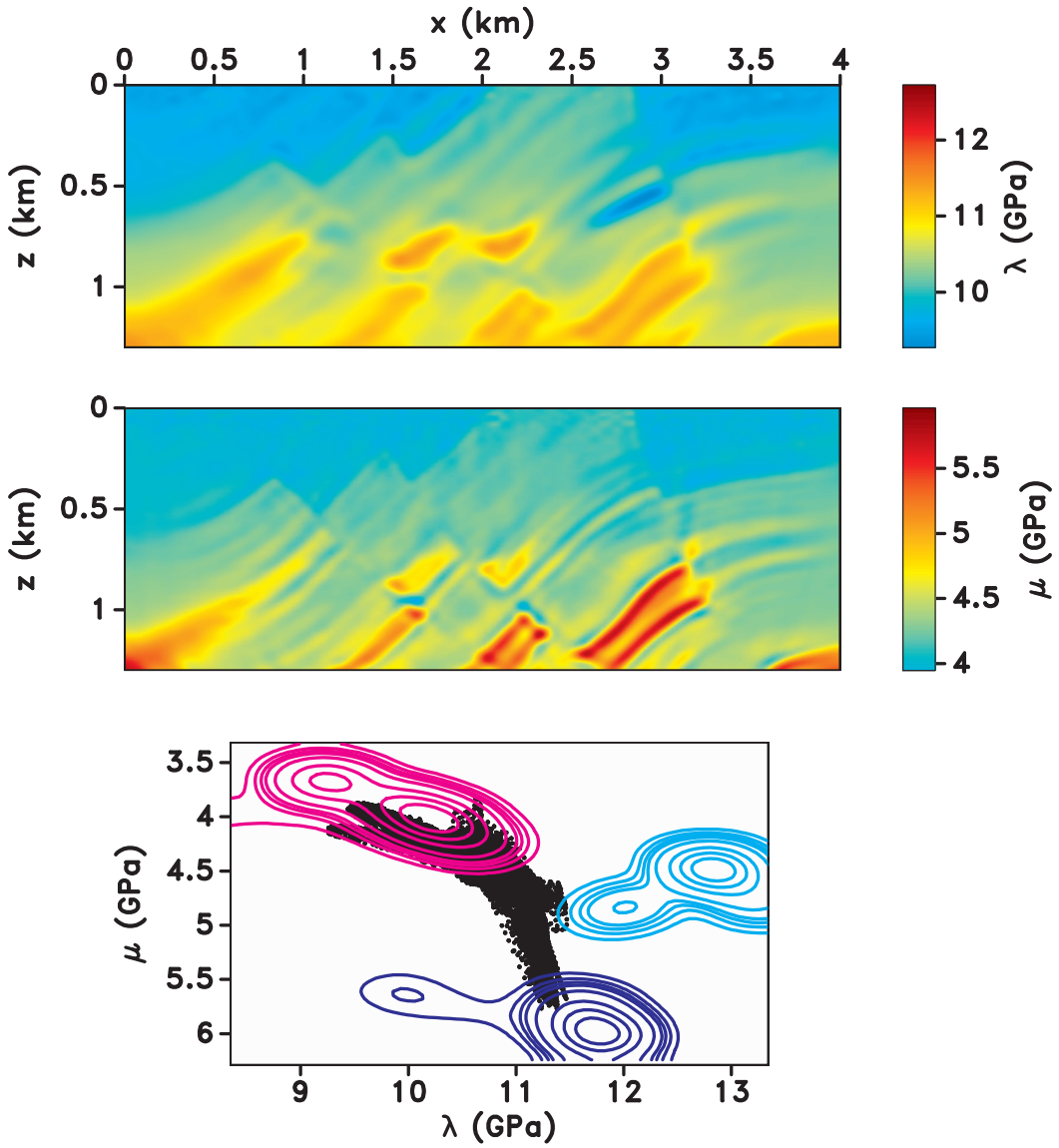

Figure 3.12: Experiment A: Recovered λ and μ models using the objective function $\mathcal{J}_D + \mathcal{J}_{P2}$. The contours with different colors overlain on the crossplot illustrate multiple PDFs used in the probabilistic penalty $\mathcal{J}_{P2}$. Note that three separate PDFs are used to constrain the model, although we display them together for simplicity.

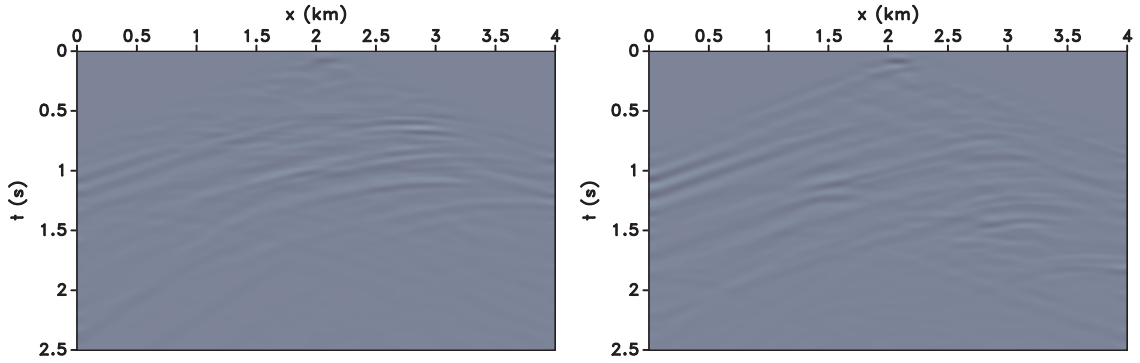

(a) (b)

Figure 3.13: Experiment A: (a) vertical and (b) horizontal components of the data residual for the inversion using the objective function $\mathcal{J}_D + \mathcal{J}_{P2}$. The predicted data are computed using the recovered models shown in Figure 3.12.

Figure 3.12 shows the recovered λ and μ models using the objective function $\mathcal{J}_D + \mathcal{J}_{P2}$. The contours correspond to three PDFs, each representing a cluster. The inverted λ and μ models shown in Figure 3.12 have comparable resolution and are closer to the true models compared with the cases when we use the objective functions $\mathcal{J}_D$ (Figure 3.7) or $\mathcal{J}_D + \mathcal{J}_{P1}$ (Figure 3.10). Additionally, the artifacts in the μ model caused by interparameter crosstalk are reduced. Notice that the crossplot built with the inverted models (Figure 3.12) shows points inside all three PDFs. Figures 3.13a and 3.13b show, respectively, the vertical and horizontal components of the data residual obtained using the recorded and the predicted data computed using the recovered models depicted in Figure 3.12. Note that the amplitudes of the data residuals are much smaller compared to the case where the data are predicted using the models obtained for the unconstrained objective function $\mathcal{J}_D$ (Figure 3.7) or for the objective function $\mathcal{J}_D + \mathcal{J}_{P1}$ (Figure 3.10).

Experiment B: clustered Marmousi 2 model with a 1D smooth initial model

For the second experiment, we use the initial λ and μ models shown in Figure 3.14. Note that the initial models are laterally homogeneous (1D), therefore FWI is subject to local minina in the absence of low frequencies. Figure 3.15 shows the comparison between

the vertical component of the simulated data computed using the homogeneous model (Figure 3.14), depicted in the background as variable density, and the vertical component of observed data, shown as an overlay in black and white wiggles. The red and blue colors in the variable density plot represent, respectively, positive and negative amplitudes. Note that the time delay is larger than half a period, as the positive amplitudes of the simulated data occur after the peak of each wiggle trace. Figure 3.15 proves that cycle skipping occurs using the basic 1D models.

Figure 3.16 shows the recovered λ and μ models using the objective function $\mathcal{J}_D$. As for the experiment A (Figure 3.7), the recovered μ model has more structural detail than the recovered λ model (Figure 3.16). Additionally, the inversion is not able to recover the amplitude of the high velocity anomalies present at the bottom part of the true models (Figure 3.3), as the initial model is too far from the truth (Figure 3.14). Moreover, the crossplot shown in Figure 3.16 does not resemble the true model (Figure 3.3).

Figure 3.17 shows the recovered λ and μ models using the objective function $\mathcal{J}_D+\mathcal{J}_{P1}$. As for the experiment A (Figure 3.12), the contours represent a single PDF with three clusters, which is used in the penalty term. The inversion recovers better the amplitude of the high velocity anomalies in the models compared with the cases when we use the objective function $\mathcal{J}_D$ (Figure 3.16).

Figure 3.18 shows the recovered λ and μ models using the objective function $\mathcal{J}_D+\mathcal{J}_{P2}$. As for the experiment A (Figure 3.12), the contours correspond to three PDFs. The inversion recovers the high velocity model anomalies, so λ and μ Figure 3.18 are better recovered compared with the cases when we use the objective functions $\mathcal{J}_D$ (Figure 3.16) and $\mathcal{J}_D+\mathcal{J}_{P1}$ (Figure 3.17). The models shown in Figure 3.18 prove that, in the absent of low frequencies, the petrophysical penalty term based on multiple PDFs helps to avoid cycle skipping and leads inversion to converge towards models (Figure 3.18) close to the true models (Figure 3.3).

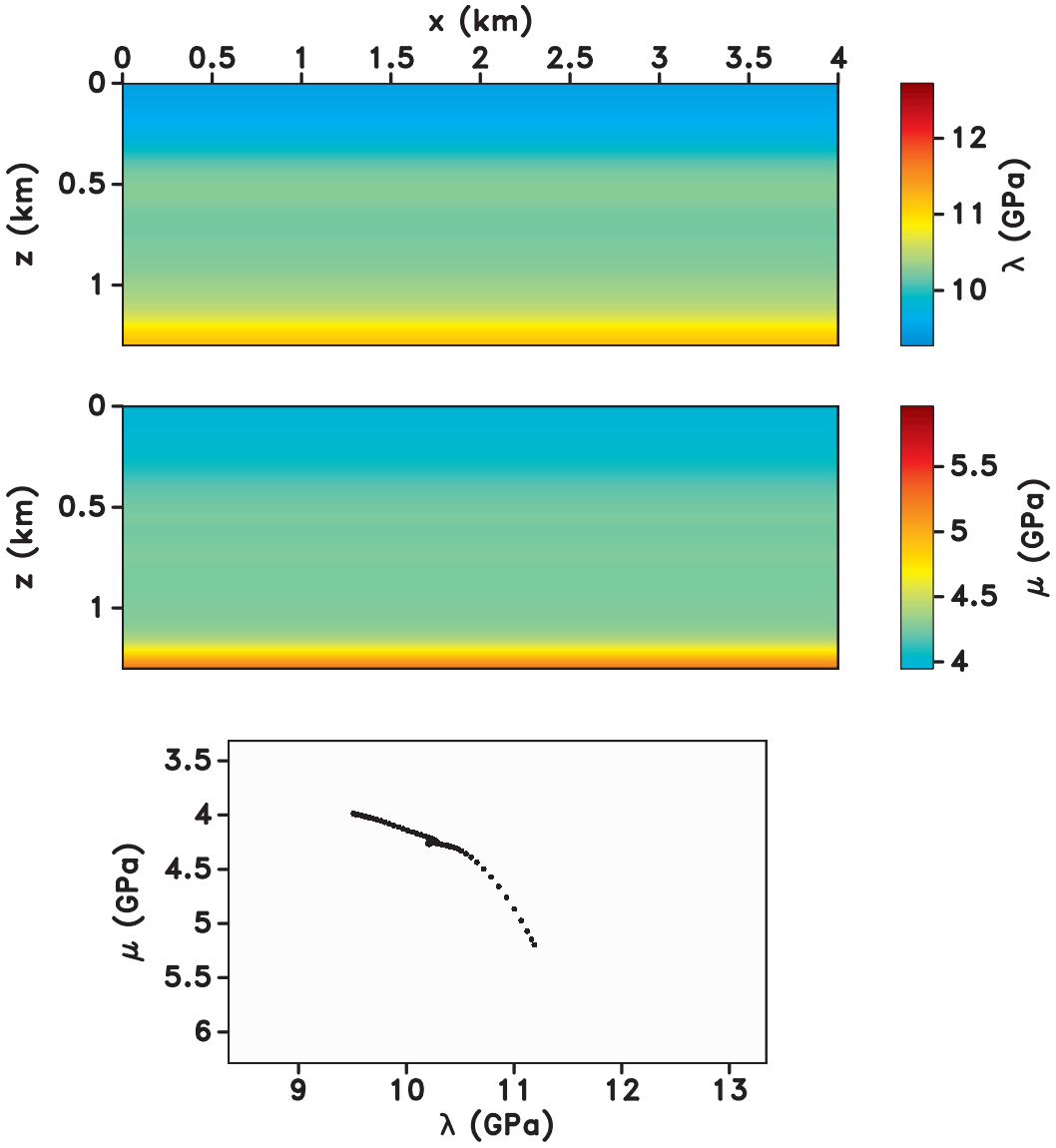

Figure 3.14: Experiment B: Initial λ and μ models and their crossplot in the $\lambda - \mu$ space. As these models are far from the true models (Figure 3.3), the inversion does not converge to a global minimum.

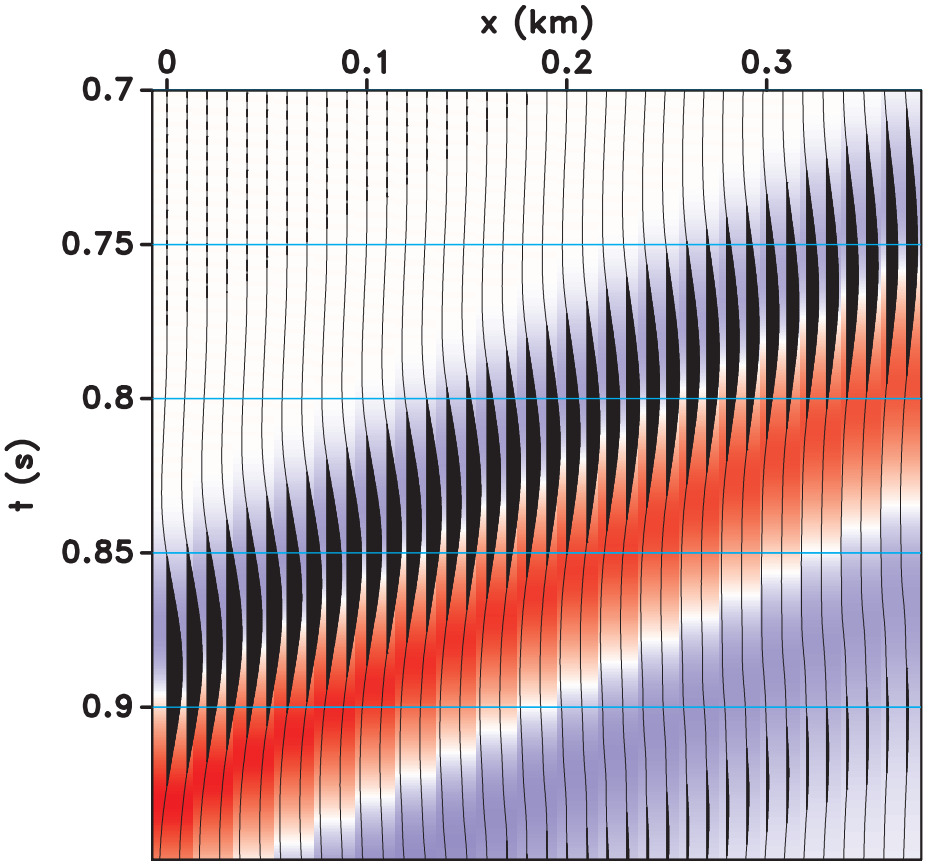

Figure 3.15: Experiment B: illustration of cycle skipping with the 1D starting model. The variable density plot in the background represents the vertical component of the simulated data computed using the initial 1D model (Figure 3.14) and the overlaying black and white wiggles are the vertical component of observed data.

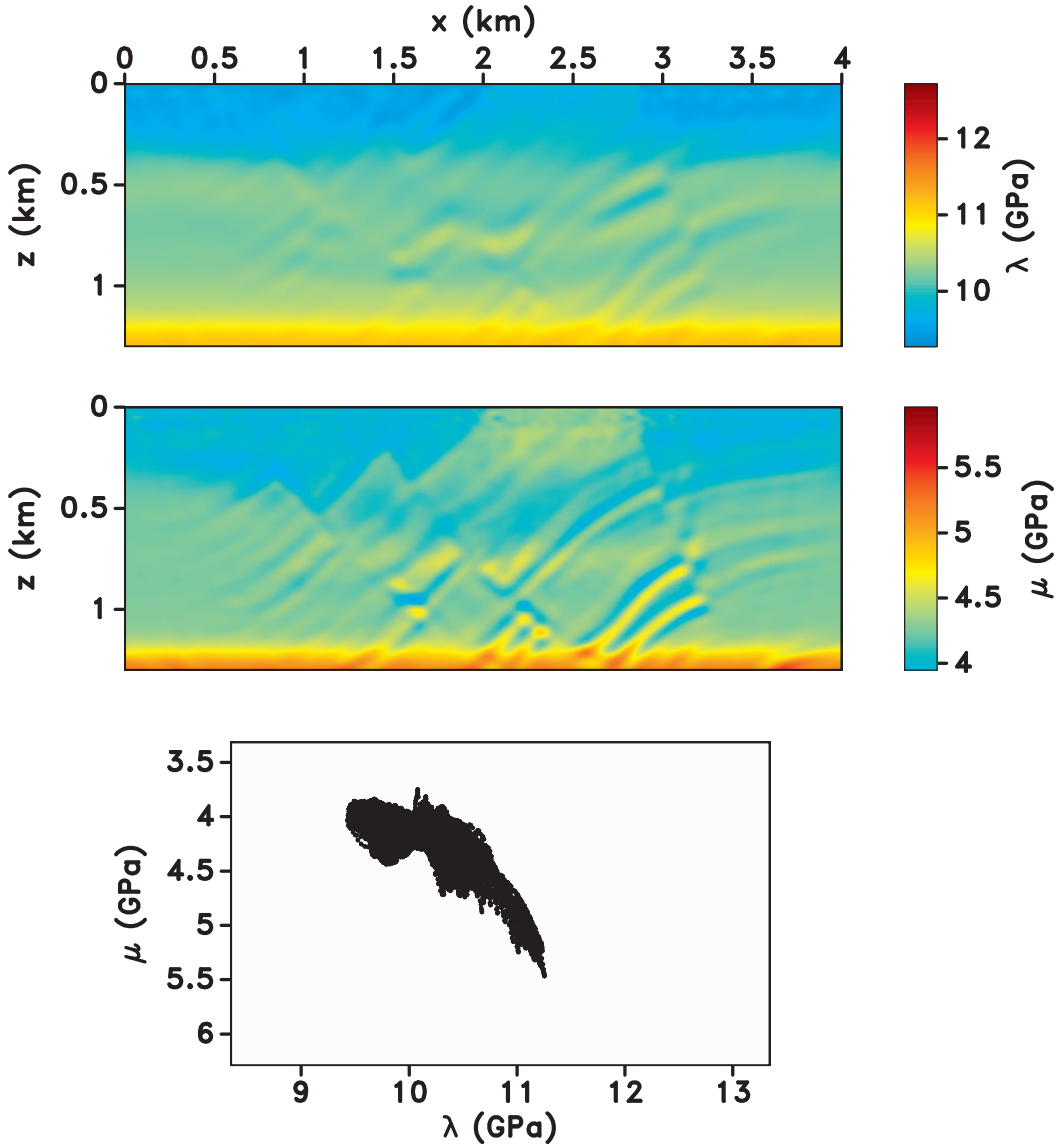

Figure 3.16: Experiment B: Recovered λ and μ models using the objective function $\mathcal{J}_D$. The inaccuracy of the initial models (Figure 3.14) leads FWI a local minimum.

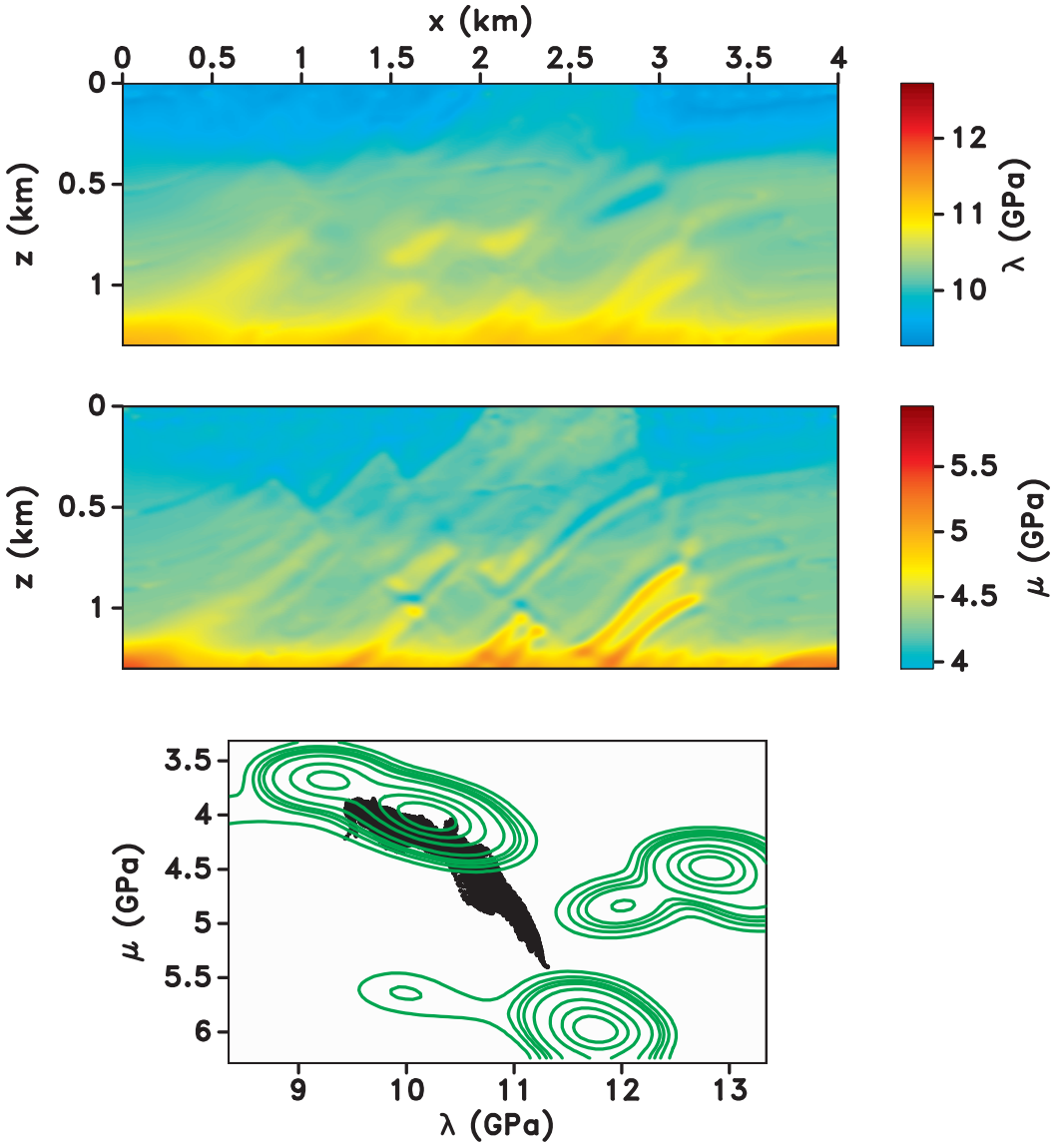

Figure 3.17: Experiment B: Recovered λ and μ models using the objective function $\mathcal{J}_D + \mathcal{J}_{P1}$. The green contours overlain on the crossplot illustrate the probabilistic penalty term based on a single PDF.

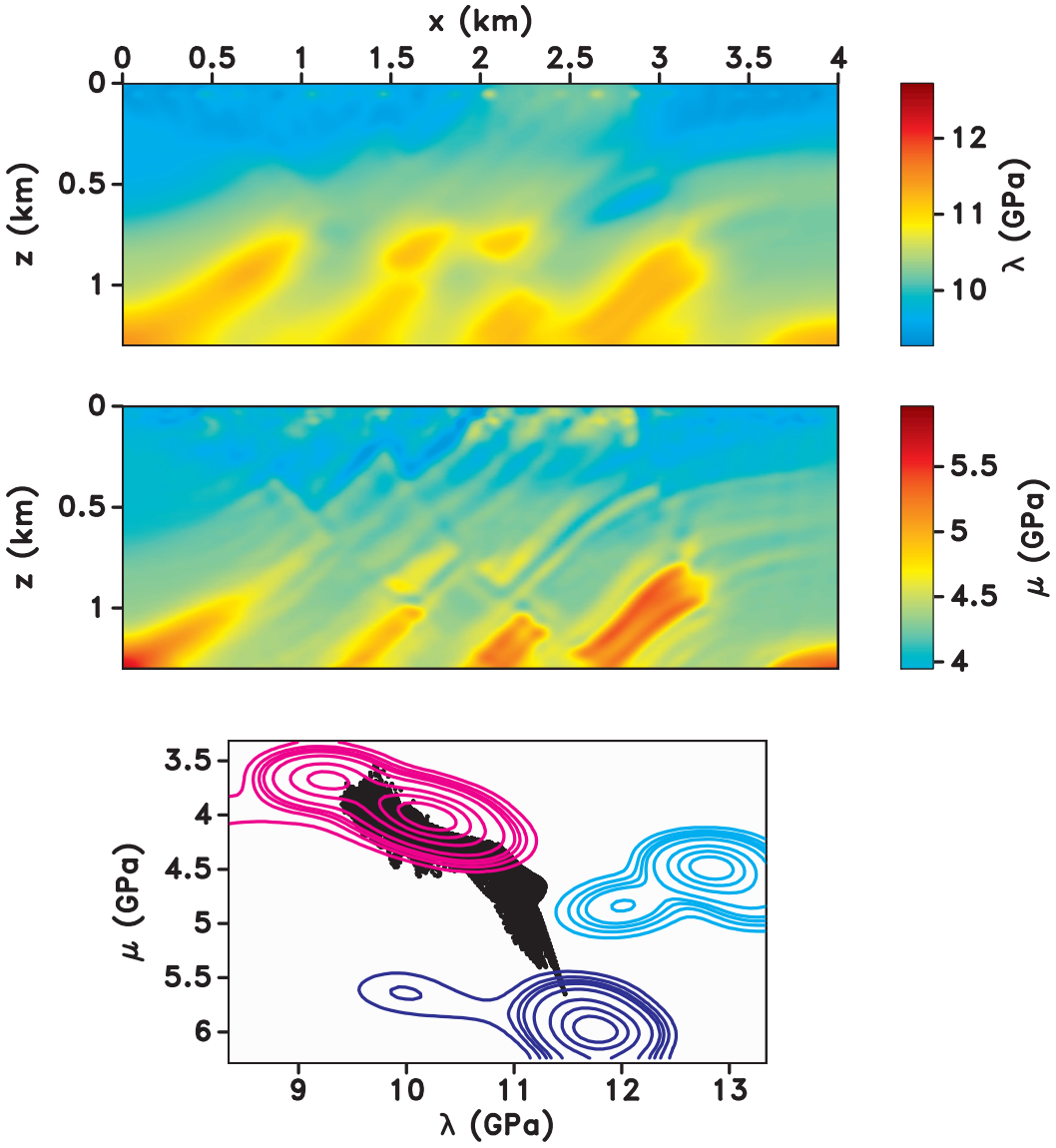

Figure 3.18: Experiment B: Recovered λ and μ models using the objective function $\mathcal{J}_D + \mathcal{J}_{P2}$. The contours with different colors overlain on the crossplot illustrate the multiple PDFs used in the probabilistic penalty.

3.3.2 Marmousi 2 model with clustering

The third synthetic example uses a portion of the Marmousi 2 model (Martin et al., 2002), but we do not modify the models to represent well-defined and distinct lithologies. Figure 3.19 shows the correct λ and μ models, the well locations and the crossplot of the model parameters. For this example, we simulate a multicomponent ocean bottom seismic survey (OBS) with a line of receiver at the water bottom ($z = 0.17\,\text{km}$) and 20 evenly spaced pressure sources located at $z = 0.05\,\text{km}$. We use a 7.5 Hz peak Ricker source wavelet. Figure 3.20 shows the initial λ and μ models and the corresponding crossplot in the model parameter space.

Figure 3.21 shows the recovered λ and μ models using the objective function $\mathcal{J}_D$. Once again, one can notice that the inverted μ model has higher spatial resolution. Also, the μ model has spurious artifacts due to parameter crosstalk. The main structures in the initial λ model (Figure 3.20) conform to the true λ model (Figure 3.19) and are not preserved during the unconstrained inversion (Figure 3.21). Additionally, the crossplot shown in Figure 3.21 does not resemble that of the true model (Figure 3.19) because the updates are not restricted to a feasible petrophysical region.

For the inversions using petrophysical information, we use the crossplot shown in Figure 3.22, which corresponds to the λ and μ values extracted at the wells located at $x = 1.1$, 2.0 and 3.0 km (Figure 3.19). Note that this crossplot does not describe distinct lithologies. Therefore, one can choose to use a single PDF (Figure 3.23a) to constrain the entire model using the objective function $\mathcal{J}_D + \mathcal{J}_{P1}$. However, we use K-means clustering to separate the petrophysical information depicted in Figure 3.22 into multiple PDFs and then employ the objective function $\mathcal{J}_D + \mathcal{J}_{P2}$. A crucial step for K-means clustering technique is defining the number of clusters. One can do it by analyzing and interpreting the well logs and identifying different classes of lithology, such as, shale, sandstone, limestone and salt. For this example, we define four clusters (Figure 3.23b), consistent with this portion of the Marmousi 2 model that we use has four lithologies.

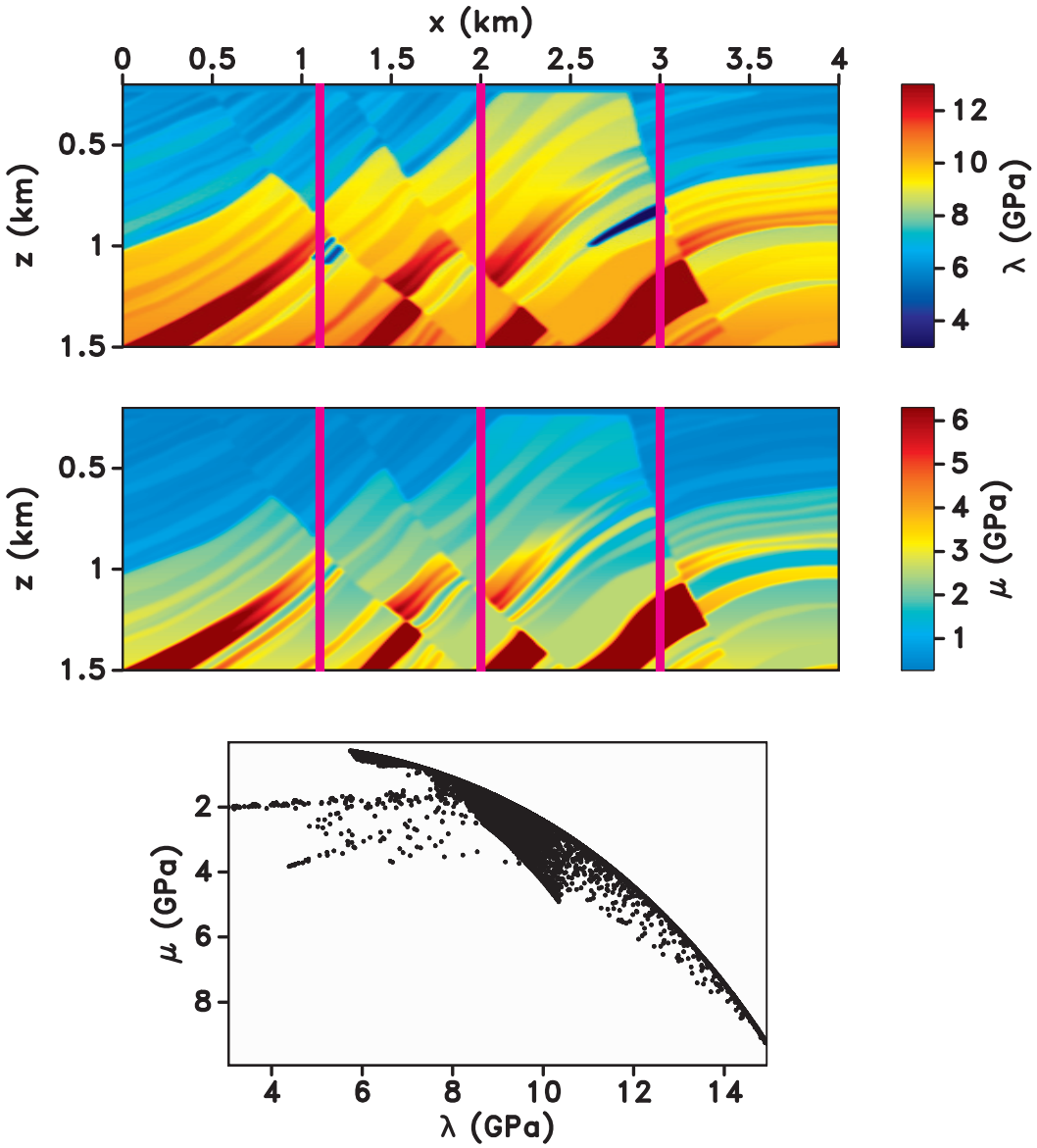

Figure 3.19: True λ and μ models and their crossplot for the inversion with clustering. The vertical lines correspond to well locations that provide information for the petrophysical penalty term.

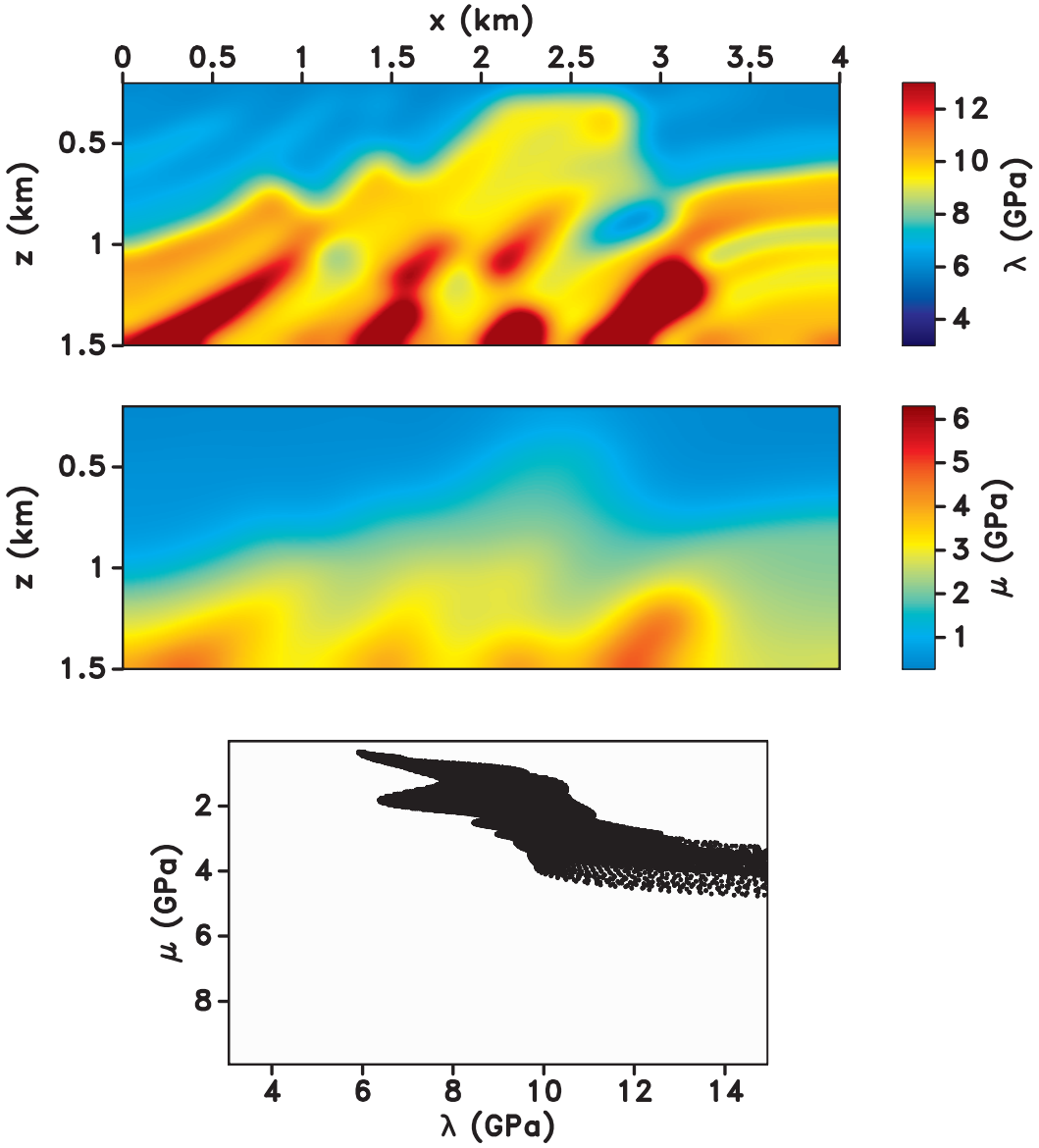

Figure 3.20: Initial λ and μ models and their crossplot in the $\lambda - \mu$ space for the inversion with clustering.

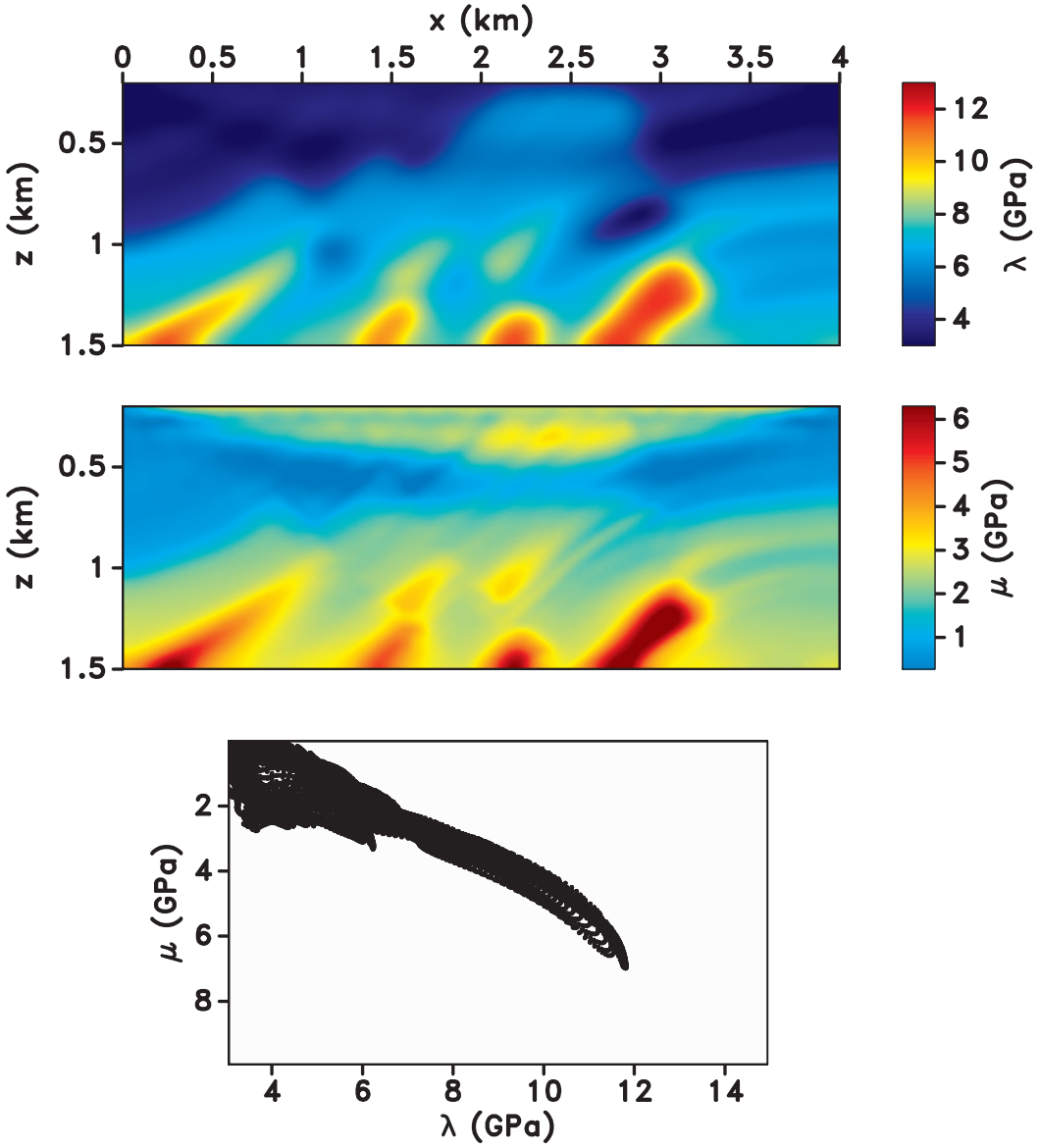

Figure 3.21: Recovered λ and μ models obtained using the objective function $\mathcal{J}_D$ for the inversion with clustering.

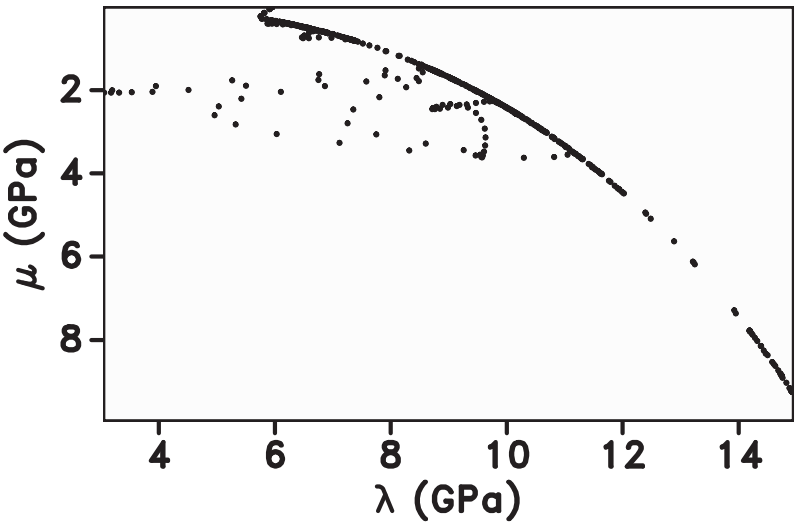

Figure 3.22: Crossplot of λ and μ provided by the well logs indicated in Figure 3.19. Note that different lithologies are not distinct in the petrophysical space.

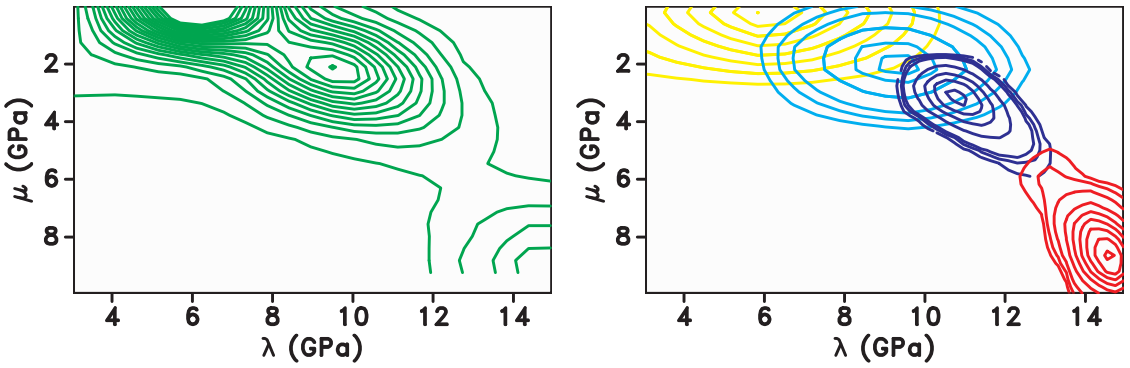

(a) (b)

Figure 3.23: (a) PDF associated with the term $\mathcal{J}_{P1}$ and (b) PDF associated with the term $\mathcal{J}_{P2}$ for the inversion with clustering. We estimate the PDFs in (a) and (b) from the well logs shown in Figure 3.22.

Figure 3.24 shows the recovered λ and μ models using the objective function $\mathcal{J}_D + \mathcal{J}_{P1}$. Note that both λ and μ models have resolution and are better recovered compared with the cases when we use the objective functions $\mathcal{J}_D$ (Figure 3.21). Additionally, the μ model artifacts caused by interparameter crosstalk are attenuated. However, the inverted λ model depicted in Figure 3.24 is noisy and does not show blocky structures above $x = 1.0\,\text{km}$.

Figure 3.25 shows the recovered λ and μ models using the objective function $\mathcal{J}_D + \mathcal{J}_{P2}$. The contours correspond to the four PDFs used to define the petrophysical probabilistic penalty term. Both λ and μ inverted models depicted in Figure 3.25 show high resolution and are closer to the true models compared with the cases when we use the objective functions $\mathcal{J}_D$ (Figure 3.21) or $\mathcal{J}_D + \mathcal{J}_{P1}$ (Figure 3.24). The μ model shown in Figure 3.25 shows reduced crosstalk, and the λ model has blocky structure that conform to the true models (Figure 3.19).

3.4 Conclusions

We develop a strategy for incorporating petrophysical information into elastic full waveform inversion through a penalty term based on multiple probability density functions. We demonstrate that imposing this kind of penalty improves the quality of the recovered subsurface models and better represents feasible lithologies. Through several synthetic examples, we verify the effectiveness of the proposed method in leading inversion towards the true models. We also show that the quality of the recovered models can be compromised when the penalty function is based on a single probability density function, while petrophysical information indicates the occurrence of different lithologies in the subsurface. We demonstrate that K-means clustering can be used to separate the petrophysical data into different lithological units in order to compute multiple corresponding probability density functions. In addition, we prove that explicitly incorporating petrophysical information into the FWI framework alleviates cycle skipping and mitigates the crosstalk between elastic parameters.

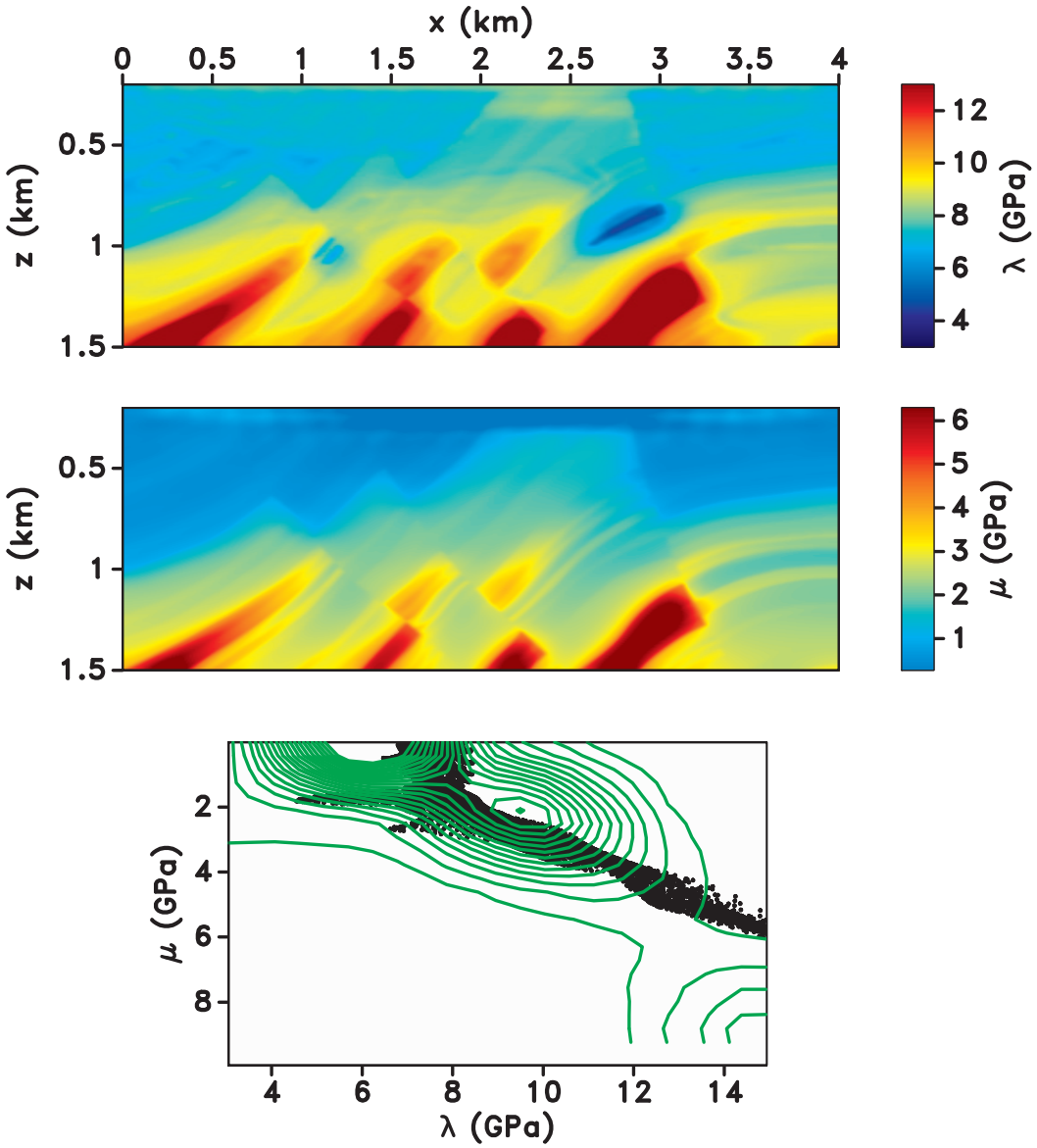

Figure 3.24: Recovered λ and μ models using the objective function $\mathcal{J}_D+\mathcal{J}_{P1}$ for the inversion with clustering. The green contours overlain on the crossplot illustrate the probabilistic penalty term based on a single PDF $\mathcal{J}_{P1}$.

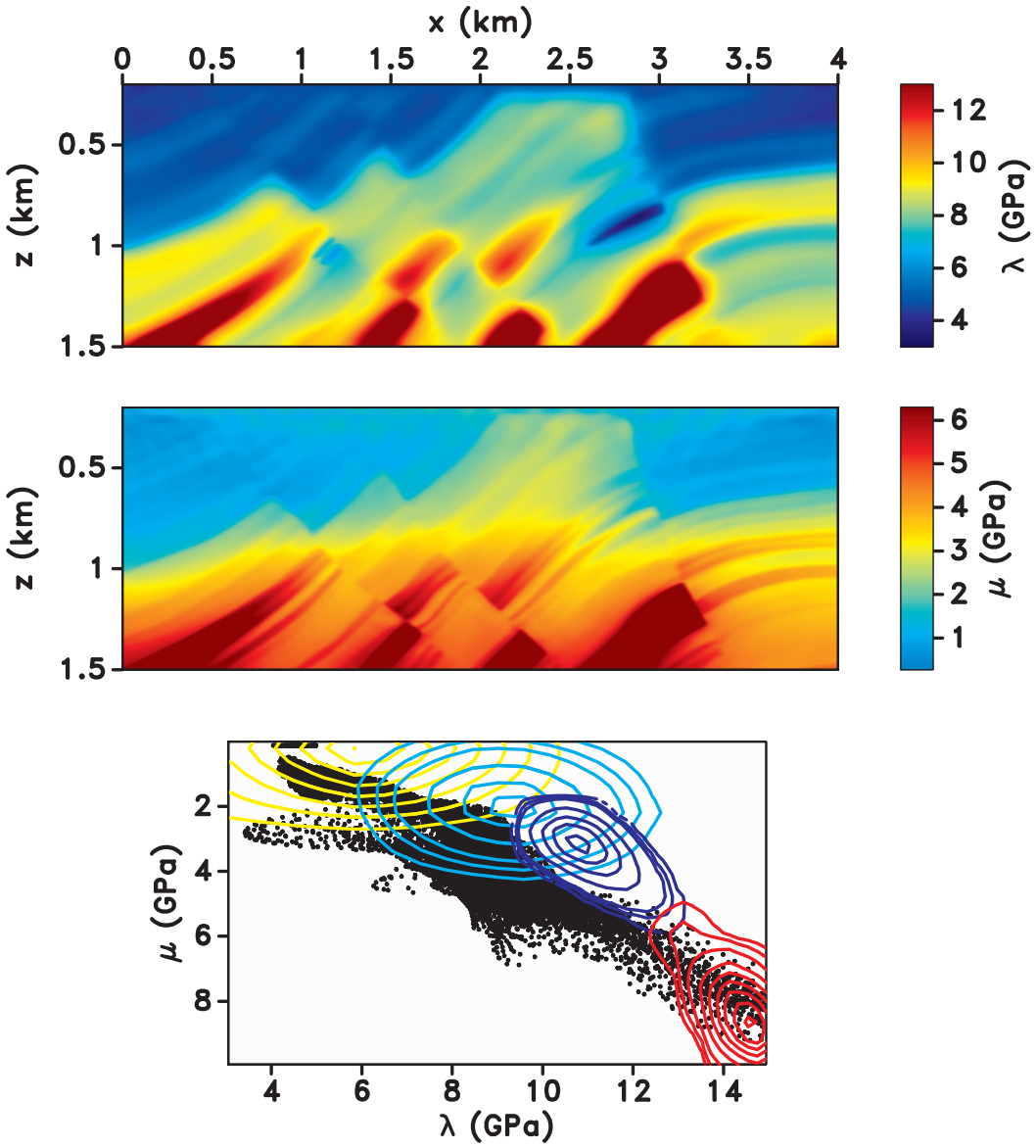

Figure 3.25: Experiment A: Recovered λ and μ models using the objective function $\mathcal{J}_D + \mathcal{J}_{P2}$ for the inversion with clustering. The contours with different colors overlain on the crossplot illustrate the multiple PDFs used in the probabilistic penalty $\mathcal{J}_{P2}$.

3.5 Acknowledgments

We acknowledge CAPES (Brazilian Federal Agency for Support and Evaluation of Graduate Education) for financial support (Finance Code 001). We thank the sponsors of the Center for Wave Phenomena (CWP), whose support made this research possible. The synthetic examples in this paper uses the Madagascar open-source software package (Fomel et al., 2013) freely available from http://www.ahay.org.

CHAPTER 4

ELASTIC ANISOTROPIC FULL WAVEFORM INVERSION USING PROBABILISTIC PETROPHYSICAL CONSTRAINTS

Full waveform inversion (FWI) is formulated as an inverse problem driven by a wave equation and it works by iteratively minimizing an objective function that measures the misfit between observed and predicted data in the least-squares sense. However, FWI suffers from significant problems. First, the objective function is multimodal and thus the inverse problem solved by gradient techniques may not lead to the globally optimal solution. This phenomenon is due to cycle skipping which occurs when the starting models are unable to predict data that match the observed data to better than half a cycle at the lowest usable frequencies available within the data set. Second, as the simulated data are computed using a two-way wave equation, all wave propagation mechanisms are not adequately considered if one does not assume a structure of the stiffness tensor that truly represents the subsurface. Third, FWI implementations using an elastic wave equation estimate multiple parameters representing different physical properties of the subsurface, which increases the null space of the parameter space, leading to a larger domain of ambiguity and increasing the number of models that can equally well explain the data. Depending on the parameterization used for inversion, elastic properties may be coupled and updates of one parameter may impact others, an effect known as interparameter crosstalk. In addition, some combinations of model parameters can be lithologically implausible or impossible (e.g., negative Poisson ratio), and thus not represent feasible lithological units. We derive anisotropic models of subsurface properties using elastic full-waveform inversion and explicitly impose petrophysical penalties to guide models toward realistic lithology, i.e., to models consistent with the seismic data as well as with the petrophysical context in the area of study. This methodology reduces the potential negative impact of cycle skipping, mitigates the artifacts created by interpa-

rameter crosstalk, and avoids geologically implausible earth models. We define this penalty using probability density functions (PDFs) derived from petrophysical information, such as well logs. The combined FWI objective function leads to robust anisotropic subsurface models that represent plausible lithologies, while at the same time leading to data predictions consistent with the observations.

4.1 Introduction

Full waveform inversion (FWI) (Tarantola, 1984) relies on accurate wavefield simulation, and thus seismic modeling should simulate the physics of wave propagation as accurately as possible (Pratt, 1999; Sirgue and Pratt, 2004; Tarantola, 1984; Virieux and Operto, 2009). A common assumption in conventional FWI is that the subsurface is described by isotropic model parameters. However, the increasing number of acquired offsets and azimuths require that we also account for the influence of anisotropy as an indispensable factor in fitting seismic field data (Plessix and Cao, 2010). Seismic anisotropy is particularly important to account for the different scales of subsurface heterogeneity, within the signal bandwidth, as well as alignment of subsurface cracks and layers (Tsvankin, 2012).

Compared to implementations using the anisotropic acoustic wave equation (Plessix and Cao, 2011; Wang and Tsvankin, 2018; Warner et al., 2013; Wu and Alkhalifah, 2016), elastic anisotropic FWI more accurately describes the physics of wave propagation in the subsurface (Kamath and Tsvankin, 2016; Kamath et al., 2017; Pan et al., 2020; Singh et al., 2020). However, the intrinsic non-linearity, ill-posedness, and interparameter trade-off of elastic anisotropic FWI increases the possibility of being trapped in local minima and the likelihood of generating geologically infeasible inverted models (Operto et al., 2013).

A widely used option to reduce the null space in non-linear and ill-posed problems, such as FWI, is adding a model regularization term to the objective function (Tarantola, 2005; Tikhonov and Arsenin, 1977), as regularization can decrease the number of possible solutions to the inverse problem, thus making the objective function more convex, which may prevent the inversion to converge to a local minimum. In addition, regularization can mitigate

imaging artifacts and it allows different levels of model shaping. For example, Tikhonov regularization can produce smooth models (Asnaashari et al., 2013), while total variation (TV) techniques preserves edges and sharp interfaces in the recovered models (Guitton, 2012; Zhang et al., 2019b). An alternative is to include a prior model term if additional information, such as well logs, is available before the inversion, in order to drive it in a specific direction (Asnaashari et al., 2013; Zhang et al., 2018).

However, even when incorporating model regularization in the FWI objective function, the model parameters are still updated independently, and may represent unfeasible lithologies. Additionally, these regularization methods that use prior models operate in the spatial domain and their efficiency strongly relies on accurate geological information about the entire studied region, while prior petrophysical information derived from well logs or other sources characterizes the model only at sparse locations. To address this issue, one can use penalties or constraints that operate in the model parameter space, in order to constrain the relationship between the model parameters during the inversion, without the need to assume prior models or to consider sharp or smooth subsurface representations (Aragao and Sava, 2020a,b; Duan and Sava, 2016; Manukyan et al., 2018; Rocha and Sava, 2018). When the elastic parameters have structural similarity, one can constrain the inversion using the approach proposed by Manukyan et al. (2018), which helps mitigate the artifacts produced by interparameter crosstalk and delivers elastic models with similar spatial resolution. Duan and Sava (2016) and Rocha and Sava (2018) use a petrophysical penalty function based on a logarithmic function that assumes a linear relationship between the model parameters to constrain, respectively, elastic wavefield tomography and elastic reflection waveform inversion. The logarithmic constraint imposes a physical bound for the elastic parameters, which is based on the available well log information, and it works with user-defined parameters whose selection may be challenging, especially when the elastic parameters do not follow a linear relationship.

Alternatively, Aragao and Sava (2020a,b) propose to explicitly use petrophysical information into elastic full waveform inversion and constrain wavefield inversion to models that satisfy prior knowledge about the subsurface model properties, and their petrophysical relationships. They explicitly incorporate petrophysical information in elastic FWI to recover models that honor both geohysical and petrophysical data. They achieve this goal by formulating a penalty function, based on a single probability density function (PDF) (Aragao and Sava, 2020a) or on multiple PDFs (Aragao and Sava, 2020b), into the elastic isotropic FWI objective function.

Here, in order to recover anisotropic models, we use a petrophysical penalty similar to the one proposed by Aragao and Sava (2020b) to guide multidimensional anisotropic models towards solutions that satisfy the known anisotropic petrophysical properties. We define the petrophysical penalties based on multiple PDFs, each representing a different lithological unit that are defined by using K-means clustering (Hartigan, 1975; MacQueen, 1967).

In the following sections, we discuss the implementation of elastic anisotropic FWI using the petrophysical penalty, and we illustrate the efficiency of the proposed technique with numerical examples. We show how the anisotropic probabilistic petrophysical penalty term based on different PDFs can deliver models with high resolution that are closer to the true models compared with the cases of unconstrained inversion or when petrophysical constraints based on a single PDF is used to characterize the entire inverted model.

4.2 Method

Consider the elastic wave equation,

$$\rho \frac{\partial^2 u_i}{\partial t^2} = \frac{\partial}{\partial x_j}\left(c_{ijkl}\frac{\partial u_l}{\partial x_k}\right) + f_i, \tag{4.1}$$

where $\mathbf{u}(e, \mathbf{x}, t)$ is the elastic displacement, $\mathbf{f}(e, \mathbf{x}, t)$ is the source function, e, $\mathbf{x}$ and t are, respectively, the experiment index, space coordinates and time, and c_{ijkl} is the fourth-order stiffness tensor, which is responsible for the material properties. The equation above is valid for homogeneous, linearly elastic and arbitrary anisotropic media.

As the stiffness tensor possesses many different symmetries, it can be represented in the form of a 6×6 symmetric matrix C, such that each anisotropic model is characterized by a specific structure of the stiffness matrix (Tsvankin, 2012). The stiffness matrix C for a transversely isotropic medium with a vertical symmetry axis (VTI) has only 5 different independent coefficients: C_{11}, C_{13}, C_{33}, C_{55} and C_{66}. These elements, combined with density ρ, are used to determine the Thomsen parameters:

- P-wave vertical velocity: $V_{P0} = \sqrt{C_{33}/\rho}$;
- S-wave vertical velocity: $V_{S0} = \sqrt{C_{55}/\rho}$;
- $\epsilon = (C_{11} - C_{33})/2C_{33}$;
- $\delta = [(C_{13} + C_{55})^2 - (C_3 3 - C_{55})^2]/[2C_{33}(C_3 3 - C_{55})]$;
- $\gamma = (C_{66} - C_{55})/2C_{55}$.

Considering the vector of elastic model parameters $\mathbf{m}(\mathbf{x})$, we solve the full waveform inverse problem by minimizing an objective function $\mathcal{J}(\mathbf{u}, \mathbf{m})$ consisting of a term that estimates the misfit between the predicted and observed data $\mathcal{J}_D(\mathbf{u}, \mathbf{m})$ and a term that applies model constraints using a petrophysical penalty term, $\mathcal{J}_P(\mathbf{m})$, as proposed by Aragao and Sava (2020a):

$$\mathcal{J}(\mathbf{u}, \mathbf{m}) = \mathcal{J}_D(\mathbf{u}, \mathbf{m}) + a\, \mathcal{J}_P(\mathbf{m}), \tag{4.2}$$

where the scalar parameter a determines the strength of $\mathcal{J}_P$ in the objective function.

The data misfit term $\mathcal{J}_D$ is based on the l_2 norm of the residuals $\mathbf{r}_D(e, \mathbf{x}, t)$ between the modeled data and the observed data. We use the adjoint state method (Kamath and Tsvankin, 2016; Plessix, 2006) for the evaluation of the gradient of the objective function, where the subsurface property updates are obtained by applying the cross-correlating imaging condition to the spatial derivatives of the forward-propagated source wavefield and the backward-propagated adjoint wavefield, obtained by extrapolating the misfit between the recorded and simulated data.

We define $\mathcal{J}_P(\mathbf{m})$ based on the distances relative to all points of a multimodal PDF describing the petrophysical relations between the components of the anisotropic model parameters. This PDF is determined from well log data, for example, and represented by coordinates $\mathbf{p}$. For any given model represented by $\mathbf{m}$, we compute a distance to any point of the distribution by

$$d(\mathbf{m}, \mathbf{p}) = \|\mathbf{m} - \mathbf{p}\|_2. \tag{4.3}$$

Then, using the probability density $f(\mathbf{p})$ described by the petrophysical PDF, we determine the distance $D(\mathbf{m})$ from $\mathbf{m}$ to the entire distribution as

$$\frac{1}{D(\mathbf{m})} = \sum_{\mathbf{p}} \frac{f(\mathbf{p})}{d(\mathbf{m}, \mathbf{p})}. \tag{4.4}$$

Finally, the penalty term $\mathcal{J}_P$ is defined as

$$\mathcal{J}_P = a \sum_{\mathbf{m}} D(\mathbf{m}), \tag{4.5}$$

where the scalar parameter a determines the strength of the penalty term in the objective function.

Aragao and Sava (2020b) implement a modification to the technique proposed by Aragao and Sava (2020a) by considering multiple PDFs in order to build $\mathcal{J}_P$, such that each PDF represents a different lithological unit, and that is the approach we apply here. In this way, we refer to the objective function composed by the data misfit and the petrophysical probabilistic penalty term based on a single PDF as $\mathcal{J}_D + \mathcal{J}_{P1}$, and to the objective function composed by the data misfit and the petrophysical probabilistic penalty term based on multiple PDFs as $\mathcal{J}_D + \mathcal{J}_{P2}$.

4.3 Examples

We illustrate the technique with a portion of the Marmousi 2 model, where the available petrophysical information does not indicate the occurrence of separate lithological units. As proposed by Aragao and Sava (2020b), we use the K-means clustering technique to categorize the petrophysical information into multiple clusters, which represents different lithologies, in order to create different PDFs for the petrophysical penalty term. We compare inversions using only the data misfit term $\mathcal{J}_D$, with inversions combining data misfit with the petrophysical penalty based on a single PDF $\mathcal{J}_D + \mathcal{J}_{P1}$, or multiple PDFs $\mathcal{J}_D + \mathcal{J}_{P2}$.

We consider the anisotropic elastic model parameters as $\mathbf{m} = \{V_{P0}, V_{S0}, V_{P,hor}, V_{P,nmo}\}$, such that $V_{P,hor} = V_{P0}\sqrt{1+2\epsilon}$ and $V_{P,nmo} = V_{P0}\sqrt{1+2\delta}$. Figure 4.1 shows the correct V_{P0} V_{S0}, $V_{P,hor}$ and $V_{P,nmo}$ models and the well locations. We simulate a multicomponent survey with a line of receiver at $z = 0.05\,\text{km}$ and 50 evenly spaced sources located at $z = 0.025\,\text{km}$. Figure 4.2 shows the initial model parameters.

In order to calculate the petrophysical penalty, one needs to evaluate distances to all points of a 4D PDF determined from well logs, represented by coordinates $\mathbf{p} = \{V_{P0_p}, V_{S0_p}, V_{P,hor_p}, V_{P,nmo_p}\}$. Figure 4.3 shows contours representing 2D projections of the single 4D PDF for combinations of every two parameters related to the petrophysical constraint based on a single PDF associated with the term $\mathcal{J}_{P1}$. One can note that all 2D projections depicted in Figure 4.3 have similar trends among one another. In this way, it is expected that the recover models also share a similar trend, which enforced by the petrophysical constraints, resulting in comparable resolution. The same fact is expected for the multiple PDFs related to the term $\mathcal{J}_{P2}$.

Figure 4.4 shows the recovered models using the objective function $\mathcal{J}_D$. One can notice that all models have spurious artifacts due to interparameter crosstalk. Additionally, the model parameters have different resolutions due to the source-receiver geometry. As waves propagate predominantly close to the vertical direction, the inverted $V_{P,hor}$ (Figure 4.4c) model presents smaller resolution than the other parameters (Figures 4.4a, 4.4b and 4.4d).

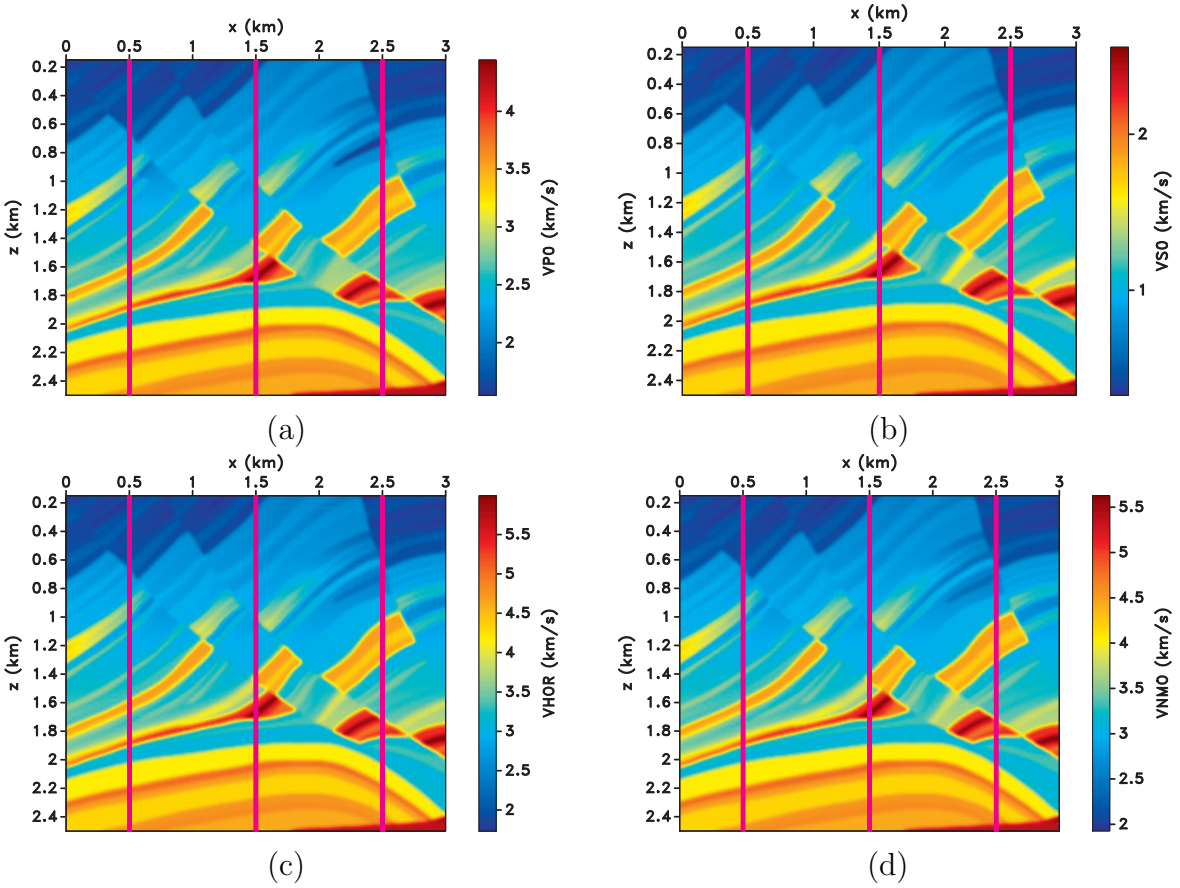

Figure 4.1: True (a) V_{P0}, (b) V_{S0}, (c) $V_{P,hor}$ and (d) $V_{P,nmo}$ models. The vertical lines correspond to well locations that provide information for the petrophysical penalty term.

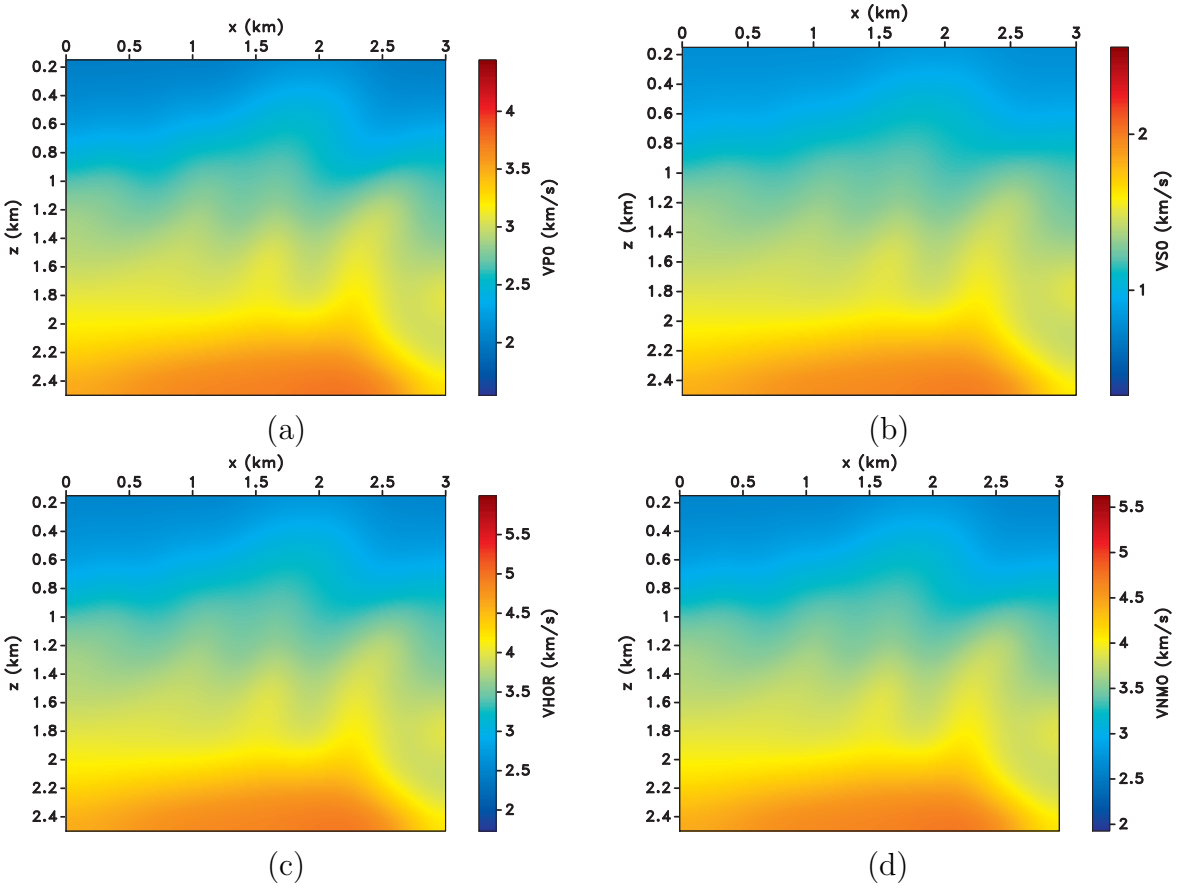

Figure 4.2: Initial (a) V_{P0}, (b) V_{S0}, (c) $V_{P,hor}$ and (d) $V_{P,nmo}$ models, which we obtain by smoothing the true models.

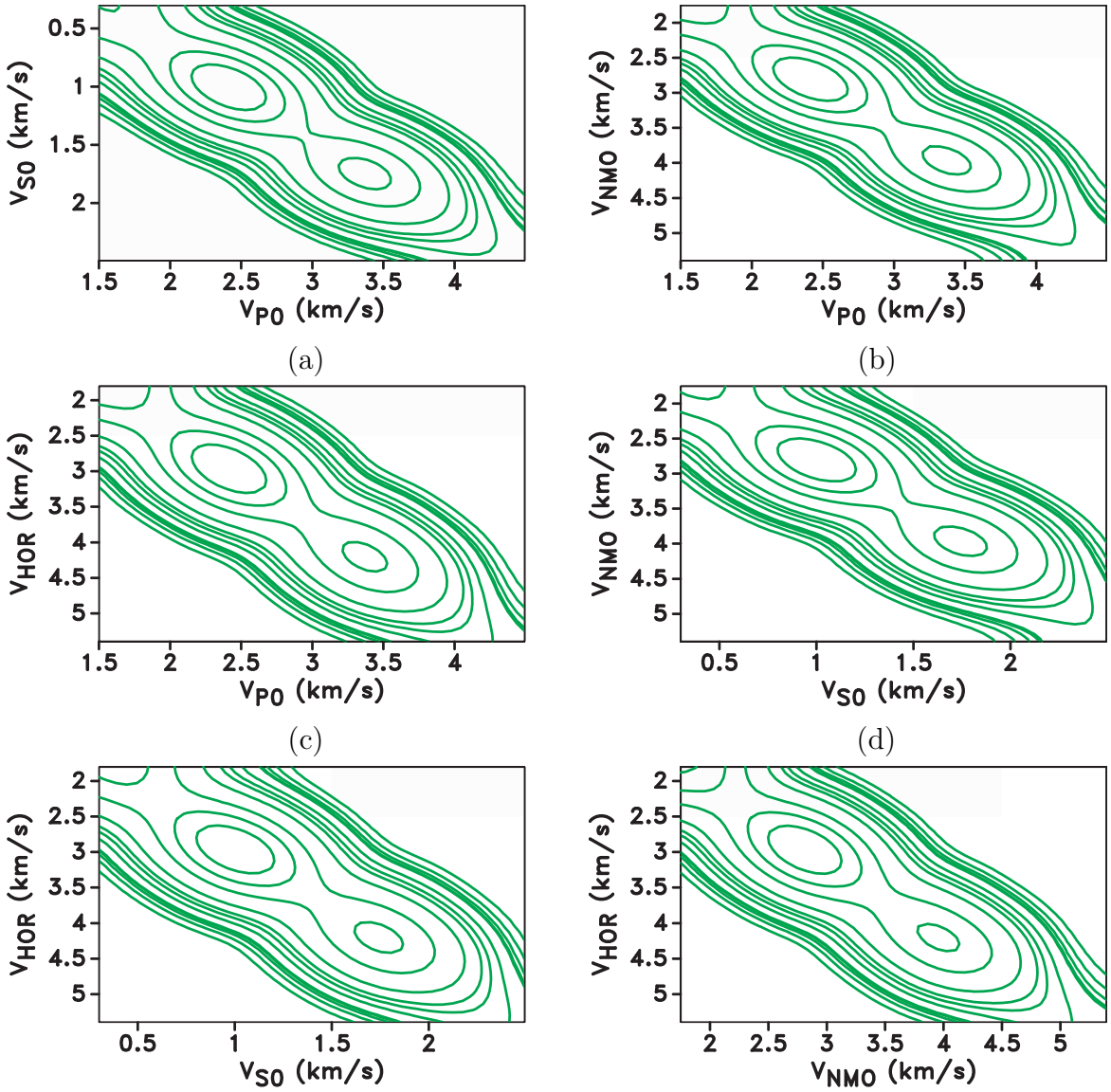

Figure 4.3: Contours representing 2D projections of the 4D PDF associated with the term $\mathcal{J}_{P1}$ for the parameters (a) V_{P0} and V_{S0}, (b) V_{P0} and $V_{P,nmo}$, (c) V_{P0} and $V_{P,hor}$, (d) V_{S0} and $V_{P,nmo}$, (e) V_{S0} and $V_{P,hor}$, and (f) $V_{P,hor}$ and $V_{P,nmo}$. In each plot, the contour lines surround locations of peak, such that the probability values increase from the edge to the center. We estimate these PDFs from the well logs shown in Figure 4.1.

Figure 4.5 shows the recovered models using the objective function $\mathcal{J}_D + \mathcal{J}_{P1}$. The models are more blocky and conform better to the true models (Figure 4.1) than the models recovered using the $\mathcal{J}_D$ objective function (Figure 4.4). Moreover, all models depicted in Figure 4.5 have similar resolution, as the petrophysical constraint $\mathcal{J}_{P1}$ represented by the PDFs in Figure 4.3 enforce the model parameters to have similar trends.

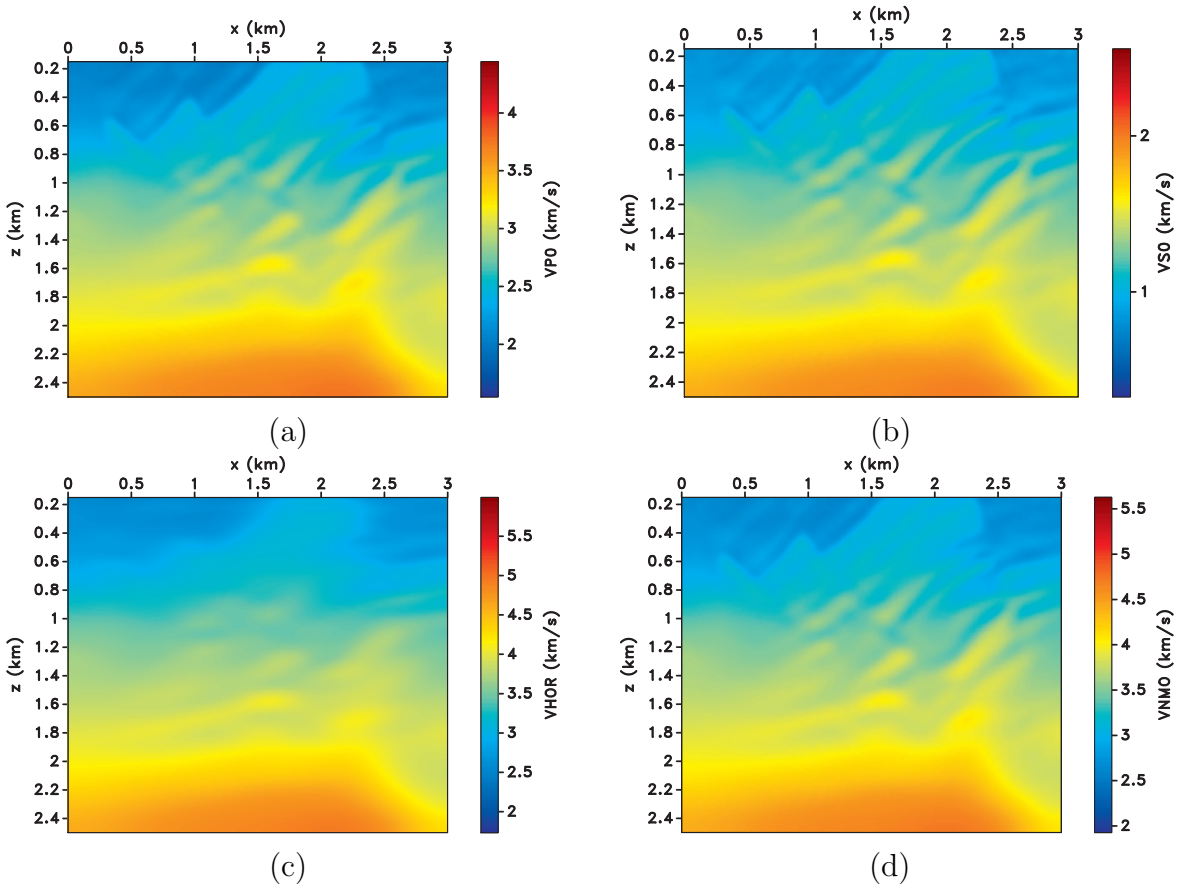

Figure 4.4: Recovered (a) V_{P0}, (b) V_{S0}, (c) $V_{P,hor}$ and (d) $V_{P,nmo}$ models using the objective function $\mathcal{J}_D$.

Figure 4.6 shows the recovered models using the objective function $\mathcal{J}_D + \mathcal{J}_{P2}$. We use 4 clusters for the algorithm. The inverted models depicted in Figure 4.6 show high resolution and are closer to the true models (Figure 4.1) compared with the cases when we use the objective functions $\mathcal{J}_D$ (Figure 4.4) or $\mathcal{J}_D + \mathcal{J}_{P1}$ (Figure 4.5). Therefore, the subsurface structure and the magnitude of the model anomalies are better recovered when using an

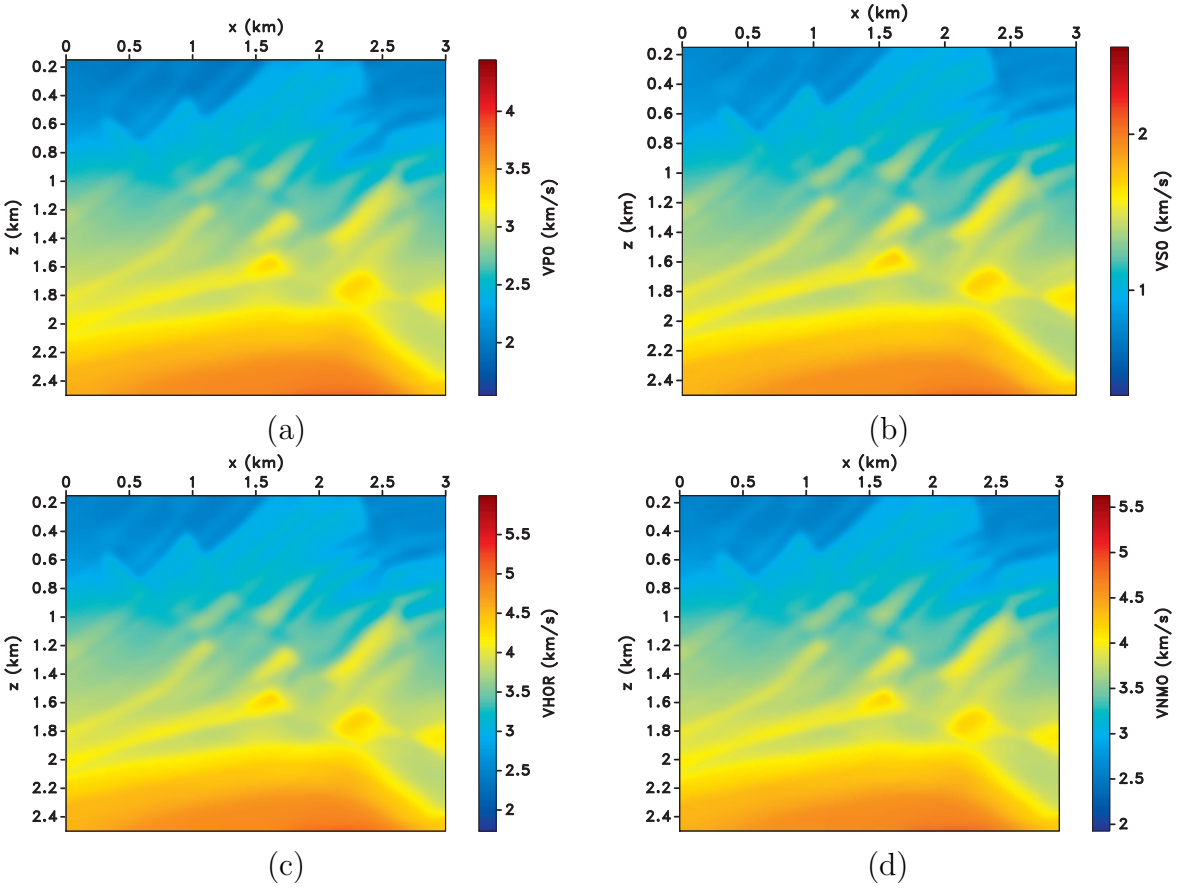

Figure 4.5: Recovered (a) V_{P0}, (b) V_{S0}, (c) $V_{P,hor}$ and (d) $V_{P,nmo}$ models using the objective function $\mathcal{J}_D + \mathcal{J}_{P1}$.

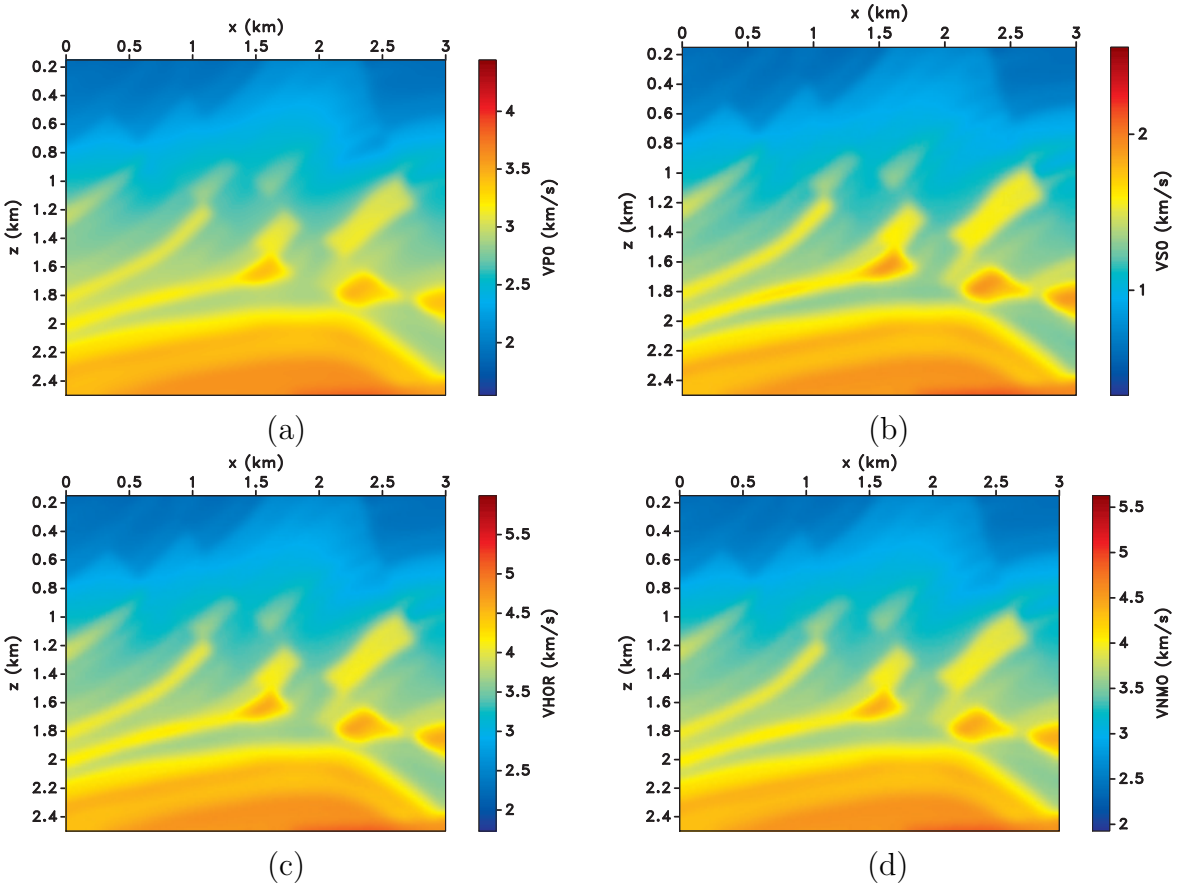

Figure 4.6: Recovered (a) V_{P0}, (b) V_{S0}, (c) $V_{P,hor}$ and (d) $V_{P,nmo}$ models using the objective function $\mathcal{J}_D + \mathcal{J}_{P2}$.

objective function that incorporates petrophysical information, and takes into account that the subsurface is composed of multiple lithologies.

Figures 4.7 and 4.8 show, respectively, the vertical and horizontal components of the residual constructed using, from the left to the right, the initial models (Figure 4.2), and the recovered models shown in Figures 4.4, 4.5 and 4.6. Note that the amplitudes of the data residuals obtained using the predicted data computed using the recovered models depicted in Figure 4.6 are much smaller compared to the case where the data are predicted using the models obtained for the unconstrained objective function $\mathcal{J}_D$ (Figure 4.4) or for the objective function $\mathcal{J}_D + \mathcal{J}_{P1}$ (Figure 4.5). Therefore, the multi-cluster petrophysical penalty term allows us to recover models that are more kinematically accurate then in the case of an objective function purely based on the data misfit $\mathcal{J}_D$ or an objective function that uses a petrophysical penalty based on a single PDF $\mathcal{J}_D + \mathcal{J}_{P1}$.

4.4 Conclusions

We propose to incorporate petrophysical information into elastic anisotropic full waveform inversion (FWI) through a penalty term based on probability density functions (PDFs). We demonstrate that imposing this penalty improves the quality of the recovered anisotropic subsurface models and helps guide the results towards a more geologically plausible solution, while mitigating crosstalk artifacts and reducing the non-linearity and the ill-posedness nature of multiparameter FWI. Finally, we show that by using the penalty term based on multiple PDFs we can further enhance the resolution and accuracy of the anisotropic model parameters, which helps predicting multicomponent data that match the observed data with accurate amplitude and phase.

4.5 Acknowledgements

We acknowledge CAPES (Brazilian Federal Agency for Support and Evaluation of Graduate Education) for financial support. We thank the sponsors of the Center for Wave Phenomena (CWP), whose support made this research possible. The synthetic examples in this

paper uses the Madagascar open-source software package (Fomel et al., 2013) freely available from http://www.ahay.org.

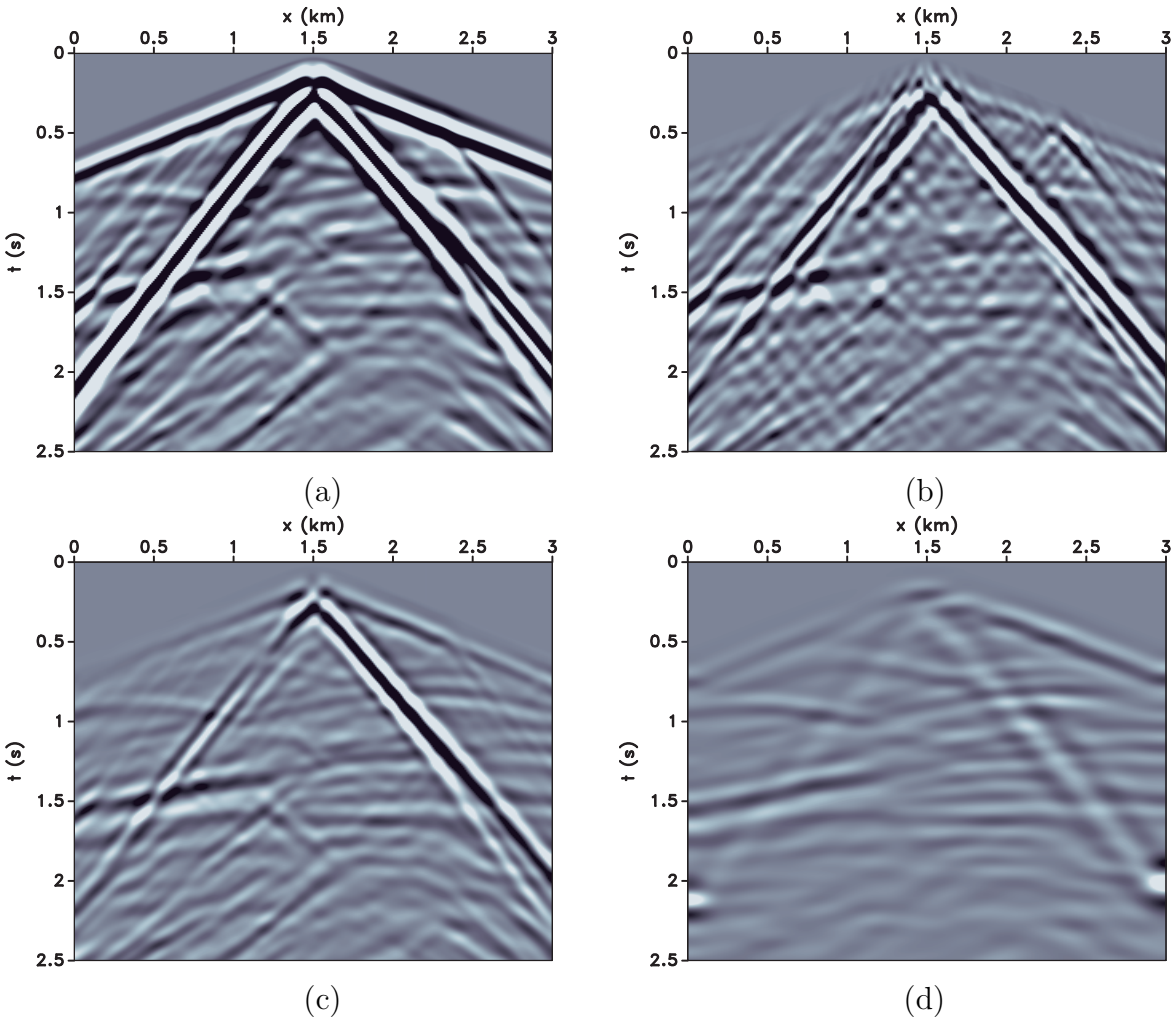

Figure 4.7: Vertical component of the data residuals using (a) the initial models (Figure 4.2), (b) the models recovered using the objective function $\mathcal{J}_D$ (Figure 4.4), (c) or $\mathcal{J}_D + \mathcal{J}_{P1}$ (Figure 4.5) (d) or $\mathcal{J}_D + \mathcal{J}_{P2}$ (Figure 4.6).

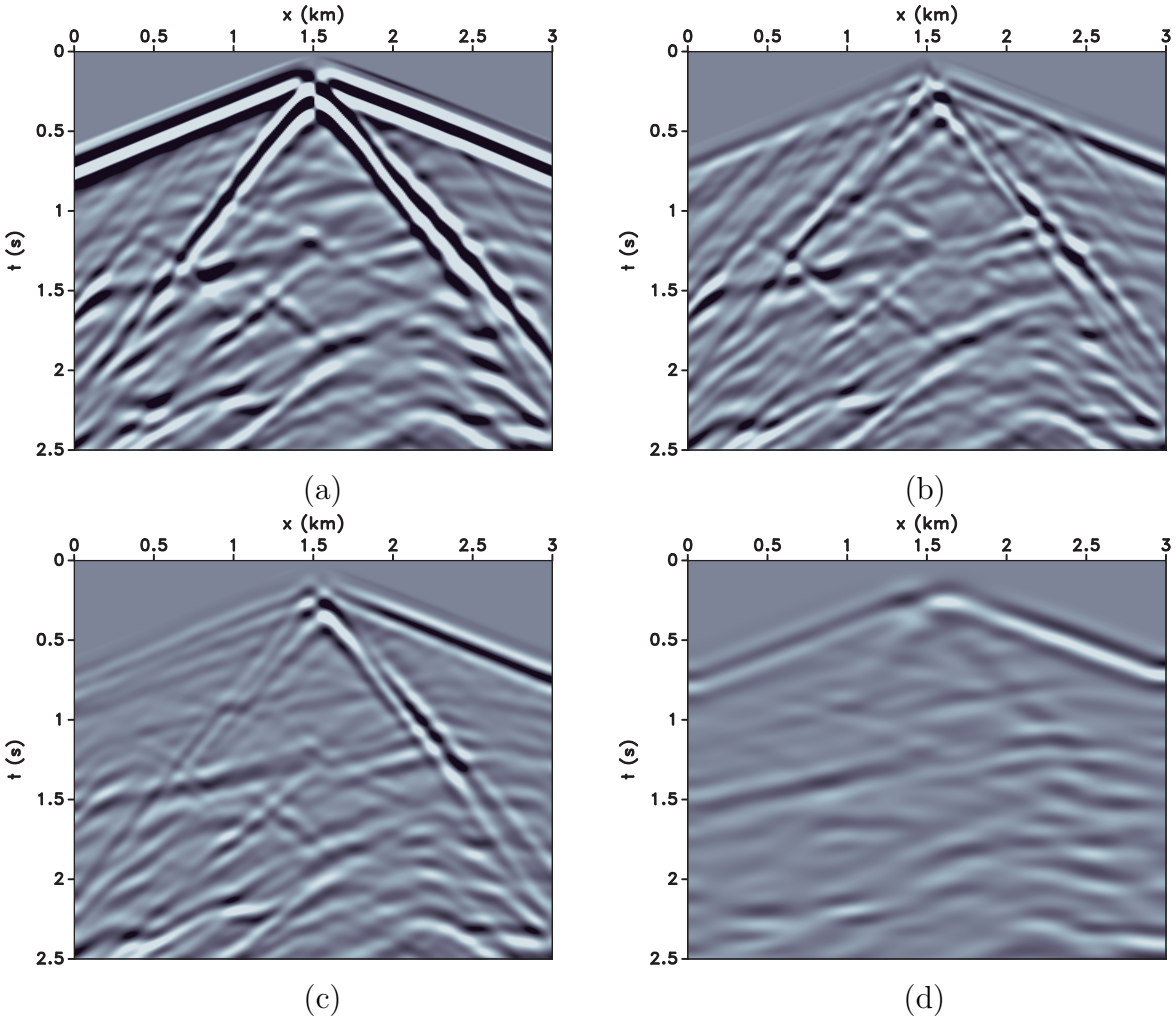

Figure 4.8: Horizontal component of the data residuals using (a) the initial models (Figure 4.2), (b) the models recovered using the objective function $\mathcal{J}_D$ (Figure 4.4), (c) or $\mathcal{J}_D + \mathcal{J}_{P1}$ (Figure 4.5) (d) or $\mathcal{J}_D + \mathcal{J}_{P2}$ (Figure 4.6).

CHAPTER 5

VISCOELASTIC FULL-WAVEFORM INVERSION WITH SPATIAL PROBABILISTIC PETROPHYSICAL CONSTRAINTS

A paper submitted to *Geophysical Prospecting*

Odette Aragao[1,2], Paul Sava[2]

Shallow low-velocity anomalies, caused for example by gas clouds, impose challenges to seismic processing and imaging, as they severely affect the phase and amplitude of seismic waveforms by dispersion and energy dissipation. In such situations, reliable estimation of attenuation is crucial for techniques exploiting wave propagation through the Earth. Viscoelastic full-waveform inversion (QEFWI) can provide robust estimation and high-resolution elastic models of attenuation and velocity simultaneously, but the recovered models may be geologically implausible and contaminated with artifacts due to the inherent interparameter crosstalk between velocity and attenuation. To mitigate this problem, we explicitly control the inverted viscoelastic models using petrophysical information derived from independent sources of information in the studied region. We consider spatial distribution patterns to classify the petrophysical data, and build probability density functions that are the foundation of a penalty term incorporated in the objection function. Our formulation of the petrophysical penalty based on multiple probability density functions accounts for uncertainty related to the distance from the well locations and can incorporate any other spatial patterns known in the investigated area. The proposed QEFWI objective function confines the inverted velocity and attenuation models to a feasible petrophysical space, while at the same time reducing the misfit between observed and modeled data, as required by conventional full-waveform inversion (FWI). We demonstrate that the proposed methodology leads

[1]Primary researcher and author.
[2]Department of Geophysics, Colorado School of Mines, Golden, Colorado, United States of America.

FWI to viscoelastic models that are realistic and consistent with the underlying geology, unlike models obtained without petrophysical information. Our formulation is robust to uncertainty of the petrophysical information, and models obtained with the proposed technique facilitate stable wavefield extrapolation in regions of arbitrary model complexity.

5.1 Introduction

Seismic waves are disperse and attenuate when propagating through the Earth due to its viscoelastic properties, which reduces their amplitude and distorts the phase of the waveforms (Carcione et al., 1988a,b; Robertsson et al., 1994). Estimating attenuation coefficients is crucial for reliable seismic data processing and imaging (Causse and Ursin, 2000; Dai and West, 1994; Guo et al., 2016; Millet et al., 1995; Zhu et al., 2014), as well as for rock physics studies, since viscoelastic parameters provide useful information related to the rock matrix and fluids present in the reservoirs (Johnston et al., 1979; Odebeatu et al., 2006; Tiwari and McMechan, 2007). Nevertheless, deriving accurate attenuation subsurface models using seismic data is still ambitious due to the fact that seismic data capture only partially the behavior of the subsurface elastic system.

Anelastic effects can be quantified through attenuation coefficients represented by the quality factor Q. The central-frequency shift (CFS) (Quan and Harris, 1997) and spectral-ratio (SR) (Bath, 1974; Behura and Tsvankin, 2009; Hackert and Parra, 2004; Sams and Goldberg, 1990) ray-based methods are conventionally used to estimate attenuation coefficients. However, both approaches are highly sensitive to noise and limited to geological settings characterized by non-complex structures (de Castro Nunes et al., 2011). Alternatively, Shen et al. (2018a,b) propose an inversion strategy to quantify attenuation quality factors Q using seismic migrated images, by performing one-way wave-equation migration analysis. As the method proposed by Shen et al. (2018a,b) relies on accurate subsurface velocity models, Q estimation may be ambiguous and possibly incorrect when the migrated images are generated with innacurate velocity.

Full-waveform inversion (FWI) (Tarantola, 1984) is a powerful tool for building high-resolution earth models for exploration geophysics and global seismology. FWI has the advantage of using more accurate simulations of wavefield propagation, considering both amplitude and phase information (Pratt, 1999; Sirgue and Pratt, 2004; Tarantola, 1984; Virieux and Operto, 2009), in comparison with other techniques that rely only on kinematic information, using one-way wave equations (Biondi, 2002; Ristow and Ruhl, 1994; Sava and Fomel, 2003; Shen and Calandra, 2005) or ray tracing (Bishop et al., 1985; Liu, 1997; Zhou, 2003). Conventionally, FWI solves a nonlinear inverse problem, constrained with a wave equation, by minimizing an objective function that quantifies the residuals between modeled seismic data and recorded seismic waveforms. Hence, FWI is potentially a powerful tool to provide robust quality factors Q when the attenuation properties of the Earth are considered during wavefield extrapolation.

Compared to viscoacoustic FWI (Bai and Yingst, 2013; Cheng et al., 2015; Hicks and Pratt, 2001; Kamei and Pratt, 2013; Kurzmann et al., 2013; Malinowski et al., 2011a; Metivier et al., 2015; Operto et al., 2015; Plessix et al., 2016; Prieux et al., 2013), viscoelastic FWI (QEFWI) better describes the Earth properties as it takes into account anelastic phenomena and thus adequately describes significant wave propagation mechanisms, such as the correct amplitude and phase of the seismic wavefields (Bai et al., 2017; Brossier, 2011; Fabien-Ouellet et al., 2017; Fichtner and van Driel, 2014; Pan and Innanen, 2019; Trinh et al., 2019). Therefore, if anelastic phenomena are neglected when describing wave propagation mechanisms in the presence of strong attenuative structures (e.g. gas clouds), the inversion is prone to fail and deliver inaccurate subsurface models.

The success of FWI depends on many factors, such as the acquisition geometry, availability of low frequencies in the recorded data, the accuracy of the initial models, noise and modeling errors (Virieux and Operto, 2009). FWI is a highly non-linear and ill-posed problem and, because of the oscillatory nature of the seismic waves, the objective function based on the L_2 norm of the residuals is non-convex (Symes, 2008). A major manifestation of the

non-convexity of the L_2 norm objective function happens when FWI becomes trapped in a local minimum due to cycle skipping, which occurs when the initial models are not accurate enough to predict data that match observations within half of the dominant period of the seismic signal.

The simultaneous estimation of velocity and attenuation impose further difficulties to FWI. Joint estimation of multiple models of subsurface properties increases the number of model combinations that can equally well explain the data, thus leading to severe ambiguity (Operto et al., 2013). Additionally, different velocity and attenuation properties are coupled by similar radiation patterns and updates of velocity parameters could be mapped into the estimation of attenuation coefficients, and vice-versa, an effect known as interparameter crosstalk, which produces unwanted artifacts and biased models (Kamei and Pratt, 2013; Keating and Innanen, 2019a,b; Malinowski et al., 2011a; Metivier et al., 2015; Operto et al., 2013; Ouellet et al., 2017; Yang et al., 2018). Therefore, when these parameters are updated simultaneously, but independently, the inversion may deliver artifact-contaminated models that do not represent feasible geological units. An option to account for the interparameter crosstalk is to use techniques that approximate the inverse multiparameter Hessian using Newton-based optimization methods Keating and Innanen (2019a); Metivier et al. (2015); Yang et al. (2018). However, calculating the inverse Hesssian information significantly increases the computational cost of FWI, especially for 3D models.

For multiparameter FWI applications that do not consider attenuation effects, but are also hampered by interparameter trade-off artifacts, several author have proposed penalties or constraints in order to constrain the relationship between the model parameters during the inversion (Aragao and Sava, 2020a,b; Duan and Sava, 2016; Manukyan et al., 2018; Rocha and Sava, 2018). This strategy reduces the non-linearity and ill-posedness nature of the inverse problem, while mitigating the artifacts produced by the crosstalk between the inverted parameters. This idea can also be applied to viscoelastic FWI, as discussed next.

Aragao and Sava (2020a) propose a general, flexible, and automated technique to incorporate petrophysical information into elastic FWI (EFWI). They exploit the petrophysical data as a penalty term of the objective function to impose limitations on what models are acceptable as solutions to the inverse problem, thus guiding them toward realistic lithologies. They use a probability density function (PDF) in order to constrain EFWI without defining specific analytic relationships between the elastic properties. Aragao and Sava (2020b) adapt this idea by building a penalty term using multiple PDFs, each representing a different lithological unit that are defined by K-means clustering (Hartigan, 1975; MacQueen, 1967). Both works demonstrate that explicit probabilistic petrophysical penalties increase the robustness of multiparameter FWI, and lead to reliable elastic models that are geologically plausible, while reducing the non-linearity and ill-posed nature of FWI and mitigating artifacts produced by interparameter crosstalk. However, the method proposed by Aragao and Sava (2020b) does not account for the occurrence of distinct lithological units as a function of position, which reduce the flexibility of the method in areas of high lithologic heterogeneity.

Rock physics properties are influenced by the basin type, the depositional environment and the burial history of the sediments (Mavko et al., 2003). Because of the increase in pressure and temperature, sedimentary rocks harden and compact with depth, which affects their velocity and attenuation. In addition, different depositional environment systems are mainly responsible for lateral variations in rock formations (Avseth et al., 2010). Therefore, accounting for known spatial trends in the petrophysical data improves the accuracy of the petrophysical penalty that augments the QEFWI objective function, and leads to velocity and attenuation models that better represent the subsurface geology.

In this paper, we reduce the non-linearity and ill-posedness of the QEFWI and mitigate the artifacts produced by interparameter crosstalk using petrophysical penalties defined based on multiple position-dependent PDFs. We consider PDFs adapted to subsurface regions characterized by varying petrophysical data, e.g. lithological trends with depth or layering. We exploit well logs to determine intervals with distinct lithologies or formations.

When well logs are available at multiple locations, we use localized PDFs based on the position of the wells. As in the cases presented by Aragao and Sava (2020a,b), the methodology we propose here naturally mitigates the artifacts produced by the interparameter crosstalk between the anelastic parameters and helps to resolve the high-resolution velocity and attenuation models simultaneously.

In the following sections, we discuss the implementation of QEFWI using the proposed petrophysical penalty, and we present numerical examples of application of the proposed technique to illustrate its efficiency. We use two synthetic examples that contains shallow layers of low velocity anomalies (e.g. gas clouds) to show that the petrophysical penalty delivers models with high resolution and more accurate than models obtained with unconstrained inversion. Our technique achieve this accuracy by mitigating the crosstalk between velocity and attenuation, as well as by enforcing that the recovered models are consistent with the underlying petrophysics.

5.2 Theory

Due to their implementation simplicity, viscoacoustic or viscoelastic FWI are often formulated in the frequency-domain (Kamei and Pratt, 2013; Malinowski et al., 2011b; Operto et al., 2015). However, because of the heavy computational and memory requirements, frequency-domain cannot handle large-scale simulations (Operto et al., 2007). Therefore, the time-domain formulation is the most approach when performing FWI using attenuation parameters at several scales (Bai et al., 2014; Plessix et al., 2016; Trinh et al., 2019).

To simulate viscoelastic wave propagation in heterogeneous VTI (transversal isotropic with a vertical symmetry axis) media in the time domain, we describe the elastic anisotropic attenuation by a function with a single relaxation mechanism to facilitate the computational efficiency of the method, as discussed by Bai and Tsvankin (2016),

$$\Psi_{ijkl}(t) = C^R_{ijkl}(1 + \tau_{ijkl}e^{-t/\tau^\sigma})H(t), \tag{5.1}$$

where C^R_{ijkl} is the "relaxed stiffness", τ^σ is the stress relaxation time related to the dominant frequency, the parameters τ_{ijkl} describe the difference between the stress and strain relaxation time and quantify the magnitude of anisotropic attenuation. $H(t)$ is the Heaviside function and t denotes time.

The "unrelaxed stiffness" C^U_{ijkl} corresponds to $\Psi_{ijkl}(t=0)$, such that $C^U_{ijkl} = C^R_{ijkl}(1+\tau_{ijkl})$, and the difference

$$\Delta C_{ijkl} = C^U_{ijkl} - C^R_{ijkl}, \tag{5.2}$$

is proportional to τ_{ijkl}. Thus, ΔC_{ijkl} reflects on the magnitude of attenuation in anisotropic media, since τ is inversely proportional to the quality factor Q, such that $\tau_{ijkl} \approx 2/Q_{ijkl}$,

We describe the P- and SV-wave attenuation in VTI media with Thomsen-style parameters (Zhu and Tsvankin, 2006). The parameters $A_{P0} \approx 1/(2Q_{P0})$ and $A_{S0} \approx 1/(2Q_{S0})$ correspond to the P- and SV-wave attenuation coefficients, respectively; ϵ_Q corresponds to the fractional difference between the horizontal and vertical P-wave attenuation coefficients; and δ_Q is related to the curvature of the P-wave attenuation coefficient at the symmetry axis. One can combine these anisotropic attenuation parameters to C^U_{ijkl} in order to compute ΔC_{ijkl} and then estimate quality factor elements Q_{ijkl}.

The viscoelastic stress-strain relationship is given by

$$\sigma_{ij} = C^U_{ijkl}\,\epsilon_{kl} + \Delta C_{ijkl}\,r_{kl}, \tag{5.3}$$

where σ_{ij} and ϵ_{kl} are the stress and strain tensor, respectively, and r_{kl} are the memory variables, which are used to facilitate the finite-difference numerical implementation on the time-domain (Bai and Tsvankin, 2016; Robertsson et al., 1994).

In this paper, we solve the FWI problem in order to recover only v_{P0} and A_{P0} (or Q_{P0}). We set the other velocity (v_{S0}, ϵ and δ) and attenuation parameters (A_{S0}, ϵ_Q and δ_Q) to their true values during the inversion. Thus, we reduce the overall ambiguity of the inverse problem while investigating if explicitly incorporating petrophysical data into the objective function in a probabilistic approach help us to recover geologically feasible velocity v_{P0}

and attenuation A_{P0} parameters that are inverted simultaneously. Then, we minimize an objective function $\mathcal{J}$ composed of the data misfit term $\mathcal{J}_D$ and a petrophysical term that penalizes the models using petrophysical information $\mathcal{J}_P$

$$\mathcal{J}(\mathbf{u}, V_{P0}, A_{P0}) = \mathcal{J}_D(\mathbf{u}, V_{P0}, A_{P0}) + a\,\mathcal{J}_P(V_{P0}, A_{P0}), \tag{5.4}$$

where $\mathbf{u}(e, \mathbf{x}, t)$ is the viscoelastic wavefield, e and $\mathbf{x}$ are, respectively, the experiment index and space coordinates; and the scalar parameter a determines the strength of $\mathcal{J}_P$ in the objective function. The data misfit term $\mathcal{J}_D$ is based on the l_2-norm of the residuals $\mathbf{r}_D(e, \mathbf{x}, t)$ between the modeled data and the observed data, such that

$$\mathbf{r}_D(e, \mathbf{x}, t) = \mathbf{W}_u(e, \mathbf{x}, t)\mathbf{u}_s(e, \mathbf{x}, t) - \mathbf{d}_{obs}(e, \mathbf{x}, t), \tag{5.5}$$

where $\mathbf{W}_u(e, \mathbf{x}, t)$ are weights that restrict the source wavefield $\mathbf{u}_s(e, \mathbf{x}, t)$ to the known receiver locations, and $\mathbf{d}_{obs}(e, \mathbf{x}, t)$ are the observed data. We compute the gradient of $\mathcal{J}_D$ in respect to the model parameters using the adjoint-state method (Bai et al., 2017; Plessix, 2006).

Aragao and Sava (2020a) propose the use of petrophysical data to determine a single PDF in order to compute the penalty $\mathcal{J}_P$ for elastic full-waveform inversion in order to recover the Lamé parameters λ and μ. The PDF is represented in the petrophysical space by coordinates $\mathbf{p}$, and the components of the model parameters are represented by the vector $\mathbf{m}(\mathbf{x})$ that depends on position $\mathbf{x}$. They use the probability density $f(\mathbf{p})$ derived from the petrophysical data to determine the distance $D(\mathbf{m})$ from $\mathbf{m}$ to the entire distribution $f(\mathbf{p})$ as

$$\frac{1}{D(\mathbf{m})} = \sum_{\mathbf{p}} \frac{f(\mathbf{p})}{d(\mathbf{m}, \mathbf{p})}, \tag{5.6}$$

where $d(\mathbf{m}, \mathbf{p})$ corresponds to the distance from any given model represented by coordinates $\mathbf{m}$ to any point $\mathbf{p}$ in the petrophysical space:

$$d(\mathbf{m}, \mathbf{p}) = \|\mathbf{m} - \mathbf{p}\|_2. \tag{5.7}$$

Finally, Aragao and Sava (2020a) define the penalty term as

$$\mathcal{J}_P = \sum_{\mathbf{m}} D(\mathbf{m}). \tag{5.8}$$

Based on the definition of $\mathcal{J}_P$, one can notice that $D(\mathbf{m})$ is small in the proximity of large values of $f(\mathbf{p})$ and it increases away from the distribution. Also, the gradient of $D(\mathbf{m})$ is close to zero in the region where $f(\mathbf{p})$ is high. Thus, once the parameters $\mathbf{m}$ of the updated model at a specific location is consistent with the distribution given by the PDF, the data misfit $\mathcal{J}_D$ fully controls the gradient and the action of the petrophysical penalty term ceases. Therefore, the value of a in equation 5.4 does not need to be adjusted during the inversion, i.e., we do not need to use a dynamic decreasing weighting of the penalty term in the objective function because the value of $\mathcal{J}_P$ naturally decreases as inversion progresses and the updated models become consistent with the petrophysical data.

Aragao and Sava (2020b) propose to use multiple PDFs obtained by clustering petrophysical information when calculating the penalty term, such that each PDF represents a different lithological unit that is determined by applying K-means clustering, a machine learning unsupervised technique, to the petrophysical data. Nevertheless, the technique presented by Aragao and Sava (2020b) does not consider spatial trends in the petrophysical data, which occurs as rock physics properties vary laterally and with depth because of depositional and burial regimes (Avseth et al., 2010; Mavko et al., 2003).

Here, we modify the idea proposed by Aragao and Sava (2020c), to use a petrophysical penalty term based on multiple PDFs that take into account subsurface distribution patterns, due to composition, porosity, pore-pressure, or compaction, as the seismic signature of a formation may change significantly with varying depth, for example. Rock physics spatial trends describe how the elastic properties of a formation vary vertically and laterally, and thus this approach can be particularly useful when lithological knowledge of the subsurface is available in the studied region. In order to construct the spatially-variable PDFs, we interpret the petrophysical data and classify different lithologies or formations according to their spatial location. We identify regions where the values of the viscoelastic properties

have similar range, possibly indicating a distinct formation or lithology. The probabilistic petrophysical penalty $\mathcal{J}_P$ is based on spatially-variable PDFs and it can account for the spatial uncertainty related to the relative position of the wells.

As the viscoelastic model parameters v_{P0} and A_{P0} have different magnitude and units, we define $\mathbf{m}(\mathbf{x}) = \{c_v\, v_{P0}(\mathbf{x}),\, c_A\, A_{P0}(\mathbf{x})\}$ and $\mathbf{p} = \{c_v\, v_{P0p},\, c_A\, A_{P0p}\}$, using coefficients c_v and c_A with units and magnitude inverse to v_{P0} and A_{P0}, respectively. Assuming we have n PDFs defined at different positions in the model, we consider $f_i(\mathbf{p})$ as the probability density of the i-*th* PDF, $i = 1 \ldots n$. Therefore, we can determine the distance $D_i(\mathbf{m})$ from the model parameter $\mathbf{m}(\mathbf{x})$ to the i-*th* distribution as

$$\frac{1}{D_i(\mathbf{m})} = \sum_{\mathbf{p}} \frac{f_i(\mathbf{p})}{d_i(\mathbf{m}, \mathbf{p})}, \tag{5.9}$$

where $d_i(\mathbf{m}, \mathbf{p})$ corresponds to the distance from any given model represented by coordinates $\mathbf{m}$ to any point in the petrophysical space. Then, we can formulate a combined petrophysical penalty term $\mathcal{J}_P$ as

$$\mathcal{J}_P = \sum_{i=1}^{n} \sum_{\mathbf{m}} K_i(\mathbf{m}) D_i(\mathbf{m}), \tag{5.10}$$

such that $K_i(\mathbf{m})$ are non-overlapping masks or weighting operators that can overlap in particular areas. The role of K_i are to associate each point in the model to its correspondent PDF $f_i(\mathbf{p})$. On one hand, if $K_i(\mathbf{m})$ is just a mask, then the weights related to the distance of the model points to the well locations are not taken into account. In this case, the elements of $K_i(\mathbf{m})$ are equal to 1 for the points in the model that are characterized by the PDF $f_i(\mathbf{p})$, or 0 otherwise. On the other hand, if one sets $K_i(\mathbf{m})$ as a weighting operator in order to consider uncertainty in the calculation of the petrophysical penalty, $K_i(\mathbf{m})$ is a nonnegative matrix, such that its elements are equal to 1 at the wells and sum to 1 away from the wells. For instance, one can use Gaussian functions to simulate the decrease as a function of distance from the wells. The weighting operators may overlap in some points of the model if one prefers to use more than a single PDF to constrain these points, such that each PDF has a relative contribution for the petrophysical penalty.

5.3 Examples

We illustrate the efficiency of our method in delivering geologically feasible velocity and attenuation parameters with two synthetic examples and compare inversions using our proposed methodology with the alternative using only the data misfit term.

For the first example, we use a simple structure with rectangular low-velocity anomalies and a deep horizontal reflector. The low velocity anomalies simulate gas clouds, and the presence of these shallow anomalies can cause strong lateral and vertical variations of seismic wave velocities, as well as significant scattering and amplitude loss due to absorption. We aim to verify if the viscoelastic FWI is successful in imaging the deep reflector as well as the low velocity anomalies when well-log information based on spatial trends in the petrophysical data is incorporated into the inversion. We assume that different spatial trends are well defined by well logs. We show that the probabilistic penalty term based on spatially-variable PDFs guides the inversion toward more accurate models compared to the cases of viscoelastic FWI unconstrained by petrophysical information.

In the second example, we use a complex model with a more realistic geological setting featuring shallow gas and localized slow velocity anomalies. We define $K_i(\mathbf{m})$ as masks for broad regions of the model defined using the initial models. We demonstrate that petrophysical penalties based on spatially-variable PDFs deliver accurate model updates and mitigate the strong interparameter crosstalk artifacts between velocity and attenuation parameter that severely hamper the models recovered using only the data misfit.

5.3.1 Model 1: Rectangular low-velocity anomalies

This synthetic example (Figure 5.1) uses a model with two rectangular low-velocity anomalies centered at $x = 1.0$ km, with 0.6 km width and 0.03 km thickness, and a horizontal reflector at $z = 1.25$ km. We use 41 evenly spaced sources at $z = 0.02\,\text{km}$ and a line of multicomponent geophones at $z = 0.05\,\text{km}$ in order to simulate the multicomponent data. We initiate the inversion with models of constant $v_{P0} = 2.0\,\text{km/s}$ and $A_{P0} = 0.005$

(i.e., $Q_{P0} = 100$), which correspond to the background of the true models (Figure 5.1). We keep the velocity parameters v_{S0}, ϵ and δ equal to their true values during the inversion: $\epsilon = 0.25$ and $\delta = 0.05$, and $v_{S0} = 1.0\,\mathrm{km/s}$ and $v_{S0} = 1.5\,\mathrm{km/s}$ above and below the reflector (Figure 5.1), respectively. We choose these values in order to ensure stability during the wavefield extrapolation in the time domain when using the finite-difference method. We also keep the attenuation parameters A_{S0}, ϵ_Q and δ_Q constant during the inversion, so we reduce the ambiguity among the attenuation parameters.

We consider that prior petrophysical data, corresponding to v_{P0}, from a well located at $x = 1.0\,\mathrm{km}$ are available (Figure 5.2a). We simulate the well log by adding random noise to the true model (Figure 5.1) at $x = 1.0\,\mathrm{km}$. Many methods have been proposed in order to estimate P- and S-wave attenuation logs from available well log data (Cheng et al., 1982; Neep, 1995; Sun et al., 2000), since Q_{P0} values correlate well with petrophysical properties, and thus, we assume that an empirical A_{P0} well log derived from a given method is available. For this example, we set $c_v = 1\,s/km$ and $c_A = 100$. Figure 5.2b shows the considered well log for $c_A\,A_{P0} = 50/Q_{P0}$.

The well logs in Figure 5.2 indicate the occurrence of four intervals with different velocity and attenuation properties. Therefore, we define the probability distributions $f_i(\mathbf{p})$ and the operators K_i, $i = 1 \ldots 4$. $f_1(\mathbf{p})$ and $f_4(\mathbf{p})$ use the well log above $z = 0.36\,\mathrm{km}$ and below $z = 1.22\,\mathrm{km}$, respectively; $f_2(\mathbf{p})$ uses the well log between $z = 0.36\,\mathrm{km}$ and $z = 0.56\,\mathrm{km}$, and $f_3(\mathbf{p})$ uses the well log between $z = 0.56\,\mathrm{km}$ and $z = 1.22\,\mathrm{km}$. Figures 5.3a-d show the distributions $f_i(\mathbf{p})$, $i = 1 \ldots 4$, respectively. We consider all K operators as masks, i.e., we do not account for uncertainty related to the distance between the well locations and the points in the model. The four masks shown in Figure 5.4 indicate in which region each PDF $f_i(\mathbf{p})$ is defined. One can notice that we simply established the operators K_i as defined from the depth extent of each formation.

Figures 5.5a-d display the distances $D(\mathbf{m})$ and the gradient of the petrophysical terms for $f_i(\mathbf{p})$, $i = 1 \ldots 4$, respectively. One can notice that, when a point $\mathbf{m}$ in the updated model is

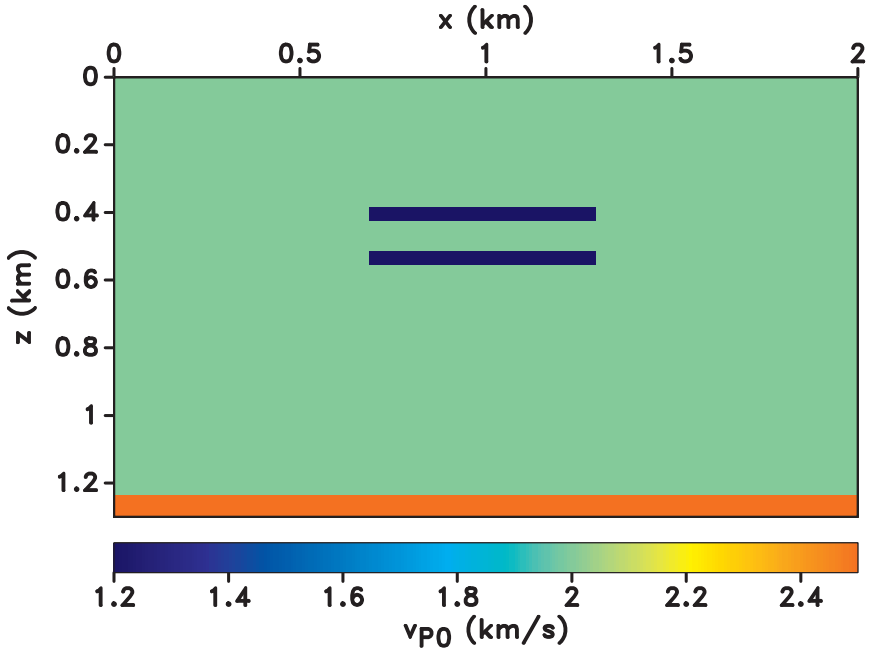

(a)

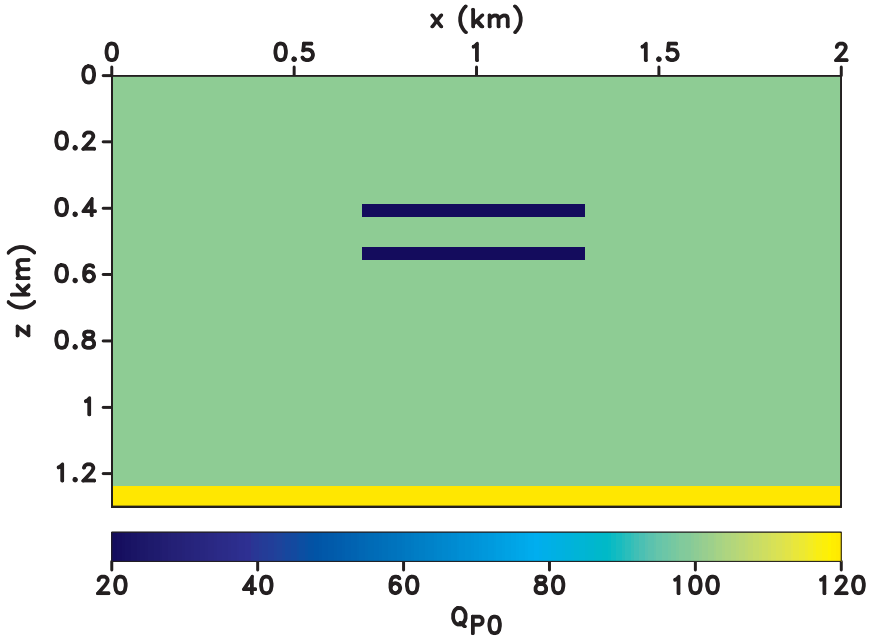

(b)

Figure 5.1: Synthetic models for (a)v_{P0} and (b)Q_{P0}.

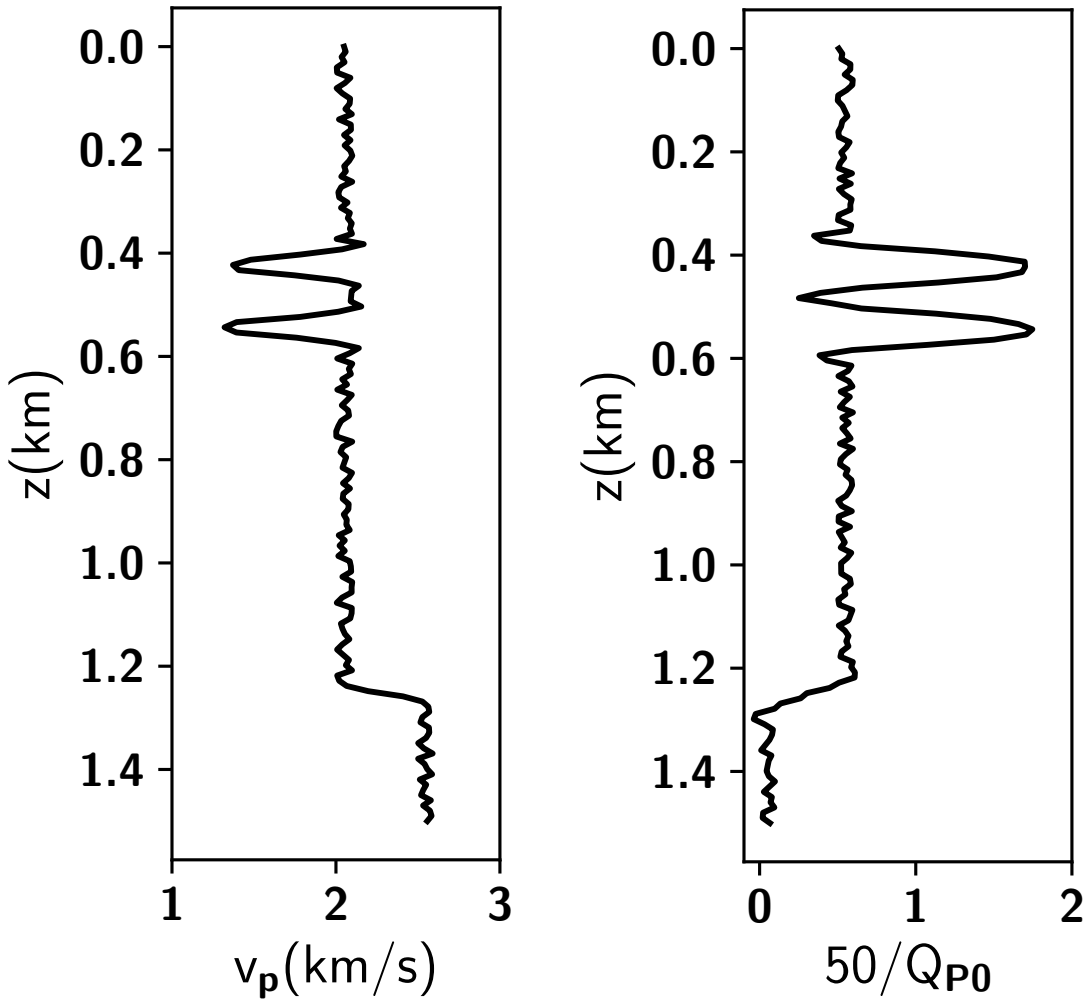

(a) (b)

Figure 5.2: Hypothetical (a) v_P and (b) Q_{P0} logs at $x = 1.0\,\text{km}$ in the model depicted in Figure 5.1. We add random noise to the models to calculate v_P and assume that Q_{P0} is determined using an empirical relationship between seismic attenuation and petrophysical properties.

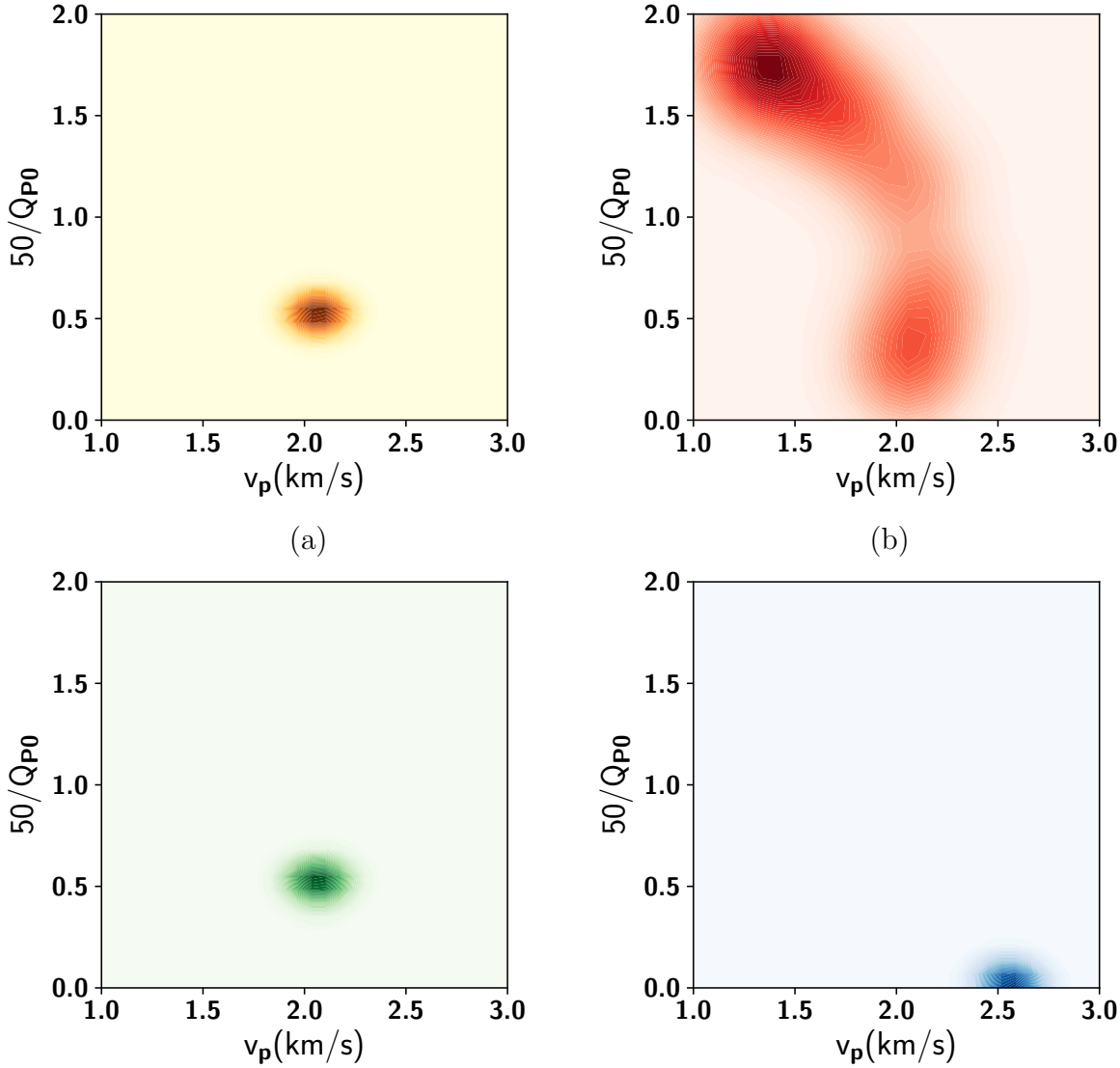

Figure 5.3: The distributions (a) f_1, (b) f_2, (c) f_3, and (d) f_4 using the spatial trends in petrophysical information from the well log in Figure 5.2.

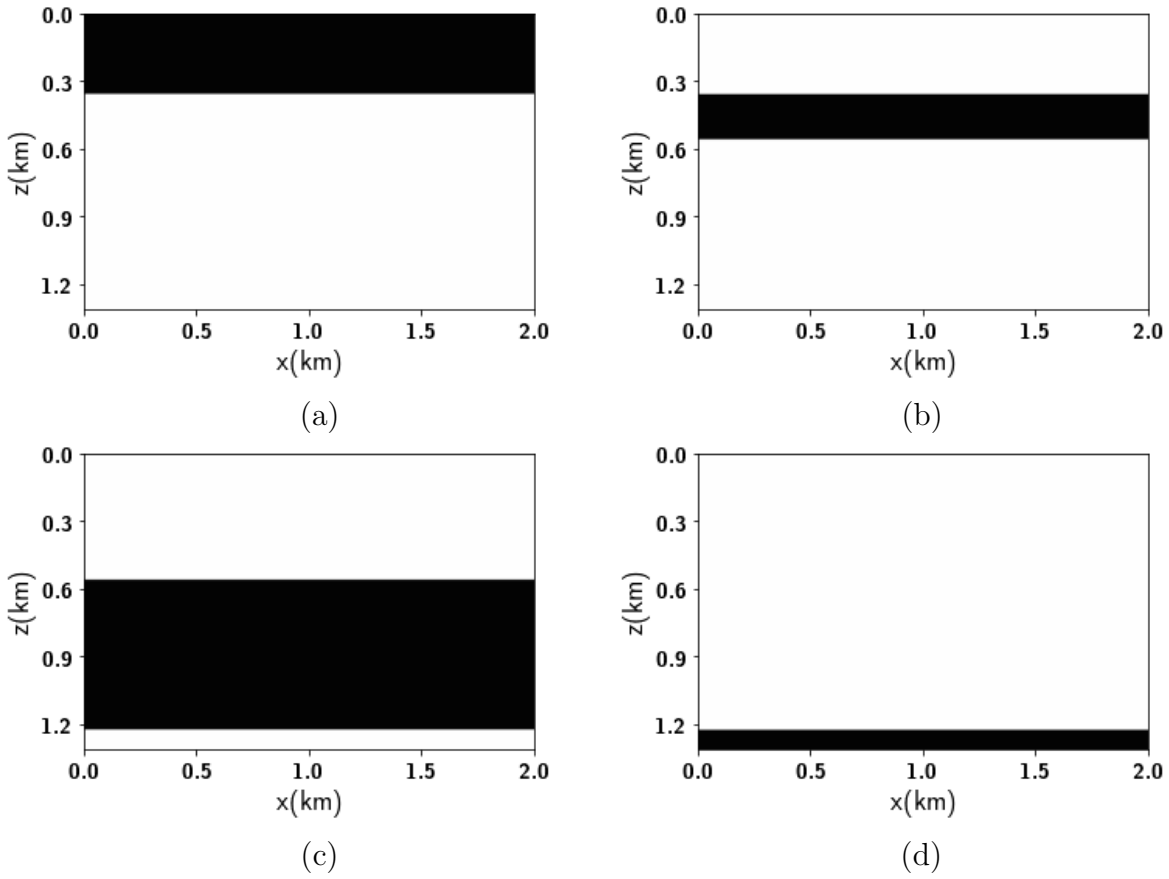

Figure 5.4: Mask operators used to constrain PDFs at corresponding spatial locations. Panels (a)-(d) correspond to K_1-K_4. Black regions correspond to 1, and white to 0.

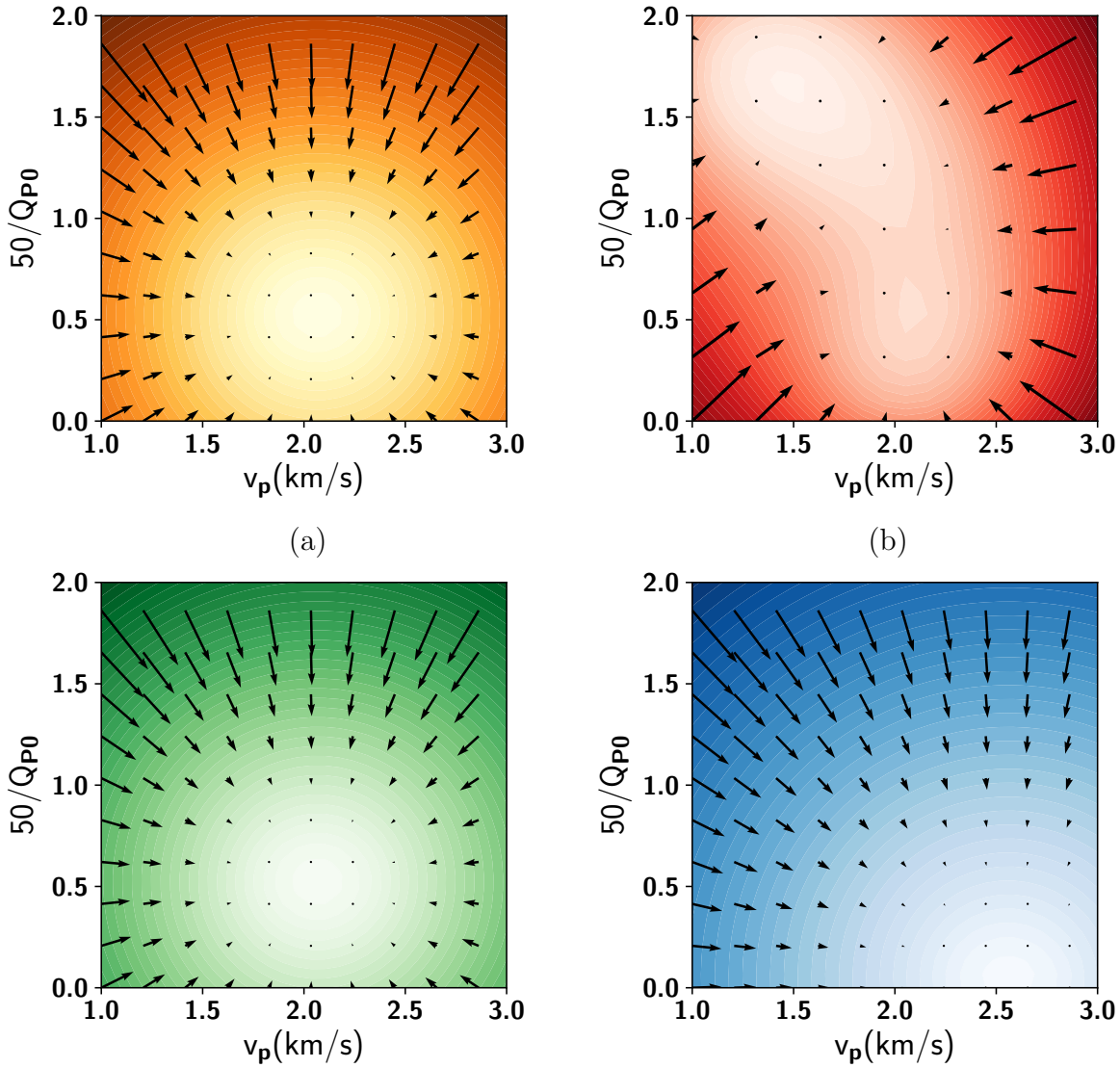

Figure 5.5: The distance $D_i(\mathbf{m})$ and its gradient for the distributions (a) f_1, (b) f_2, (c) f_3, and (d) f_4 (Figure 5.3). Note that high probability models are associated with small values of $D_i(\mathbf{m})$ and with zero petrophysical gradients..

consistent with the distribution given by its correspondent PDF, the distance $D(\mathbf{m})$ and its gradient are both zero. In this case, the data misfit $\mathcal{J}_D$ fully controls the inversion gradient for that point, as discussed earlier. Otherwise, the corresponding penalty forces the model to comply with the underlying petrophysical PDF.

Figure 5.6 shows the recovered v_{P0} and Q_{P0} models using the objective function $\mathcal{J}_D$. Without imposing any petrophysical penalties, the reflector at $z = 1.25\,\text{km}$ (Figure 5.1) cannot be identified in both models, as the reflector is likely masked by the multiples that are created by the gas cloud layers. In addition, the gas clouds are not recovered during the inversion. Also, the Q_{P0} model is strongly hampered by non-geological artifacts due to the severe trade-off between the attenuation and velocity parameters, as well as the limited acquisition coverage and illumination.

Figure 5.7 shows the recovered v_{P0} and Q_{P0} models when the objective function is defined with a petrophysical penalty based on multiple PDFs that exploit the spatial trends derived from the well logs (Figure 5.2). In this case, the reflector at $z = 1.25\,\text{km}$ (Figure 5.1) can be identified in both models as the petrophysical constraint $\mathcal{J}_P$ enforces that the properties of the models for the deep areas are different than the others (Figure 5.2), as one can notice by comparing Figure 5.3d to Figures 5.3a-c. Additionally, because of the PDF that describes the model for the region where the gas clouds are located (Figure 5.3b), the low velocity anomalies are recovered in both models (Figure 5.7). However, as the anomalies are thin and close to each other, and due to the relative small aperture and low frequency of 10 Hz used for inversion, FWI does not have sufficient resolution to separate the gas bodies. Notwithstanding, the inverted models depicted in Figure 5.7 are less affected by interparameter crosstalk effects than the models recovered using only the data misfit (Figure 5.6).

5.3.2 Model 2: BP 2004 Benchmark

The second synthetic example uses the right portion of the BP 2004 Benchmark model (Billette and Brandsberg-Dahl, 2005), which simulates a geological environment with localized slow velocity anomalies and shallow gas. The velocity estimation for this part of the BP

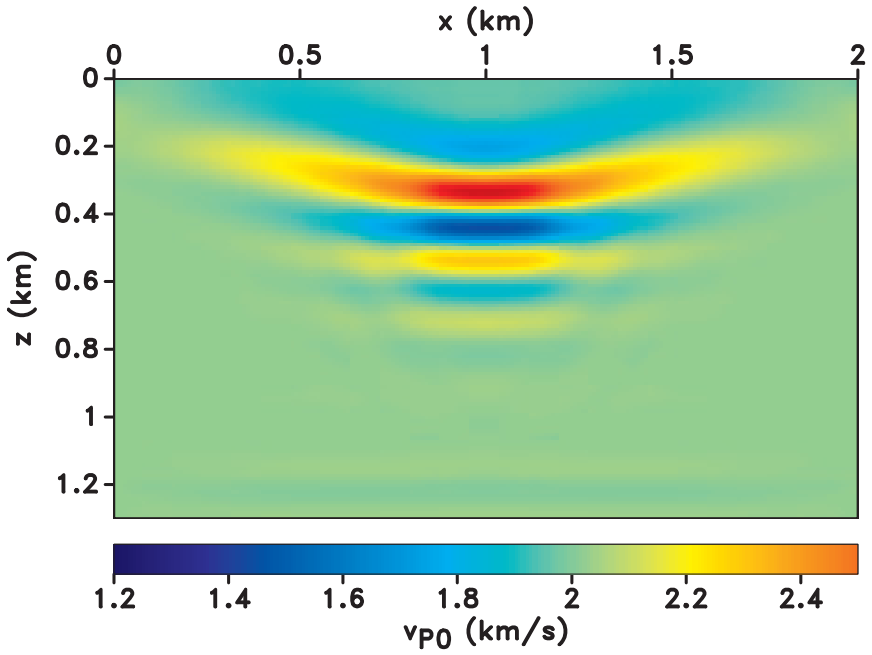

(a)

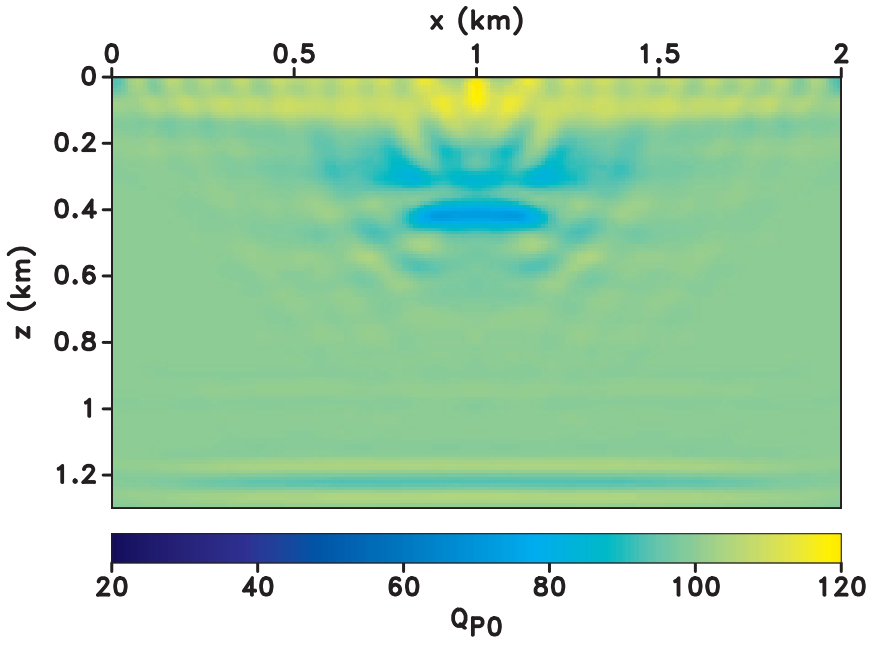

(b)

Figure 5.6: Recovered (a) v_{P0} and (b) Q_{P0} models obtained using the objective function $\mathcal{J}_D$. The inversion is not able to recover the low velocity anomalies and the deep reflector present in the true models (Figure 5.1).

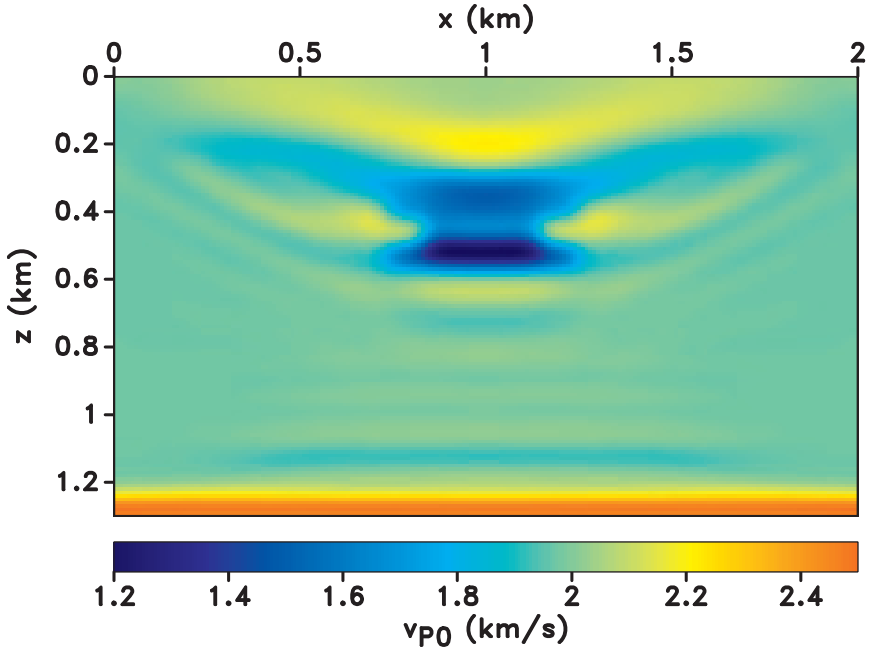

(a)

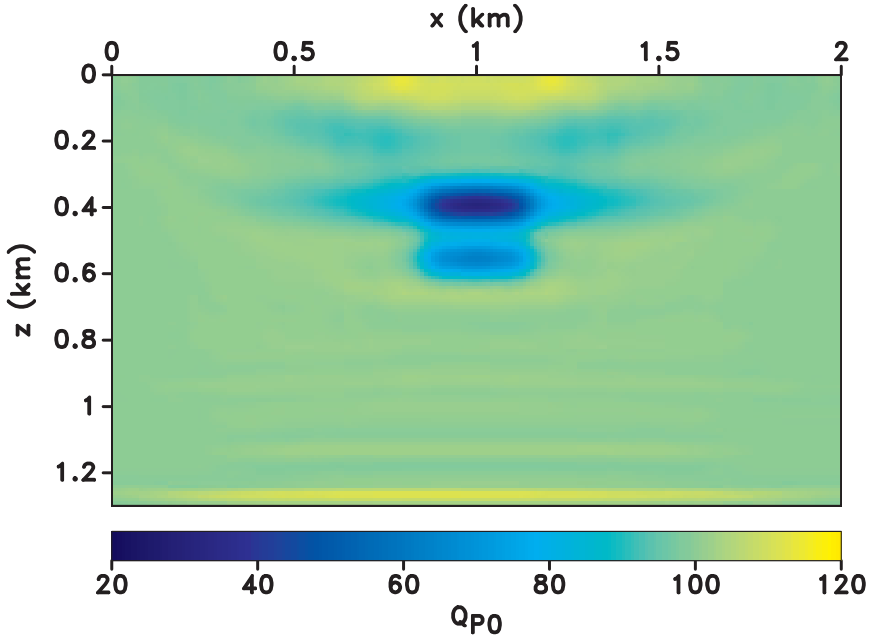

(b)

Figure 5.7: Recovered (a) v_{P0} and (b) Q_{P0} models obtained using the objective function $\mathcal{J}_D + \mathcal{J}_P$, where $\mathcal{J}_P$ is based on multiple PDFs, determined considering spatial trends in the available petrophysical data (Figure 5.2). The inverted models are closer to the true models (Figure 5.1) compared to the cases when we use only the data misfit (Figure 5.6).

model is considered challenging due to the presence of the subtle velocity anomalies stacked on top of one-another.

The original BP 2004 Benchmark model is acoustic and composed of velocity and density models. Hence, in order to perform viscoelastic inversion, we use the original v_{P0} model (Figure 5.8a) to construct the attenuation parameters Q_{P0} (Figure 5.8b) and Q_{S0} (Figure 5.9b), as well as the shear velocity model v_{S0} (Figure 5.9a). We set 160 and 140 as the maximum values in the scale bar of all figures corresponding to Q_{P0} and Q_{S0}, respectively, for plotting purposes. For the water layer, we use $Q_{P0} = 10000$ and $Q_{S0} = 5000$, so A_{P0} and A_{S0} are approximately zero. For the same reasons we state in the previous example, we keep the velocity parameters v_{S0} (Figure 5.9a), ϵ and δ, and the attenuation parameters A_{S0} (Figure 5.9b), ϵ_Q and δ_Q equal to their true values during the inversion. We build the initial Q_{P0} (or A_{P0}) model by removing the gas and other low-velocity anomalies from the original model (Figure 5.8b) to investigate if we are able to recover these anomalies after the inversion.

We simulate a multicomponent ocean bottom seismic survey (OBS) with a line of receivers at the water bottom and 101 evenly spaced pressure sources located at $z = 0.02\,\text{km}$. We use a 7.5 Hz peak Ricker source wavelet and initiate the inversion with the v_{P0} and Q_{P0} models depicted in Figure 5.10. We consider that prior petrophysical data from wells located at $x = 2.1,\ 3.9\,\text{km}$ are available. As in the previous example, we assume that an empirical A_{P0} well log derived from a given method is available, and we use the actual values extracted from the true model (Figure 5.8b) at the well locations. For this example, we set $c_v = 1\,\text{s/km}$ and $c_A = 400$.

In order to define a penalty term based on multiple PDFs associated with spatial trends in the petrophysical data, we consider $K_i(\mathbf{m})$ as mask operators for inversion that are not simply established using blocks defined from the depth extent of formations intercepted in the wells, but instead capture the rough structure of the background model. We use the initial Q_{P0} model (Figure 5.10b) to define two constant zones, and define the mask operators

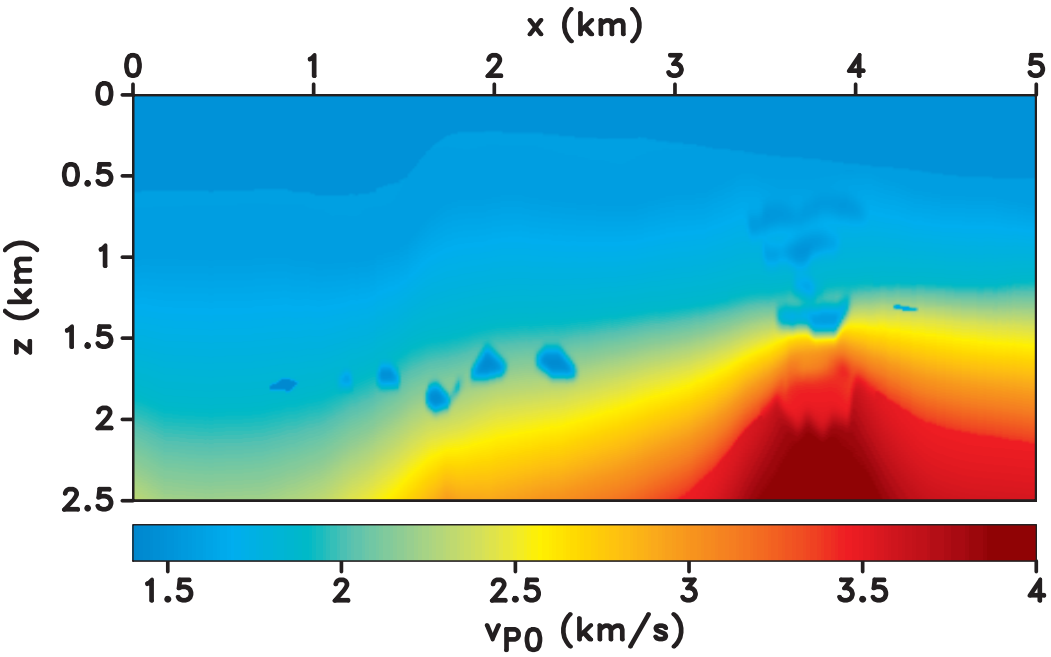

(a)

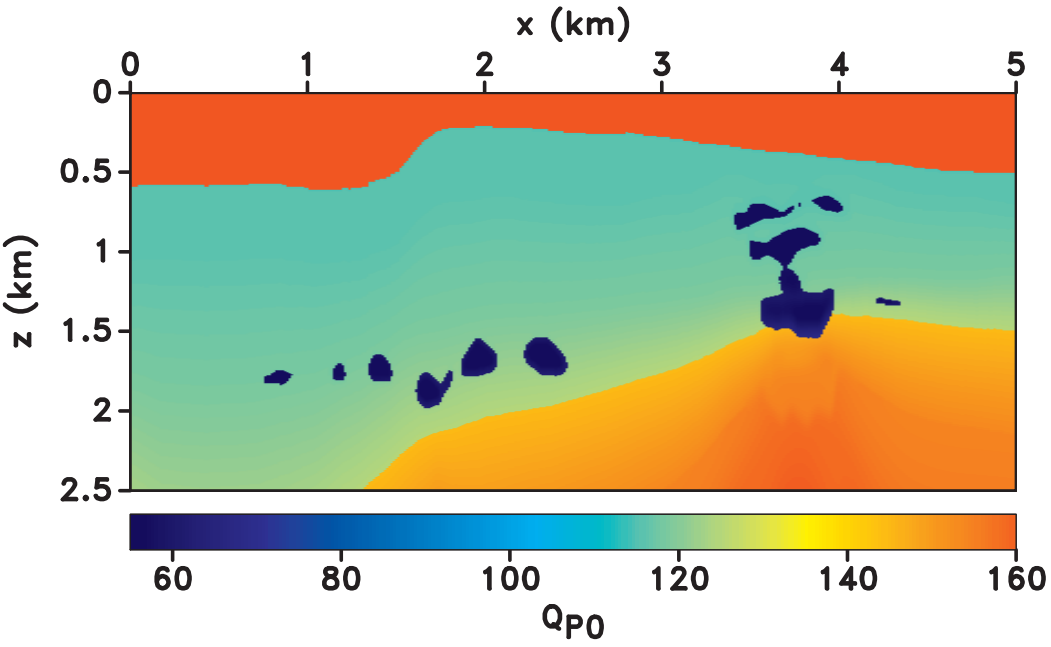

(b)

Figure 5.8: BP 2004 Benchmark model: Synthetic models for (a) v_{P0} and (b) Q_{P0}.

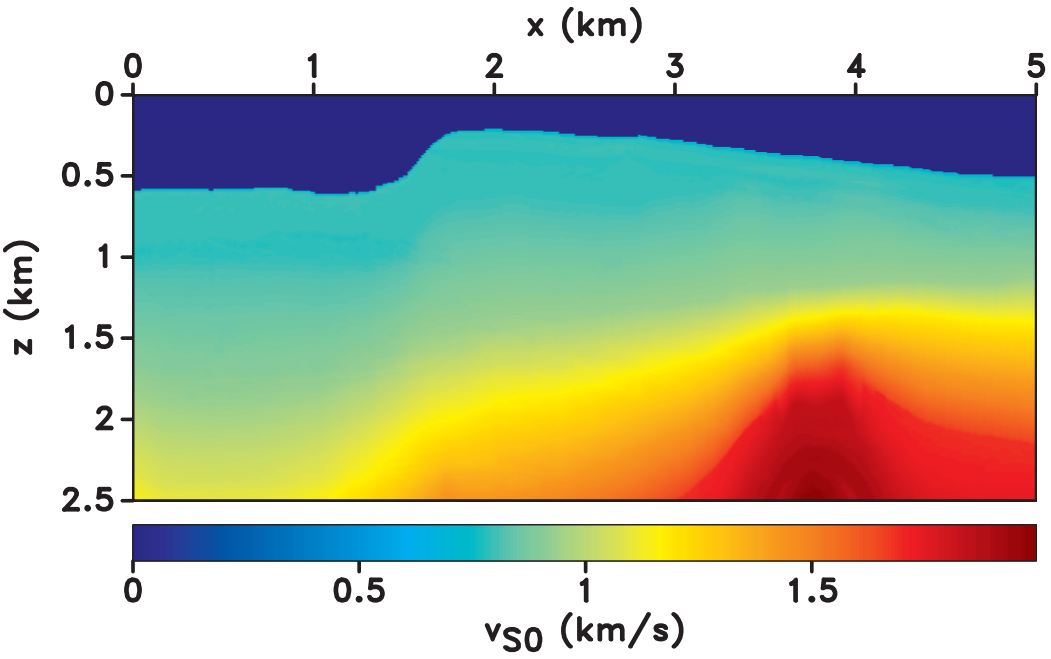

(a)

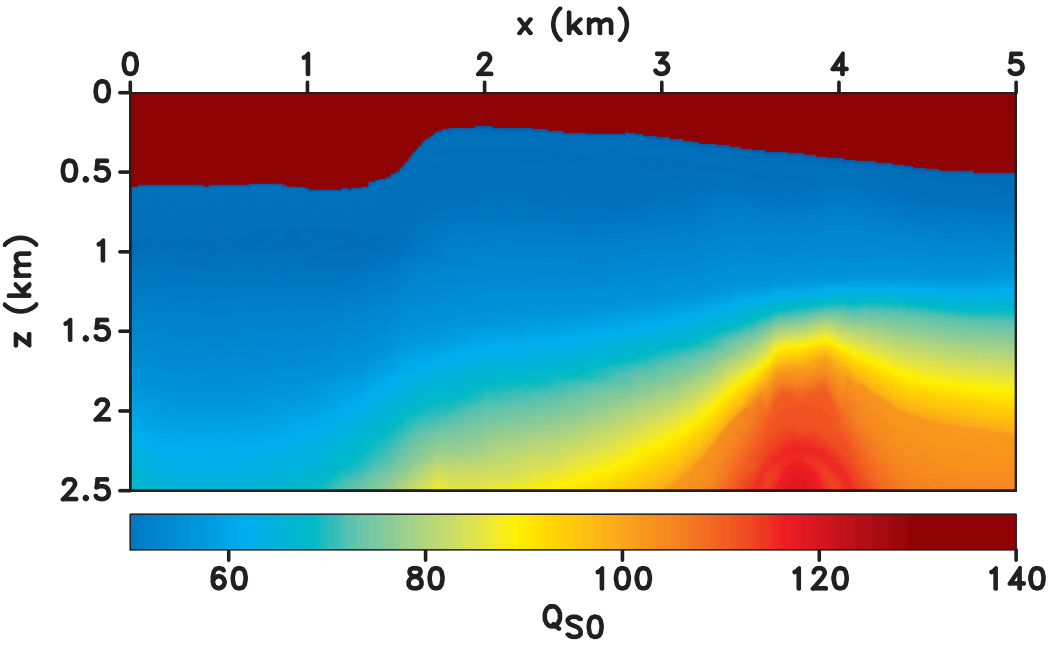

(b)

Figure 5.9: BP 2004 Benchmark model: Synthetic models for (a) v_{S0} and (b) Q_{S0}.

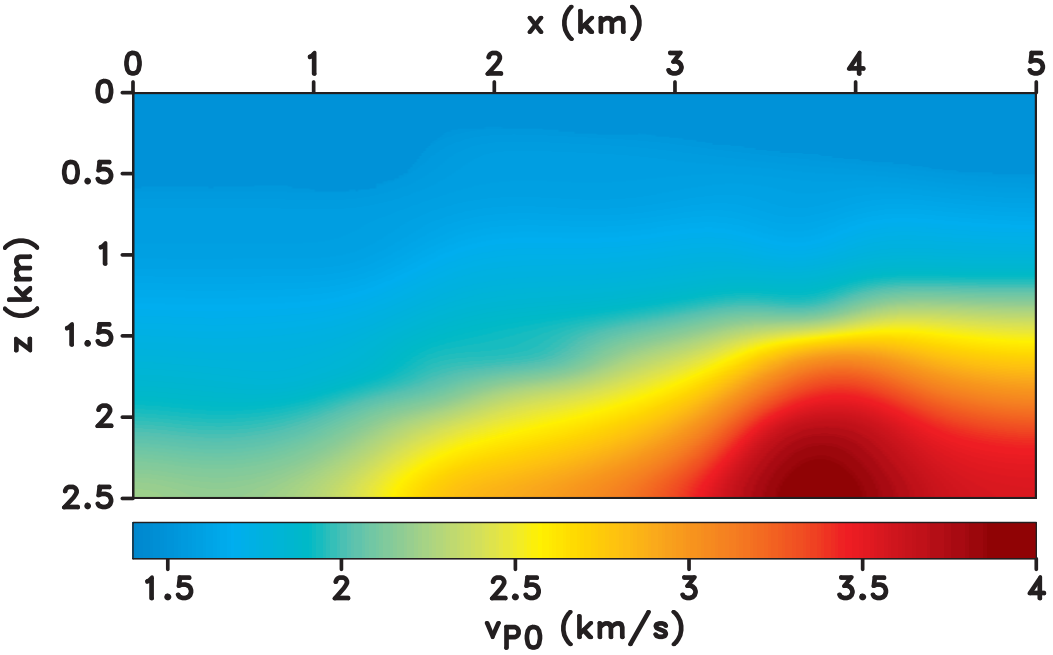

(a)

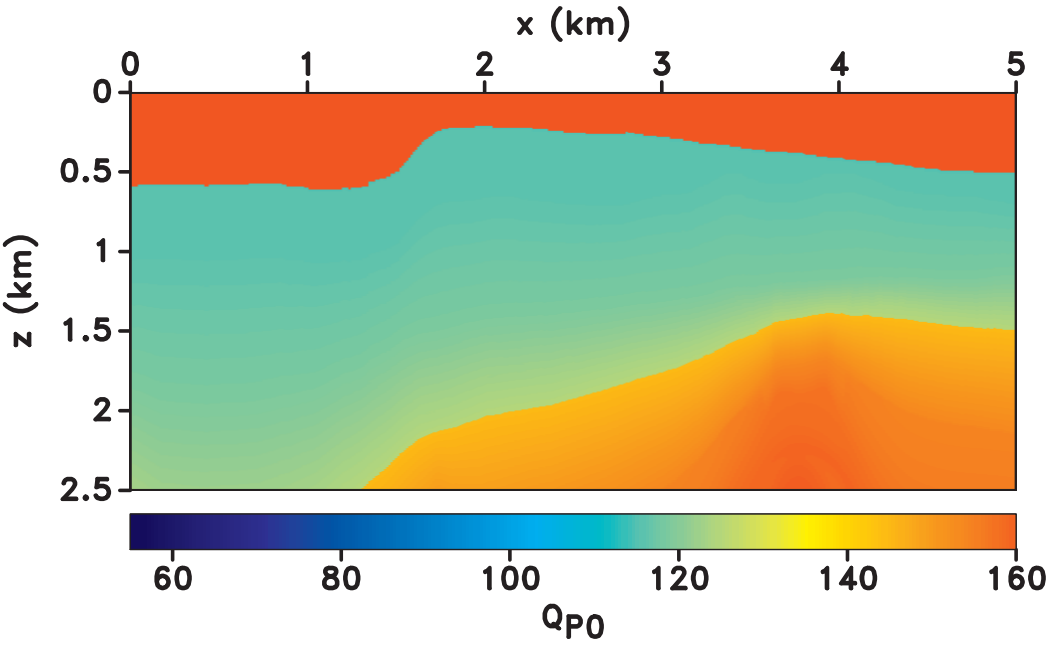

(b)

Figure 5.10: BP 2004 Benchmark model: Initial models, (a) v_{P0} and (b) Q_{P0} used for the viscoelastic waveform inversion.

depicted in Figure 5.11. We determine the probability distributions $f_1(\mathbf{p})$ and $f_2(\mathbf{p})$, using the well log data corresponding to each region (Figure 5.12). Figures 5.13a and 5.13b display the distances $D_1(\mathbf{m})$ and $D_2(\mathbf{m})$, and the correspondent gradient of the petrophysical terms for $f_1(\mathbf{p})$ and $f_2(\mathbf{p})$, respectively. As in the previous example, the distance $D_i(\mathbf{m})$ and the associated objective function-gradient are both zero when the model $\mathbf{m}$ at a given location in the updated model is consistent with the distribution given by its correspondent PDF.

Figure 5.14 shows the recovered v_{P0} and Q_{P0} models using the objective function $\mathcal{J}_D$. As we do not include petrophysical information during inversion, the gas clouds and other shallow anomalies are not well recovered during the inversion in both models. Additionally, without petrophysical information, the velocity errors cause higher errors in the attenuation model. As a consequence, both models are contaminated with non-geological artifacts due to parameter crosstalk, which severely deteriorates the quality of the recovered models.

Figure 5.15 shows the recovered v_{P0} and Q_{P0} models when the objective function is based on multiple spatially-variable PDFs that use the mask operators shown in Figure 5.11. In this case, the gas anomalies and other shallow anomalies are well recovered (Figure 5.15). The models depicted in Figure 5.15 are less affected by crosstalk artifacts and closer to true models (Figure 5.8) than the models inverted using only the data misfit (Figure 5.14). The recovered Q_{P0} shown in Figure 5.15b proves that the petrophysical penalty term based on multiple PDFs constrains the low velocity anomalies that are not present in the initial model (Figure 5.10b) when velocity and attenuation parameters are inverted simultaneously. If more well logs were available, one could define a larger number of mask operators to recover amplitudes for the low velocity anomalies that are even closer to the true models (Figure 5.8). In this case, the interpretation of the petrophysical data may define narrower regions, each related to a different mask K_i, such that the corresponding PDF $f_i(\mathbf{p})$ delineates the spatial trends more accurately.

Figure 5.16 shows the first 3.5 s of the vertical and horizontal components of the data residual for the central shot: before inversion (Figures 5.16a and 5.16b), using the models

recovered with the objective function $\mathcal{J}_D$ (Figures 5.16c and 5.16d), and with the objective function $\mathcal{J}_D + \mathcal{J}_P$ (Figures 5.16e and 5.16f). Notice that the amplitudes of the data residuals using the models recovered with the objective function based on multiple spatially-variable PDFs (Figures 5.16e and 5.16f) are smaller compared to the case where the data are predicted using the models recovered with unconstrained inversion (Figures 5.16c and 5.16d), which indicates that the recovered v_{P0} and Q_{P0} models using the objective function $\mathcal{J}_D + \mathcal{J}_P$ (Figure 5.15) are more accurate kinematically compared to the models recovered using the objective function $\mathcal{J}_D$ (Figure 5.14). In addition, Figure 5.17 shows the normalized objective function for the constrained (solid line) and unconstrained inversion (dashed line). One can note that, compared with the unconstrained case, the constrained inversion reduces more the misfit between the observed data and the simulated data using the inverted models after 100 iterations, with faster convergence. Finally, vertical profiles from the inverted Q_{P0} model at $x = 3.75$ km are shown in Figure 5.18 where the black line indicate the true model, and the pink, green and red correspond, respectively, to the initial model (Figure 5.10b), and the models recovered in the unconstrained (Figure 5.14b) and constrained (Figure 5.15b) inversions. Considering that the initial model does not present the attenuation anomalies, we are able to recover the anomalies that better represent the true model after the inversion when we use the objective function $\mathcal{J}_D + \mathcal{J}_P$.

5.4 Conclusions

We describe an approach to incorporate petrophysical information into the objective function of viscoelastic full-waveform inversion (FWI) using a penalty term based on probability density functions (PDFs) that take into account the spatial distribution of petrophysical properties that allows us to account for the spatial variation of subsurface properties. We formulate a penalty term based on multiple probability density functions that could also account for positioning uncertainty, when applied away from the well locations. By incorporating petrophysical information into the inversion, we reduce the non-linearity and ill-posedness of multiparameter FWI and we mitigate the artifacts created by the crosstalk

between the velocity and attenuation parameters, while ensuring that the inversion delivers feasible subsurface models, and recover structures such as shallow low-velocity anomalies and deep reflectors that are not recovered when inversion is performed using only the data misfit. Our technique guides the inversion to models characterized by reduced interparameter crosstalk, improves the model spatial resolution in areas of poor illumination, and steers the inversion toward geologically plausible earth models that are consistent with the seismic data, as well as with the underlying petrophysics. The proposed method is directly applicable to monitoring carbon dioxide geological sequestration, as well as to monitoring production of multi-layer reservoirs.

5.5 Acknowledgements

We acknowledge CAPES (Brazilian Federal Agency for Support and Evaluation of Graduate Education) for financial support. We thank the sponsors of the Center for Wave Phenomena (CWP), whose support made this research possible. The synthetic examples in this paper uses the Madagascar open-source software package (Fomel et al., 2013) freely available from http://www.ahay.org.

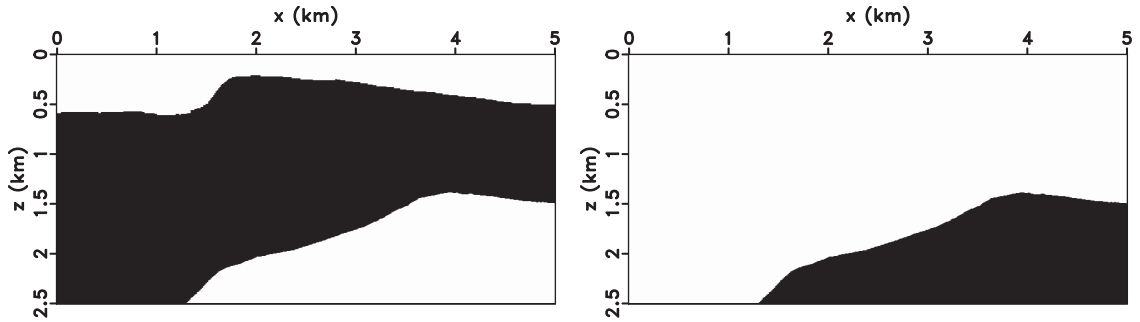

(a) (b)

Figure 5.11: BP 2004 Benchmark model: Mask operators (a) K_1 and (b) K_2 used to constrain petrophysical PDFs at corresponding spatial locations. Black regions correspond to 1, and white to 0.

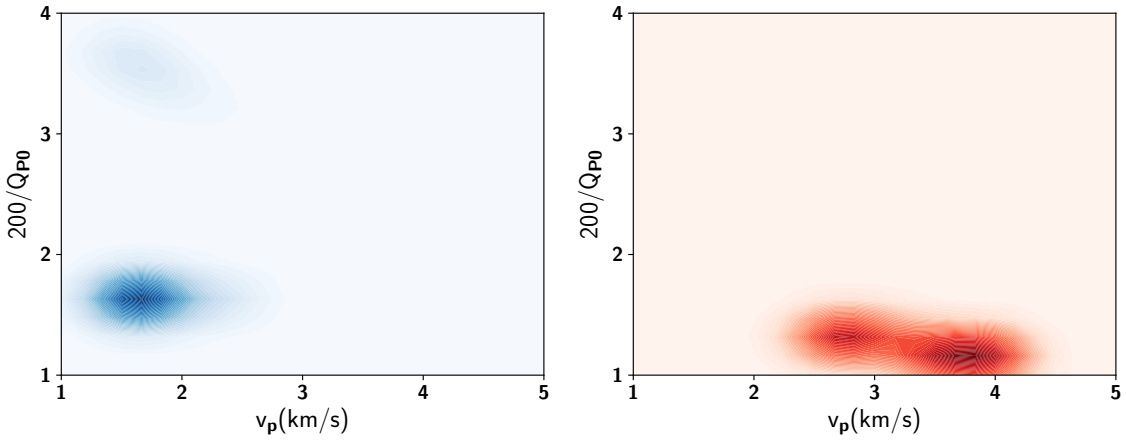

(a) (b)

Figure 5.12: BP 2004 Benchmark model: The distributions (a) f_1 and (b) f_2 using the spatial trends in petrophysical information from the well logs at $x = 2.1\,\text{km}$ and $x = 3.9\,\text{km}$.

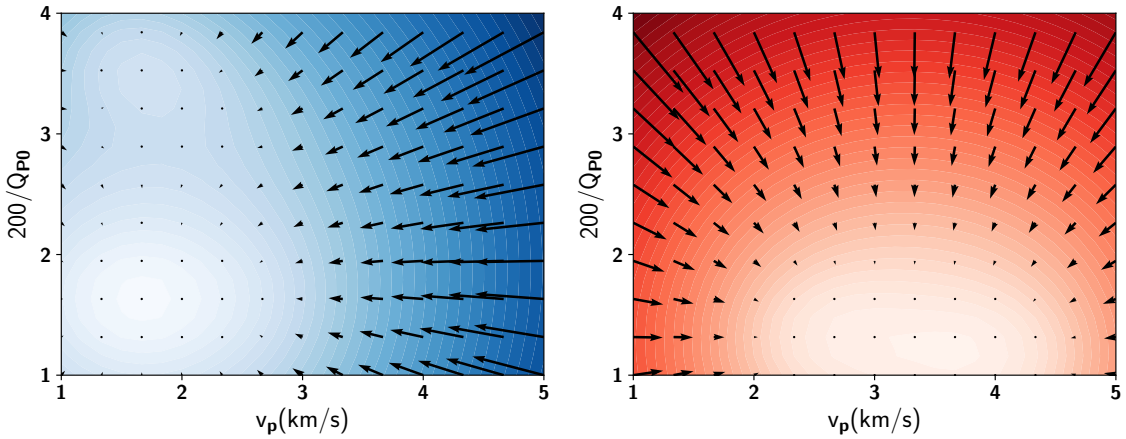

(a) (b)

Figure 5.13: BP 2004 Benchmark model: The distances (a) $D_1(\mathbf{m})$ and (b) $D_2(\mathbf{m})$, and their gradients. The high probability models are associated with small values of $D_i(\mathbf{m})$ and with zero gradients.

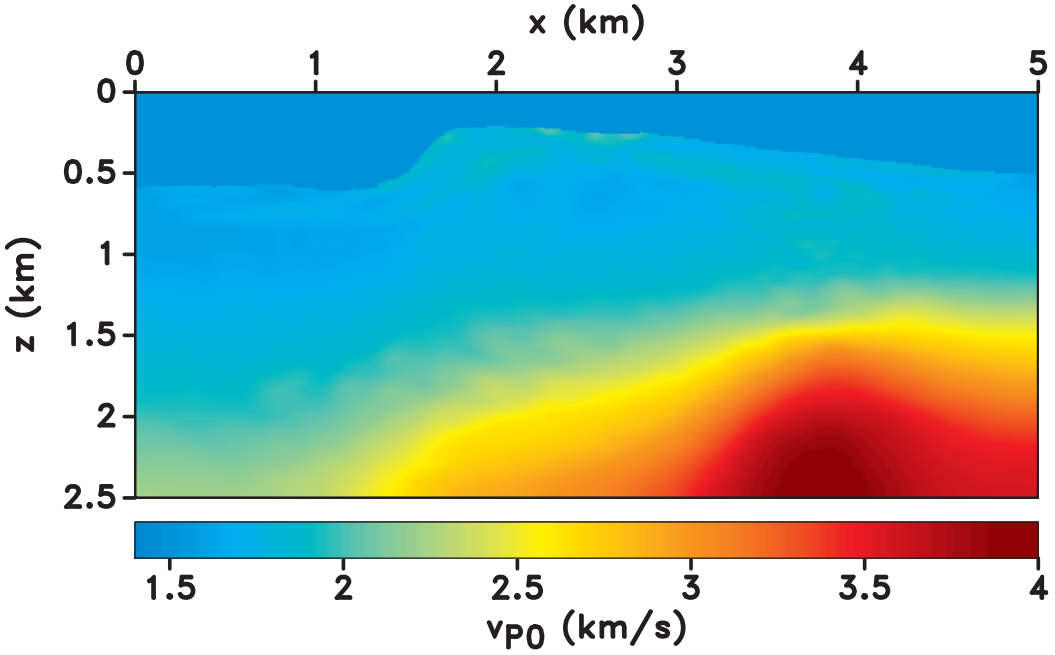

(a)

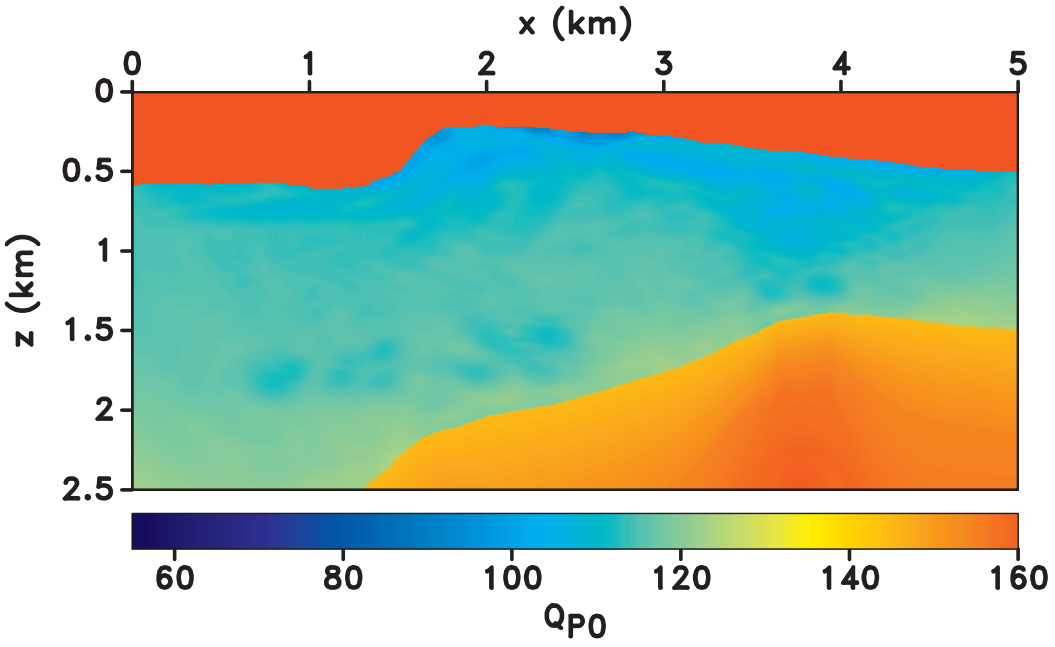

(b)

Figure 5.14: BP 2004 Benchmark model: Recovered (a) v_{P0} and (b) Q_{P0} models obtained using the objective function $\mathcal{J}_D$. The inversion is not able to recover the low velocity anomalies and the models are contaminated with artifacts due to the interparameter cross-talk between velocity and attenuation parameters.

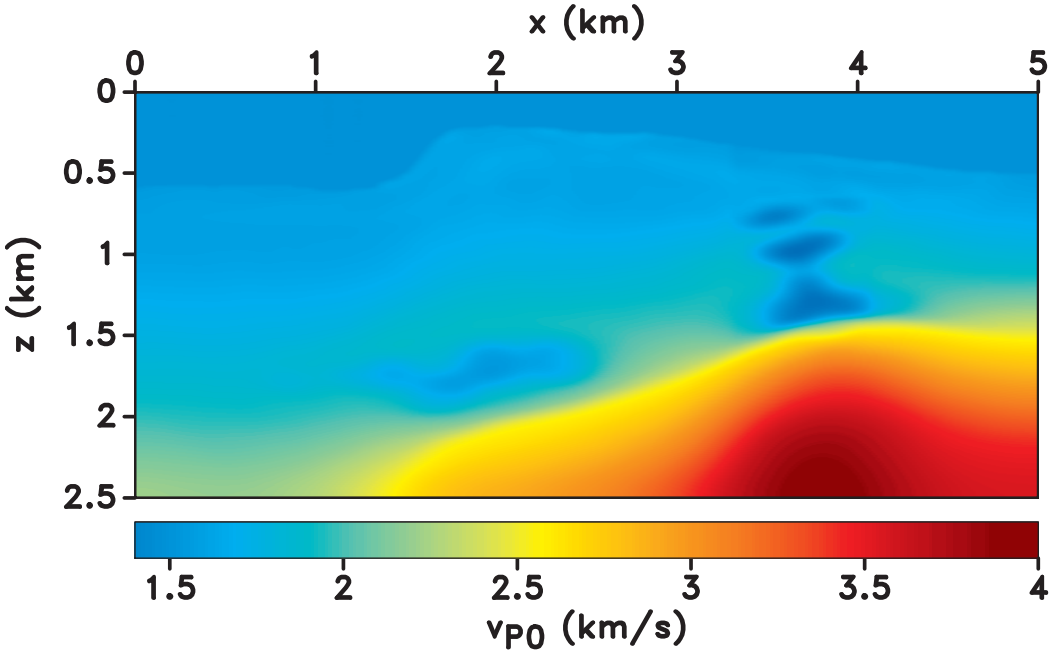

(a)

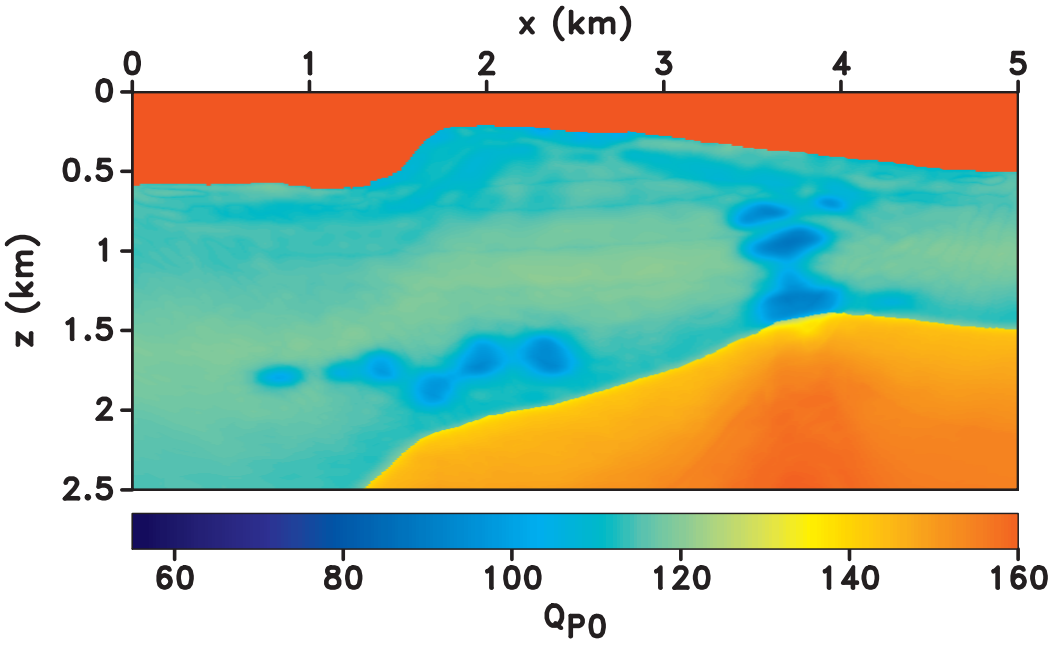

(b)

Figure 5.15: BP 2004 Benchmark model: Recovered (a) v_{P0} and (b) Q_{P0} models obtained using the objective function $\mathcal{J}_D + \mathcal{J}_P$, where $\mathcal{J}_P$ is based on multiple PDFs, which are determined considering spatial trends in the available petrophysical data. With petrophysical penalties, the inversion is able to recover the low velocity anomalies in both models.

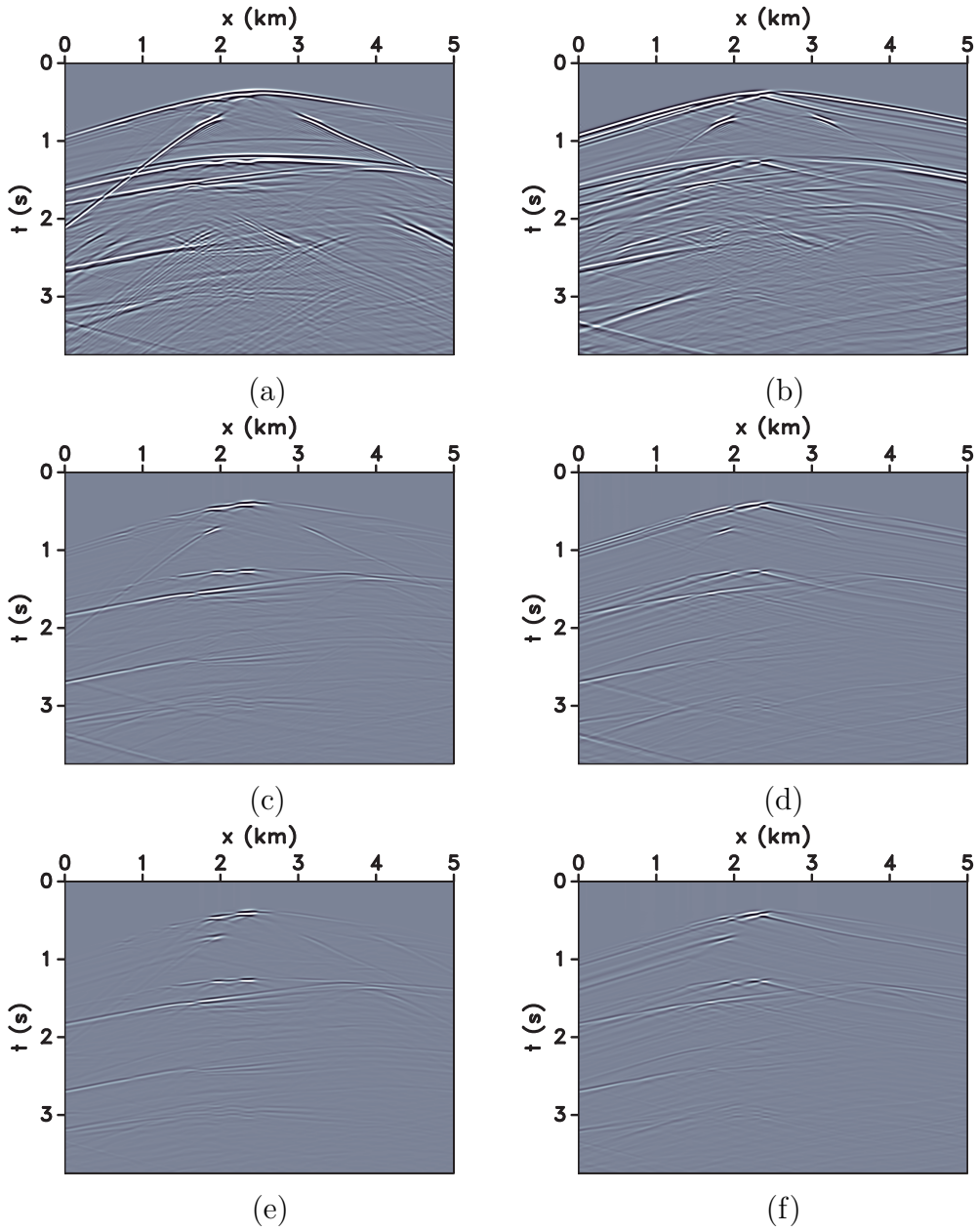

Figure 5.16: BP 2004 Benchmark model: (a) vertical and (b) horizontal components of the data residual using the initial models (Figure 5.10) for the central shot; (c) vertical and (d) horizontal components of the data residual, where the predicted data is simulated using the models recovered with unconstrained inversion (Figure 5.14) for the central shot; (e) vertical and (f) horizontal components of the data residual, where the predicted data is simulated using the models recovered with constrained inversion (Figure 5.15) for the central shot.

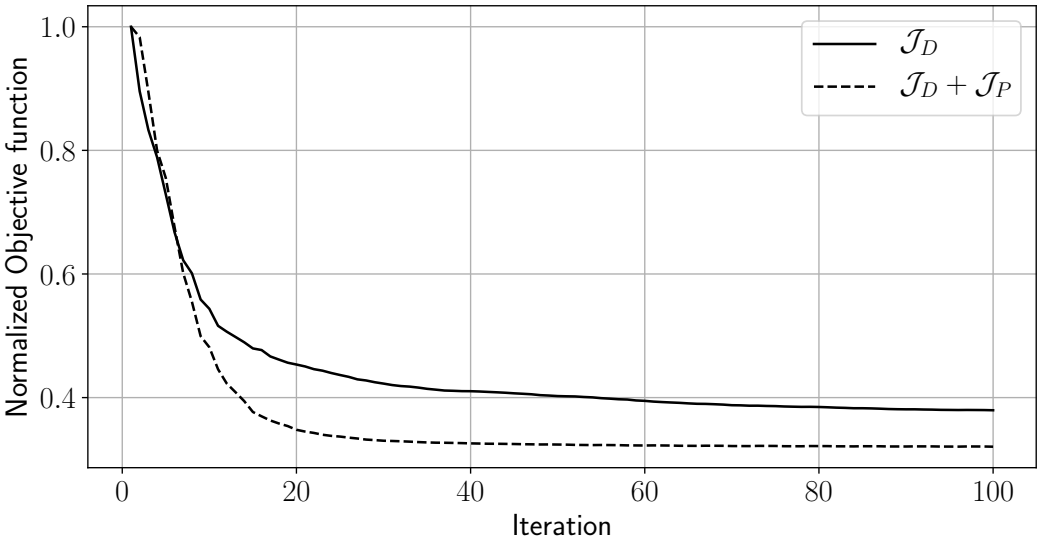

Figure 5.17: BP 2004 Benchmark model: normalized objective functions for unconstrained (solid line) and constrained (dashed line) QEFWI. Note how constrained inversion performs better than the unconstrained in terms of both convergence speed and misfit reduction.

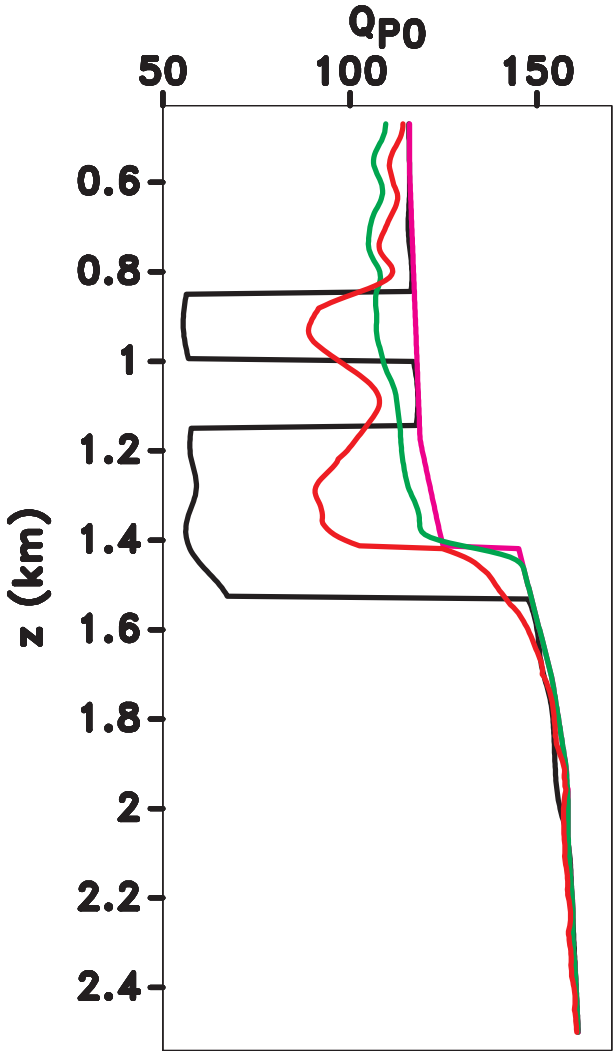

Figure 5.18: BP 2004 Benchmark model: Comparison between Q_{P0} models: true (black line), initial (pink), and updated models using for the unconstrained (green) and constrained (red) inversion for a vertical profile at $x = 3.75$ km.

CHAPTER 6

EXPLICIT CONTROL OF NUMERICAL DISPERSION AND INSTABILITY IN WAVEFIELD MODELING AND INVERSION

Full waveform inversion (FWI) is a nonlinear inverse problem that refines an initial model by iteratively matching the recorded with the modeled data. The success of FWI relies on accurate and efficient wavefield modeling. The finite-difference method (FDM) is one of the most popular techniques used for this purpose because of its easy implementation and small memory requirement. However, depending on the spatial and temporal discretization, FDM may encounter numerical dispersion and instabilities, which degrade the quality of the simulated wavefields. The conventional FWI objective function, formulated based on data misfit, may lead to situations where the updated models violate conditions that are necessary to guarantee modeling stability. We propose to address this problem by explicitly incorporating a stability constraint into the inversion through a penalty term based on a probability density functions (PDF) that represents the range of velocities in which numerical dispersion and instabilities do not occur. This penalty term prevents updated models from entering into a petrophysical configuration that leads to dispersion and instability for specific choices of sampling parameters. Through elastic synthetic examples, we demonstrate the benefits of including this stability constraint into the FWI framework, as it ensures the efficiency of the FDM engine, while at the same time increasing the quality of the recovered models.

6.1 Introduction

Full waveform inversion (FWI) is one of the most promising technique among all wavefield tomography methods, as it uses most of the information provided by seismic data to deliver high resolution models of subsurface properties. The inverse problem is constrained by a wave

equation and it is solved by iteratively minimizing an objective function, which computes the misfit between observed and modeled data (Tarantola, 1984; Virieux and Operto, 2009).

The computational cost of methods based on a wave equation is dominated by the numerical wavefield extrapolation, i.e., simulating the propagation of seismic waves through earth models. Additionally, the accuracy and efficiency of the FWI engine relies on the quality of wavefield modeling. In order to calculate both spatial and time derivatives needed for numerical solutions to a wave equation, one may use the finite-difference method (FDM), which replaces derivatives with finite-difference approximations of limited accuracy. FDM is preferred over other numerical methods for wave equation simulation because of its simple implementation and reduced computational cost (Dablain, 1986; Kelly et al., 1976; Moczo et al., 2004; Virieux, 1986).

The accuracy of FDM depends on spatial and temporal discretization. On the one hand, a fine spatial grid increases the precision of computed derivatives while significantly increasing the computational cost. On the other hand, coarse grids reduce the modeling costs but introduce numerical errors in the simulations, causing phase distortions in the modeled wavefield. Additionally, large time steps may cause instabilities of the wavefield extrapolation (Courant et al., 1967), thus hampering FWI. Therefore, it is important to determine appropriate grid sizes in order to avoid numerical distortions and instabilities and increase the computational efficiency, while assuring that the modeling is accurate (Alford et al., 1974; Boore, 1972; Courant et al., 1967; Dablain, 1986; Wu et al., 1996).

Courant et al. (1967) propose the CFL condition, which defines an upper time step limit for stable finite-difference solutions of partial differential equations. If this condition is violated, large errors are produced during the simulation. The CFL condition is directly related to the spatial grid size and to the maximum velocity of the medium. Dablain (1986) shows that numerical dispersion can be avoided by sampling with enough number of grid points per minimum wavelength, i.e., the computation grid depends on the minimum velocity of the medium and on the maximum frequency. Therefore, the space and time discretization

cannot be arbitrarily chosen as they depend on the medium properties.

During FWI, the gradient of the objective function purely based on the misfit between observed and predicted data may lead to model updates that violate the CFL condition or cause undesirable dispersion, which results in inaccurate models. Therefore, one needs to ensure that the inversion does not produce models with a velocity larger than the one used to establish the CLF condition, or smaller than the one used to determine the spatial grid.

A broadly used way to ensure that inversion updates do not violate the CFL condition is to enforce an upper and a lower limit that truncates artificially for the inverted parameters. With this strategy, all model updates smaller or larger than the clip values are set to the constant lower or upper bounds, respectively, thus leading to unfeasible model parameter distributions. This strategy may also not be suitable for multiparameter full-waveform inversion, where multiple physical properties are inverted for simultaneously. As each parameter has its own upper and lower limits, if one of the parameters is clipped while the others are not, the recovered model parameters can become unphysical or lithologically implausible.

We propose to avoid numerical instabilities during multiparameter inversion by explicitly incorporating a stability constraint into the FWI objective function, based on a probability density function (PDF), defining the range of parameters for which the wavefield simulations remain stable. This technique ensure that the simultaneous update of multiple parameters produce physical and plausible combinations of the recovered model parameters. We use the formulation proposed by Aragao and Sava (2020a,b) in order to recover models that do not violate the CFL condition or create numerical dispersion. The performance of the proposed methodology is illustrated with synthetic elastic examples.

6.2 Method

We consider the isotropic elastic wave equation

$$\ddot{\mathbf{u}} - V_P^2 \left[\nabla(\nabla \cdot \mathbf{u})\right] + V_S^2 \left[\nabla \times (\nabla \times \mathbf{u})\right] = \mathbf{f}, \tag{6.1}$$

where $\mathbf{u}(e, \mathbf{x}, t)$ is the elastic wavefield, $\mathbf{f}(e, \mathbf{x}, t)$ is the source function, and e, $\mathbf{x}$ and t are, respectively, the experiment index, space coordinates and time. The model parameters, V_P and V_S, are P- and S-waves velocities, respectively.

We solve the full-waveform inversion problem by minimizing an objective function $\mathcal{J}(\mathbf{u}, V_P, V_S)$ consisting of a term that estimates the misfit between the predicted and observed data $\mathcal{J}_D(\mathbf{u}, V_P, V_S)$ using the L-2 norm, and a stability penalty $\mathcal{J}_S(V_P, V_S)$ that prevents numerical instabilities and grid dispersion during the FWI process:

$$\mathcal{J}(\mathbf{u}, V_P, V_S) = \mathcal{J}_D(\mathbf{u}, V_P, V_S) + \mathcal{J}_S(V_P, V_S). \tag{6.2}$$

During the numerical modeling, the phase velocity becomes a function of the spatial grid and the phase velocity may be different than the true velocity when using an insufficient number of grid points per wavelength, affecting the high-frequency content of the data and, consequently, creating numerical dispersion (Alford et al., 1974; Boore, 1972). For implementing fourth-order finite difference methods, if the grid size in any dimension is coarser than a quarter of the minimum wavelength, numerical grid dispersion may occur, leading to wavefield extrapolation instability. Therefore, the efficiency of the wavefield modeling can be quantified by the relationship (Dablain, 1986):

$$\Delta x \leq \frac{\lambda_{min}}{4} = \frac{V_{min}}{4 f_{max}}, \tag{6.3}$$

where Δx represents the spatial grid in any direction, λ_{min} and V_{min} correspond, respectively to the minimum wavelength and the minimum velocity, and f_{max} is the maximum frequency.

Additionally, numerical instabilities may occur when one uses a propagation timestep that does not respect the CFL condition (Courant et al., 1967), which is given by

$$\Delta t \leq \mathcal{C} \frac{\Delta x}{V_{max}}, \tag{6.4}$$

where Δt represents the time step, $\mathcal{C}$ is the Courant number and V_{max} corresponds to the maximum velocity. The CFL condition is a necessary condition for avoiding dispersion when numerically solving partial differential equations.

Furthermore, for multiparameter inversion that uses only the data misfit, model parameter updates may produce unphysical models (e.g., negative velocities), which also lead to instabilities in wavefield extrapolation. In order to purposefully prevent numerical instabilities and numerical dispersion, we design a stability penalty $\mathcal{J}_S$ in the elastic FWI (EFWI) objective function. We adapt the formulation of the probabilistic petrophysical constraint proposed by Aragao and Sava (2020a,b), which is not calculated in the physical space domain, but in the space formed by the model parameters. We define a probability density function (PDF) that represents the range of model parameters for which wavefield simulations remain stable. The PDF is represented by coordinates $\mathbf{p}$ and probability density $b(\mathbf{p})$, such that $b = 0$ for combinations of parameters that cause wavefield simulation instability. Representing the elastic model components by the vector $\mathbf{m}(\mathbf{x}) = \{V_P(\mathbf{x}), V_S(\mathbf{x})\}$, we define the stability penalty as

$$\mathcal{J}_S = a \sum_{\mathbf{m}} D(\mathbf{m}), \tag{6.5}$$

such that the scalar parameter a determines the relative strength of the stability term in the objective function and $D(\mathbf{m})$ represents the distance from a particular combination of model parameters $\mathbf{m}$ to the entire distribution and it is given by

$$\frac{1}{D(\mathbf{m})} = \sum_{\mathbf{p}} \frac{b(\mathbf{p})}{\|\mathbf{m} - \mathbf{p}\|_2}. \tag{6.6}$$

The gradients of $\mathcal{J}_S$ with respect to the model parameters V_P and V_S are, respectively,

$$\frac{\partial \mathcal{J}_S}{\partial V_P} = a\, D^2(\mathbf{m}) \sum_{\mathbf{p}} \frac{b(\mathbf{p})\,(V_P - V_{Pp})}{(\,\|\mathbf{m} - \mathbf{p}\|_2\,)^3}, \tag{6.7}$$

and

$$\frac{\partial \mathcal{J}_S}{\partial V_S} = a\, D^2(\mathbf{m}) \sum_{\mathbf{p}} \frac{b(\mathbf{p})\,(V_S - V_{Sp})}{(\,\|\mathbf{m} - \mathbf{p}\|_2\,)^3}. \tag{6.8}$$

The value of $\mathcal{J}_S$ is determined by the distance to high probabilities in the model parameter space, i.e., by the distance to the combinations of V_P and V_S such that the wavefield extrapolation is stable. Therefore, outside the stability region defined by the PDF, the gradient of

$\mathcal{J}_S$ explicitly forces the models towards the stable region. For points $\mathbf{m}(\mathbf{x}) = \{V_P(\mathbf{x}), V_S(\mathbf{x})\}$ inside the stability region, the data misfit $\mathcal{J}_D$ fully controls the total gradient (Aragao and Sava, 2020a).

6.3 Examples

We illustrate our EFWI method with two synthetic examples and compare inversions using just the data misfit term $\mathcal{J}_D$ with inversion that also use stability constraints $\mathcal{J}_S$.

6.3.1 Gaussian Anomalies

The synthetic models depicted in Figure 6.1 contain two positive Gaussian anomalies centered at $(1.2, 0.75)$ and $(1.2, 1.75)$ km. There are 40 vertical displacement sources in a well at $x = 0.05$ km and a line of geophones at $x = 2.35$ km. For this experiment, we use the following parameters: $f_{max} = 15\,\text{Hz}$; $\lambda_{min} \approx 33.3\,\text{m}$; and the minimum velocity for the S-wave and maximum velocity for the P-wave are, respectively, $V_{Smin} = 500\,\text{m/s}$ and $V_{Pmax} = 2000\,\text{m/s}$. Therefore, the maximum spatial grid is 8 m and, for $\mathcal{C} = 0.5$, the time step needs to be smaller than 0.0023 s.

For $\Delta x = 8\,\text{m}$ and $\Delta t = 0.002\,\text{s}$, the inversion is stable when velocities are in the range [480, 2000] m/s, which conforms to the true models (Figure 6.1). Inverted velocities outside this range produce wrong models and also cause wavefield simulation instabilities. Therefore, this example illustrates how we can avoid numerical dispersion and also prevent the inversion to generate wrong models by using the stability penalty, which constrains the range of updated velocities.

We start the inversion with a model with constant $V_P = 1500\,\text{m/s}$ and $V_S = 500\,m/s$. Considering the range of velocities for which the wavefield simulations are stable, the inversion becomes unstable when we have V_S updates below $-20\,\text{m/s}$ or when V_P updates above 500 m/s. Therefore, we define a PDF for calculating the stability penalty consisting of the distribution shown in Figure 6.2a. Note that the probability density is zero for velocities that produce wave propagation instability. Figure 6.2b displays the distance $D(\mathbf{m})$ and the

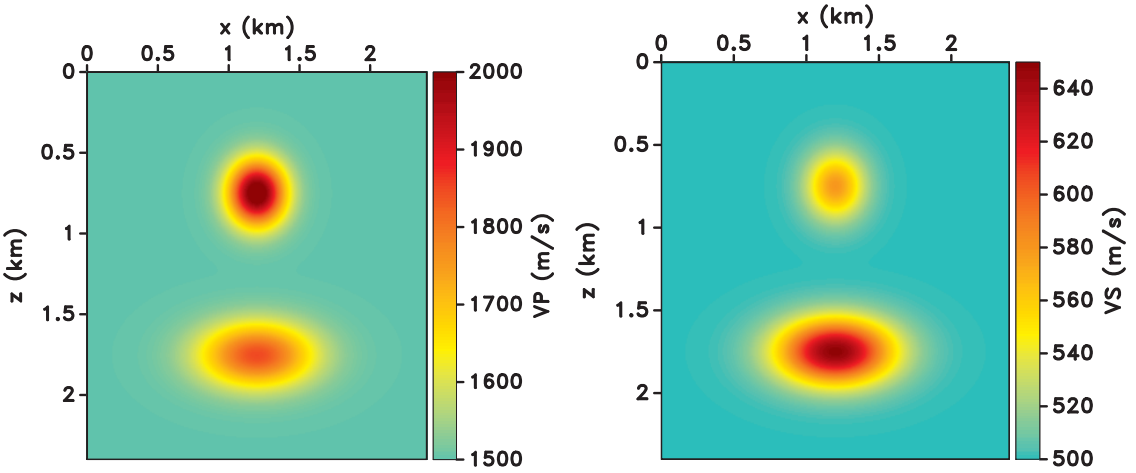

(a) (b)

Figure 6.1: Synthetic models with two positive Gaussian anomalies for the (a) V_P and (b) V_S models centered at $(1.2, 0.75)$ km and $(1.2, 1.75)$ km.

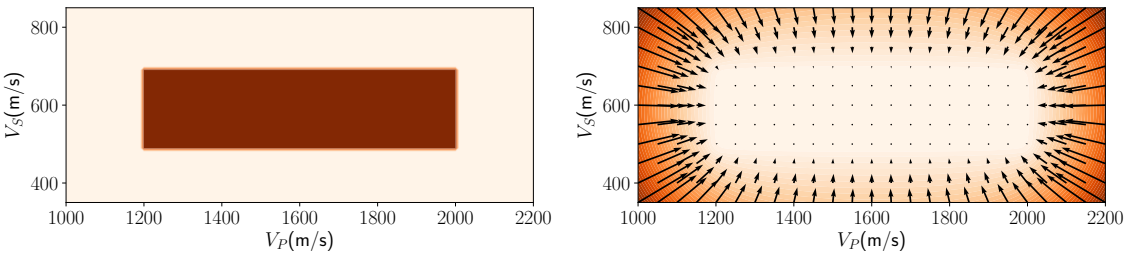

(a) (b)

Figure 6.2: (a) Example of a PDF consisting of boxcar function representing the range of velocities in which the forward simulations remain stable. (b) The distance $D(\mathbf{m})$ and its gradient. Models inside the boxcar function are subjected to zero gradients from the stability constraint, and thus inversion in this region is driven solely by the data misfit.

gradient of $D(\mathbf{m})$, which are both zero in the region of stability. If the inverted velocities are inside the range defined by the PDF (Figure 6.2a), the data misfit $\mathcal{J}_D$ fully controls the inversion gradient as the gradients of $\mathcal{J}_S$ are zero. Otherwise, the stability constraint produces a gradient that drives the updated models to the region of stability defined by the PDF.

Without the stability constraint, we observe numerical dispersion in the inversion after few iterations. The inversion updates in Figure 6.3 show that, without imposing stability constraints, the V_S model has updates smaller than $-20\,\mathrm{m/s}$, producing velocities that are smaller than $480\,\mathrm{m/s}$, thus creating wavefield extrapolation instability. Additionally, the inversion that uses just the data misfit produces negative anomalies (Figure 6.3) at the locations of the positive anomalies of the true models (Figure 6.1). Therefore, inversion based only in $\mathcal{J}_D$ produces wrong velocity models in addition to numerical dispersion.

When we include the stability constraints into the inversion objective function, inversion proceeds without any instability. The recovered models after 50 iterations are shown in Figure 6.4. Although the inverted models have artifacts related to the interparameter crosstalk between the elastic parameters and to the limited acquisition aperture, both anomalies have amplitude and shape closer to the true models (Figure 6.1). The inversion updates (Figure 6.5) demonstrate that the stability constraint secures the FWI stability and efficiency.

6.3.2 Marmousi model

The second synthetic example uses a portion of the Marmousi 2 model (Martin et al., 2002). Figure 6.6 shows the correct V_P and V_S models. We simulate a multicomponent ocean bottom seismic survey (OBS) with a line of receiver at the water bottom ($z = 0.2\,\mathrm{km}$) and 100 evenly spaced pressure sources located at $z = 0.05\,\mathrm{km}$. Figure 6.7 shows the initial V_P and V_S models.

Without the stability penalty, the inversion becomes unstable after 3 iterations. The updated models are in Figure 6.8, showing that V_S has negative values, which prevent further updates. Then, conventional inversion is not able to produce long-wavelength updates which

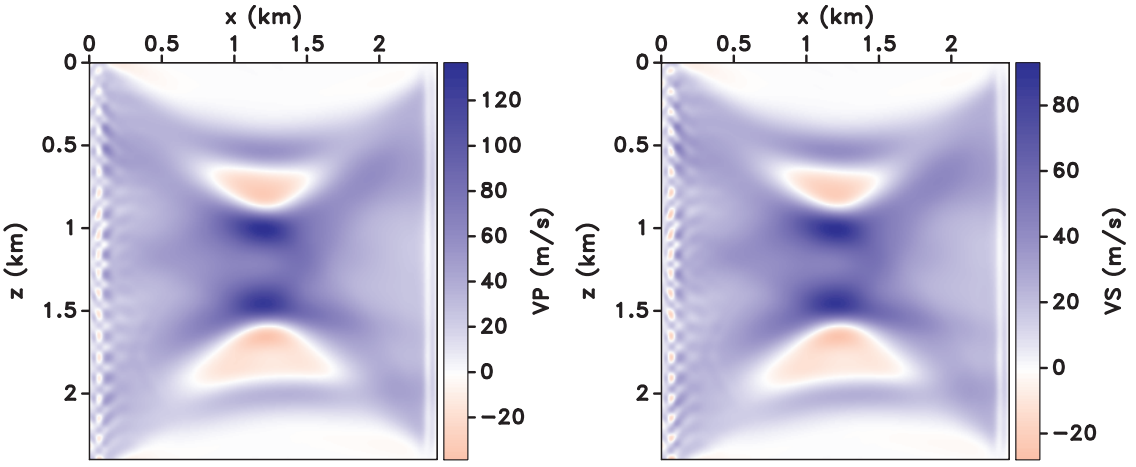

(a) (b)

Figure 6.3: Inversion updates for the (a) V_P and (b) V_S models using the objective function $\mathcal{J}_D$ after 5 iterations. The V_S updates below $-20\,\mathrm{m/s}$ cause inversion instabilities.

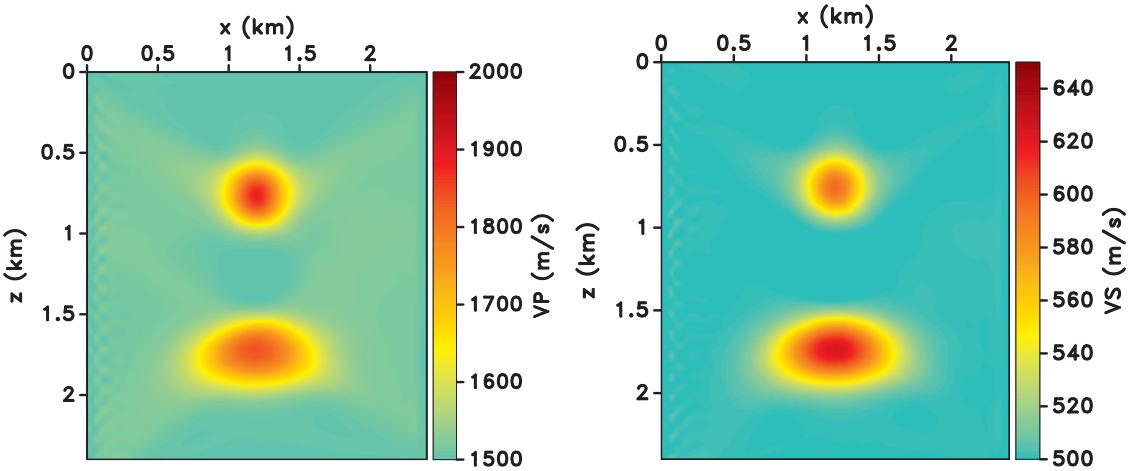

(a) (b)

Figure 6.4: Recovered (a) V_P and (b) V_S models using the objective function $\mathcal{J}_D + \mathcal{J}_S$ after 50 iterations.

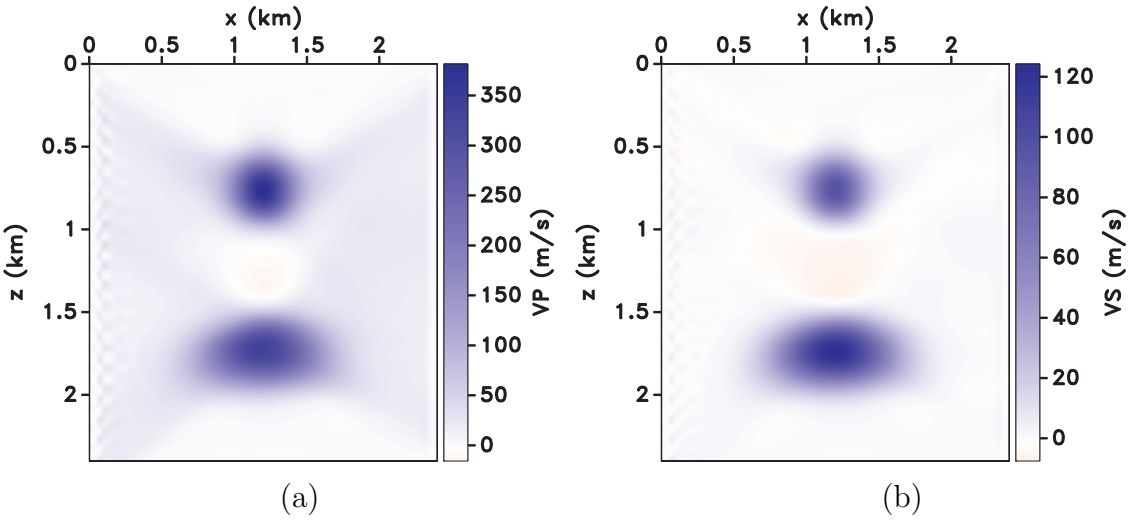

Figure 6.5: Inversion updates for the (a) V_P and (b) V_S models using the objective function $\mathcal{J}_D + \mathcal{J}_S$ after 50 iterations. Note that the inversion does not produce any updates below $-20\,\mathrm{m/s}$ for the V_S model, thus avoiding modeling instability.

deteriorates the quality of the recovered models.

The stability penalty eliminates this problem. The recovered models after 50 iterations are shown in Figure 6.9. Even though the recovered V_P and V_S models are contaminated with high-wavenumber artifacts in addition to the artifacts due to the inherent interparameter cross-talk of EFWI, the inversion delivers long-wavelength updates and produces high resolution models. In order to further enhance the quality of the inverted models, one can also include petrophysical constraints or a regularization term in the objective function (Aragao and Sava, 2020a,b).

6.4 Conclusions

We develop a strategy for incorporating a stability constraint into elastic full waveform inversion (EFWI) through a penalty term based on a probability density function (PDF) that defines the range of velocities for which wave propagation is stable. When the updated models are inside the stability region defined by the PDF, the inversion is fully controlled by the misfit between the observed and predicted data. We demonstrate that imposing this penalty avoids numerical dispersion and instabilities during the wavefield simulations and

helps guide the inverted models towards an accurate solution. Through synthetic examples, we verify the effectiveness of the proposed methodology in leading inversion towards the true models, while preventing updates that hamper the accuracy and stability of the finite difference method.

6.5 Acknowledgments

We acknowledge CAPES (Brazilian Federal Agency for Support and Evaluation of Graduate Education) for financial support. We thank the sponsors of the Center for Wave Phenomena (CWP) for additional support of this research. The synthetic examples in this paper use the Madagascar open-source software package (Fomel et al., 2013) freely available from http://www.ahay.org.

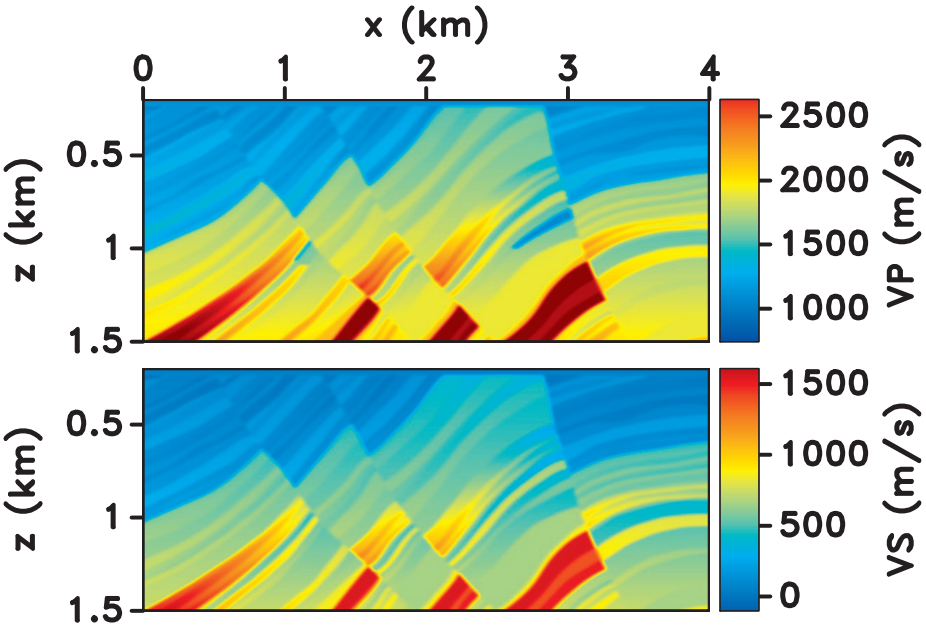

Figure 6.6: Marmousi 2 model: true V_P and V_S models.

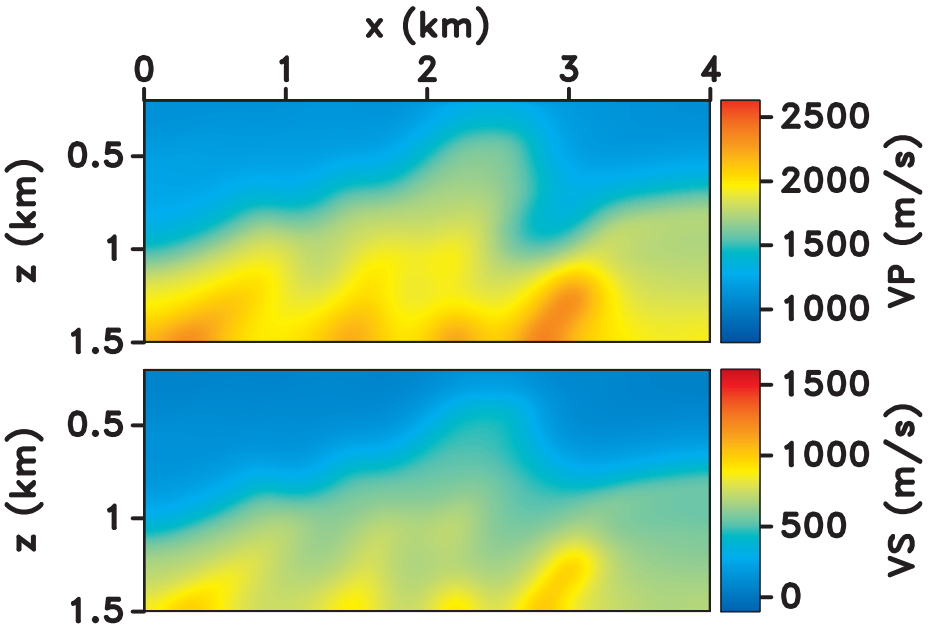

Figure 6.7: Marmousi 2 model: initial V_P and V_S models, obtained by smoothing the true models (Figure 6.6).

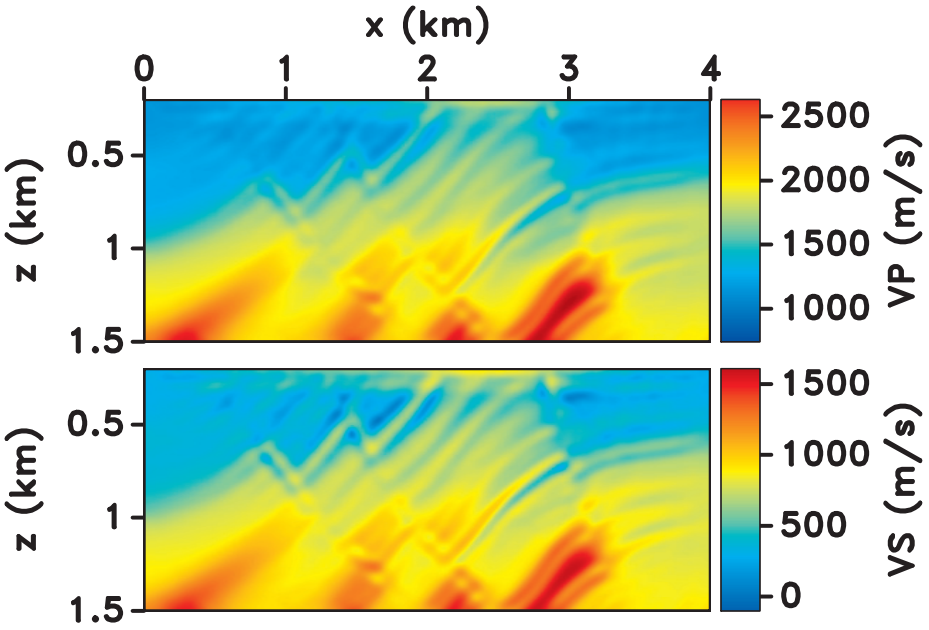

Figure 6.8: Marmousi 2 model: recovered V_P and V_S models using objective function $\mathcal{J}_D$. The inverted V_S model has negative values, which cause wavefield simulation instability.

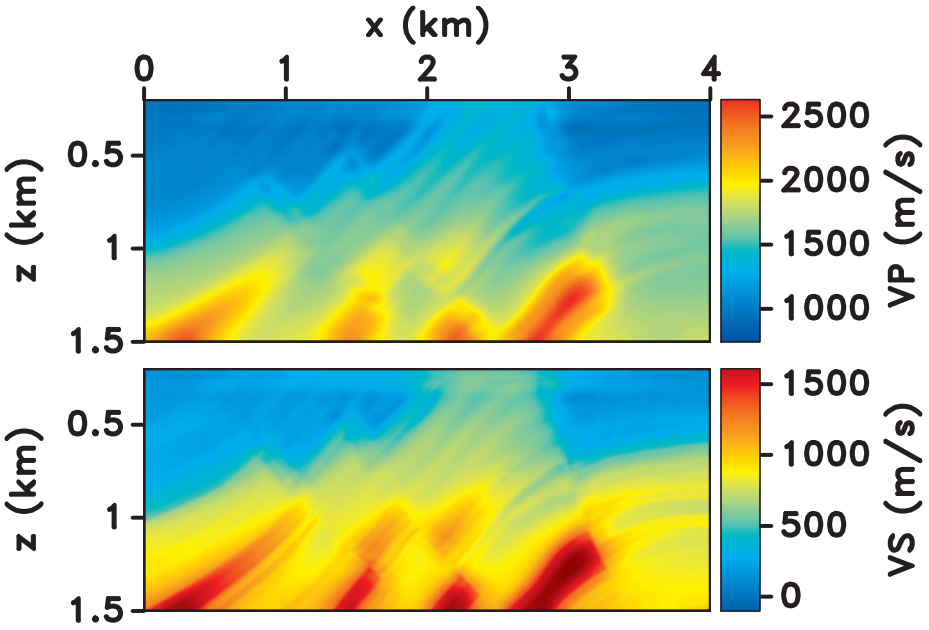

Figure 6.9: Marmousi 2 model: recovered V_P and V_S models using the objective function $\mathcal{J}_D + \mathcal{J}_S$. The stability penalty prevents negative V_S velocities, thus guaranteeing modeling stability.

CHAPTER 7

CONCLUSION

In this thesis, I propose a strategy to incorporate petrophysical information into multiparameter full-waveform inversion (FWI) using a penalty term based on a probabilistic approach that uses probability density functions (PDFs). I present the general idea of the penalty term based on a single PDF and discuss its impact in elastic isotropic FWI (Chapter 2). I also present a way of building the penalty term using multiple PDFs, each representing a different lithological unit (Chapter 3). Similarly, I test the method using elastic anisotropic media, where seek to overcome the challenge of accurately inverting four physical subsurface model parameters simultaneously (Chapter 4).

The technology proposed in Chapters 2, 3 and 4 do not consider spatial trends in the petrophysical information or uncertainty in the calculation of the penalty term related to the distance from certain areas of the models to the wells. To overcome these limitations, I generalize the formulation of the penalty term and prove its efficiency on the difficult task of inverting accurate velocity and attenuation parameters simultaneously through viscoelastic FWI (QEFWI). This technology is directly applicable to monitoring carbon dioxide geological sequestration, as well as to monitoring hydrocarbon production of multi-layer reservoirs.

The success of the FWI described in Chapters 2, 3, 4 and 5 relies on accurate wavefield extrapolation. During the inversion process, inefficiently constrained model parameter updates can cause dispersion or instability in wavefield modeling implemented by the finite-different method (FDM). In Chapter 6, I propose a way of adapting the petrophysical term to function as a stability penalty term. I demonstrate that the stability penalty term ensures the robustness of the FWI engine by preventing updates that hamper modeling accuracy and stability.

As the technique proposed here strongly depends on petrophysical information, it is important to ensure that this prior information is reliable and accurate. For instance, when using well log data to form the petrophysical probability density function, one should account for the presence of washouts and mudcakes in the borehole, which can substantially deteriorate the quality of the acquired petrophysical data, and thus guide full-waveform inversion to models inconsistent with the subsurface.

My thesis demonstrates the effectiveness of the probabilistic penalty term with various complex synthetic models. For future work, it is important to validate this method using field data, particularly for exploration fields with available petrophysical data from well logs or from core analysis. The methodology proposed here has the potential to be applicable to other geophysical fields, e.g. non-seismic inversion of multiple parameters, since one can formulate the petrophysical penalty term for any combination of physical parameters supporting geophysical inversion. For instance, this technique can be used for joint inversion of seismic and gravity data, which aims to estimate velocity and density simultaneously for independent, and possibly limited, seismic and gravity measurements. If sonic and density well logs are available, one could build a petrophysical PDF representing these parameters and use it to constrain the multiparameter inverted models to a predefined petrophysical region that simultaneously satisfies both measurements, as well as the prior geological knowledge in the area.

Multiparameter full-waveform inversion augmented with petrophysical information based on the framework I propose in this thesis would increase the feasibility of seismic imaging in complex environments and would allow comprehensive and accurate seismic interpretation and, consequently, better characterization of subsurface reservoirs. Superior and higher-resolution imaging and interpretation would not only increase reservoir productivity, but would also mitigate the environmental impact of oil and gas production, with broad societal consequences.

REFERENCES CITED

Alford, R. M., K. R. Kelly, and D. M. Boore, 1974, Accuracy of finite-difference modeling of the acoustic wave equation: Geophysics, **39**, 834–842.

Alkhalifah, T., and Y. Choi, 2014, From tomography to fwi with a single objective function: Geophysics, **79**, no. 2, R55–R61.

Aragao, O., and P. Sava, 2019, Elastic full waveform inversion probabilistic petrophysical model constraints: 89th Annual International Meeting, SEG, Expanded Abstracts, 1425–1429.

———, 2020a, Elastic full-waveform inversion probabilistic petrophysical model constraints: Geophysics, **85**, no. 2, R101–R111.

———, 2020b, Elastic full waveform inversion with probabilistic petrophysical clustering: Geophysical Prospecting, **68**, no. 4, 1341 – 1355.

———, 2020c, Elastic full-waveform inversion with spatial probabilistic petrophysical constraints: SEG International Exposition and 90th Annual Meeting, Expanded Abstracts, 730–734.

Asnaashari, A., R. Brossier, S. Garambois, F. Audebert, P. Thore, and J. Virieux, 2013, Regularized seismic full waveform inversion with prior model information: Geophysics, **78**, R25–R36.

Avseth, P., T. Mukerji, and G. Mavko, 2010, Quantitative seismic interpretation: applying rock physics tools to reduce interpretation risk: Cambridge University Press.

Bai, J., and D. Yingst, 2013, Q estimation through waveform inversion: Presented at the 75th European Association of Geoscientists and Engineers Conference and Exhibition, EAGE, Extended Abstracts.

Bai, J., D. Yingst, R. Bloor, and J. Leveille, 2014, Viscoacoustic waveform inversion of velocity structures in the time domain: Geophysics, **79**, no. 3, R103–R119.

Bai, T., and I. Tsvankin, 2016, Time-domain finite-difference modeling for attenuative anisotropic media: Geophysics, **81**, no. 2, C69–C77.

Bai, T., I. Tsvankin, and X. Wu, 2017, Waveform inversion for attenuation estimation in anisotropic media: Geophysics, **82**, no. 4, WA83–WA93.

Bath, M., 1974, Spectral analysis in geophysics: Developments in solid earth geophysics: Elsevier Science Publishing Co.

Baumstein, A., 2013, POCS-based geophysical constraints in multiparameter full wavefield inversion: Presented at the 75th Annual International Conference and Exhibition, EAGE, Extended Abstracts.

Behura, J., and I. Tsvankin, 2009, Estimation of interval anisotropic attenuation from reflection data: Geophysics, **74**, no. 6, A69–A74.

Billette, F., and S. Brandsberg-Dahl, 2005, The 2004 BP velocity benchmark, *in* 67th Annual Internat. Mtg., EAGE, Expanded Abstracts: EAGE, B035.

Biondi, B., 2002, Stable wide-angle Fourier finite-difference downward extrapolation for 3-D wavefields: Geophysics, **67**, no. 3, 872–882.

———, 2006, 3D seismic imaging: Society of Exploration Geophysics.

Bishop, T. N., K. P. Bube, R. T. Cutler, R. T. Langan, P. L. Love, J. R. Resnick, R. T. Shuey, D. A. Spindler, and H. W. Wyld, 1985, Tomographic determination of velocity and depth in laterrly varying media: Geophysics, **50**, no. 6, 903–923.

Boore, D. M., 1972, Finite Difference Methods for Seismic Wave Propagation in Heterogeneous Materials: Methods in Computational Physics: Advances in Research and Applications, **11**, 1–37.

Brossier, R., 2011, Two-dimensional frequency-domain visco-elastic full waveform inversion: Parallel algorithms, optimization and performance: Computer and Geosciences, **37**, 444–445.

Carcione, J. M., D. Kosloff, and R. Kosloff, 1988a, Viscoacoustic wave propagation simulation in the earth: Geophysics, **53**, 769–777.

———, 1988b, Wave propagation simulation in a linear viscoacoustic medium: Geophysical Journal International, **93**, 393–407.

Causse, E., and B. Ursin, 2000, Viscoacoustic reverse-time migration: Journal of Seismic Exploration, **9**, 165–184.

Cheng, C. H., M. N. Toksoz, and M. E. Wills, 1982, Determination of in situ attenuation from full waveform acoustic logs: J. Geophys. Res., **87**, 5477–5484.

Cheng, X., K. Jiao, D. Sun, and D. Vigh, 2015, A new approach of viscoacoustic waveform inversion in the time domain: SEG International Exposition and 85th Annual Meeting, Expanded Abstracts, 1183–1187.

Courant, R., K. Friedrichs, and H. Lewis, 1967, On the partial difference equations of mathematical physics: IBM Journal of Research and Development, **11**, 215–234.

Dablain, M. A., 1986, The application of high-order differencing to the scalar wave equation: Geophysics, **51**, no. 1, 54–66.

Dai, N., and G. F. West, 1994, Inverse Q migration: SEG International Exposition and 64th Annual Meeting, Expanded Abstracts, 1418–1421.

de Castro Nunes, B. I., W. E. D. Medeiros, A. F. do Nascimento, and J. A. de Morais Moreira, 2011, Estimating quality factor from surface seismic data: A comparison of current approaches: Journal of Applied Geophysics, **75**, 161–170.

Diaz, E., and P. Sava, 2017, Cascaded wavefield tomography and inversion using extended common-image-point gathers: A case study: Geophysics, **82**, no. 5, S391–S401.

Djebbi, R., and T. Alkhalifah, 2018, Frequency domain multi-parameter acoustic inversion for transversely isotropic media with a vertical axis of symmetry: Geophysics, **84**, no. 1, C1–C14.

Duan, Y., and P. Sava, 2016, Elastic wavefield tomography with physical model constraints: Geophysics, **81**, no. 6, R447–R456.

Fabien-Ouellet, G., E. Gloaguen, and B. Giroux, 2017, Time domain viscoelastic full waveform inversion: Geophysical Journal International, **209**, 1718–1734.

Fichtner, A., and M. van Driel, 2014, Models and Fréchet kernels for frequency-(in)dependent Q: Geophysical Journal International, **198**, 1878–1889.

Fomel, S., P. Sava, I. Vlad, Y. Liu, and V. Bashkardin, 2013, Madagascar: open-source software project for multidimensional data analysis and reproducible computational experiments: Journal of Open Research Software, 8th ed., DOI: http://dx.doi.org/10.5334/jors.ag, **1**.

Guitton, A., 2012, Blocky regularization schemes for full-waveform inversion: Geophysical Prospecting, **60**, 870–884.

Guo, P., G. A. McMechan, and H. Guan, 2016, Comparison of two viscoacoustic propagators for Q-compensated reverse time migration: Geophysics, **81**, no. 5, S281–S297.

Hackert, C. L., and J. O. Parra, 2004, Improving Q estimates from seismic reflection data using well-log-based localized spectral correction: Geophysics, **69**, 1521–1529.

Hartigan, J. A., 1975, Clustering algorithms: John Wiley & Sons.

Hicks, G., and R. Pratt, 2001, Reflection waveform inversion using local descent methods: Estimating attenuation and velocity over a gas-sand deposit: Geophysics, **66**, 598–612.

Johnston, D. ., M. Toksoz, and A. Timur, 1979, Attenuation of seismic waves in dry and saturated rocks — Part 2: Mechanisms: Geophysics, **44**, 691–711.

Jun, H., J. Kwon, C. Shin, H. Zhou, and M. Cogan, 2017, Regularized Laplace-Fourier-domain full waveform inversion using a weighted L-2 objective function: Pure and Applied Geophysics, **174**, no. 3, 955–980.

Kamath, N., and I. Tsvankin, 2016, Elastic full-waveform inversion for VTI media: methodology and sensitivity analysis: Geophysics, **81**, no. 2, C53–C68.

Kamath, N., I. Tsvankin, and E. Diaz, 2017, Elastic full-waveform inversion for VTI media: A synthetic parameterization study: Geophysics, **82**, no. 5, C163–C174.

Kamei, R., and R. Pratt, 2013, Inversion strategies for visco-acoustic waveform inversion: Geophysical Journal International, **194**, no. 2, 859–884.

Keating, S., and K. A. Innanen, 2019a, Parameter crosstalk and leakage between spatially separated unknowns in viscoelastic full-waveform inversion: Geophysics, **85**, no. 4, R397–R408.

———, 2019b, Parameter crosstalk and modelling errors in viscoacoustic seismic full waveform inversion: Geophysics, **84**, no. 4, R641–R653.

Kelly, K. R., R. W. Ward, S. Treitel, and R. M. Alford, 1976, Synthetic seismograms: a finite-difference approach: Geophysics, **41**, 2–27.

Kurzmann, A., A. Przebindowska, D. Kohn, and T. Bohlen, 2013, Acoustic full waveform tomography in the presence of attenuation: A sensitivity analysis: Geophysical Journal International, **195**, 985–1000.

Liu, Z., 1997, An analytical approach to migration velocity analysis: Geophysics, **62**, no. 4, 1238–1249.

MacQueen, J. B., 1967, Some methods for classification and analysis of multivariate observations: Presented at the 5th Berkeley Symposium on Mathematical Statistics and Probability.

Malinowski, M., S. Operto, and A. Ribodetti, 2011a, High-resolution seismic attenuation imaging from wide-aperture onshore data by visco-acoustic frequency-domain full-waveform inversion: Geophysical Journal International, **186**, 1179–1204.

———, 2011b, High-resolution seismic attenuation imaging from wide-aperture onshore data by visco-acoustic frequency-domain full-waveform inversion: Geophysical Journal International, **186**, no. 3, 1179–1204.

Manukyan, E., H. Maurer, and A. Nuber, 2018, Improvements to elastic full-waveform inversion using cross-gradient constraints: Geophysics, **83**, no. 2, R105–R115.

Martin, G., K. Marfut, and S. Larsen, 2002, Marmousi-2, an updated model for the investigation of avo in structurally complex areas: 72nd Annual International Meeting, SEG, Expanded Abstracts,, 1979–1982.

Masmoudi, N., and T. Alkhalifah, 2018, Full waveform inversion in acoustic orthorhombic media and application to a north sea data set: Geophysics, **83**, no. 5, C179–C193.

Mavko, G., T. Mukerji, and J. Dvorkin, 2003, The rock physics handbook: tools for seismic analysis of porous media: Cambridge University Press.

Metivier, L., R. Brossier, S. Operto, and J. Virieux, 2015, Acoustic multiparameter FWI for the reconstruction of P-wave velocity, density and attenuation: Preconditioned truncated Newton approach: SEG International Exposition and 85th Annual Meeting, Expanded Abstracts, 1198–1203.

Millet, R., R. Sollie, and K. Hokstad, 1995, Prestack depth migration with compensation for absorption and dispersion: Geophysics, **60**, 1485–1494.

Moczo, P., J. Kristek, and L. Halada, 2004, The finite-difference method for seismologists. an introduction: Comenius University.

Mora, P., 1989, Inversion = migration + tomography: Geophysics, **54**, 1575–1586.

Neep, J. P., 1995, Robust estimation of P-wave attenuation from full waveform array sonic data: J. Seis. Expl., **4**, 329–344.

Odebeatu, E., J. Zhang, M. Chapman, E. Liu, and X. Y. Li, 2006, Application of spectral decomposition to detection of dispersion anomalies associated with gas saturation: The Leading Edge, **25**, 206–210.

Oh, J., M. Kalita, and T. Alkhalifah, 2018, 3d elastic full waveform inversion using p-wave excitation amplitude: Application to real obc data: Geophysics, **83**, no. 2, R129–R140.

Operto, J. S., P. Amestoy, J. Y. L'excellent, L. Giraud, and H. B. H. Ali, 2007, 3D finite-difference frequency-domain modeling of visco-acoustic wave propagation using a massively parallel direct solver: A feasibility study: Geophysics, **72**, no. 5, SM195–SM211.

Operto, J. S., A. Miniussi, R. Brossier, L. Combe, L. Metivier, V. Monteiller, A. Ribodetti, and J. Virieux, 2015, Efficient 3-D frequency-domain mono-parameter full-waveform inversion of ocean-bottom cable data: Application for Valhall in the visco-acoustic vertical transverse isotropic approximation: Geophysical Journal International, **202**, 1362–1391.

Operto, S., Y. Gholami, V. Prieux, A. Ribodetti, R. Brossier, L. Metivier, and J. Virieux, 2013, A guided tour of multiparameter full-waveform inversion with multicomponent data: from theory to practice: The Leading Edge, **32**, no. 9, 1040–1054.

Ouellet, G. F., E. Gloaguen, and B. Giroux, 2017, Time domain viscoelastic full waveform inversion: Geophysical Journal International, **209**, 1718—-1734.

Pan, W., and K. A. Innanen, 2019, Case History: Amplitude-based misfit functions in viscoelastic full-waveform inversion applied to walk-away vertical seismic profile data: Geophysics, **84**, no. 5, B335–B351.

Pan, W., K. A. Innanen, and Y. Wang, 2020, Parameterization analysis and field validation of VTI-elastic full waveform inversion in a walk-away vertical seismic profile configuration: Geophysics, **85**, no. 3, B87–B107.

Peters, B., Z. Fang, B. R. Smithyman, and F. J. Herrmann, 2015, Regularizing waveform inversion by projections onto intersections of convex sets: Presented at the 77th European Association of Geoscientists and Engineers Conference and Exhibition.

Peters, B., and F. Herrmann, 2017, Constraints versus penalties for edge-preserving full-waveform inversion: The Leading Edge, **36**, no. 1, 94–100.

Peters, B., B. R. Smithyman, and F. Herrmann, 2019, Projection methods and applications for seismic nonlinear inverse problems with multiple constraints: Geophysics, **84**, no. 2, R251–R269.

Plessix, R. E., 2006, A review of the adjoint-state method for computing the gradient of a functional with geophysical applications: Geophysical Journal International, **167**, no. 2, 495–503.

Plessix, R. E., and Q. Cao, 2010, A parametrization study for surface seismic full waveform inversion in an acoustic vertical transversely isotropic medium: Geophysical Journal International, **185**, 539–556.

———, 2011, A parameterization study for surface seismic full waveform inversion in an acoustic vertical transverssely isotropic medium: Geophysical Journal International, **185**, 539–556.

Plessix, R. E., A. Stopin, H. Kuehl, V. Goh, and K. Overgaag, 2016, Visco-acoustic Full Waveform Inversion: 78th European Association of Geoscientists and Engineers Conference and Exhibition, EAGE, Expanded Abstracts, 1–5.

Pratt, R. G., 1990, Inverse theory applied to multi-source cross-hole tomography: Geophysical Prospecting, **38**, 311–329.

———, 1999, Seismic waveform inversion in the frequency domain. Part 1: Theory and verification in a physical scale model: Geophysics, **64**, 888–901.

Pratt, R. G., Z. M. Williamson, and M. Warner, 1996, Two-dimensional velocity model from wide-angle seismic data by wavefield inversion: Geophysical Journal International, **124**, 323–340.

Prieux, V., R. Brossier, S. Operto, and J. Virieux, 2013, Multiparameter full waveform inversion of multicomponent ocean-bottom-cable data from Valhall field. Part I: Imaging compressional wavespeed, density and attenuation: Geophysical Journal International, **194**, 1640–1664.

Quan, Y., and J. M. Harris, 1997, Seismic attenuation tomography using the frequency shift method: Geophysics, **62**, 895–905.

Ristow, D., and T. Ruhl, 1994, Fourier finite-difference migration: Geophysics, **59**, no. 3, 1882–1893.

Robertsson, J. O., J. O. Blanch, and W. W. Symes, 1994, Viscoelastic finite-difference modeling: Geophysics, **59**, 1444–1456.

Rocha, D., and P. Sava, 2018, Elastic reflection waveform inversion with petrophysical model constrains: 88th Annual International Meeting, SEG, Expanded Abstracts, 1203–1207.

Sams, M., and D. Goldberg, 1990, The validity of Q estimates from borehole data using spectral ratios: Geophysics, **55**, 97–101.

Sava, P., and S. Fomel, 2003, Riemannian wavefield extrapolation: Geophysics, **70**, no. 3, T45–T56.

Schuster, G. T., and A. Quintus-Bosz, 1993, Wavepath eikonal traveltime inversion: Theory: Geophysics, **58**, 1314–1323.

Shen, P., and H. Calandra, 2005, One-way waveform inversion within the framework of adjoint state differential migration: SEG International Exposition and 75th Annual Meeting, Expanded Abstracts, 1709–1712.

Shen, Y., B. Biondi, and R. Clapp, 2018a, Q-model building using one-way wave-equation migration q analysis — part 1: Theory and synthetic test: Geophysics, **83**, no. 2, S93–S109.

———, 2018b, Q-model building using one-way wave-equation migration q analysis — part 2: 3D field-data test: Geophysics, **83**, no. 2, S111–S126.

Singh, S., I. Tsvankin, and E. Z. Naeini, 2018, Bayesian framework for elastic full-waveform inversion with facies information: The Leading Edge, **37**, no. 12, 866–944.

———, 2020, Full-waveform inversion with borehole constraints for elastic VTI media: Geophysics, **85**, no. 6, R553–R563.

Sirgue, L., and R. Pratt, 2004, Efficient waveform inversion and imaging: a strategy for selecting temporal frequencies: Geophysics, **69**, 231–248.

Sun, X., X. Tang, C. H. Cheng, and L. N. Frazer, 2000, P- and S-wave attenuation logs from monopole sonic data: Geophysics, **65**, no. 2, 755–765.

Symes, W. W., 2008, Migration velocity analysis and waveform inversion: Geophysical Prospecting, **56**, no. 6, 765–790.

Taillandier, C. M., M. Noble, H. Chauris, and H. Calandra, 2009, First-arrival traveltime tomography based on the adjoint-state method: Geophysics, **74**, WCB1–WCB10.

Tarantola, A., 1984, Inversion of seismic reflection data in the acoustic approximation: Geophysics, **49**, 1259–1266.

———, 1986, A strategy for nonlinear elastic inversion of seismic reflection data: Geophysics, **51**, 1893–1903.

———, 1988, Theoretical background for the inversion of seismic waveforms including elasticity and attenuation: Pure and Applied Geophysics, **128**, 365–399.

———, 2005, Inverse Problem Theory and Methods for Model Parameter Estimation: Society for Industrial and Applied Mathematics.

Tikhonov, A., and V. Arsenin, 1977, Solution of ill-posed problems: Winston and Sons.

Tiwari, U. K., and G. A. McMechan, 2007, Effects of incomplete parameterization on full-wavefield viscoelastic seismic data for petrophysical reservoir properties: Geophysics, **72**, no. 3, O9–O17.

Trinh, P. T., R. Brossier, L. Metivier, L. Tavard, and J. Virieus, 2019, Efficient time-domain 3D elastic and viscoelastic full-waveform inversion using a spectral element method on flexible Cartesian-based mesh: Geophysics, **84**, no. 1, P61–P83.

Tsvankin, I., 2012, Seismic signatures and analysis of reflection data in anisotropic media: Society of Exploration Geophysics.

Virieux, J., 1986, P-SV wave propagation in heterogeneous media: Velocity-stress finite-difference method: Geophysics, **51**, no. 4, 889–901.

Virieux, J., and S. Operto, 2009, An overview of full-waveform inversion in exploration geophysics: Geophysics, **74**, no. 6, WCC1–WCC26.

Wang, X., and I. Tsvankin, 2018, Methodology of waveform inversion for acoustic orthorombic media: Journal of Seismic Exploration, **27**, 201–226.

Warner, M., A. Ratcliffe, T. Nangoo, J. Morgan, A. Umpleby, N. Shah, V. Vinje, I. Atekl, L. Guasch, C. Win, G. Conroy, and A. Bertrand, 2013, Anisotropic 3D full-waveform inversion: Geophysics, **78**, no. 2, R59–R80.

Woodward, M. J., 1992, Wave-equation tomography: Geophysics, **57**, 15–26.

Wu, W. J., L. R. Lines, and H. X. Lu, 1996, Analysis of higher-order, finite-difference schemes in 3-D reverse-time migration: Geophysics, **61**, 845–956.

Wu, Z., and T. Alkhalifah, 2016, Waveform inversion for acoustic VTI media in frequency domain: SEG International Exposition and 86th Annual Meeting, Expanded Abstracts, 1184–1189.

Yang, P., R. Brossier, L. Metivier, J. Virieux, and W. Zhou, 2018, A time-domain preconditioned Truncated Newton approach to visco-acoustic multiparameter full waveform inversion: SIAM Journal on Scientific Computing, **40**, B1101–B1130.

Zhang, Z., and T. Alkhalifah, 2019, Regularized elastic full-waveform inversion using deep learning: Geophysics, **84**, no. 5, R741–R751.

Zhang, Z., T. Alkhalifah, E. Z. Naeini, and B. Sun, 2018, multiparameter elastic full waveform inversion with facies-based constraints: Geophysical Journal International, **213**, 2112–2127.

Zhang, Z., T. Alkhalifah, Z. Wu, Y. Liu, B. He, and J. Oh, 2019a, Normalized nonzero-lag crosscorrelation elastic full waveform inversion: Geophysics, **84**, no. 1, R1–R10.

———, 2019b, Normalized nonzero-lag crosscorrelation elastic full-waveform inversion: Geophysics, **84**, no. 1, R1–R9.

Zhou, H., 2003, Mustiscale traveltime tomography: Geophysics, **68**, no. 5, 1639–1649.

Zhu, T., J. M. Harris, and B. Biondi, 2014, Q-compensated reverse-time migration: Geophysics, **79**, no. 2, R471–R484.

Zhu, Y., and I. Tsvankin, 2006, Plane-wave propagation in attenuative transversely isotropic media: Geophysics, **71**, no. 2, T17–T30.

APPENDIX

PERMISSIONS FOR CHAPTERS

This appendix details the permissions to reproduce papers published with various publishers in the dissertation.

Permission to include work from Geophysics and from Geophysical Prospecting are shown in Figure A.1 and Figure A.2, respectively. The URL for permissions in Geophysics is `seg.org/Publications/Policies-and-Permissions/Open-Access-Policy`.

SEG Policy on Open-access Publishing

SEG provides authors a variety of open-access publishing options, including some "green" and "gold" open-access options.

SEG provides the world's premier vehicles for knowledge exchange in applied geophysics. The Society's publishing program is one such vehicle. To help attract the best scholarship and disseminate it to the widest possible audience through journals, meetings papers, and books, SEG provides authors a variety of open-access publishing options. These include some "green" open-access options that long have been features of the traditional subscription-based business model that has sustained the Society's publishing program.

In 2011, SEG went further by instituting a "gold" open-access option for its journals, transforming them into "hybrid" open-access journals. In exchange for payment of an author publication charge (APC) of US$2,500 plus payment of all applicable voluntary and mandatory page and color charges, SEG agreed to remove access barriers to full-text presentations of the author's paper on SEG publications sites. Standard copyright transfer was required.

Beginning with papers published in 2014, this gold open-access option is expanded with additional copyright and licensing options, and the policy also is extended to meetings papers and book chapters. These changes make all SEG publications compliant with requirements in place and emerging from a variety of research funders and their overseers, such as Research Councils UK (RCUK), the European Commission, and the U.S. Office of Science and Technology Policy. Also, some aspects of SEG's green open-access policy are refined.

In October 2015, the SEG Board of Directors approved a policy change removing the requirement of authors to pay all voluntary charges for open-access papers for papers submitted on or after 15 October 2015. Authors must pay mandatory charges and the $2,500 open-access fee.

Here are features of open-access options available to authors, or in cases of works made for hire, their employers:

Traditional publication (including green open access)

- No author publication charge (APC) is levied, although payment of mandatory page charges are assessed and payment of voluntary charges is requested. Relief from mandatory charges may be requested under SEG's hardship relief policy.
- Copyright is transferred to SEG.
- Authors/employers retain proprietary rights such as the right to patentable subject matter and the right to make oral presentation of the work with full citation and proper copyright acknowledgment.
- Authors/employers enjoy the right to prepare and hold copyright in derivative publications based on the paper provided that the derivative work is published subsequent to the official date of the original paper's publication by SEG.
- Authors/employers may post a final accepted version of the manuscript or the final SEG-formatted version (book chapters excluded) on authors' personal websites, employers' websites, or in institutional repositories operated and controlled exclusively by authors' employers provided that:
  1. the SEG-prepared version is presented without modification;
  2. copyright notice and a full citation appear with the paper;
  3. a link to the SEG version of record in the SEG Digital Library using Digital Object Identifier (DOI) permalinks is provided;
  4. the posting is noncommercial in nature, and the paper is made available to users without charge; and
  5. that notice be provided that use is subject to SEG terms of use and conditions.
- Authors/employers may not post their articles in an institutional repository or other site in which the content is required to carry or is implied as carrying a license contrary to SEG copyright and terms of use and terms of this policy.
- Authors/employers may post to their own websites a preprint (a version prior to SEG peer review) of a submitted manuscript provided that the posting is accompanied by prominent notice that the paper is under review for publication by SEG and the publication to which the manuscript has been submitted is identified. Upon publication of the paper by SEG, the author must replace any previously posted electronic versions of the paper with either (a) a full citation to the SEG-published work with a DOI permalink to the paper's abstract or (b) the final version of the manuscript or SEG-formatted version (book chapters excluded) subject to SEG conditions for such posting.
- Authors may reuse all or part of their papers published with SEG in a thesis or dissertation that authors write and are required to submit to satisfy criteria of degree-granting institutions.
- Authors/employers have the nonexclusive right, after publication by SEG, to give permission to third parties to republish print versions of the paper, or excerpts therefrom, without obtaining permission from SEG, provided that:
  1. the SEG-prepared version is not used for this purpose;
  2. the paper is not republished in another journal or book; and
  3. the third party does not charge a fee. Permission must be obtained from SEG for other republication of the paper.

Figure A.1: Permission from *Geophysics* hightlighted in yellow.

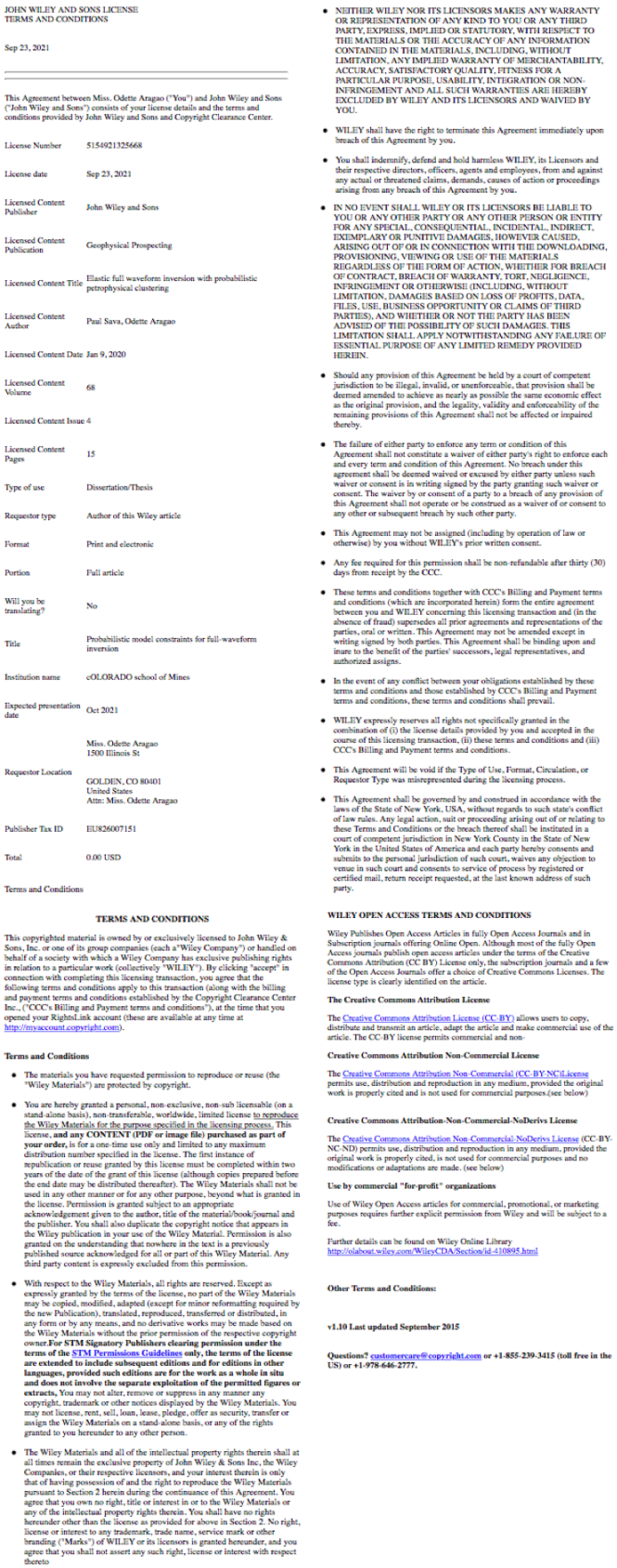

JOHN WILEY AND SONS LICENSE
TERMS AND CONDITIONS

Sep 23, 2021

This Agreement between Miss. Odette Aragao ("You") and John Wiley and Sons ("John Wiley and Sons") consists of your license details and the terms and conditions provided by John Wiley and Sons and Copyright Clearance Center.

License Number	5154921325668
License date	Sep 23, 2021
Licensed Content Publisher	John Wiley and Sons
Licensed Content Publication	Geophysical Prospecting
Licensed Content Title	Elastic full waveform inversion with probabilistic petrophysical clustering
Licensed Content Author	Paul Sava, Odette Aragao
Licensed Content Date	Jan 9, 2020
Licensed Content Volume	68
Licensed Content Issue	4
Licensed Content Pages	15
Type of use	Dissertation/Thesis
Requestor type	Author of this Wiley article
Format	Print and electronic
Portion	Full article
Will you be translating?	No
Title	Probabilistic model constraints for full-waveform inversion
Institution name	cOLORADO school of Mines
Expected presentation date	Oct 2021
Requestor Location	Miss. Odette Aragao 1500 Illinois St GOLDEN, CO 80401 United States Attn: Miss. Odette Aragao
Publisher Tax ID	EU826007151
Total	0.00 USD

Terms and Conditions

TERMS AND CONDITIONS

This copyrighted material is owned by or exclusively licensed to John Wiley & Sons, Inc. or one of its group companies (each a"Wiley Company") or handled on behalf of a society with which a Wiley Company has exclusive publishing rights in relation to a particular work (collectively "WILEY"). By clicking "accept" in connection with completing this licensing transaction, you agree that the following terms and conditions apply to this transaction (along with the billing and payment terms and conditions established by the Copyright Clearance Center Inc., ("CCC's Billing and Payment terms and conditions"), at the time that you opened your RightsLink account (these are available at any time at http://myaccount.copyright.com).

Terms and Conditions

- The materials you have requested permission to reproduce or reuse (the "Wiley Materials") are protected by copyright.
- You are hereby granted a personal, non-exclusive, non-sub licensable (on a stand-alone basis), non-transferable, worldwide, limited license to reproduce the Wiley Materials for the purpose specified in the licensing process. This license, **and any CONTENT (PDF or image file) purchased as part of your order**, is for a one-time use only and limited to any maximum distribution number specified in the license. The first instance of republication or reuse granted by this license must be completed within two years of the date of the grant of this license (although copies prepared before the end date may be distributed thereafter). The Wiley Materials shall not be used in any other manner or for any other purpose, beyond what is granted in the license. Permission is granted subject to an appropriate acknowledgement given to the author, title of the material/book/journal and the publisher. You shall also duplicate the copyright notice that appears in the Wiley publication in your use of the Wiley Material. Permission is also granted on the understanding that nowhere in the text is a previously published source acknowledged for all or part of this Wiley Material. Any third party content is expressly excluded from this permission.
- With respect to the Wiley Materials, all rights are reserved. Except as expressly granted by the terms of the license, no part of the Wiley Materials may be copied, modified, adapted (except for minor reformatting required by the new Publication), translated, reproduced, transferred or distributed, in any form or by any means, and no derivative works may be made based on the Wiley Materials without the prior permission of the respective copyright owner.**For STM Signatory Publishers clearing permission under the terms of the STM Permissions Guidelines only, the terms of the license are extended to include subsequent editions and for editions in other languages, provided such editions are for the work as a whole in situ and does not involve the separate exploitation of the permitted figures or extracts,** You may not alter, remove or suppress in any manner any copyright, trademark or other notices displayed by the Wiley Materials. You may not license, rent, sell, loan, lease, pledge, offer as security, transfer or assign the Wiley Materials on a stand-alone basis, or any of the rights granted to you hereunder to any other person.
- The Wiley Materials and all of the intellectual property rights therein shall at all times remain the exclusive property of John Wiley & Sons Inc, the Wiley Companies, or their respective licensors, and your interest therein is only that of having possession of and the right to reproduce the Wiley Materials pursuant to Section 2 herein during the continuance of this Agreement. You agree that you own no right, title or interest in or to the Wiley Materials or any of the intellectual property rights therein. You shall have no rights hereunder other than the license as provided for above in Section 2. No right, license or interest to any trademark, trade name, service mark or other branding ("Marks") of WILEY or its licensors is granted hereunder, and you agree that you shall not assert any such right, license or interest with respect thereto
- NEITHER WILEY NOR ITS LICENSORS MAKES ANY WARRANTY OR REPRESENTATION OF ANY KIND TO YOU OR ANY THIRD PARTY, EXPRESS, IMPLIED OR STATUTORY, WITH RESPECT TO THE MATERIALS OR THE ACCURACY OF ANY INFORMATION CONTAINED IN THE MATERIALS, INCLUDING, WITHOUT LIMITATION, ANY IMPLIED WARRANTY OF MERCHANTABILITY, ACCURACY, SATISFACTORY QUALITY, FITNESS FOR A PARTICULAR PURPOSE, USABILITY, INTEGRATION OR NON-INFRINGEMENT AND ALL SUCH WARRANTIES ARE HEREBY EXCLUDED BY WILEY AND ITS LICENSORS AND WAIVED BY YOU.
- WILEY shall have the right to terminate this Agreement immediately upon breach of this Agreement by you.
- You shall indemnify, defend and hold harmless WILEY, its Licensors and their respective directors, officers, agents and employees, from and against any actual or threatened claims, demands, causes of action or proceedings arising from any breach of this Agreement by you.
- IN NO EVENT SHALL WILEY OR ITS LICENSORS BE LIABLE TO YOU OR ANY OTHER PARTY OR ANY OTHER PERSON OR ENTITY FOR ANY SPECIAL, CONSEQUENTIAL, INCIDENTAL, INDIRECT, EXEMPLARY OR PUNITIVE DAMAGES, HOWEVER CAUSED, ARISING OUT OF OR IN CONNECTION WITH THE DOWNLOADING, PROVISIONING, VIEWING OR USE OF THE MATERIALS REGARDLESS OF THE FORM OF ACTION, WHETHER FOR BREACH OF CONTRACT, BREACH OF WARRANTY, TORT, NEGLIGENCE, INFRINGEMENT OR OTHERWISE (INCLUDING, WITHOUT LIMITATION, DAMAGES BASED ON LOSS OF PROFITS, DATA, FILES, USE, BUSINESS OPPORTUNITY OR CLAIMS OF THIRD PARTIES), AND WHETHER OR NOT THE PARTY HAS BEEN ADVISED OF THE POSSIBILITY OF SUCH DAMAGES. THIS LIMITATION SHALL APPLY NOTWITHSTANDING ANY FAILURE OF ESSENTIAL PURPOSE OF ANY LIMITED REMEDY PROVIDED HEREIN.
- Should any provision of this Agreement be held by a court of competent jurisdiction to be illegal, invalid, or unenforceable, that provision shall be deemed amended to achieve as nearly as possible the same economic effect as the original provision, and the legality, validity and enforceability of the remaining provisions of this Agreement shall not be affected or impaired thereby.
- The failure of either party to enforce any term or condition of this Agreement shall not constitute a waiver of either party's right to enforce each and every term and condition of this Agreement. No breach under this agreement shall be deemed waived or excused by either party unless such waiver or consent is in writing signed by the party granting such waiver or consent. The waiver by or consent of a party to a breach of any provision of this Agreement shall not operate or be construed as a waiver of or consent to any other or subsequent breach by such other party.
- This Agreement may not be assigned (including by operation of law or otherwise) by you without WILEY's prior written consent.
- Any fee required for this permission shall be non-refundable after thirty (30) days from receipt by the CCC.
- These terms and conditions together with CCC's Billing and Payment terms and conditions (which are incorporated herein) form the entire agreement between you and WILEY concerning this licensing transaction and (in the absence of fraud) supersedes all prior agreements and representations of the parties, oral or written. This Agreement may not be amended except in writing signed by both parties. This Agreement shall be binding upon and inure to the benefit of the parties' successors, legal representatives, and authorized assigns.
- In the event of any conflict between your obligations established by these terms and conditions and those established by CCC's Billing and Payment terms and conditions, these terms and conditions shall prevail.
- WILEY expressly reserves all rights not specifically granted in the combination of (i) the license details provided by you and accepted in the course of this licensing transaction, (ii) these terms and conditions and (iii) CCC's Billing and Payment terms and conditions.
- This Agreement will be void if the Type of Use, Format, Circulation, or Requestor Type was misrepresented during the licensing process.
- This Agreement shall be governed by and construed in accordance with the laws of the State of New York, USA, without regards to such state's conflict of law rules. Any legal action, suit or proceeding arising out of or relating to these Terms and Conditions or the breach thereof shall be instituted in a court of competent jurisdiction in New York County in the State of New York in the United States of America and each party hereby consents and submits to the personal jurisdiction of such court, waives any objection to venue in such court and consents to service of process by registered or certified mail, return receipt requested, at the last known address of such party.

WILEY OPEN ACCESS TERMS AND CONDITIONS

Wiley Publishes Open Access Articles in fully Open Access Journals and in Subscription journals offering Online Open. Although most of the fully Open Access journals publish open access articles under the terms of the Creative Commons Attribution (CC BY) License only, the subscription journals and a few of the Open Access Journals offer a choice of Creative Commons Licenses. The license type is clearly identified on the article.

The Creative Commons Attribution License

The Creative Commons Attribution License (CC-BY) allows users to copy, distribute and transmit an article, adapt the article and make commercial use of the article. The CC-BY license permits commercial and non-

Creative Commons Attribution Non-Commercial License

The Creative Commons Attribution Non-Commercial (CC-BY-NC)License permits use, distribution and reproduction in any medium, provided the original work is properly cited and is not used for commercial purposes.(see below)

Creative Commons Attribution-Non-Commercial-NoDerivs License

The Creative Commons Attribution Non-Commercial-NoDerivs License (CC-BY-NC-ND) permits use, distribution and reproduction in any medium, provided the original work is properly cited, is not used for commercial purposes and no modifications or adaptations are made. (see below)

Use by commercial "for-profit" organizations

Use of Wiley Open Access articles for commercial, promotional, or marketing purposes requires further explicit permission from Wiley and will be subject to a fee.

Further details can be found on Wiley Online Library http://olabout.wiley.com/WileyCDA/Section/id-410895.html

Other Terms and Conditions:

v1.10 Last updated September 2015

Questions? customercare@copyright.com or +1-855-239-3415 (toll free in the US) or +1-978-646-2777.

Figure A.2: Permission from John Wiley and Sons, publisher for *Geophysical Prospecting*.